

Environmental Effects on the Photophysics and Photochemistry of Some Aromatic Molecules

Roza Abdulrazaq Salih Al- Aqar

A PhD Thesis submitted to:

Newcastle University – School of Natural and Environmental
Sciences



December 2017

Declaration

I certify that this thesis titled “**Environmental Effects on the Photophysics and Photochemistry of Some Aromatic Molecules**” is my own work and effort has not previously been submitted for a degree or other qualification in this or any other university. Where other sources of information have been used, they have been acknowledged.

Roza Abdulrazaq Salih Al-Aqar

December 2017

Certificate of approval

I confirm that, to the best of my knowledge, this thesis is from the student's own work and effort, and all other sources of information used have been acknowledged. This thesis has been submitted with my approval and has been prepared under my supervision at the School of Natural and Environmental Sciences for the degree of PhD in Physical Chemistry.

Prof. Anthony Harriman

December 2017

Abstract

Aromatic molecules, especially polycyclic hydrocarbons, form a key cornerstone of molecular photophysics and have led to the identification of most of the main concepts, including excimer and exciplex formation. Derivatives of these compounds, most notably those including heteroatoms in the molecular framework, have expanded the field and provided many important applications. As such, the subject remains vibrant and progressive and there remains considerable interest in understanding the fundamental photophysical properties of aromatic molecules in solution and solid phases. In this thesis, we report the photophysical and photochemical properties of selected aromatic molecules with the intention of exposing the underlying environmental effects. The compounds have either been synthesized by specialist research groups or obtained from commercial sources.

Chapter 1 presents a summary of the photophysical properties of aryl hydrocarbons and considers some of the better known examples of how selective substitution affects these properties. The chapter draws heavily on literature citations and seeks to introduce some of the subtleties of the field, focussing on fundamental aspects. The key objective is to enquire into how small structural changes influence the photophysics of these molecules and to consider the further effects caused by a change in environment. Basic theoretical considerations, such as the energy-gap law and the Strickler-Berg expression, are covered and the importance of spin-orbital coupling is highlighted.

Chapter 2 is the first discussion chapter and deals with the structural dynamics and barrier crossing observed for a fluorescent O-doped polycyclic aromatic hydrocarbon. These materials are finding increasing applications in the emerging field of molecular-based organic electronics. It is shown that the oxygen atoms incorporated into the molecular backbone introduce unexpected flexibility such that the molecule functions as a fluorescent rotor. Temperature- and viscosity-dependence studies are used to calculate torsional barriers for the target molecule.

Chapter 3 continues the discussion by way of considering the quest for highly fluorescent chromophores and introduces 1H,3H-isochromeno[6,5,4-mna]xanthene-1,3-dione. This compound, synthesized in-house, shows classical photophysical behaviour and has been studied in a range of organic solvents and at different temperatures. As a small molecule, with a relatively high dipole moment, this highly planar, rigid dye absorbs at around 420 nm, which is ideal for excitation with a blue laser diode, and is extremely stable towards prolonged illumination. Under near-UV excitation, the dye readily sensitises free-radical polymerisation, forming a plastic film with excellent optical

transparency. Weakly structured emission is observed with a small Stokes' shift and remains essentially insensitive to changes in solvent polarity. For example, in tetrahydrofuran the fluorescence quantum yield is 0.96 while the excited-singlet state lifetime is 7.4 ns. Quantum chemical calculations provide further insight into the electronic nature of the dye in solution.

Chapter 4 represents a departure from the above approach and considers the fluorescence quantum yield of cresyl violet, a well-known emission standard for the red region. It is shown that this compound is highly susceptible to self-association in all solvents other than the smaller alcohols. The fluorescence quantum yield depends markedly on concentration, solvent polarity, temperature, etc. and we have attempted to quantify these various factors. The photophysical properties of cresyl violet are highly complicated and great caution should be exercised when using this compounds as a reference for fluorescence quantum yields.

Chapter 5 describes exciton migration and surface trapping for a photonic crystal displaying charge-recombination fluorescence. The compound of interest is highly polar and the emission properties in solution depend markedly on the polarity of the surrounding solvent. Somewhat unusually, single crystals of this compound are reasonably fluorescent under near-UV illumination due to relatively slow charge recombination. The crystal can be doped with Rhodamine B, but the added dye adsorbs into a surface layer rather than interchelating into the bulk of the crystal. Excitation of the crystal leads to intense fluorescence from Rhodamine B even at astonishingly low dopant levels. Kinetic studies are used to formulate a mechanism for exciton migration and trapping.

Chapter 6 describes the results collected for some water-soluble food dyes. The motivation for this work stems from a growing awareness of the need to avoid any kind of toxic compounds when developing practical applications. In fact, there are many dyes that have been used in the food industry for centuries and are believed to be essentially harmless. The cost and inconvenience inherent to testing new reagents for toxicity seems certain to cause renewed interest in these ancient dyes. Here, we explore the kinetics for photochemical bleaching of Phloxine B, Erythrosine, and Riboflavin in water. Some observations are raised regarding the relative stabilities and breakdown mechanisms. One of the systems studied here, namely the photolysis of Erythrosine, will form the basis of an undergraduate laboratory practical experiment.

Chapter 7 summarises the experimental methods used throughout this work. Materials were obtained through other sources but all the spectroscopic studies were completed in-house. Fluorescence spectroscopy has been the main workhorse and we have amplified the work by examining the effects of the surrounding medium on the emission properties of the target compound. Temperature has been varied from 77K to over 200 °C using different experimental set-ups while special adapters have

been designed for handling polymeric films or crystals. In all cases, the spectroscopic data were removed from the operating computer and analysed separately using homemade procedures. These are explained in the chapter.

Acknowledgements

In the Name of Allah, the Most Gracious, the most Merciful.

I would like to express my gratitude to Allah (God) for giving me the patience, strength, and aid to do this work.

I would like to give a special thanks to my supervisor professor Anthony Harriman for his guidance, encouragement, great support throughout my PhD research study. His patience and support helped me overcome many crisis situations and finish my thesis. I also want to thank to my second supervisor professor Andrew Benniston, for his advice. I would like to thank Dr. Corinne Wills and Dr. Paul Waddell for their assistance in NMR spectroscopy and X-ray crystallography analysis, respectively.

I would like to give a special thanks for the Molecular Photonics Laboratory members especially to Joshua Karlsson for his kindness and support.

My heartfelt thanks and gratitude to my family especially my beloved mother Khadeeja Hasan for her care and her continuous prayers for me and to my loved father Abdulrazaq Salih for his encouragement (God bless them both). Also many thanks to my beloved sister Afrodet Abdulrazaq for her extraordinary support, continues care, and for all the good times and memories.

I would like to say thank you for my sponsor the Higher Committee for Education Development in Iraq (HCED) for funding my study.

List of publications

1. Al- Aqar, R.; Avis, D.; Benniston, A. C.; Harriman, A. *RSC Adv.* **2014**, 4, 53072.
2. Al- Aqar, R.; Atahan, A.; Benniston, A. C.; Perks, T.; Waddell, P. G.; Harriman, A. *Chem. Eur. J.* **2016**, 22, 15420.
3. Al- Aqar, R.; Benniston, A. C.; Harriman, A.; Perks, T. *ChemPhotoChem.* **2017**, 1, 198.
4. Karlsson, J. K. G.; Woodford, O. J.; Al-Aqar, R.; Harriman, A. *J. Phys. Chem. A.* **2017**, 121, 8569.

Contents

Title page	i
Declaration	ii
Certificate of approval	iii
Abstract	iv
Acknowledgements	vii
List of publications	viii
Contents	ix
Chapter 1. Introduction	1
1.1 Background	2
1.2 Outline	3
1.3 New fluorophores	4
1.4 Charge recombination fluorescence	10
1.5 Self-association in the context of fluorescence	12
1.6 Photostability of organic dyes	18
1.7 Solid-state fluorescence	22
1.8 References	25
Chapter 2. Internal Geometry Changes and Barrier Crossing for an O-Doped Polycyclic Aromatic Hydrocarbon	31
2.1 Introduction	32
2.2 Optical properties of PXX in solution	36
2.3 Conclusion	53
2.4 References	54
Chapter 3. The quest for highly fluorescent chromophores: Evaluation of 1<i>H</i>,3<i>H</i>-isochromeno [6,5,4-<i>mna</i>] xanthene-1,3-dione (CXD)	59
3.1 Introduction	60
3.2 Background	62
3.3 Optical spectroscopy	64
3.4 Photochemical stability	71
3.5 Photo-induced polymerization	72
3.6 Afterthought	76
3.7 Conclusion	82
3.8 References	83

Chapter 4. Cresyl Violet: A Convenient Fluorescence Standard for the Red Spectral Region?	85
4.1 Introduction	86
4.2 Absorption and fluorescence spectral measurements in absolute ethanol	88
4.3 Effect of solvent	92
4.4 Optical properties for cresyl violet in water	101
4.5 Structure of the dimer	106
4.6 Conclusion	108
4.7 References	109
Chapter 5. A Small Organic Molecule Displaying Charge-Recombination Fluorescence in Liquid and Solid Phases	111
5.1 Introduction	112
5.2 Electrochemistry	114
5.3 Photophysical properties in the solution	115
5.4 Photochemical stability of MBIC	130
5.5 Protonation of the amino group	131
5.6 Photophysics of Crystalline MBIC	132
5.7 Conclusion	145
5.8 References	146
Chapter 6. Photochemical Bleaching of Certain Non-toxic Dyes in Aqueous Solution	151
6.1 Introduction	152
6.2 Erythrosine	153
6.2.1 Background	153
6.3 Phloxine B	160
6.4 Riboflavin	166
6.5 Conclusion	174
6.6 References	175
Chapter 7. Experimental Details	185
7.1 Materials	188
7.2 UV-Visible Absorption Spectroscopy	189
7.3 Emission Spectroscopy	190
7.4 Fluorescence Lifetime Measurements	192
7.5 Electrochemistry	193
7.6 Laser Flash Photolysis	194
7.7 Preparation of solid samples	194
7.8 Light-initiated Polymerization	195
7.9 Photo-bleaching Studies	195


7.10 Fluorescence Quantum Yield	196
7.11 Jablonski Diagram	197
7.12 Radiative Rate Constant.....	198
7.13 Non-radiative Decay	199
7.14 Vibrational Analysis.....	200
7.15 References	202
7.16 General conclusion and outlook.....	203

Chapter 1.

Introduction

Giacomo Luigi Ciamician: Father of Modern Molecular Photochemistry

Born	August 25, 1857(1857-08-25) Trieste, Austria
Died	January 2, 1922 (aged 64) Bologna, Italy
Education	University of Vienna
Employer	University of Bologna



His first photochemistry experiment was published in 1886 and was titled "On the conversion of quinone into quinol by light".

PROFESSOR CIAMICIAN IS OFTEN REFERRED TO AS THE FATHER OF PHOTOCHEMISTRY BECAUSE OF HIS PIONEERING EXPERIMENTS IN ITALY USING THE BRIGHT SUNSHINE.

1.1 Background

Photochemistry has been a recognised branch of science for several hundred years and began as a serious topic with the rooftop experiments of Ciamician in Italy between 1900 and 1914. His first publication in this new area was published in 1886 and was titled "On the conversion of quinone into quinol."¹ This type of outdoor research was continued in Egypt by Alexander Schönberg in the late 1930s. Schönberg, an exiled German scientist, used the endless sunshine of Cairo to drive his experiments.² Later, photochemistry moved indoors and made use of steady-state illumination provided by arc lamps. The laws of photochemistry began to appear during the early part of the twentieth century and a major advance followed the discovery of the triplet-excited state by Lewis and Kasha in 1944.³ Indeed, Kasha played a massive role in shaping the fundamental nature of photochemistry. Recognition of long-range electronic energy transfer by Forster⁴ in 1948 added a new dimension to the subject. The notion of interactions between widely spaced molecules was nothing short of revolutionary at the time. Dexter⁵ completed the concept of electronic energy transfer by reporting on electron exchange at close contact. Perhaps the single most important advance was introduced by Norrish and Porter⁶ when they announced the concept of flash photolysis. For the first time, it became possible to identify intermediate species by way of optical absorption spectroscopy and to monitor their decay kinetics. This technique, which has evolved from millisecond time resolution to monitoring events on timescales of less than 50 femtoseconds, has provided photochemistry with the most advanced tools needed to decipher reaction mechanisms. We are now, with the work of Zewail,⁷ able to monitor and detect transition states.

As photochemistry has evolved, so has our understanding of photobiology. It has been recognised for several centuries that photosynthesis requires light but slowly the underlying mechanisms responsible for plant growth have been unravelled. The reaction centres⁸ and light-harvesting antennae⁹ of plants and photosynthetic bacteria have been subjected to unparalleled investigation and the main components have been identified. Rates of light-induced electron transfer and electronic energy transfer have been delineated and used to suggest reaction pathways. The role of the protein matrices has been deduced and the energetics for the photochemical steps have been explored. We know now a great amount about how Nature controls the processes of photosynthesis but new discoveries continue to be reported. Electronic energy transfer across the Fenna-Matthews-Olsen complex,¹⁰ for example, is believed to involve quantum coherence. Other important processes, such as damage repair in DNA,¹¹ and the discovery of fluorescent proteins¹² continue to surprise the photochemist and to add to the mysteries of the subject.

Industrial photochemistry has been slow to follow the academic research but is now an important part of modern technology. Conducting polymers¹³ have been primarily responsible for the emergence of technological applications of photochemistry. Organic light-emitting devices¹⁴ are common nowadays and photodynamic therapy¹⁵ is an important tool in the fight against cancer. The urgent need for renewable energy sources has added impetus to the field of artificial photosynthesis. Computational photochemistry has also grown in stature and provides deep insight into likely reaction intermediates, such as conical intersections, pinhole sinks and multi-excitonic states. Excited state multiplication by way of singlet exciton fission¹⁶ brings further excitement to the field.

Photochemistry is in a healthy state. There is a constant need for new fluorophores and selective analytical reagents. Advanced spectroscopic tools continue to appear and computational methods become ever more user-friendly. The power of photochemistry, especially as an energy source, has been appreciated by politicians and the growth of photovoltaic panels seems to be assured. It is a good time to be working in the field.

1.2 Outline

This thesis is primarily concerned with the fluorescence properties of organic chromophores. In fact, fluorescence spectroscopy is a very well established subject with a wide variety of instrumentation available from commercial sources. Fluorescence is one specific form of luminescence, and can be classified as prompt, delayed or generated. The latter form includes chemiluminescence, electro-generated luminescence and so on. The term fluorescence was introduced by Stokes¹⁷ in the middle of the 19th century and the distinction from phosphorescence was made on the basis of the duration of the emission once the light source had been extinguished. The modern understanding of luminescence revolves around the Perrin-Jablonski diagram¹⁸ (Figure 1) which categorises emitting species according to their spin multiplicity. We now specify fluorescence as originating from a singlet-excited state and phosphorescence as emission from a triplet-excited state. Of course, paramagnetic species and lanthanide ions add complications because of their involvement of multiplet states. A nice account of the history of luminescence has been given by Valeur and Berberan-Santos.¹⁹ It might be noted in passing that the area around Newcastle played an important role in luminescence since this is where the first emissive minerals (e.g. fluorite) were discovered. Such minerals fascinated the public and much of the scientific community and required great ingenuity to decipher the origin of the luminescence effects. It is also pertinent to mention that applications of fluorescence appeared almost as soon as the first materials were discovered. One such application involved the fluorescence tube introduced by Becquerel in 1857.²⁰

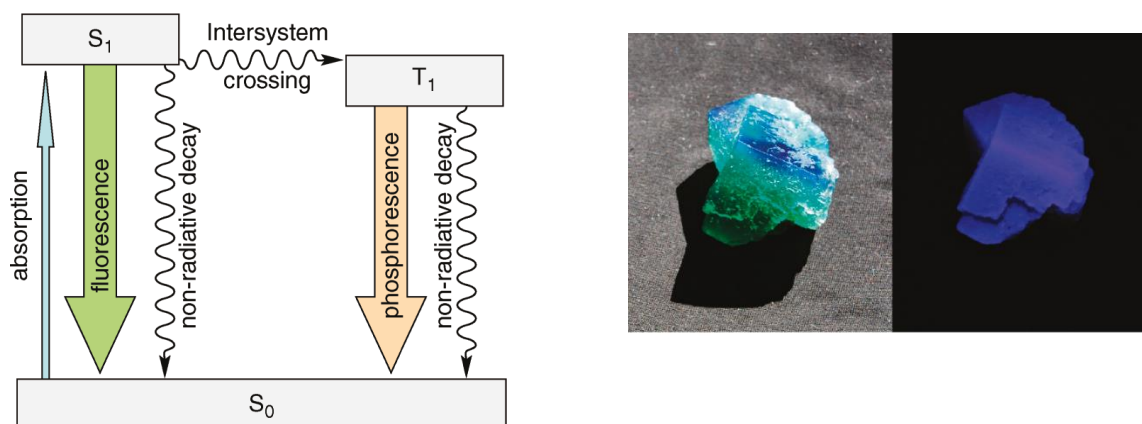


Figure 1. Example of a crude Perrin-Jablonski diagram (left-hand side) emphasizing the spin multiplicity of the states. The right-hand side shows the mineral known as fluorite under room light and black (i.e., UV) light.

Our work seeks to build on an enormous wealth of prior discoveries made in the general area of luminescence spectroscopy. We are concerned with several interrelated topics. Firstly, we consider the need for new organic fluorophores given the great number of such compounds already known in the literature. Then, we reflect on the special properties imported by dipolar compounds that undergo charge-recombination fluorescence. Thirdly, we give some thought to organic compounds that emit in the solid state, especially when in the form of crystals. How to quantify fluorescence by the ratiometric method is also considered, with reference to the red region of the spectrum. Next, we give some consideration to the problem of dimer formation, a process which usually loses fluorescence intensity. We look specifically at some dimeric fluorophores which emit. Finally, to be useful, organic fluorophores must be light-stable and readily available. Thus, we turn our attention to the photostability of some common organic chromophores. To complete this introduction we now address some of this topics and provide a small amount of background information taken from the literature.

1.3 New fluorophores

The drive for new fluorophores arises from several factors, mostly related to applications. The rules governing the photophysical properties of organic emitters were established many decades ago and there is not too much new information for us to learn. Increasing the stability and compatibility is of considerable importance in respect to designing improved fluorescent systems. Just as important is the need to identify compounds that absorb and emit at specific wavelengths. Inexpensive LED

excitation sources have fuelled the need to obtain quite specific excitation wavelengths while biological applications demand fluorophores emitting in the far-red region. Below we show a series of fluorophores each selective for a particular wavelength region (Figure 2). It will be noted that most of these dyes possess highly conjugated molecular backbones that render the dyes susceptible to attack by radicals and by singlet molecular oxygen.

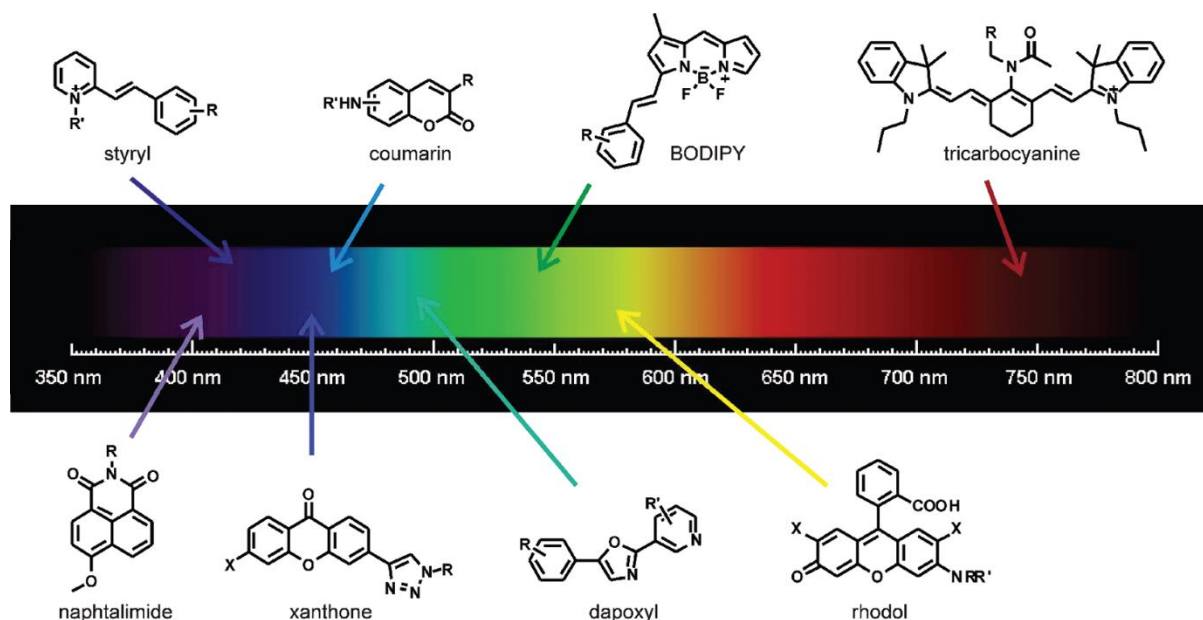


Figure 2. Examples of an organic fluorophores that absorb and emit at different parts of the electromagnetic spectrum. The figure is adapted from ref. 21.

In our laboratory, and indeed throughout the School of Chemistry at Newcastle University, the boron dipyrromethene (BODIPY) family of organic dyes²² has been prevalent. The first BODIPY studied at Newcastle was reported in 2005²³ and more than 70 publications have appeared in the subsequent years. These BODIPY compounds are easily functionalised (Figure 3) to give an army of derivatives. A characteristic feature of BODIPY is their very high fluorescence quantum yield, which approaches 100% in many cases. Triplet formation is hindered by poor spin-orbit coupling properties while the absorption maximum can be tuned over a very wide range by increasing the conjugation length. The latter is easily achieved by extending the aromatic core or by attaching unsaturated units to the periphery of the dipyrin residue.²⁴ An example of expanding the aromatic core is provided in Figure 4, while red-emitting dyes built by attaching styryl-like residues are also illustrated in the same figure.

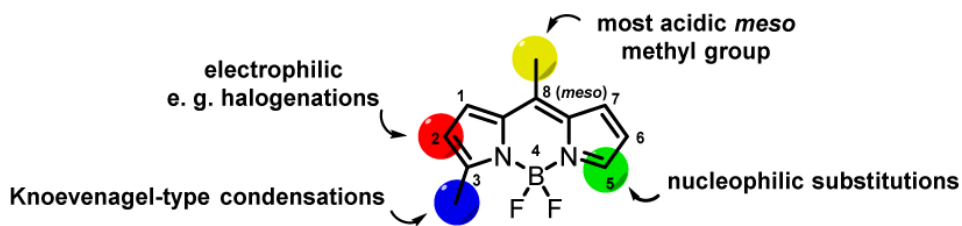


Figure 3. Generic framework pattern for the popular boron dipyrromethene family of dyes showing one of several common numbering systems and illustrating the most notable substitution sites. Note the position of the meso-site. Figure adapted from ref. 25.

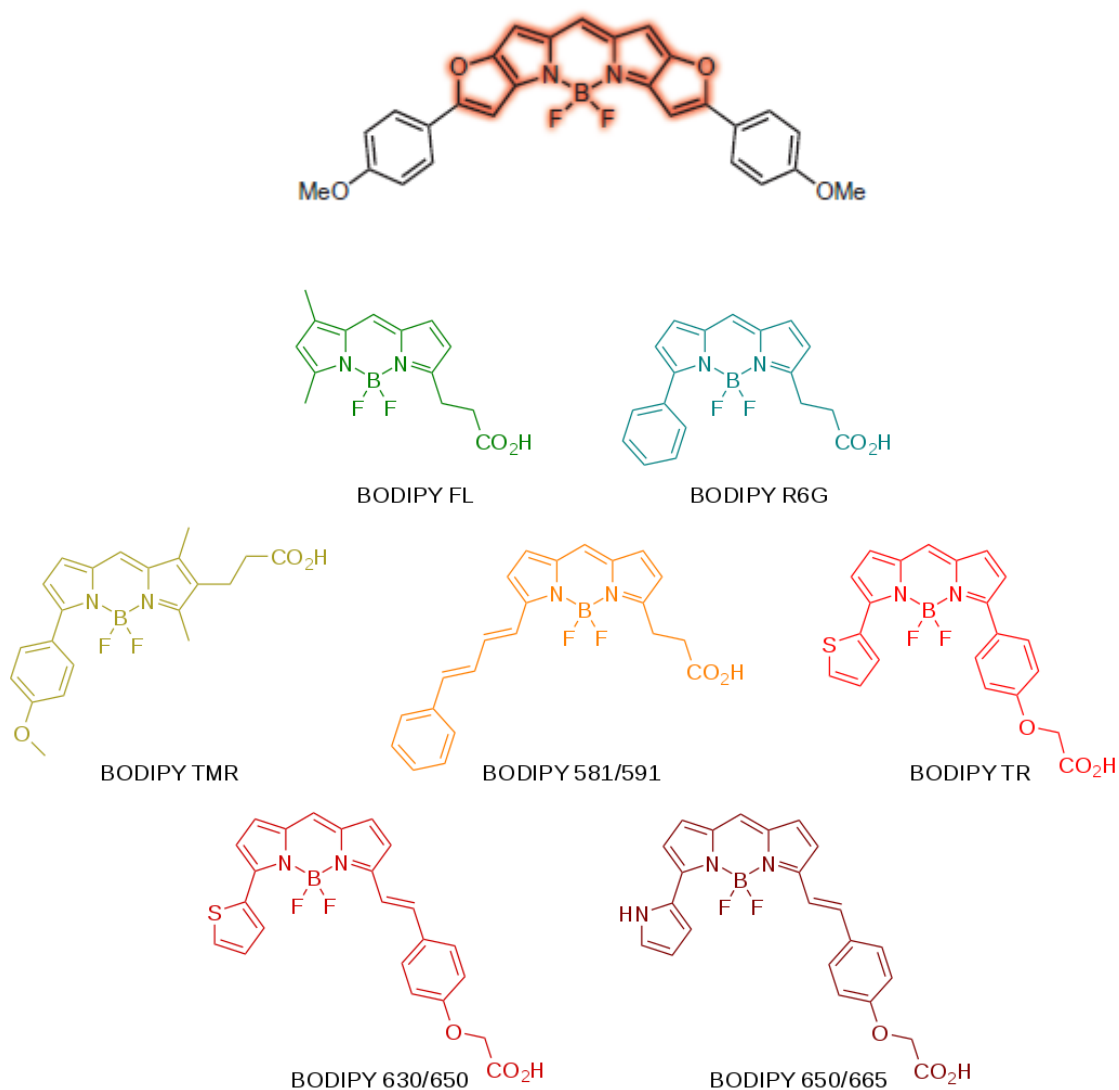


Figure 4. Illustration of a small part of the vast collection of BODIPY dyes available in the scientific literature. The upper panel is from ref. 26 while the lower panel is taken from ref. 27. The range of compounds shows ways to expand the aromatic core and thereby lower the excitation energy.

Below is illustrated a nice example of extending the conjugation length for a BODIPY dye.²⁸ Thus, the absorption and fluorescence maxima undergo substantial red shifts as the peripheral group is cyclised to the periphery of the dipyrin unit (Figure 5). At each stage, the bands move towards lower energy. Cyclisation helps to force the appendage into a planar geometry, thereby maximising the extent of π -conjugation. This strategy is much more powerful than simply linking the same substituent to the dipyrin in a way that facilitates simple rotation.

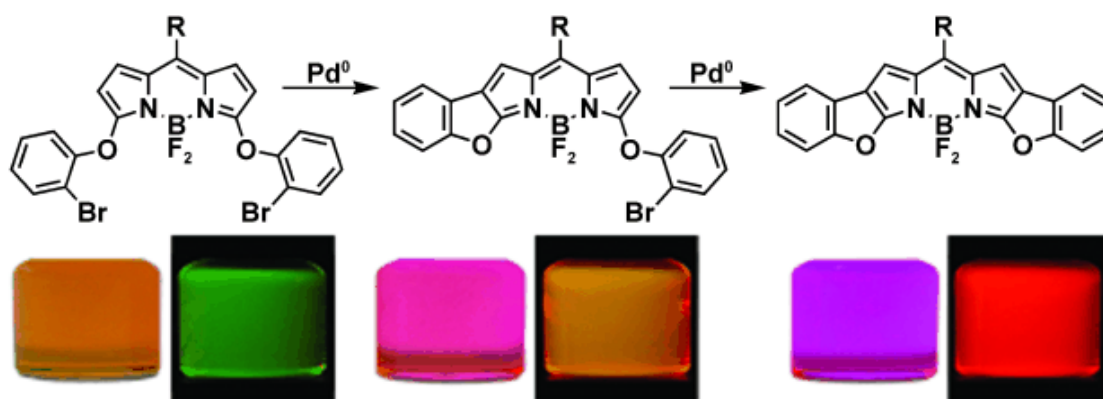


Figure 5. Example of sequential expansion of the dipyrin unit by cyclisation of an appended substituent. The panels below the chemical formula illustrate the colour observed under room light (i.e., absorption) and black (i.e., fluorescence).

A separate feature of conventional BODIPY dyes relates to the effect of including an unconstrained meso-phenyl ring.²⁹ Usually, the dipyrin unit is equipped with 1,7-methyl groups which serve the purpose of forcing the meso-phenyl ring into an almost orthogonal orientation. Steric hindrance with the substituents prevents the aryl group from completing a full rotation around the connecting C-C linkage. However, releasing the blocking methyl groups allows the phenyl ring to oscillate about the connection with a wide variance of dihedral angles. Full rotation is hindered by clashes between the respective hydrogen atoms but this is allowed if the dipyrin unit buckles slightly.³⁰ This steric distortion is possible at high temperature and in low viscosity medium but becomes increasingly hindered as friction with the surrounding medium increases. The net result is the construction of a molecular-scale rotor (Figure 6). The rotor can be used to monitor changes in temperature, pressure or viscosity. Following the original work by Holten et al.³¹ many related BODIPY-based molecular rotors have been discussed.

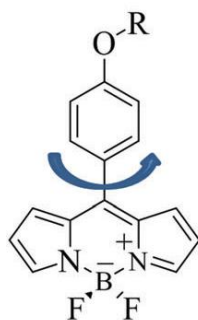


Figure 6. Example of a putative molecular-scale rotor for monitoring changes in local rheology. The logic behind the sensor is that the ease of rotation controls the fluorescence yield and, in turn, is controlled by frictional forces with the surrounding medium. See ref. 32 for a more complete description.

A further topic of great interest involving BODIPY dyes is the construction of modules able to display fast intramolecular electronic energy transfer (EET). Indeed, many BODIPY derivatives have been synthesized³³ whereby one or more aryl hydrocarbons are attached to the dipyrrolic core. Selective illumination into the appended aryl hydrocarbon is followed by rapid EET to the BODIPY fluorophore. The main purpose of such molecular dyads is to expand the Stokes shift,³⁴ which is rather small for BODIPY. Such properties are useful in fluorescence microscopy where filters are used to exclude stray excitation light from reaching the detector. A tremendous range of dyads has been reported over recent years, many equipped with pyrene residues as the energy donor. A few such derivatives are shown in Figure 7. The aryl hydrocarbon can be attached at the meso-position, through the dipyrrolic nucleus or by replacement of the B-F bonds. The latter strategy, termed “chemistry at boron”, was pioneered by Ziessel³⁵ and has proved to be extremely useful.

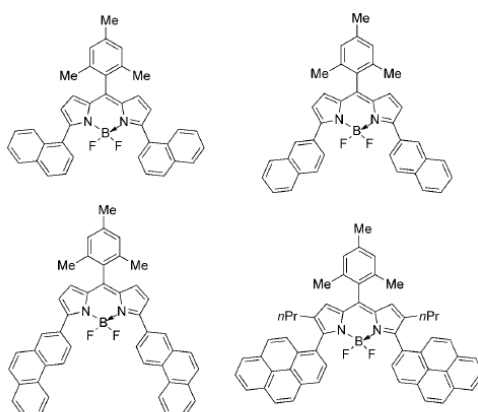


Figure 7. Selected examples of BODIPY derivatives fitted with ancillary aryl hydrocarbons that might display fast intramolecular EET (see ref. 36).

These cascade-type molecular dyads can also be used to construct clever analytical probes. An example is shown in Figure 8.³⁷ Here, excitation of the terminal BODIPY dye (Fluorophore 1) switches on rapid intramolecular EET to the second dye (Fluorophore 2). This second BODIPY dye, which absorbs and emits at longer wavelength, is equipped with a macrocycle. The presence of a nitrogen atom at the bridgehead of the macrocycle quenches fluorescence from Fluorophore 2 because of competing light-induced electron transfer. The effective electron donor is the lone pair of electrons localised on the N atom. This lone pair can be used to bind adventitious cations, such as mercury(II) ions, within the cavity of the macrocycle. As such, light-induced electron transfer is extinguished and Fluorophore 2 shows strong fluorescence. Many such fluorescent sensors are known.

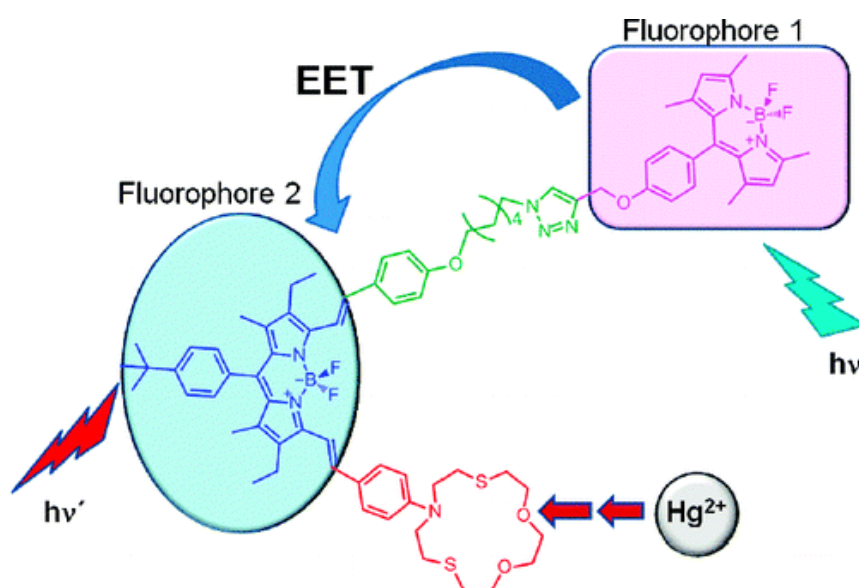


Figure 8. An example of a 3-component molecular sensor for added cations. Fluorescence from Fluorophore 2 is used to measure the concentration of added cation.

It is simply not possible to cover all of the interesting BODIPY-based dyes that have been reported in recent years. The subject is growing at a rapid rate. New derivatives appear weekly. The BODIPY family has been enlarged by addition of new members such as BOPHY³⁸ and BORANIL³⁹ and research in this area shows no sign of abating. Alternatives to BODIPY include dyes such as the xanthenes (Figure 9), which themselves show interesting properties. A strength of these dyes is their solubility in water, which makes them attractive as biochemical markers or sensitizers.

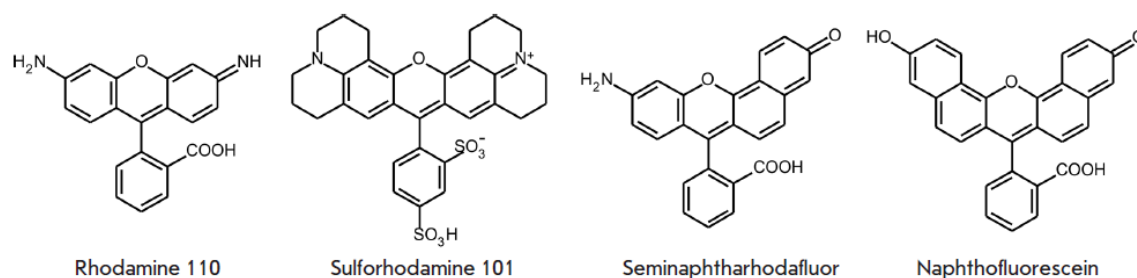


Figure 9. Examples of typical xanthene dyes used as fluorescent labels. The figure is adapted from ref. 40.

1.4 Charge recombination fluorescence

Many molecular dyads have been designed to undergo light-induced charge transfer upon excitation. The resultant charge-separated state is subject to fast recombination and/or intersystem crossing to the triplet manifold. This type of photochemistry represents the initial step in attempts to mimic natural photosynthesis and is of great importance. In certain cases, the charge-separated state can decay by way of fluorescence. Such cases invariably involve a change in geometry that minimises electronic coupling between the charges (Figure 10). Now, the fluorescence properties will be highly dependent on the polarity of the surrounding medium and its viscosity and on the nature of the reactants. This behaviour can be exploited to design interesting sensors. Over the past few years, many such dyads have been reported,⁴¹ including compounds based on the BODIPY framework.⁴² Here, we review a few of the well-known examples of molecules undergoing charge-recombination fluorescence in solution.

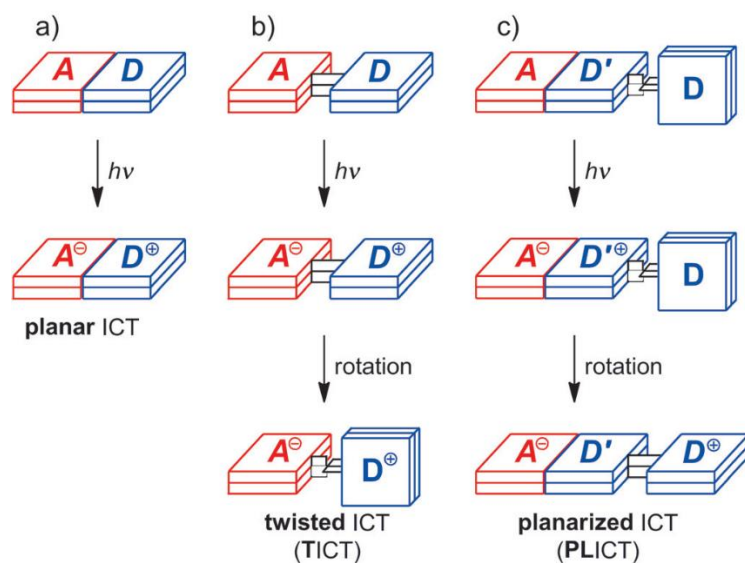


Figure 10. Generic illustration of light-induced twisted intramolecular charge-transfer (TICT) state formation in a molecular dyad. Illumination switches on charge transfer in competition to fluorescence. Often, this is accompanied by a substantial change in geometry to the TICT state that can fluoresce. The figure is adapted from ref. 43.

The change in geometry is quite crucial for this type of system and is further illustrated below in Figure 11. This refers to a somewhat different type of molecular system in as much as excitation generates a Franck-Condon state where the geometry is similar to that of the ground state. In competition to radiative decay, electron transfer can take place to form a charge-separated state. Only the locally-excited state is fluorescent; the charge-separated state undergoes nonradiative decay to reform the ground state or to populate the triplet manifold. The fluorescence properties are now controlled by the rate of charge separation, which should depend on the nature of the local environment. On rare occasions, the charge-separated state might fluoresce – thereby giving rise to dual fluorescence. The latter is very interesting and has the makings of an extremely sensitive fluorescence sensor. It is the equivalent of excimer or exciplex formation.⁴⁴

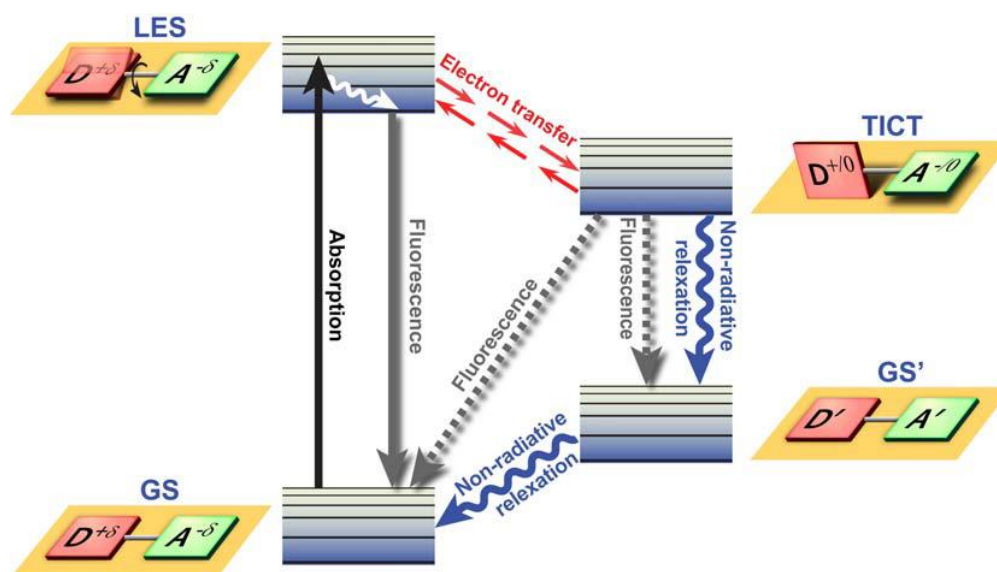


Figure 11. A further illustration of light-induced intramolecular charge transfer in a molecular dyad (adapted from ref. 45). Note the change in geometry that occurs after charge transfer. The so-formed TICT state can display fluorescence in competition with nonradiative deactivation for form either a locally-excited triplet state or the corresponding ground state.

1.5 Self-association in the context of fluorescence

It is common practice to use dilute (typically in the region of μM) solutions for steady-state fluorescence spectroscopy. This is to avoid problems from self-absorption and non-linearity with respect to absorption profiles, especially for fluorophores having high molar absorption coefficients. A further issue with higher concentrations relates to self-association of the emitter at the ground-state level. This particular problem first came to light when studying chlorophyll in solution as a crude representative of the light-harvesting antenna inherent to green plants and most photosynthetic bacteria. At the time, the detailed structure of the light-harvesting machinery was unknown and it was considered that the chlorophyll pigments were randomly embedded in a lipid matrix. Beddard and Porter⁴⁶ were the first to show that the fluorescence quantum yield for chlorophyll-a in solution decreased dramatically at higher concentrations, even after corrections for self-absorption. This effect was attributed to the formation of a non-fluorescence dimer at the ground-state level. This type of behaviour became regarded as normal and it is generally considered that dimers do not emit. In contrast, many planar molecules form fluorescent excimers, J-aggregates and H-aggregates under appropriate conditions. Nonetheless, abnormalities in fluorescence properties at elevated concentration are usually dismissed as dimer formation. As a side line, we note that the structure of light-harvesting antennae from plants is highly elaborate and it is clear that Nature takes immense

trouble to avoid direct contact between adjacent chlorophyll molecules.⁴⁷ This is achieved by using a protein matrix to position the pigments at very precise locations (Figure 12). We cannot hope to do the same in solution.

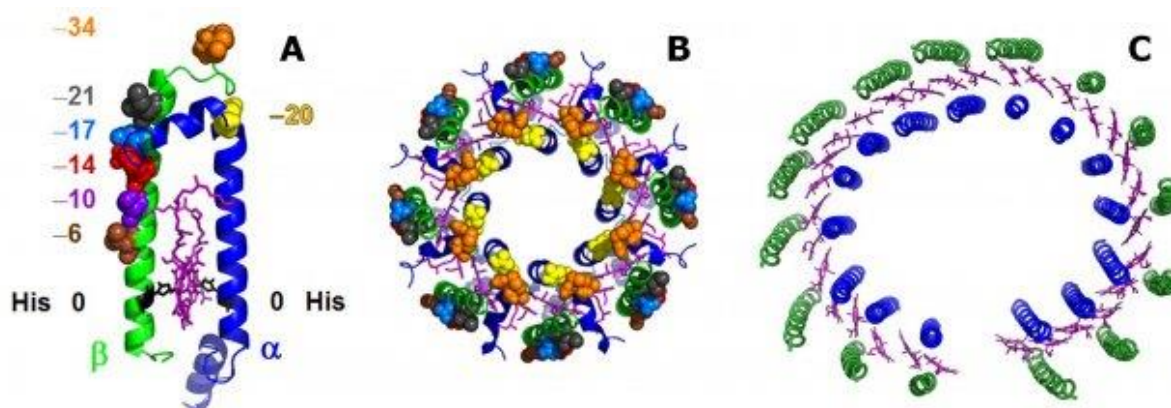


Figure 12. Various illustrations of the natural photosynthetic light-harvesting antenna. Slide A shows a segment of chlorophyll-carotene residue held in place by the protein. Slide B shows how a circle of chlorophyll-carotene residues is assembled to form an individual cluster of chromophores. Slide C indicates how sets of circles, each absorbing at different wavelengths, are assembled to improve the light-harvesting capacity. Adapted from ref. 48.

Dimer formation is usually apparent from significant changes in the absorption spectrum and from non-linear Beer-Lambert law plots. At higher concentration, the absorption spectrum of the dimer can be resolved. Often, this is split into higher- and lower-energy components according to the analysis introduced by Kasha.⁴⁹ The formation of such homo-dimers induces short (H-dimer) or long (J-dimer) wavelength shifts of the absorption spectrum and invariably leads to a loss of fluorescence. Some dimers, for example those formed from Rhodamine dyes,⁵⁰ retain some fluorescence in solution (Figure 13).

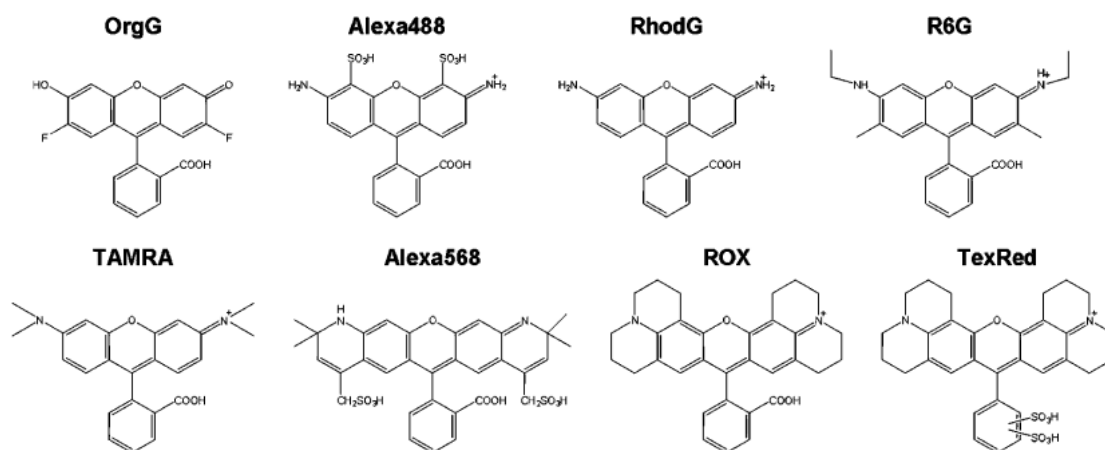


Figure 13. Chemical formulae for several Rhodamine fluorophores known to form fluorescent dimers in solution.

Kasha's excitonic coupling theory⁵¹ is widely used to analyse the absorption spectra for dimers in solution in order to determine structural parameters. A key feature of the analysis is that the mutual alignment of the transition dipole moment vectors is responsible for the splitting of the absorption profile into two bands. The ratio of oscillator strengths for these bands gives important information about the molecular alignment while the energy gap between the two bands tells us something about the distance between the two chromophores (Figure 14). To study the dimer in isolation from the respective monomers, it is common to synthesize covalently-linked bichromophores⁵² where self-association can be achieved at relatively low concentration. This situation is illustrated in Figure 15 for some BODIPY-based bichromophores.⁵³

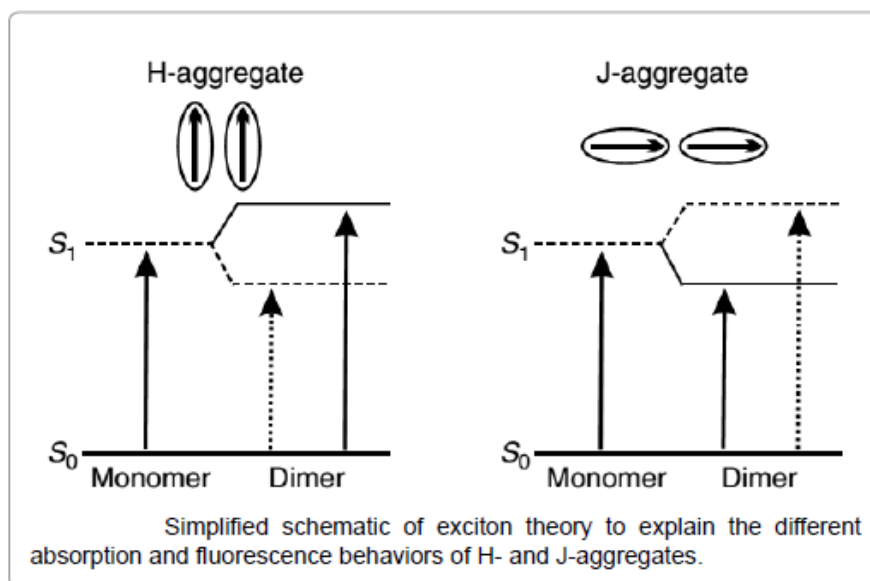


Figure 14. Illustration of the model developed by Kasha to explain the absorption spectra of molecular dimers. The figure is adapted from ref. 54.

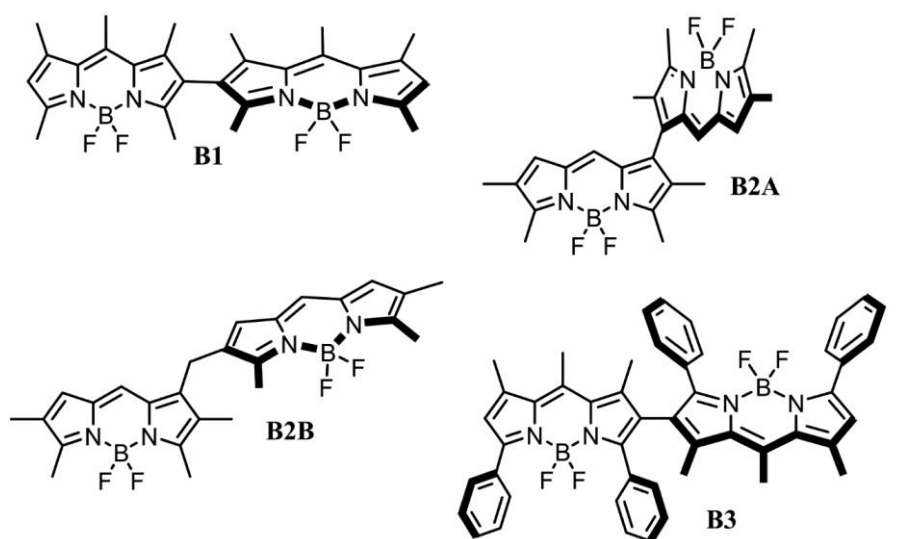


Figure 15. Chemical formulae for some BODIPY-based bichromophores used to confirm the applicability of Kasha's theory to molecular dimer formation. See ref. 53 for further details.

By careful design of the molecular system, it is possible to achieve quite complex structures in solution. An interesting case is shown in Figure 16 for some interlocking perylene molecules.⁵⁵ Here, a covalently-linked bichromophore is built in such a way that the two perylene units are held too far apart to form a dimer. However, on increasing the concentration, two bichromophores approach each other and form an interlocked tetramer. The individual perylene units can associate in such a way as

to maximise orbital overlap. Such structures are highly sensitive to the nature of the solvent and are formed only in those solvents that disfavour solubility.

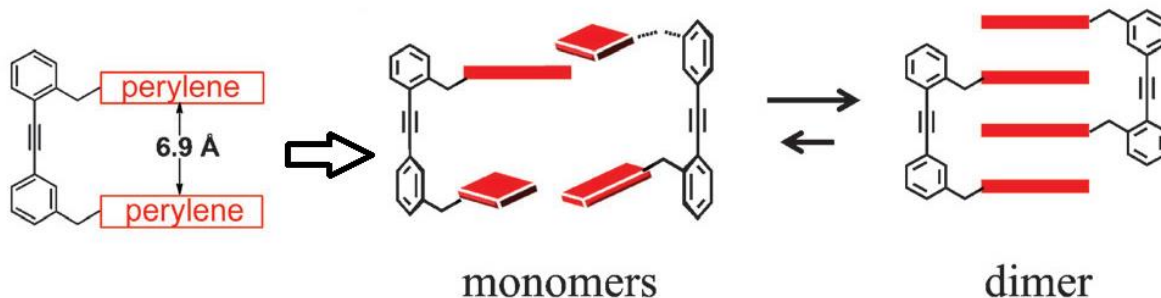


Figure 16. Schematic representation of the self-association pattern for the perylene-based bichromophore described in ref. 55. It is not possible for the two perylene residues in a single bichromophore to form a “dimer” but association of two bichromophore molecules facilitates assembly of the “tetramer”.

Other means of inducing dimer formation include equipping the dye with the necessary functions for efficient hydrogen bond formation.⁵⁶ This weak interaction brings together the chromophores in a way that favours their mutual association. This is a good way to generate hetero-dimers. An interesting example of hydrogen bond based aggregation is illustrated in Figure 17. Here, an amino-based dye is attached at both ends of a short polymer chain. On dispersing the molecule in certain solvents, the terminal dyes enter into hydrogen bonding interactions with a second dye, creating a complex network of entangled chains.⁵⁷ The weak interaction between the dyes allows fluorescence.

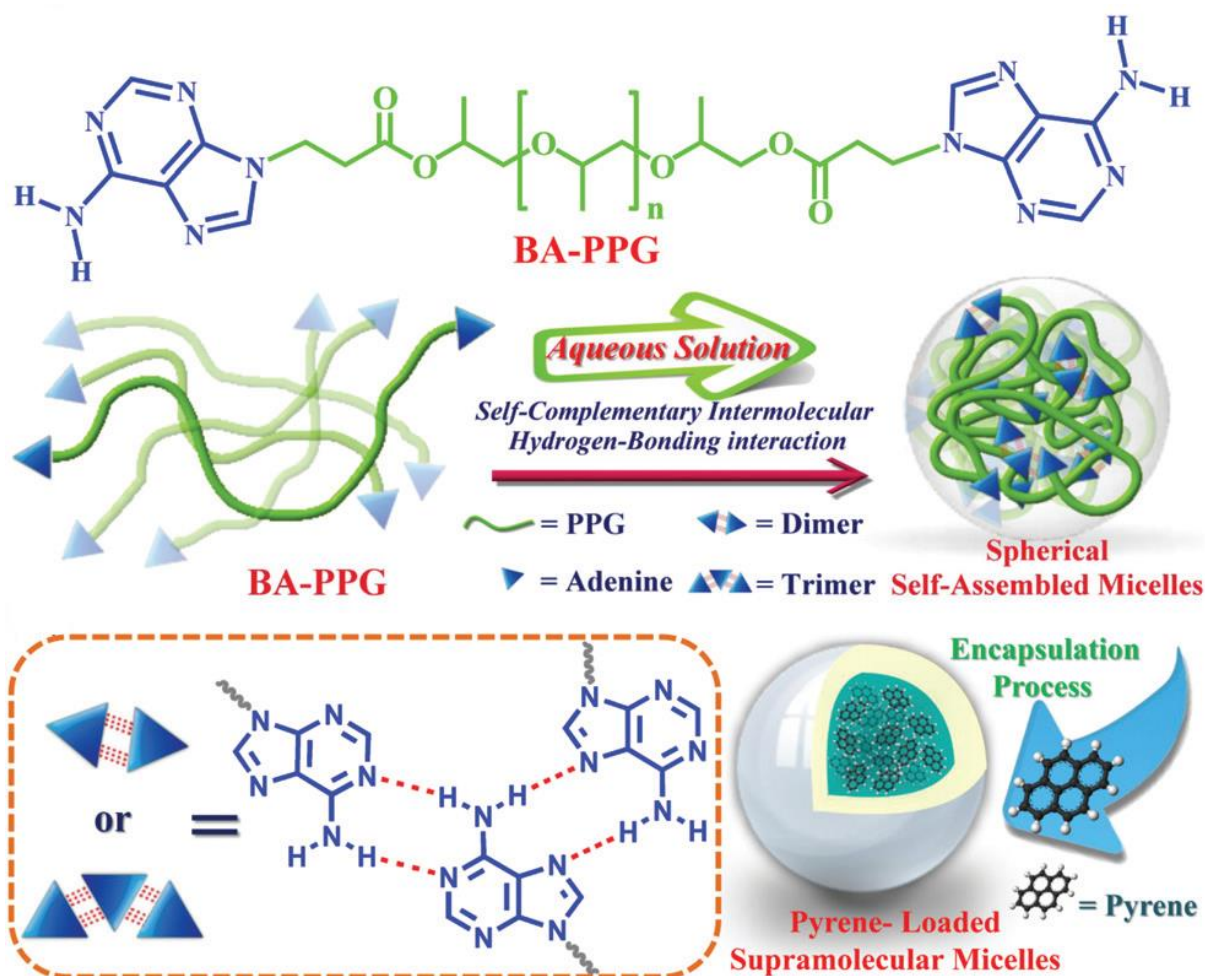


Figure 17. Pictorial representation of chain entanglement induced by hydrogen bond formation. See ref. 57 for a full description of this effect. The entangled network is considered to provide a micelle-like sphere that can solubilise added solutes, like pyrene.

A common approach to modifying the structure of organic dyes to facilitate solubility in water is to attach ionic groups to the periphery. The preferred group is a sulfonic acid residue. This group localises the charge and has minimal effect on the electronic properties of the dye. As a water-solubilising entity, the sulfonic acid residue is reasonably effective but it often requires more than one such group per dye molecule. Even then, dimer formation is a common occurrence. A way around this problem is to use a micellar distribution to solubilise the neutral dye. Alternatively, cationic charges can be introduced by incorporating aza nitrogen groups into the molecular backbone. In fact, a multitude of dyes has been generated using this latter strategy. The synthetic procedure usually introduces two aza groups per dye molecule and this sets up a series of resonance forms with the positive charge oscillating between two nitrogen atoms. Examples of this type of dye are shown in Figure 18.

These oxazine dyes are strongly fluorescent,⁵⁸ weakly soluble in water and sensitive to self-association in solution. They have been studied in detail⁵⁹ because of their interesting fluorescence properties and

because several derivatives intercalate into DNA. Later in this thesis, we raise the likelihood that cresyl violet forms strongly emissive dimers in water. Part of the interest in these oxazine dyes stems from the fact that their absorption and emission maxima fall in the far-red region. There are not so many water-soluble dyes available for this spectral window and cresyl violet,⁶⁰ in particular, has found great popularity as a fluorescent standard. Facile dimerization is obviously an issue for a standard compound.

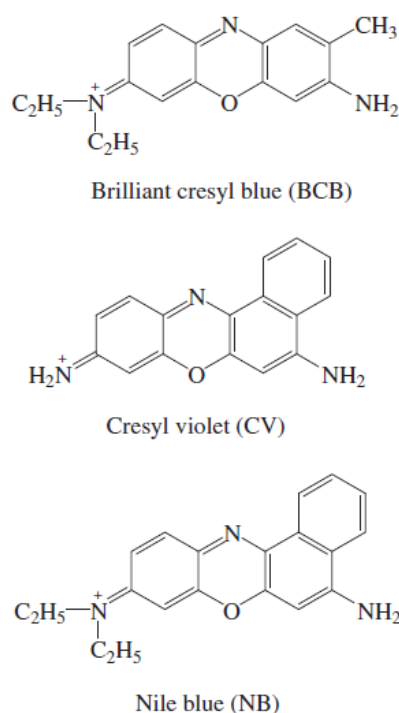


Figure 18. Representative chemical formulae for popular oxazine dyes that undergo self-association in water. The figure is adapted from ref. 61.

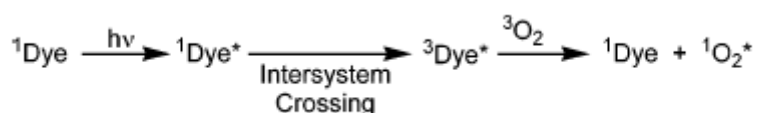
1.6 Photostability of organic dyes

It seems that barely a day goes by without there being a report of a “new application” for a particular fluorescent dye. Often, the molecular structure is complex with multiple components that need to operate in sequence. Such compounds are expensive to synthesize and are usually available only in small quantities. To make matter worse, the application requires the user to record the fluorescence intensity as a function of time but no consideration is given as to the stability of the dye. Instead, the introduction to the work contains a sentence along the following lines: “The fluorescent centre is based on the BODIPY motif which is well known to be robust, highly fluorescent and photostable.” Such sentiments have little value. There are, in fact, few detailed studies about the photostability of organic dyes under operating conditions. Some dyes are undoubtedly stable towards light and, to be fair, some applications might require the dye to disappear once its job is done. In natural

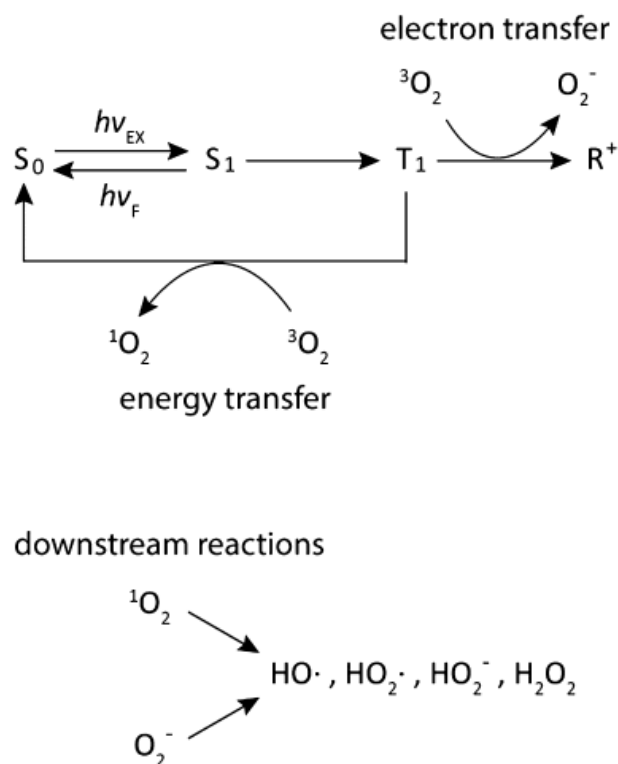
photosynthesis, the pigments are destroyed during the autumn only to re-appear the following spring. Almost no attention has been given to the possibility of restoring artificial chromophores that have faded on exposure to light. It is more common to restrict the exposure time such that photochemical bleaching is not a problem on that time scale.

Photochemical bleaching can be useful. For example, the process known as Fluorescence Recovery After Photofading (FRAP)⁶² is a method used routine in biochemistry to measure diffusion coefficients. Photodegradable plastics are invaluable in the fight against urban pollution. Photo-activators used to initiate paint drying or polymerisation need to fade under near-UV light so as to avoid discolouring the medium. In other cases, screens or filters can be employed to offset the damage caused by long illumination periods but, unlike natural systems, we have not developed systems that can be repaired. There is a need, therefore, to better understand the photo-fading process so that it might be minimized.

The term “photobleaching” (or photo-fading) refers to those systems where the chromophore is converted into a colourless species under illumination. The process might involve several distinct steps, leading to the involvement of coloured intermediates, or pass directly to a transparent product without obvious involvement of intermediates. This latter case probably means that any intermediates bleach faster than does the original chromophore so they do not contribute to the overall absorption spectrum. The most common type of photochemical bleaching involves molecular oxygen as a critical reactant⁶³ (Scheme 1). This is most conveniently achieved by invoking a long-lived triplet-excited state of the chromophore. The triplet can react with molecular oxygen by way of electronic energy transfer to form singlet molecular oxygen. This species is highly reactive towards unsaturated bonds. An alternative reaction involves electron transfer from the triplet state to oxygen to form the superoxide ion (Scheme 2). The latter is an excellent bleach. Subsequent reactions of the activated oxygen species leads to attack on the ground-state chromophore resulting in loss of conjugation.



Scheme 1. Generic scheme to indicate the usual method for producing singlet oxygen via a photosensitised process. The scheme is adapted from ref. 64.



Scheme 2. Reactive oxygen species formed *via* the reactions between molecular oxygen ($^3\text{O}_2$) and the sensitizer. The scheme is adapted from ref. 65.

Singlet-excited states are more resistant towards photochemical bleaching⁶⁶ but this happens easily when the light source is delivered via a microscope. The high photon density achieved under these conditions favours singlet-singlet annihilation, leading to light-induced electron transfer. Such steps are believed to be important for the photobleaching behaviour of perylene diimide (PDI) and terrylene diimide (TDI) derivatives (Figure 19).⁶⁷ In such cases, the bleaching chemistry populates a dark state which, in part, recovers to regenerate the original chromophore. Under the microscope, this recovery leads to fluorescence blinking and, with cyanine dyes,⁶⁸ is the basis for super-resolution microscopy.

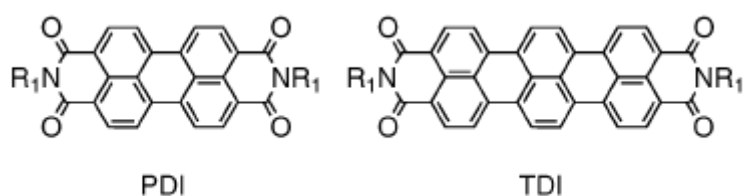


Figure 19. The chemical structures of perylene diimide (PDI) and terrylene diimide (TDI).

In the presence of substrates, such as proteins, activated oxygen can react to form various oxy-radicals which can cause substantial levels of photobleaching. Such chemistry can involve chain reactions because of the proliferation of free radicals. These processes are difficult to stop once initiation has taken place but, in certain cases, can be used productively. We refer to processes such as photodynamic therapy (PDT) where singlet oxygen is deliberately entered into the system to cause the maximum amount of destructive damage. Apart from destroying tumours, PDT can be used to demolish stocks of unwanted chemicals and to breakdown polymer residues. In such cases, the chromophore is quickly lost from the system. A quite different case where photochemical bleaching can be useful is in the form of photochemical actinometers (Figure 20). Here, bleaching is progressive and, by comparing the residual colour at different stages of illumination, it is possible to determine the exposure time or the number of absorbed photons.

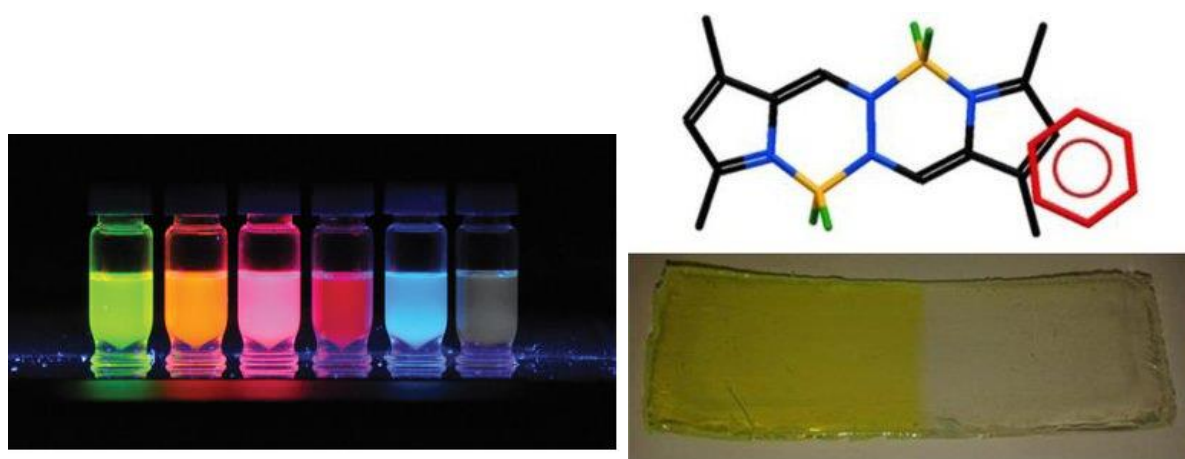


Figure 20. Examples of photochemical actinometers according to refs. 69 and 70. On the left, we have fluorophores across the visible spectrum can be engineered to be ever more photostable. On the right we have a film doped with BOPHY and subjected to progressive amounts of sunlight. The film undergoes irreversible bleaching.

Somewhat surprisingly, little attention has been given to the design of photosystems that are highly resistant to photochemical degradation. Industrial systems tend to load up the medium, usually a plastic mould, with stabilizer in the hope that this will prevent degradation. Anti-oxidants can help minimise the effects of damaging free radicals but such approaches will only delay the inevitable. Removal of molecular oxygen and moving to the solid state are obvious ways to gain temporal relief from photochemical damage but it seems that much more ingenuity is needed to develop really stable systems. One clear rationale is that short-lived excited states are less prone to photochemical damage than are longer-lived species. Thus, if the rate constant for destruction is fixed, it is less likely to compete with other deactivation processes if the rate of these reactions is fast. This basic strategy has been demonstrated⁷¹ using a multi-component molecular system that displays sequential EET steps.

In this case, the excited-state lifetime of the pigments undergoing EET is kept very short but the lifetime of the terminal acceptor remains long. Bleaching occurs selectively at the terminal acceptor. Once this species is destroyed, the next member of the cascade begins to fade under illumination. This is a very nice demonstration of how the excited-state lifetime plays a key role in minimising the effects of photochemical damage.

It has also been shown recently that autocatalysis⁷² can be very important in photodegradation of dyes.⁷³ Thus, the products formed upon bleaching of the chromophore can promote further breakdown of the chromophore. This is a critical discovery because it emphasizes the need to study photodegradation processes over extremely long timescales and not extrapolate from short exposures. A difficulty for advancing this subject is that quantum yields for photobleaching might be very low and this makes it difficult to evaluate certain reaction mechanisms. Multiple products are likely to be formed in low yield and analysis is therefore difficult. Imaginative ways to stabilise chromophores are needed and some attention needs to be given to the possibility to recover and repair the damaged chromophores. These are important challenges for the near future. One interesting system⁷⁴ along these lines is shown in Figure 21. Here, the starting compound is a perylene-BODIPY dyad but illumination leads to formation of a long-wavelength absorbing chromophore that displays high stability. Perhaps further such systems will be reported soon.

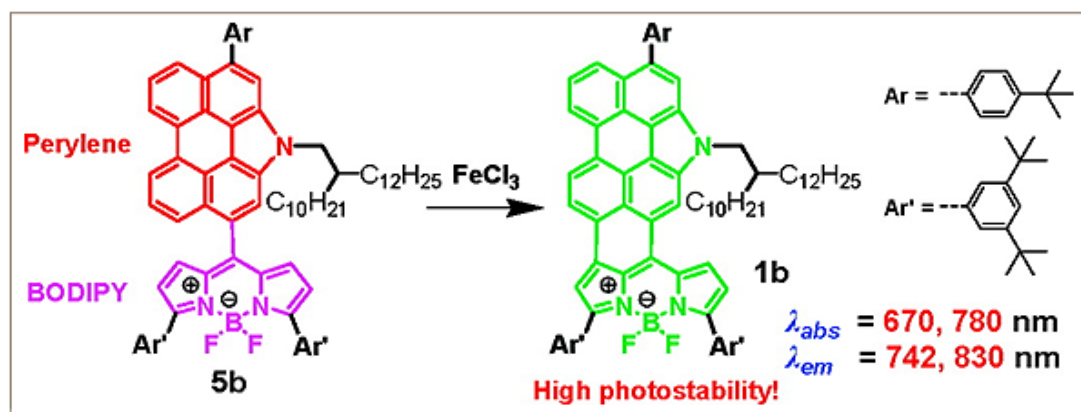


Figure 21. Example of a photoactive dyad where exposure to light leads to improved photostability through formation of an inert product. Adapted from ref. 74.

1.7 Solid-state fluorescence

There is no reason why fluorescence should be turned off by moving the emitter from solution to the solid state. Indeed, a vast array of fluorescent plastics and papers have been developed for many different industrial applications. Notable among these devices are the luminescent solar concentrators (LSCs)⁷⁵ which can be applied to sensitise solar cells and such materials. Here, the idea

is that total internal reflection prevents most of the fluorescence from escaping from the flat surfaces of the plastic sheet and instead it is concentrated at the edges.⁷⁶ Unfortunately, these systems tend to suffer badly from self-absorption and the inner-filter effect. Apart from plastics, dispersion of the emitter in other media, such as powders, proteins, DNA, micelles, etc, leads to strong fluorescence in the solid state. A key feature of these systems is that the monomeric form of the fluorescent reagent is isolated in the solid host. A more challenging case concerns the development of fluorescent crystals.⁷⁷

The main problem with detecting fluorescence from crystalline materials relates to the introduction of electronic interactions due to the close packing of the molecules. New types of nonradiative decay channels are introduced that compete effectively with radiative decay. Although certain dyes form fluorescent J-aggregates,⁷⁸ the resultant fluorescence profiles do not resemble those of the isolated molecule. Even so, some materials do exhibit quite strong fluorescence from the crystal. An example is shown in Figure 22, which is a small molecule that displays charge-recombination fluorescence.⁷⁹ The molecule is dipolar and crystallises in a structure that keeps the individual molecules apart. In this case, the fluorescence spectrum is not too far removed from that of the isolated molecule. A second example of a fluorescent crystal⁸⁰ involves a sterically constrained BODIPY emitter (Figure 23). This molecule is forced out of planarity by the strap and again the crystal packing diagram indicates that adjacent dye molecules are kept in some isolation. The result is weak emission from the crystal.

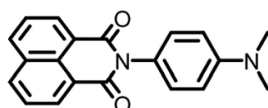


Figure 22. Chemical formula of a molecule showing charge-recombination from single crystals.

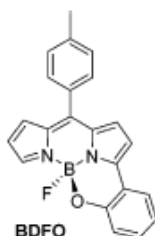


Figure 23. The chemical structure for the constrained BODIPY derivative (BDFO) known to fluoresce in the crystalline state.

Pigment Yellow⁸¹ is an example of a relatively large molecule that fluoresces in the crystalline state.⁸² This is an interesting molecule (Figure 24) because it is planar and has the features of molecules that

tend to stack in the solid state. A key feature of this system concerns the role of the substituents in controlling the crystal packing.

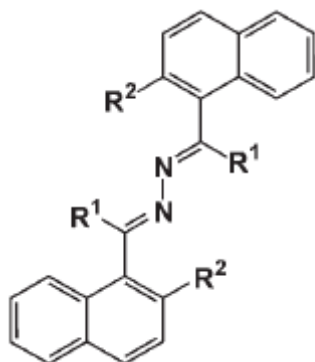


Figure 24. The chemical structure of Pigment Yellow.

Several alternatives have been designed to isolate the emitting molecules in the solid state. These include incorporating the fluorophores into porous or microheterogeneous media. This includes the use of zeolites⁸³ to accommodate the guest emitters inside the channels. Other methods of obtaining isolation include encapsulating the dye inside the cavity of an organic superstructure, such as a cyclodextrin.⁸⁴ Interesting structures can be devised in this way, including rotaxanes⁸⁵ and molecular logic gates.⁸⁶ An interesting feature of these solid-state emitters has been the recognition that, in certain cases, increased selectivity can be achieved for certain recognition patterns. This effect is illustrated below in Figure 25.

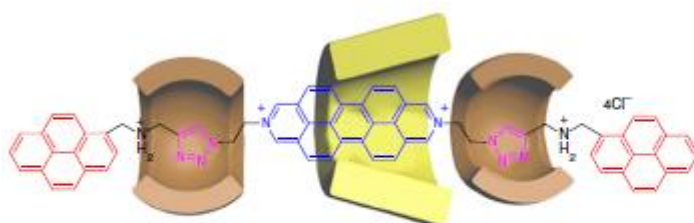


Figure 25. The structure of heterorotaxane formed by trapping a fluorescent organic compound inside a cyclodextrin cavity and capping the ends to avoid losing the sugar. The figure is adapted from ref. 85.

1.8 References

1. Nasini, R.; Brown, R.; Rée, A.; Miller, W. L.; Hewitt, J. T.; Dawson, H. M.; Knecht, E. *J. Chem. Soc.* **1926**, 129, 993.
2. Nada, A. A. *J. Chem. Educ.* **1983**, 60, 451.
3. Lewis, G. N.; Kasha, M. *J. Am. Chem. Soc.* **1944**, 66, 2100.
4. Förster, V. T. *Ann. Phys (Leipzig)*. **1948**, 2, 55.
5. Samosvat, D. M.; Chikalova-Luzina, O. P.; Vyatkin, V. M.; Zegrya, G. G. *J. Phys.: Conf. Ser.* **2016**, 769, 012078-1; Skourtis, S. S.; Liu, C.; Antoniou, P.; Virshup, A. M.; Beratan, D. N. *Proc. Natl. Acad. Sci. U.S.A.* **2016**, 113, 8115; Speiser, S. *Chem. Rev.* **1996**, 96, 1953.
6. Norrish, R. G. W.; Porter, G. *Proc. Roy. Soc. (London) A.* **1952**, 210, 439; Norrish, R. G. W.; Porter, G.; Thrush, B. A. *Proc. Roy. Soc. (London) A.* **1953**, 216, 165.
7. Zewail, A. H. *Faraday Discuss. Chem. Soc.* **1991**, 91, 207; Zewail, A. H. *J. Phys. Chem.* **1996**, 100, 12701.
8. Katz, J. J.; Norris, J. R.; Shipman, L. L.; Thurnauer, M. C.; Wasielewski, M. R. *Ann. Rev. Biophys. Bioeng.* **1978**, 7, 393; Mirkovic, T.; Ostroumov, E. E.; Anna, J. M.; Grondelle, R. V.; Govindjee; Scholes, G. D. *Chem. Rev.* **2017**, 117, 249.
9. Belgio, E.; Johnson, M. P.; Jurić, S.; Ruban, A. V. *Biophys. J.* **2012**, 102, 2761; Croce, R.; Amerongen, H. V. *Nat. Chem. Biol.* **2014**, 10, 492.
10. Wilkins, D. M.; Dattani, N. S. *J. Chem. Theory Comput.* **2015**, 11, 3411; Thyrrhaug, E.; Žídek, K.; Dostál, J.; Bína, D.; Zigmantas, D. *J. Phys. Chem. Lett.* **2016**, 7, 1653; Singh, D.; Dasgupta, S. *J. Phys. Chem. B.* **2017**, 121, 1290.
11. Sinha, R. P.; Häder, D.-P. *Photochem. Photobiol. Sci.* **2002**, 1, 225; Girard, P. M.; Francesconi, S.; Pozzebon, M.; Graindorge, D.; Rochette, P.; Drouin, R.; Sage, E. *J. Phys.: Conf. Ser.* **2011**, 261, 012002-1; Mao, P.; Wyrick, J. J.; Roberts, S. A.; Smerdon, M. J. *Photochem. Photobiol.* **2017**, 93, 216.
12. Seward, H. E.; Bagshaw, C. R. *Chem. Soc. Rev.* **2009**, 38, 2842; Drobizhev, M.; Stoltzfus, C.; Topol, I.; Collins, J.; Wicks, G.; Mikhaylov, A.; Barnett, L.; Hughes, T. E.; Rebane, A. *J. Phys. Chem. B.* **2014**, 118, 9167; Acharya, A.; Bogdanov, A. M.; Grigorenko, B. L.; Bravaya, K. B.; Nemukhin, A. V.; Lukyanov, K. A.; Krylov, A. I. *Chem. Rev.* **2017**, 117, 758.
13. Abdou, M. S. A.; Holdcroft, S. *Chem. Mater.* **1994**, 6, 962; Bryan, A. M.; Santino, L. M.; Lu, Y.; Acharya, S.; D'Arcy, J. M. *Chem. Mater.* **2016**, 28, 5989; Nguyen, D. N.; Yoon, H. *Polymers.* **2016**, 8, 118.
14. Scholz, S.; Kondakov, D.; Lüsse, B.; Leo, K. *Chem. Rev.* **2015**, 115, 8449; Liu, W.; Zheng, C.-J.; Wang, K.; Zhang, M.; Chen, D.-Y.; Tao, S.-L.; Li, F.; Dong, Y.-P.; Lee, C.-S.; Ou, X.-M.; Zhang,

- X.-H. *ACS Appl. Mater. Interfaces*. **2016**, 8, 32984; Nagai, Y.; Sasabe, H.; Takahashi, J.; Onuma, N.; Ito, T.; Ohisa, S.; Kido, J. *J. Mater. Chem. C*. **2017**, 5, 527.
15. Agostinis, P.; Berg, K.; Cengel, K. A.; Foster, T. H.; Girotti, A. W.; Gollnick, S. O.; Hahn, S. M.; Hamblin, M. R.; Juzeniene, A.; Kessel, D.; Korbelik, M.; Moan, J.; Mroz, P.; Nowis, D.; Piette, J.; Wilson, B. C.; Golab, J. *CA: Cancer J. Clin.* **2011**, 61, 250; Miyoshi, N.; Kundu, S. K.; Tuziuti, T.; Yasui, K.; Shimada, I.; Ito, Y. *Nanosci. Nanoeng.* **2016**, 4, 1.
16. Smith, M. B.; Michl, J. *Chem. Rev.* **2010**, 110, 6891; Lee, J.; Jadhav, P.; Reuswig, P. D.; Yost, S. R.; Thompson, N. J.; Congreve, D. N.; Hontz, E.; Voorhis, T. V.; Baldo, M. A. *Acc. Chem. Res.* **2013**, 46, 1300.
17. Stokes, G.G. *Philos. Trans. R. Soc. Lond.* **1852**, 142, 463.
18. Valeur, B.; Berberan-Santos, M. N. *J. Chem. Educ.* **2011**, 88, 731.
19. Valeur, B.; Berberan-Santos, M. N. *Molecular Fluorescence, Principles and applications*; 2nd ed.; Wiley - VCH Verlag GmbH & Co. KGaA: Weinheim, German, **2012**.
20. Berberan-Santos, M. N. *Fluorescence of Supermolecules, Polymers and Nanosystems, Springer Series on Fluorescence*; vol. 4; Springer - Verlag: Berlin, Heidelberg, **2008**; Coble, P. G.; Lead, J.; Baker, A.; Reynolds, D. M.; Spencer, R. G. M. *Aquatic Organic Matter Fluorescence*; Cambridge University Press: NewYork, **2014**.
21. Vendrell, M.; Zhai, D.; Er, J. C.; Chang, Y.-T. *Chem. Rev.* **2012**, 112, 4391.
22. Ulrich, G.; Ziessel, R.; Harriman, A. *Angew. Chem. Int. Ed.* **2008**, 47, 1184.
23. Ziessel, R.; Goze, C.; Ulrich, G.; Césarío, M.; Retailleau, P.; Harriman, A.; Rostron, J. P. *Chem. Eur. J.* **2005**, 11, 7366.
24. Bura, T.; Retailleau, P.; Ulrich, G.; Ziessel, R. *J. Org. Chem.* **2011**, 76, 1109; Kostereli, Z.; Ozdemir, T.; Buyukcakil, O.; Akkaya, E. U. *Org. Lett.* **2012**, 14, 3636; Nano, A.; Retailleau, P.; Hagon, J. P.; Harriman, A.; Ziessel, R. *Phys. Chem. Chem. Phys.* **2014**, 16, 10187.
25. Patalag, L. J.; Ulrichs, J. A.; Jones, P. G.; Werz, D. B. *Org. Lett.* **2017**, 19, 2090.
26. Yang, S. K.; Shi, X.; Park, S.; Ha, T.; Zimmerman, S. C. *Nat. Chem.* **2013**, 5, 692.
27. BODIPY® dyes.
28. Leen, V.; Qin, W.; Yang, W.; Cui, J.; Xu, C.; Tang, X.; Liu, W.; Robeyns, K.; Meervelt, L. V.; Beljonne, D.; Lazzaroni, R.; Tonnelé, C.; Boens, N.; Dehaen, W. *Chem. Asian J.* **2010**, 5, 2016; <https://phys.org/news/2010-09-red-synthesis-rigid-fluorophores.html>.
29. Alamiry, M. A. H.; Benniston, A. C.; Copley, G.; Elliott, K. J.; Harriman, A.; Stewart, B.; Zhi, Y.-G. *Chem. Mater.* **2008**, 20, 4024; Liu, C.-L.; Chen, Y.; Shelar, D. P.; Li, C.; Cheng, G.; Fu, W.-F. *J. Mater. Chem. C*. **2014**, 2, 5471.

30. Li, F.; Yang, S. I.; Ciringh, Y.; Seth, J.; Martin, C. H., III; Singh, D. L.; Kim, D.; Birge, R. R.; Bocian, D. F.; Holten, D.; Lindsey, J. S. *J. Am. Chem. Soc.* **1998**, 120, 10001.
31. Kee, H. L.; Kirmaier, C.; Yu, L.; Thamyongkit, P.; Youngblood, W. J.; Calder, M. E.; Ramos, L.; Noll, B. C.; Bocian, D. F.; Scheidt, W. R.; Birge, R. R.; Lindsey, J. S.; Holten, D. *J. Phys. Chem. B.* **2005**, 109, 20433.
32. Vu, T. T.; Méallet- Renault, R.; Clavier, G.; Trofimov, B. A.; Kuimova, M. K. *J. Mater. Chem. C.* **2016**, 4, 2828.
33. Burghart, A.; Kim, H.; Welch, M. B.; Thoresen, L. H.; Reibenspies, J.; Burgess, K. *J. Org. Chem.* **1999**, 64, 7813; Sobenina, L. N.; Vasil'tsov, A. M.; Petrova, O. V.; Petrushenko, K. B.; Ushakov, I. A.; Clavier, G.; Meallet- Renault, R.; Mikhaleva, A. I.; Trofimov, B. A. *Org. Lett.* **2011**, 13, 2524.
34. Chen, Y.; Zhao, J.; Guo, H.; Xie, L. *J. Org. Chem.* **2012**, 77, 2192; Qu, X.; Liu, Q.; Ji, X.; Chen, H.; Zhou, Z.; Shen, Z. *Chem. Commun.* **2012**, 48, 4600.
35. Ulrich, G.; Goeb, S.; Nicola, A. D.; Retailleau, P.; Ziessel, R. *J. Org. Chem.* **2011**, 76, 4489.
36. Schmidt, E. Y.; Zorina, N. V.; Dvorko, M. Y.; Protsuk, N. I.; Belyaeva, K. V.; Clavier, G.; Méallet- Renault, R.; Vu, T. T.; Mikhaleva, A. I.; Trofimov, B. A. *Chem. Eur. J.* **2011**, 17, 3069.
37. Atilgan, S.; Ozdemir, T.; Akkaya, E. U. *Org. Lett.* **2010**, 12, 4792.
38. Tamgho, I.-S.; Hasheminasab, A.; Engle, J. T.; Nemykin, V. N.; Ziegler, C. J. *J. Am. Chem. Soc.* **2014**, 136, 5623; Wang, J.; Wu, Q.; Yu, C.; Wei, Y.; Mu, X.; Hao, E.; Jiao, L. *J. Org. Chem.* **2016**, 81, 11316.
39. Frath, D.; Azizi, S.; Ulrich, G.; Retailleau, P.; Ziessel, R. *Org. Lett.* **2011**, 13, 3414.
40. Martynov, V. I.; Pakhomov, A. A.; Popova, N. V.; Deyev, I. E.; Petrenko, A. G. *Acta Naturae.* **2016**, 8, 33.
41. Lee, J. Y.; Kim, K. S.; Mhin, B. J. *J. Chem. Phys.* **2001**, 115, 9484; Grabowski, Z. R.; Rotkiewicz, K. *Chem. Rev.* **2003**, 103, 3899; Tanaka, H.; Shizu, K.; Nakanotani, H.; Adachi, C. *J. Phys. Chem. C.* **2014**, 118, 15985.
42. Hu, R.; Lager, E.; Aguilar-Aguilar, A.; Liu, J.; Lam, J. W. Y.; Sung, H. H. Y.; Williams, I. D.; Zhong, Y.; Wong, K. S.; Peña-Cabrera, E.; Tang, B. Z. *J. Phys. Chem. C.* **2009**, 113, 15845.
43. Haberhauer, G.; Gleiter, R.; Burkhart, C. *Chem. Eur. J.* **2016**, 22, 971.
44. Yip, W. T.; Levy, D. H. *J. Phys. Chem.* **1996**, 100, 11539; Kalinowski, J. *Mater. Sci. - Poland.* **2009**, 27, 735.
45. Drummen, G. P. C. *Molecules.* **2012**, 17, 14067.
46. Beddard, G. S.; Porter, G. *Nature.* **1976**, 260, 366; Beddard, G. S.; Carlin, S. E.; Porter, G. *Chem. Phys. Lett.* **1976**, 43, 27.

47. McDermott, G.; Prince, S. M.; Freer, A. A.; Hawthornthwaite - Lawless, A. M.; Papiz, M. Z.; Cogdell, R. J.; Isaacs, N. W. *Nature*. **1995**, 374, 517; McLuskey, K.; Prince, S. M.; Cogdell, R. J.; Isaacs, N. W. *Biochemistry*. **2001**, 40, 8783; Cogdell, R. J.; Isaacs, N. W.; Freer, A. A.; Howard, T. D.; Gardiner, A. T.; Prince, S. M.; Papiz, M. Z. *FEBS Lett.* **2003**, 555, 35.
48. Harris, M. A.; Parkes-Loach, P. S.; Springer, J. W.; Jiang, J.; Martin, E. C.; Qian, P.; Jiao, J.; Niedzwiedzki, D. M.; Kirmaier, C.; Olsen, J. D.; Bocian, D. F.; Holten, D.; Hunter, C. N.; Lindsey, J. S.; Loach, P. A. *Chem. Sci.* **2013**, 4, 3924.
49. Kasha, M. *Radiat. Res.* **1963**, 20, 55; Hestand, N. J.; Spano, F. C. *Acc. Chem. Res.* **2017**, 50, 341.
50. Ogawa, M.; Kosaka, N.; Choyke, P. L.; Kobayashi, H. *ACS Chem. Biol.* **2009**, 4, 535.
51. Kasha, M.; Rawls, H. R.; El-Bayoumi, M. A. *Pure Appl. Chem.* **1965**, 11, 371.
52. Benniston, A. C.; Copley, G.; Harriman, A.; Howgego, D.; Harrington, R. W.; Clegg, W. *J. Org. Chem.* **2010**, 75, 2018.
53. Stachelek, P.; Harriman, A. *J. Phys. Chem. A.* **2016**, 120, 8104.
54. Bhopate, D.; Kim, K-H.; Mahajan, P.; Gore, A.; Patil, S.; Majhi, S.; Naik, G.; Liang, T-T.; Ahemad, J-M.; Yu, Y-T.; Kadam, A. *J Nanomed Nanotechnol.* **2017**, 8, 1.
55. Shao, C.; Stolte, M.; Würthner, F. *Angew. Chem. Int. Ed.* **2013**, 52, 7482.
56. Valdes - Aguilera, O.; Neckers, D. C. *Acc. Chem. Res.* **1989**, 22, 171; Seki, T.; Yagai, S.; Karatsu, T.; Kitamura, A. *J. Org. Chem.* **2008**, 73, 3328.
57. Cheng, C.- C.; Huang, J. J.; Muhable, A. A.; Liao, Z.- S.; Huang, S.- Y.; Lee, S.- C.; Chiu, C.- W.; Lee, D.- J. *Polym. Chem.* **2017**, 8, 2292.
58. Drexhage, K. H. *J. Res. Natl. Bur. Stand., A.* **1976**, 80A, 421; Steinhurst, D. A.; Owrutsky, J. C. *J. Phys. Chem. B.* **2001**, 105, 3062.
59. Sauer, M.; Drexhage, K. H.; Lieberwirth, U.; Müller, R.; Nord, S.; Zander, C. *Chem. Phys. Lett.* **1998**, 284, 153; Kupstat, A.; Ritschel, T.; Kumke, M. U. *Bioconjugate Chem.* **2011**, 22, 2546.
60. Magde, D.; Brannon, J. H.; Cremers, T. L.; III, J. O. *J. Phys. Chem.* **1979**, 83, 696; Isak, S. J.; Eyring, E. M. *J. Phys. Chem.* **1992**, 96, 1738.
61. Chakraborty, A.; Adhikari, R.; Saha, S. K. *J. Mol. Liq.* **2011**, 164, 250.
62. Perry, P. A.; Fitzgerald, M. A.; Gilbert, R. G. *Biomacromolecules.* **2006**, 7, 521; Kang, M.; Day, C. A.; Kenworthy, A. K.; DiBenedetto, E. *Traffic.* **2012**, 13, 1589.
63. Georgakoudi, I.; Foster, T. H. *Photochem. Photobiol.* **1998**, 67, 612; Kanony, C.; Åkerman, B.; Tuite, E. *J. Am. Chem. Soc.* **2001**, 123, 7985.
64. Renikuntla, B. R.; Rose, H. C.; Eldo, J.; Waggoner, A. S.; Armitage, B. A. *Org. Lett.* **2004**, 6, 909.
65. Zheng, Q.; Jockusch, S.; Zhou, Z.; Blanchard, S. C. *Photochem. Photobiol.* **2014**, 90, 448.
66. Song, L.; Hennink, E. J.; Young, I. T.; Tanke, H. J. *Biophys. J.* **1995**, 68, 2588.

67. Haase, M.; Hübner, C. G.; Nolde, F.; Müllen, K.; Basché, T. *Phys. Chem. Chem. Phys.* **2011**, *13*, 1776.
68. Wei, L.; XuDong, C.; Damir, A.; AnDong, X. *Sci. China, Ser. B.* **2009**, *52*, 1148; Flors, C. *Photochem. Photobiol. Sci.* **2010**, *9*, 643.
69. Marx, V. *Nat. Methods.* **2015**, *12*, 187.
70. Woodford, O.; Harriman, A.; McFarlane, W.; Wills, C. *ChemPhotoChem.* **2017**, *1*, 317.
71. Alamiry, M. A. H.; Harriman, A.; Haefele, A.; Ziesel, R. *ChemPhysChem.* **2015**, *16*, 1867.
72. Mata-Perez, F.; Perez-Benito, J. F. *J. Chem. Educ.* **1987**, *64*, 925; Bissette, A. J.; Fletcher, S. P. *Angew. Chem. Int. Ed.* **2013**, *52*, 12800.
73. Widengren, J.; Rigler, R. *Bioimaging.* **1996**, *4*, 149; Zheng, Q.; Jockusch, S.; Zhou, Z.; Blanchard, S. C. *Photochem. Photobiol.* **2014**, *90*, 448.
74. Jiao, C.; Huang, K.-W.; Wu, J. *Org. Lett.* **2011**, *13*, 632.
75. Slooff, L. H.; Bende, E. E.; Burgers, A. R.; Budel, T.; Pravettoni, M.; Kenny, R. P.; Dunlop, E. D.; Büchtemann, A. *Phys. Stat. Sol. (RRL)*. **2008**, *2*, 257; Sark, W. G. J. H. M. V.; Barnham, K. W. J.; Slooff, L. H.; Chatten, A. J.; Büchtemann, A.; Meyer, A.; McCormack, S. J.; Koole, R.; Farrell, D. J.; Bose, R.; Bende, E. E.; Burgers, A. R.; Budel, T.; Quilitz, J.; Kennedy, M.; Meyer, T.; Donegá, C. D. M.; Meijerink, A.; Vanmaekelbergh, D. *Opt. Express.* **2008**, *16*, 21773.
76. Rowan, B. C.; Wilson, L. R.; Richards, B. S. *IEEE J. Sel. Top. Quantum Electron.* **2008**, *14*, 1312.
77. Zhou, Y.; Xiao, Y.; Li, D.; Fu, M.; Qian, X. *J. Org. Chem.* **2008**, *73*, 1571; Ozdemir, T.; Atilgan, S.; Kutuk, I.; Yildirim, L. T.; Tulek, A.; Bayindir, M.; Akkaya, E. U. *Org. Lett.* **2009**, *11*, 2105; Fu, G.-L.; Pan, H.; Zhao, Y.-H.; Zhao, C.-H. *Org. Biomol. Chem.* **2011**, *9*, 8141.
78. Kim, S.; Bouffard, J.; Kim, Y. *Chem. Eur. J.* **2015**, *21*, 17459; Sikdar, N.; Dutta, D.; Haldar, R.; Ray, T.; Hazra, A.; Bhattacharyya, A. J.; Maji, T. K. *J. Phys. Chem. C.* **2016**, *120*, 13622.
79. He, X.; Benniston, A. C.; Saarenpää, H.; Lemmetyinen, H.; Tkachenko, N. V.; Baisch, U. *Chem. Sci.* **2015**, *6*, 3525.
80. Sirbu, D.; Benniston, A. C.; Harriman, A. *Org. Lett.* **2017**, *19*, 1626.
81. Dreuw, A.; Plötner, J.; Lorenz, L.; Wachtveitl, J.; Djanhan, J. E.; Brüning, J.; Metz, T.; Bolte, M.; Schmidt, M. U. *Angew. Chem. Int. Ed.* **2005**, *44*, 7783.
82. Plötner, J.; Dreuw, A. *Phys. Chem. Chem. Phys.* **2006**, *8*, 1197; Lorenz, L.; Plötner, J.; Matylytsky, V. V.; Dreuw, A.; Wachtveitl, J. *J. Phys. Chem. A.* **2007**, *111*, 10891.
83. Mech, A.; Monguzzi, A.; Cucinotta, F.; Meinardi, F.; Mezyk, J.; Cola, L. D.; Tubino, R. *Phys. Chem. Chem. Phys.* **2011**, *13*, 5605; Ramachandra, S.; Popović, Z. D.; Schuermann, K. C.; Cucinotta, F.; Calzaferri, G.; Cola, L. D. *Small.* **2011**, *7*, 1488.
84. Liu, Y.; Wang, K.-R.; Guo, D.-S.; Jiang, B.-P. *Adv. Funct. Mater.* **2009**, *19*, 2230.

85. Hou, X.; Ke, C.; Bruns, C. J.; McGonigal, P. R.; Pettman, R. B.; Stoddart, J. F. *Nat. Commun.* **2015**, 6, 6884.
86. Silva, A. P. D.; Gunaratne, H. Q. N.; McCoy, C. P. *J. Am. Chem. Soc.* **1997**, 119, 7891; Maligaspe, E.; D'Souza, F. *Org. Lett.* **2010**, 12, 624.

Chapter 2.

Internal Geometry Changes and Barrier Crossing for an O-Doped Polycyclic Aromatic Hydrocarbon

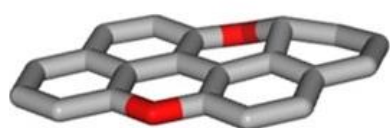


INTERNAL MOLECULAR MOTIONS THAT ACT IN A CONVERTED MANNER CAN CAUSE SERIOUS STRUCTURAL CHANGES THAT MIGHT OPEN NEW NONRADIATIVE CHANNELS FOR DECAY OF THE EXCITED STATE.

2.1 Introduction

Polycyclic aryl hydrocarbons have played a critical role in shaping the field of molecular photophysics, and among many other notable landmarks have led to the observation of excimer and exciplex fluorescence and to the recognition of almost all of the established rules and photophysics laws.^{1,2} These compounds have been exploited as the basis of many new technologies, such as singlet exciton fission,³ thermally-activated delayed luminescence,⁴ charge transport in OLEDs,⁵ and low-band gap semi-conductors.⁶ From linear acenes to disc-shape pyrenes and coronenes, the photophysical properties of polycyclic aryl hydrocarbons are determined primarily by the number of fused rings and/or the degree of conjugation and also by the local topology of the molecule. Aside from fluorescence properties, the same compounds have led to interesting phenomena associated with reversible structural modifications, including solvophobicity-driven π -stacking,⁷ liquid-crystalline materials,⁸ and conducting layers and sheets.⁹ It has to be noted however that polycyclic hydrocarbons, which are often formed during pyrolysis of organic matter, are toxic and highly persistent when released into the environment.¹⁰ Because of their strong cytotoxicity, easy metabolism and strong lipophilicity, there is growing demand to minimize the use of these materials.¹¹

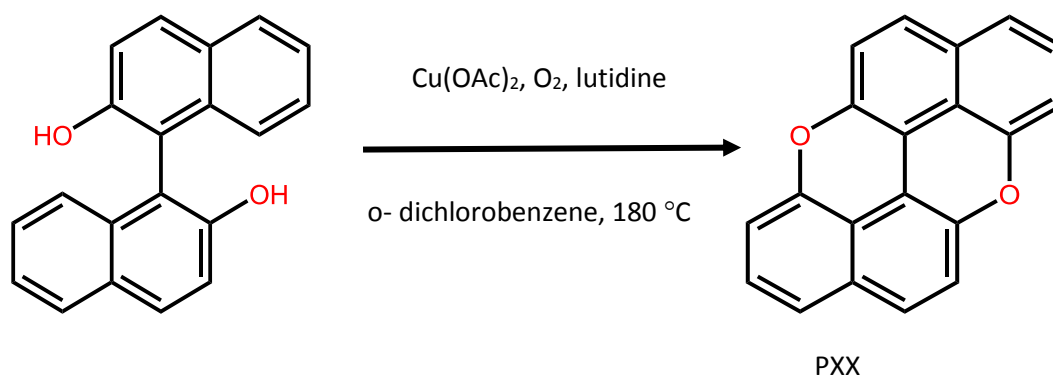
The simplest protocol for modifying the properties of classical polycyclic aryl hydrocarbons is to introduce an isostructural heteroatom into the π -conjugated pathway. There are, in fact, many derivatives of aza-aromatic compounds where one or more nitrogen atoms are incorporated in the molecular backbone.¹²⁻¹⁵ This approach affects the photophysical properties but does little to increase the solubility. Recently, there has been a move towards modifying the polycycle by the inclusion of oxygen. The resultant compounds are useful organic semi-conductors¹⁶ and possess excellent properties in terms of their processing from solution.¹⁷ Much less is known about how oxygen-doping affects the photophysical properties of the polycycle, despite the possibility that this strategy could lead to new groups of compounds with adaptable opto-electronic properties. To this end, we have examined the photophysical properties of an O-doped benzoperylene-like derivative (see opposite) in solution and in a rigid matrix. Our main interest is to elucidate if the ether bridges introduce subtle complications for understanding the molecular photophysics. It might be noted that,



according to quantum chemical calculations and the X-ray crystal structure, the presence of the O-linkages is sufficient to cause the molecular to lose planarity. No doubt, this is because of small changes in the internal bond angles and lengths but structural distortion of this type can be an important means for opening up

new nonradiative channels that assist radiationless deactivation of an excited-singlet state.

The compound under investigation here is not new,¹⁸ having been synthesized originally for use in organic solar cells, but the detailed photophysical properties of this and related compounds have not been reported in the literature. Our sample was synthesized according to (Scheme 1) by Thomas Perks of the Molecular Photonics Laboratory. It was recrystallized several times before use to give fine yellow crystals suitable for X-ray structural determination and fully characterized by spectroscopic methods. The compound gives a linear plot to the Beer-Lambert equation in dilute chloroform solution (Figure 1). The main results form the basis of a publication in ChemPhotoChem.¹⁹ Following the recommendations outlined in the original report, we abbreviate this compound as PXX and now describe the results of a detailed photophysical investigation. All the spectroscopic measurements were carried out as part of this thesis.



Scheme 1. Outline of the synthetic procedure used to prepare PXX. NB The synthesis was carried out by T. Perks from the MPL at Newcastle University.

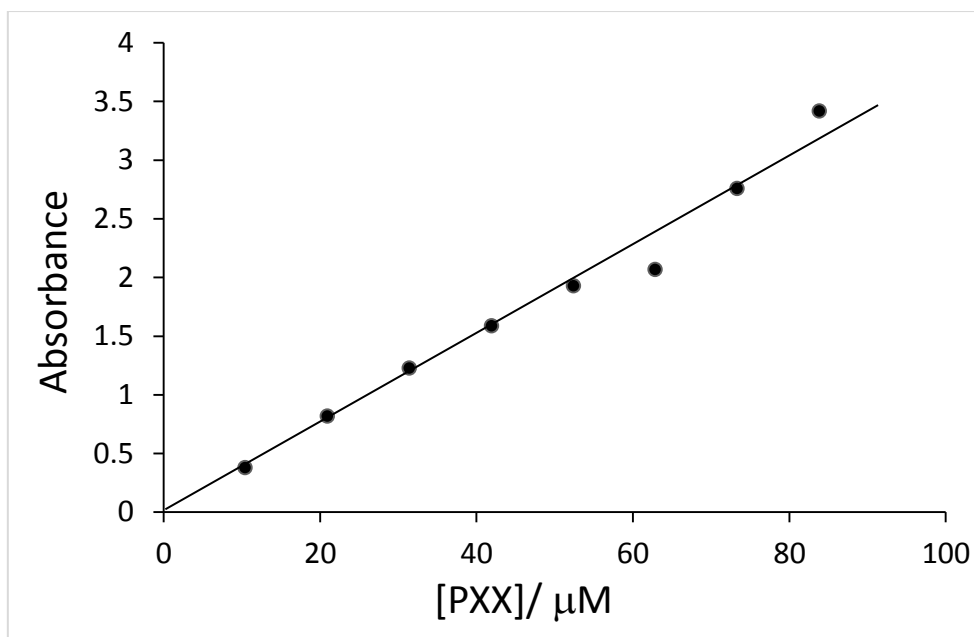


Figure 1. Beer-Lambert plot constructed for PXX in chloroform at room temperature using optical cells of varying pathlength and reconverted to 1 cm.

Part of our interest in compounds such as PXX stem from a desire to construct stable luminescent solar concentrators (LSCs) and other types of artificial light-harvesting antennae. The conventional LSC is a thin polymer plate containing a highly fluorescent dye with highly efficient solar cells carefully attached to the edges of the plate (see opposite). Light incident on the

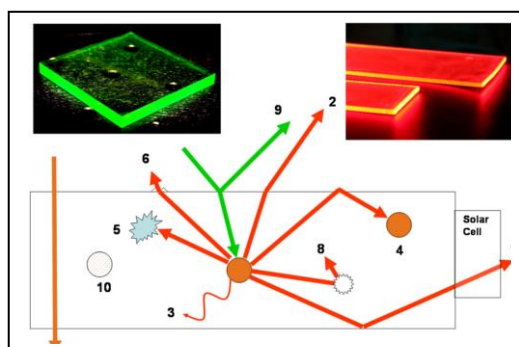


plate is absorbed by the dye. In the absence of nonradiative decay routes, the excited state of the dye will produce strong fluorescence which is trapped within the plate by internal reflection. This ensures that much of the emitted fluorescence, as much as 75% in ideal cases, reaches the solar cell and can be used for the generation of electricity. This set-up, which avoids direct illumination of the solar cell, is useful in cases where the surface area is small or the material is expensive. There are possible advantages in terms of miniaturized devices for use as medical implants and for advanced technology such as mobile phone chargers. The dye plays a critical role in performance of the LSC and needs to exhibit a large Stokes shift in order to avoid problems of self-absorption (the so-called inner-filter effect). We have successfully prepared small-scale LSCs from PXX using a water-clear, polyester casting resin doped with PXX from ethyl acetate solution. The resin is cured by the addition of methyl ethyl ketone peroxide at a loading of 2% w/w. Under these conditions, PXX displays strong fluorescence and is quite stable towards prolonged exposure to white light delivered from a 400W quartz halogen lamp.

Interestingly, there is no degradation of the dye on standing with the activator for up to 10 minutes (Figure 2).

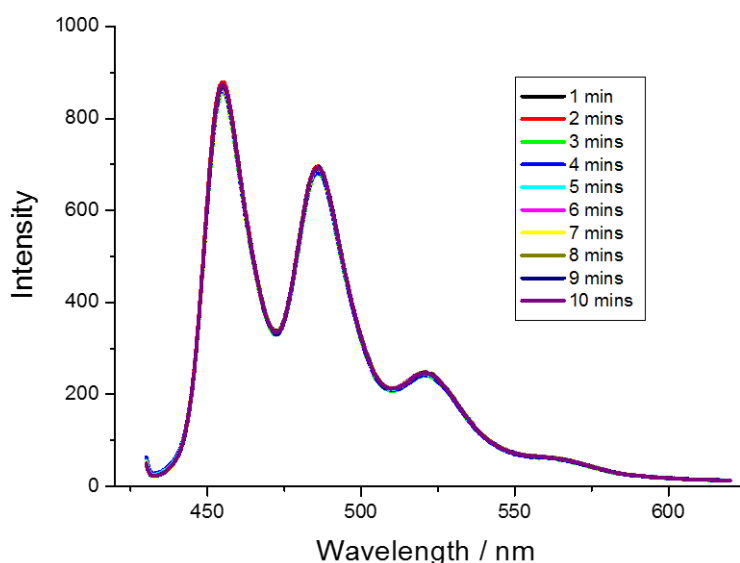
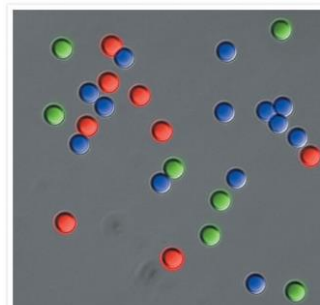


Figure 2. Fluorescence recorded for a plastic LSC prepared by incorporating PXX into the resin and curing with MEK peroxide. There is no loss of fluorescence on exposure to the activator and light.

Before starting an in-depth analysis of the photophysical properties of PXX, it seems opportune to explore the self-quenching of this compound. Such information is needed for construction of viable LSCs and for other applications. To study the concentration dependence, we opted to attach PXX to amidine latex micro-beads dispersed in droplets of n-octanol. The composite particles are used in



application, such as catalysis, coating of paper, cosmetics, and ceramics, but have now acquired a poor reputation because of their harmful effects on the environment. Here, we could stain the beads with fluorescent dye (see opposite) at various loadings. It was observed that there was no obvious sign of self-quenching for PXX concentrations ranging from 1 to 400 μM under these conditions. Problems from self-absorption, however, could be visualized by comparing the ratio of the first two emission peaks as a function of dye loading (Figure 3). This is a serious problem for LSCs.

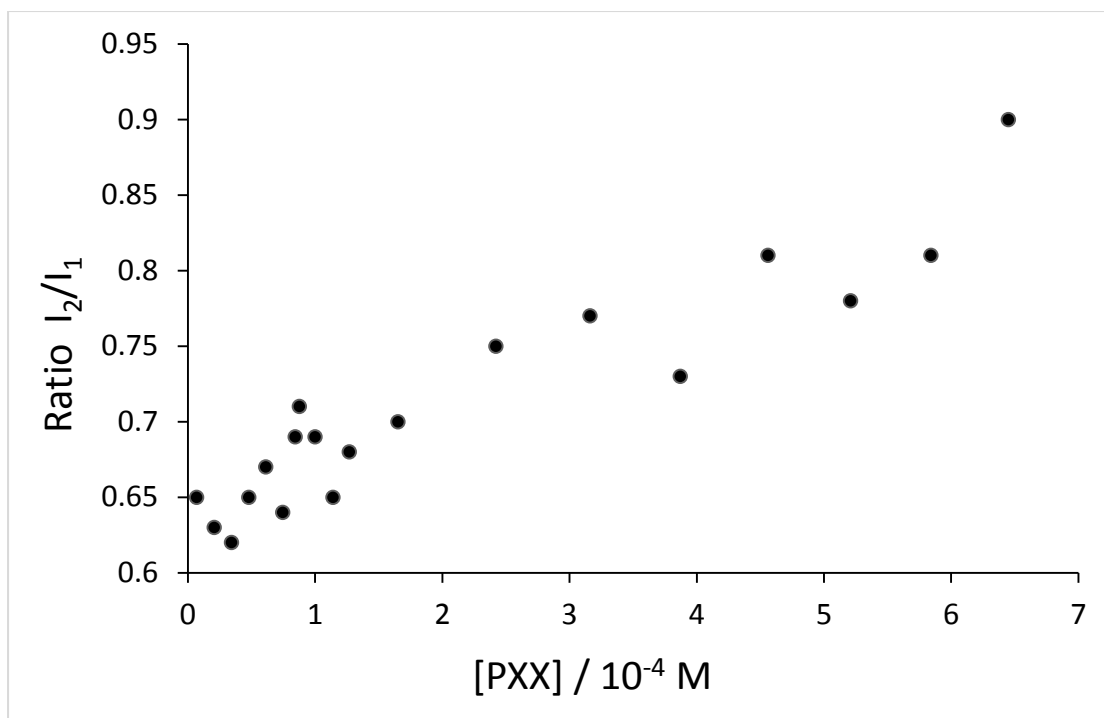


Figure 3. Effect of PXX concentration on the ratio of the first two fluorescence peaks for dye loaded onto amidine latex microbeads and dispersed in n-octanol.

2.2 Optical properties of PXX in solution

The target compound readily dissolves in common organic solvents at room temperature and exhibits a structured absorption spectrum with a low-energy threshold located at 460 nm (Figure 4). The lowest-energy transition has the appearance of a series of closely-spaced vibrational bands that, on the basis of splitting into the minimum number of Gaussian-shaped components, can be considered as overlapping series of low- and medium-frequency modes. Averaged across many different solvents, the low-frequency mode, which is clearly evident in cyclohexane solution (Figure 4), has a mean value of 490 cm^{-1} while the averaged medium-frequency mode corresponds to 1,350 cm^{-1} . The 0,0 transition, which occurs at 442 nm in cyclohexane, exhibits a slight dependence on the nature of the solvent and, for example, is found at 444 nm in toluene. (Table 1) contains a summary of the observed absorption maxima measured in a series of organic solvents at room temperature, and it can be seen that the variation is not a consequence of differing solvent polarity. In CH_2Cl_2 , the molar absorption coefficient measured at 442 nm has a value of 19,200 $\text{M}^{-1} \text{cm}^{-1}$, leading to calculation of an oscillator strength (f) for the first-allowed transition of 0.24.

The position of the absorption maximum determined for the reduced spectrum responds linearly to changes in the polarizability of the solvent²⁰ (F_N) at fixed absorbance, according to Equation 2.1 (Figure 4). Here, n is the solvent refractive index, a is the radius of a spherical cavity encompassing the

solute, ν is the barycentre of the absorption spectral profile²¹ in units of wavenumber, and the other symbols have their usual meaning. Although this is a quite well-established expression,²² there are few chromophores which show good linearity across a range of solvents that includes both protic and aprotic media. From the intercept of the linear plot to Equation 2.1, the absorption maximum for PXX *in vacuo* is extrapolated to be 426 nm while the diameter of the solvent cavity hosting PXX is predicted to be 14 Å. This latter value can be compared with molecular lengths of 11.0 Å for the long axis and 7.7 Å for the short axis, as taken from the computed molecular models.

$$\Delta\nu = \frac{3e^2}{8\pi^2c^2m} \times \frac{f}{\nu a^3} \times \frac{n^2 - 1}{2n^2 + 1} \quad \text{Equation 2.1}$$

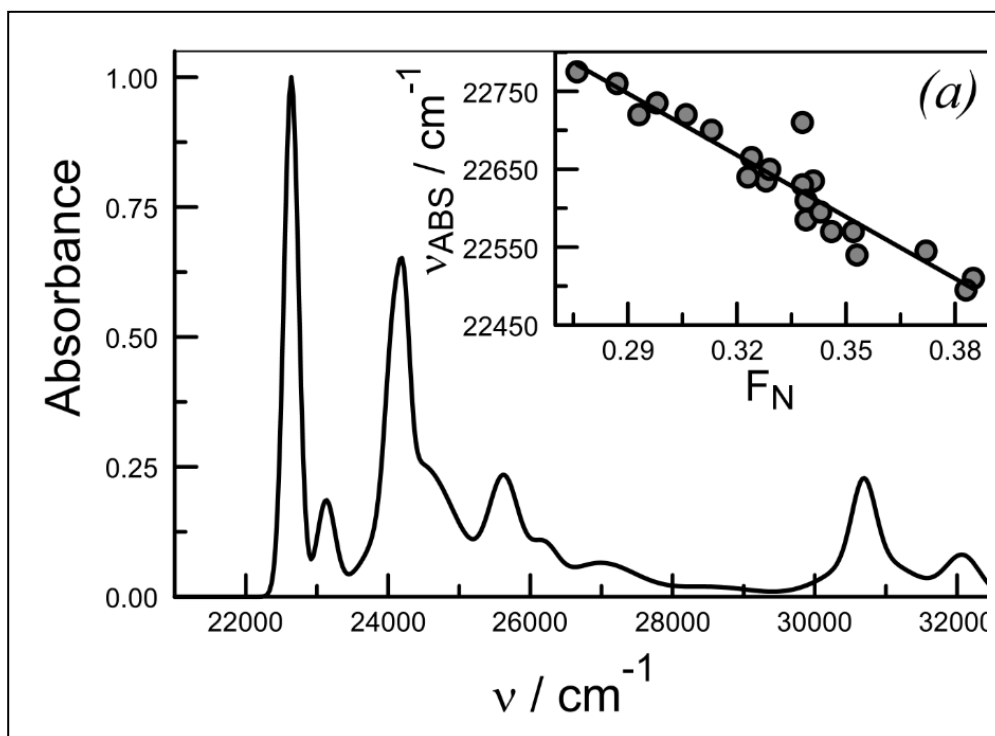


Figure 4. Example of an absorption spectrum recorded for PXX in cyclohexane solution. The wavelength scale has been converted to wavenumber so as to better indicate the symmetry of the spectrum while the inset indicates the effect of solvent polarizability of the energy of the 0,0 transition. The solvents used are mentioned in Table 1.

At room temperature, PXX shows strong fluorescence (Figure 5), with the emission spectrum showing quite reasonable mirror symmetry with the lowest-energy absorption bands. Regardless of the nature of the solvent, good agreement is observed between the excitation spectrum and the absorption spectrum. It was not possible to observe excimer fluorescence at relatively high concentrations in cyclohexane at room temperature, these conditions being fairly standard for

excimer fluorescence from many other polycyclic aryl hydrocarbons in nonpolar fluid media.²³ The fluorescence spectrum can be deconstructed into two series of Gaussian-shaped components corresponding to low- ($h\nu_L$) and medium- frequencies ($h\nu_M$) vibronic modes associated with decay of the excited state. The derived values are collated in (Table 2).

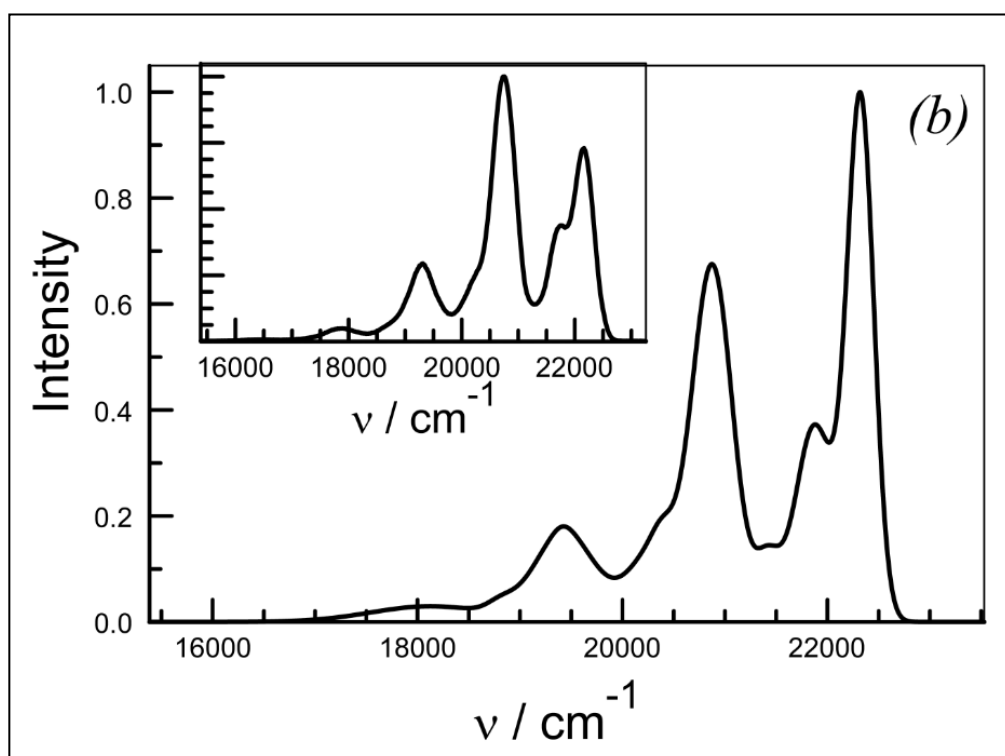


Figure 5. Fluorescence spectrum recorded for PXX in cyclohexane solution at room temperature, with the wavelength scale being converted to wavenumber. The inset shows the corresponding spectrum observed for PXX in 2-methyltetrahydrofuran at 80K.

NB TABLES 1 AND 2 APPEAR AT THE END OF THE CHAPTER FOR CONVENIENCE OF PRINTING

In each of the many solvents studied here, the Stokes shift (Δ_{SS}) is quite modest and independent of the solvent polarity; the averaged value is approximated as being 450 cm^{-1} . This finding indicates that excitation does not cause a significant perturbation of the geometry or modification of the internal dipole moment.^{1,2} There are small alterations in the position of the 0,0 fluorescence transition; for example, the 0,0 band is seen at 448 nm in cyclohexane and at 451 nm in acetonitrile (Table 1). Unlike the corresponding absorption spectrum, the 0,0 transition for the fluorescence transition does not correlate particularly well with the polarizability (F_N) of the solvent. Moreover, neither the magnitude of the Stokes shift nor the position of the fluorescence maximum correlate with the solvent polarity (F_P) as measured in terms of the Pekar function.²⁴ Furthermore, the Huang-Rhys

factors derived²⁵ for the low- (S_L) and medium-frequency (S_M) vibronic modes do not vary in a systematic fashion with properties of the solvent (Table 2). In fact, these latter parameters remain quite insensitive to changes in the local environment. We can conclude, therefore, that the spectroscopic properties are unaffected by changes in solvent and, in this respect, PXX fits with the general behaviour reported for classical aryl polycycles.^{1,2}

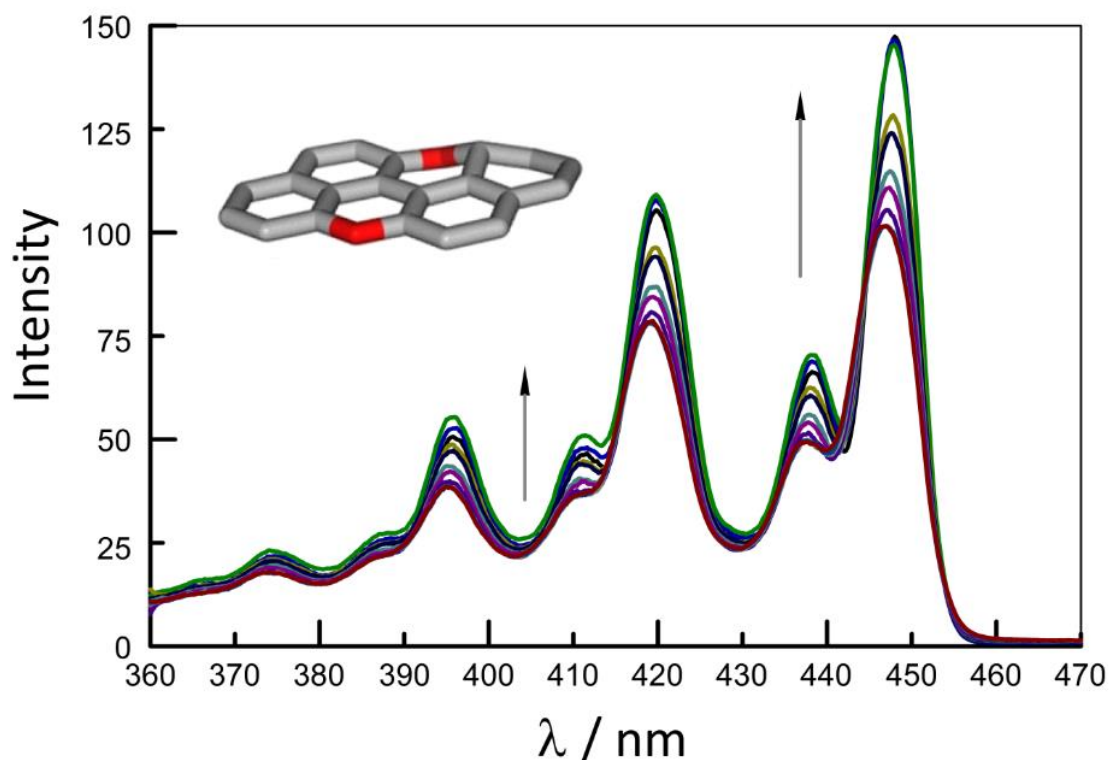


Figure 6. Examples of fluorescence excitation spectra recorded for PXX in MTHF over the temperature range 80K to 140K.

In continuing our examination of the spectroscopic properties for PXX, additional studies were made in 2-methyltetrahydrofuran (MTHF) at low temperature. It is recognised that MTHF is one of a few single solvents that forms a rigid glass at low temperature. These studies were carried out with the sample being housed in an optical cryostat. Emphasis was given to the low temperature region and it should be recalled that MTHF forms a rigid optical glass when cooled to temperatures below about 100K. The exact temperature at which this glass forms is not well characterised and might depend slightly on the rate of cooling. The melting point of 137K is better defined and, at higher temperatures, MTHF is fluid. At temperatures between 100 and 137K, MTHF exists as an amorphous glass with high viscosity but cavities where certain solutes can escape the full impact of the high viscosity. Excitation (Figure 6) and fluorescence (Figure 7a) spectra were recorded for PXX at a series of temperatures between 80 and 140K. The sample was cooled slowly so as to achieve the lowest-

energy conformation and spectra were recorded at high resolution. Spectra were transferred to a PC and analysed in order to monitor any temperature-induced effects.

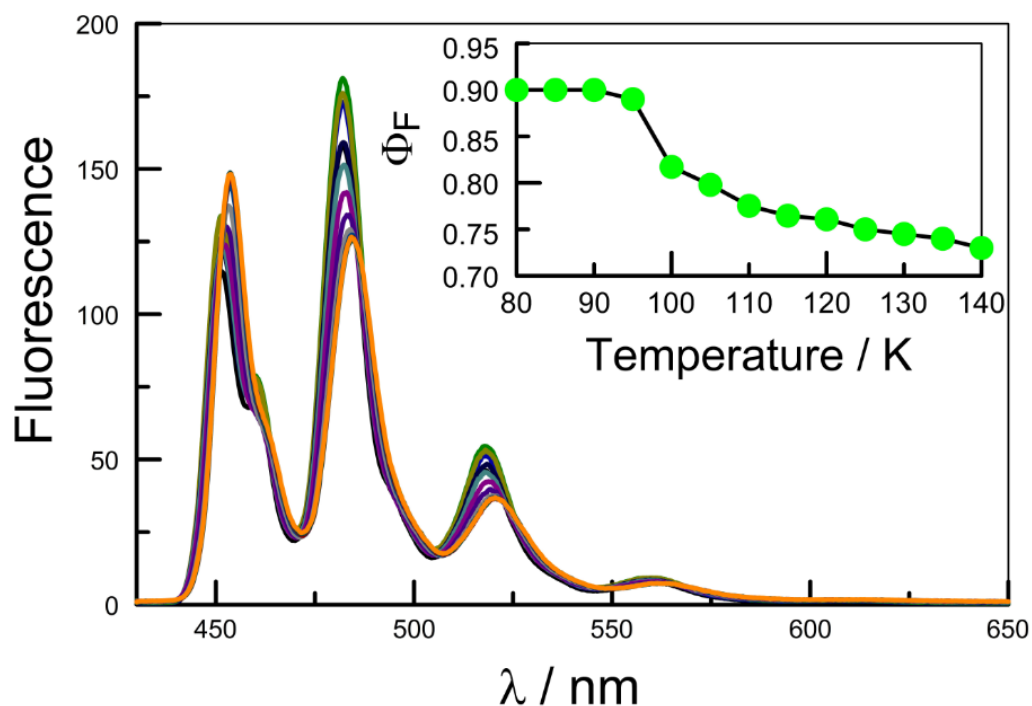


Figure 7a. Effect of temperature on the fluorescence spectral profile recorded for PXX over the temperature range from 80K to 140K. The inset shows the measured fluorescence quantum yield over the same temperature range.

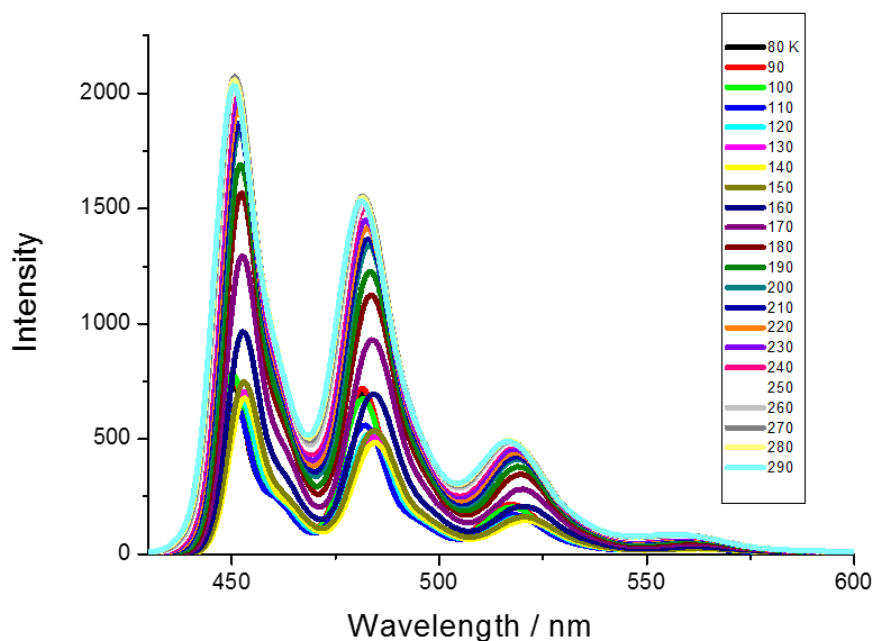


Figure 7b. Effect of temperature on the fluorescence spectral profile recorded for PXX over the temperature range from 80K to 290K.

Our results indicate that the 0,0 transitions for excitation (ν_{EXC}) and emission (ν_{FLU}) spectra shift towards higher energies with increasing temperature (Figure 8b). Below the glass transition temperature ($T_G = 137\text{K}$), both the magnitude of the Stokes shift (Δ_{SS}) and the band half-width ($\Delta\nu$) increase with increasing temperature. Analysis of the low-temperature excitation (Figure 6) and emission (Figure 7a) spectra indicates that a minimum of three vibrational modes is needed to fully explain the low-energy transition. Of these modes, those with a mean energy of 485 and 1,423 cm^{-1} are insensitive to changes in temperature but the remaining vibration, having a mean value of 1,110 cm^{-1} , increases with increasing temperature. At higher temperatures, the two medium-frequency vibrations are somewhat difficult to resolve. In contrast, the S factors for the higher-energy vibrations are strongly affected by changes in temperature but this is not so for the lowest-energy vibration (Figure 8a, inset). The medium-frequency vibrations are almost fixed in the rigid glass but decrease considerably as the glass melts, indicating a substantial structural change.

In the rigid glass, Φ_f exceeds 0.9 but begins to fall as the temperature surpasses ca. 100K, reaching a value of 0.73 at the glass transition temperature (Figure 7a inset). This change mirrors the effects noted for the Huang-Rhys factors for the medium-frequency vibronic modes (Figure 8a). The temperature dependence noted for the vibrations must reflect a change in structure. The Huang-Rhys factor, which is related to the Stokes shift Equation 2.2,²⁶ serves to indicate what proportion of the total re-organization energy is attributable to a particular vibration. Small structural changes, especially if related to the effective conjugation length, are of great significance in determining the optical performance of conjugated polymers²⁷ and related materials.²⁸ For PXX, there appears to be a possible connection between the fluorescence yield, the optical bandgap and the Huang-Rhys factors. We now explore this possibility in more detail.

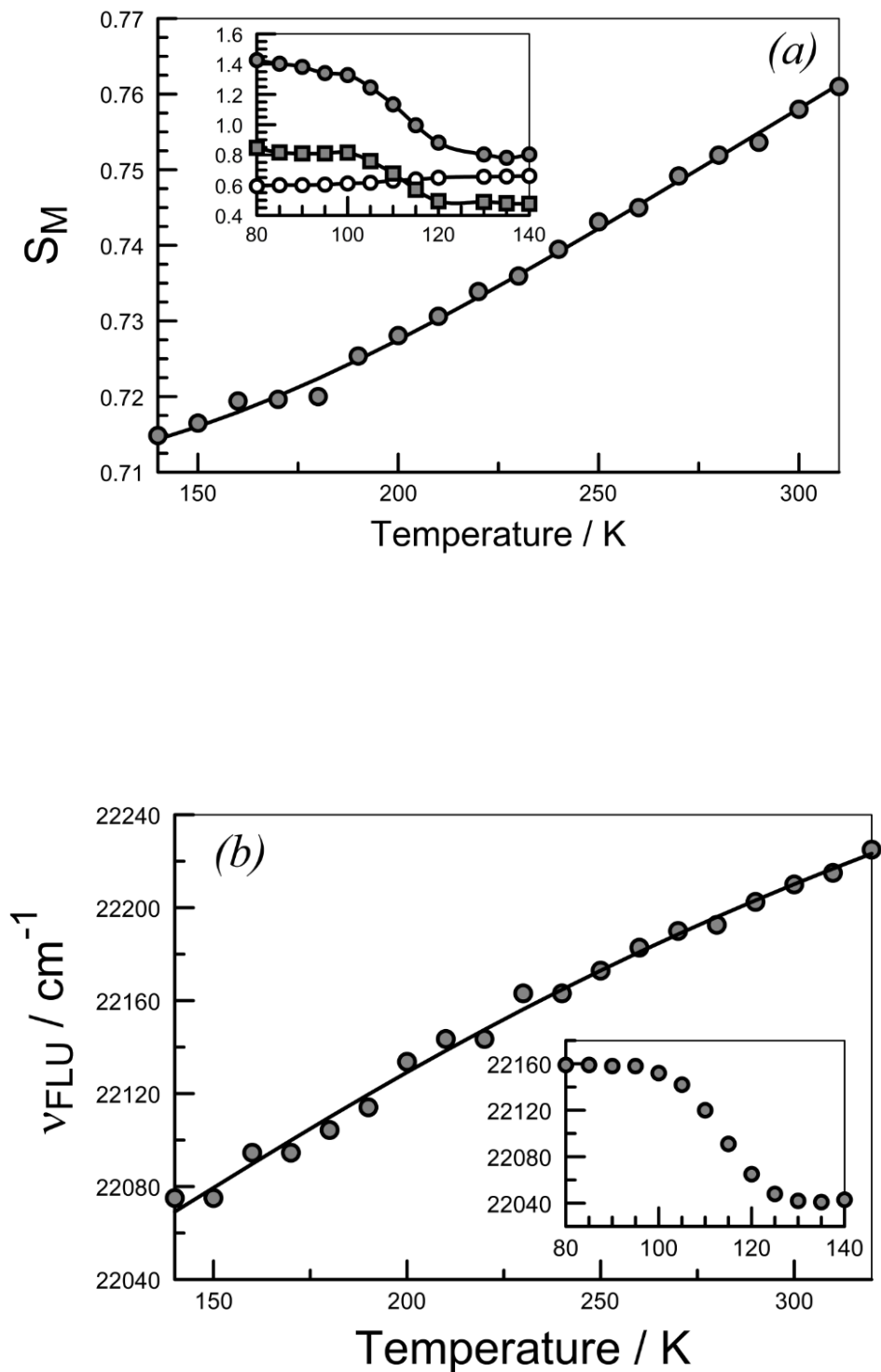


Figure 8. (a) Effect of temperature on the medium-frequency Huang-Rhys factor for PXX in liquid MTHF, with the solid line being a fit to Equation 2.4. The inset shows the temperature dependence for the Huang-Rhys factors for the 485 (o), 1110 (■) and 1423 cm^{-1} (●) vibronic modes in the glassy matrix. (b) Effect of temperature on the energy of the 0,0 fluorescence transition for PXX in liquid MTHF, with the solid line being a fit to Equation 2.3. The inset shows the same dependence for PXX in the glassy matrix.

In fluid solution, the emission maximum moves steadily towards the blue with increasing temperature over the range 130 to 290K. This smooth evolution in peak position with changing temperature does not correlate with the prediction of Equation 2.1 and, as such, cannot be explained in terms of the solvent polarizability index. Instead, the red shift on lowering the temperature can be rationalized in terms of minor structural variations that maximize the planarity of the molecule.²⁹ Such behaviour is common in conjugated polymers³⁰ and extended oligomers,³¹ where the alignment between adjacent monomers controls the conjugation length. Using the treatment developed for conducting polymers,³² it is possible to account for the temperature effect on the energy of the 0,0 emission transition in terms of Equation 2.3 (Figure 8b). Here, the limiting bandgap at low temperature (E_{00}) has a value of 22,000 cm^{-1} while the activation energy (ΔE_{00}) responsible for conformational changes at the molecular level is derived to be 2.45 kJ/mol. The remaining term, $C = 560 \text{ cm}^{-1}$, is a fitting parameter dependent on the nature of the solute and its interaction with the environment. The net result of this type of perturbation is to increase planarity of the molecule at low temperature. What this means is that the molecule cannot be entirely planar at elevated temperatures. Similar effects are not seen with conventional aryl polycycles.

$$\text{Stokes shift} = (2S - 1)h\bar{\nu} \quad \text{Equation 2.2}$$

$$\nu_{FLU} = E_{00} + \frac{C}{\exp\left(\frac{\Delta E_{00}}{RT}\right)} \quad \text{Equation 2.3}$$

$$S_M = S_0 + \frac{B}{n_0 \exp\left(\frac{\Delta E_{HR}}{RT}\right)} \quad \text{Equation 2.4}$$

Over the same temperature range, the Huang-Rhys factor (S_M) for the medium-frequency vibration in the liquid phase increases with temperature³³ according to Equation 2.4 (Figure 8a). Here, $S_0 (= 0.71)$ refers to the corresponding Huang-Rhys factor for the low temperature limit and $\Delta E_{HR} (= 4.9 \text{ kJ/mol})$ represents the activation energy associated with the underlying structural change. The term $n_0 (= 0.8)$ is the effective conjugation length³⁴ of the fluorophore at the high temperature limit while $B (= 0.28)$ is a dimensionless fitting parameter that depends on the molecule under exploration. We are unaware of any related study carried out with simple molecules that provides activation energies or effective conjugation lengths that might be compared to those found here for PXX. Similar activation energies for conformational motion have been reported³⁵ for various conjugated polymers but here the effective conjugation lengths are considerably longer than for PXX. We might expect ΔE_{HR}

and ΔE_{00} to be similar, if not identical, and, given the empirical nature of Equations 2.3 and 2.4, this seems to be the case. As such, the thermal effects found for the optical properties of PXX are attributed to some kind of internal structural change.

We were unable to detect phosphorescence for PXX in an ethanol glass at 77K, even after addition of 20% v/v iodoethane. However, the triplet-excited state could be observed by transient absorption spectroscopy following laser excitation at 440 nm of PXX in deoxygenated cyclohexane containing 20% iodoethane. The triplet differential absorption spectrum shows bleaching of the ground-state absorption band centred at around 440 nm, together with absorption around 340 and 480 nm (Figure 9). Under these conditions, the excited-triplet state decays via first-order kinetics with a lifetime of ca. 3 μ s to restore the pre-pulse baseline. The triplet lifetime is further shortened in the presence of molecular oxygen and, as expected on the basis of the heavy-atom effect,³⁶ depends on the mole fraction of iodoethane. In the absence of a heavy-atom spin perturber, it was not possible to make a meaningful estimate of the quantum yield for formation of the triplet state. Certainly, this yield is less than a few percent. The triplet differential absorption spectrum is nondescript and contains no useful spectroscopic features.

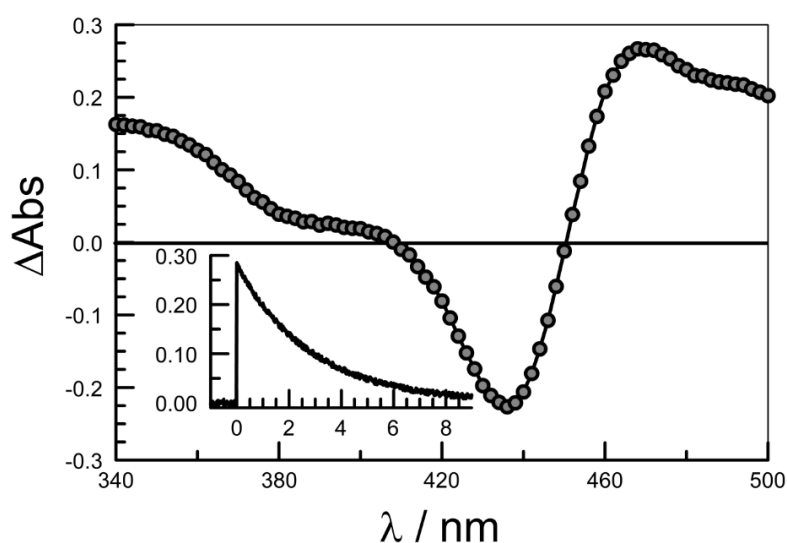


Figure 9. Transient differential absorption spectrum recorded for PXX in deoxygenated cyclohexane solution. The inset shows a typical decay trace recorded at 465 nm.

Table 3. Effect of solvent viscosity on the photophysical properties recorded for PXX in viscous media at room temperature.

Solvent	Viscosity [cP] ^a	Φ_F	τ_s [ns]	k_{RAD} [$10^8 s^{-1}$]	k_{NR} [$10^8 s^{-1}$]
DMSO ^b	1.99	0.75	6.80	1.10	0.37
PC ^c	2.50	0.82	6.90	1.18	0.27
BuOH ^d	2.54	0.83	6.65	1.25	0.26
HpOH ^e	5.77	0.93	7.55	1.24	0.09
OcOH ^f	7.36	0.91	7.65	1.19	0.12
DcOH ^g	11.79	0.97	7.55	1.29	0.04

(a) Viscosity at 25°C. (b) Dimethylsulfoxide. (c) Propylene carbonate. (d) Butan-1-ol. (e) Heptan-1-ol. (f) Octan-1-ol. (g) Decan-1-ol.

The fluorescence quantum yield (Φ_F) is reasonably high in solution but shows some dependence on the nature of the solvent (Table 1). Likewise, the excited-state lifetime (τ_s) derived from the mono-exponential decay curves is around 5 ns in most solvents but is increased in certain cases (Table 1). The corresponding rate constant (k_{RAD})³⁷ for radiative decay, after correction for minor changes in refractive index,³⁸ is insensitive to the nature of the solvent across the entire range. This parameter remains at around $1.2 \times 10^8 s^{-1}$. Unexpectedly, there is a marked change in the rate constant (k_{NR}) for nonradiative decay from the first-excited singlet state. In many solvents, k_{NR} has a mean value of $8 \times 10^7 s^{-1}$ but this decreases in longer alcohols and in viscous solvents. The net result is that Φ_F increases somewhat in the more viscous solvents, such as propylene carbonate. In fact, both Φ_F and τ_s increase steadily with increasing length of the linear alcohol (Table 3). This variation cannot be explained in terms of the energy-gap law,³⁹ light-induced charge transfer,⁴⁰ excimer formation^{1,2} or triplet population.³⁶

The idea that nonradiative decay channels for PXX might be sensitive to the viscosity of the surrounding solvent was unexpected but opens possibilities to design subtle rheology probes for highly viscous media. To examine this possibility in more detail, it was decided to study the photophysical properties of PXX in propylene carbonate as a function of temperature. This solvent is viscous and highly polar, but we have seen no indication that polarity plays any role in nonradiative decay for PXX. Classical expressions, such as the Strickler-Berg equation and the Englman-Jortner energy-gap law, do not include temperature dependent terms. As such, any pronounced temperature dependence seen in propylene carbonate might be taken as evidence for the proposed viscosity-dependent channel. Thus, in propylene carbonate, the excited-state lifetime was found to depend on

temperature in line with Equation 2.5. Here, the term k_{ACT} refers to an activated rate constant for radiationless decay of the excited-singlet state, while E_{ACT} corresponds to the accompanying activation energy. Nonlinear, least-squares iterative fitting of the experimental data (Figure 10a) allows calculation of the activationless rate constant, k_0 , as being $1.3 \times 10^8 \text{ s}^{-1}$. This value, which equates to the sum of k_{RAD} and k_{NR} , corresponds to Φ_F and τ_S values of 0.92 and 7.7 ns respectively, in the absence of the viscosity-dependent decay channel. These values are not far removed from those determined for PXX in the higher linear alcohols, such as decan-1-ol, at ambient temperature. It is also clear that k_{NR} is unimportant for PXX in most solvents. Our analysis indicates a value for k_{ACT} of $1.0 \times 10^{11} \text{ s}^{-1}$, while E_{ACT} is calculated to be 22.1 kJ mol^{-1} in propylene carbonate. That this activation energy greatly exceeds ΔE_{HR} and ΔE_{00} is taken to indicate that a major contributor to the dynamics is associated with structural changes in the solvent layer. In particular, the viscosity of propylene carbonate is known⁴¹ to be a complex function of temperature and this term is likely to be a major part of the measured E_{ACT} value.

$$\frac{1}{\tau_S} = k_0 + k_{ACT} \exp\left(-\frac{E_{ACT}}{RT}\right) \quad \text{Equation 2.5}$$

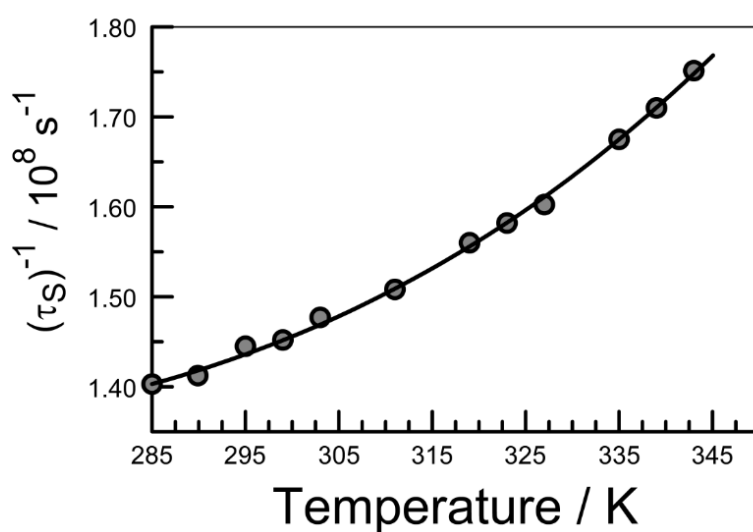


Figure 10a. Effect of temperature on the excited state lifetime for PXX in propylene carbonate solution. The solid circles refer to data points while the curve corresponds to a best fit to Equation 2.5 with the parameters mentioned in the text.

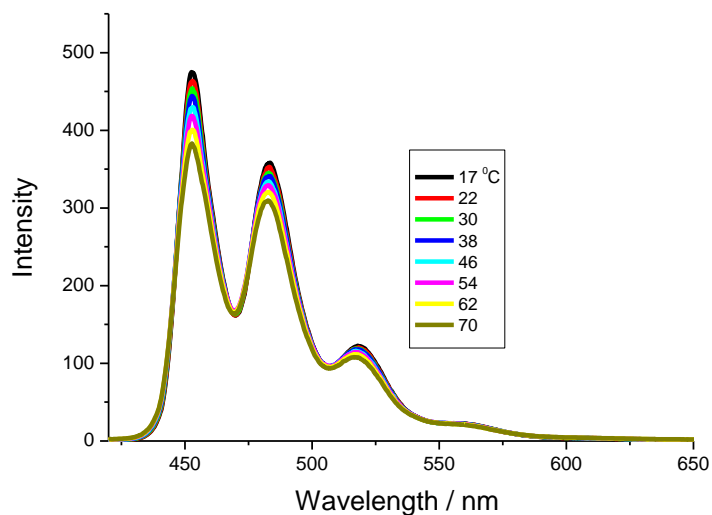


Figure 10b. Effect of temperature on the fluorescence spectral profile and relative intensity for PXX in propylene carbonate.

Similar behavior is observed in n-heptanol solution (Figure 11), where increasing temperature leads to a marked loss of fluorescence. Analysis in terms of Equation 2.5 allows derivation of the key parameters as outlined above. Nonlinear, least-squares iterative fitting of the experimental data leads to estimation of the activationless rate constant, k_0 , as being $1.2 \times 10^8 \text{ s}^{-1}$. This value roughly equates to the sum of k_{RAD} and k_{NR} . Our analysis indicates a value for k_{ACT} of $7 \times 10^{10} \text{ s}^{-1}$, while E_{ACT} is calculated to be 30 kJ mol^{-1} in n-heptanol. A clear difference between the two solvents relates to the opportunity for hydrogen bonding between the alcohol and the oxygen atoms present in the solute. Such structures are likely to be transient but to be “stable” on the timescale of our fluorescence measurements.

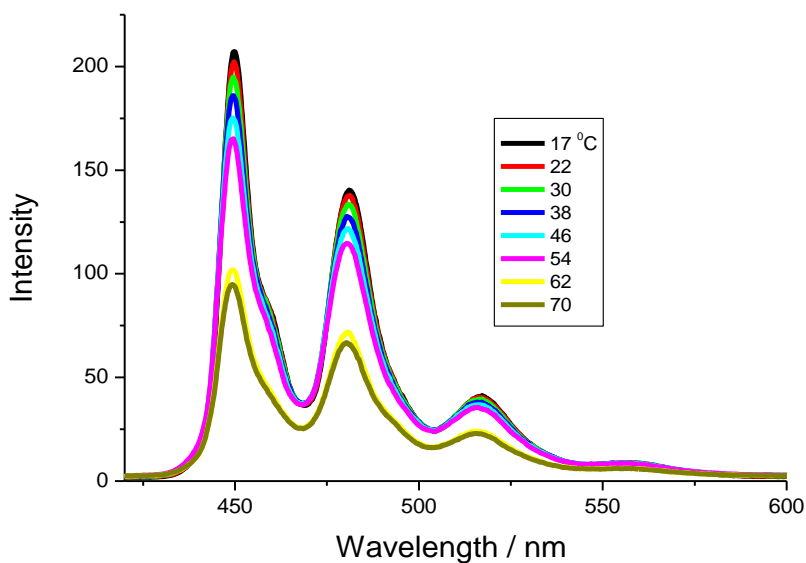


Figure 11. Effect of temperature on the emission spectral profile recorded for PXX in n-heptanol.

Our understanding of the situation existing in non-viscous solvents is illustrated by way of the potential energy diagram given as (Figure 12). Here, excitation of the ground state results in population of the corresponding excited-singlet state, S_1 , which retains a similar geometry to that of the ground state. However, the excited state is able to cross a barrier and thereby access a new state having a different geometry. This new state is referred to as S_T , where T stands for trap. The Englman-Jortner energy gap law indicates that S_T will decay rapidly to the ground state, with a rate constant of k_T . As such, the rate limiting step associated with S_T will be k_{ACT} . This latter process is strongly activated so that the rate of populating the trap becomes temperature dependent. To account for the apparent viscosity effect, it simply follows that the barrier height, E_{ACT} , is set by some kind of geometrical transformation. Friction between the surrounding solvent and the solute will now control the barrier crossing process.

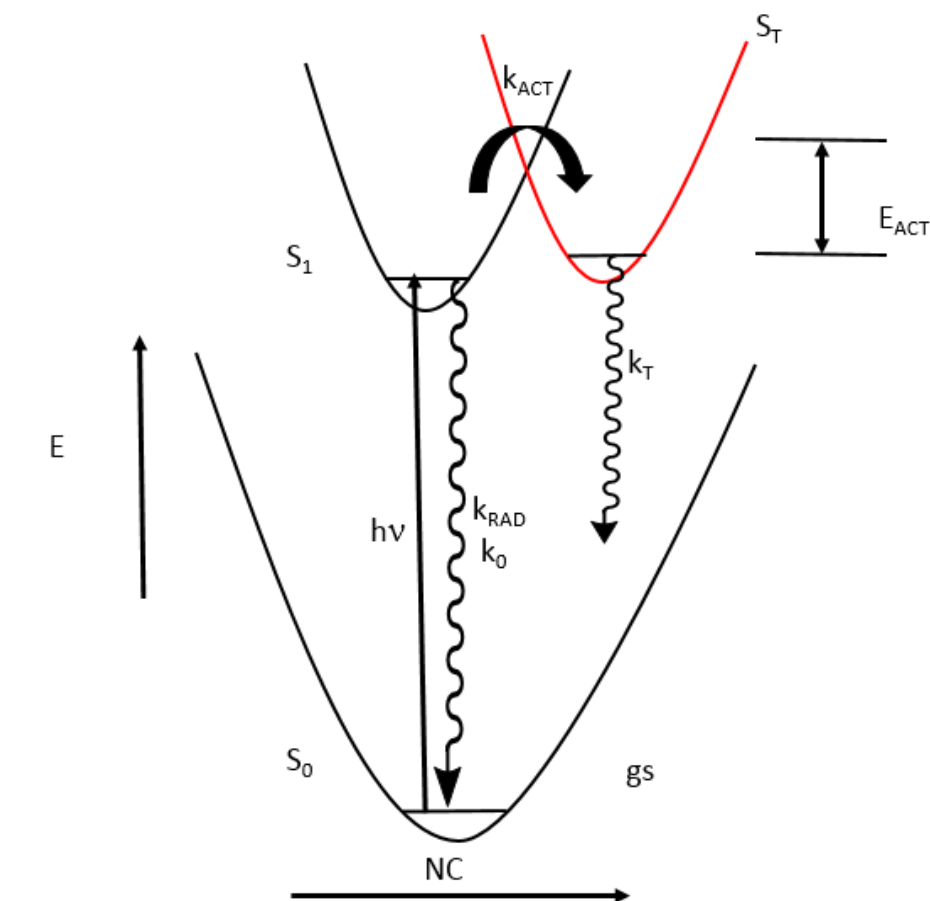
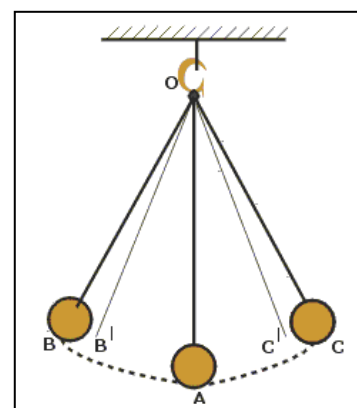


Figure 12. Simple representation of the potential energy diagram proposed for PXX in solution. Excitation of the ground state (gs , S_0) results in population of the Franck-Condon excited state (S_1), which retains a similar geometry. This excited state can pass over a modest barrier (E_{ACT}) to access a new conformation (S_T). This latter state is strongly coupled to S_0 so that population of S_T serves to promote nonradiative decay of S_1 .

The involvement of an activated radiationless decay pathway is quite rare for an aryl polycycle and suggests that this new avenue is in some way associated with the ether bridges. The only logical answer is that the bridged oxygen atoms facilitate an internal structural change. Thus, Φ_F increases in viscous media while τ_S heads to a maximum value that is similar to the inverse of k_{RAD} (Table 1). On the assumption that k_{NR} is insignificant in comparison to k_{RAD} and k_{ACT} , as is the case in propylene carbonate, it appears that k_{ACT} is dependent



on the shear viscosity (η) of the solvent (Figure 14). Under such conditions, the activated channel can be related to hydrodynamic friction between the oscillating nuclear fragment and the hindering solvent.⁴² In a crude sense, this nuclear motion is reminiscent of a simple pendulum under resistance from the atmosphere (i.e., gravity). The pendulum is dampened in viscous media but the period is extended in less viscous solvents. Eventually, the elasticity of the covalent bonds will limit the scope

of the movement and, at this limit, the solvent will no longer exert an influence of the ability to access the deactivation channel. The excited-state lifetime will be viscosity independent under such limits.

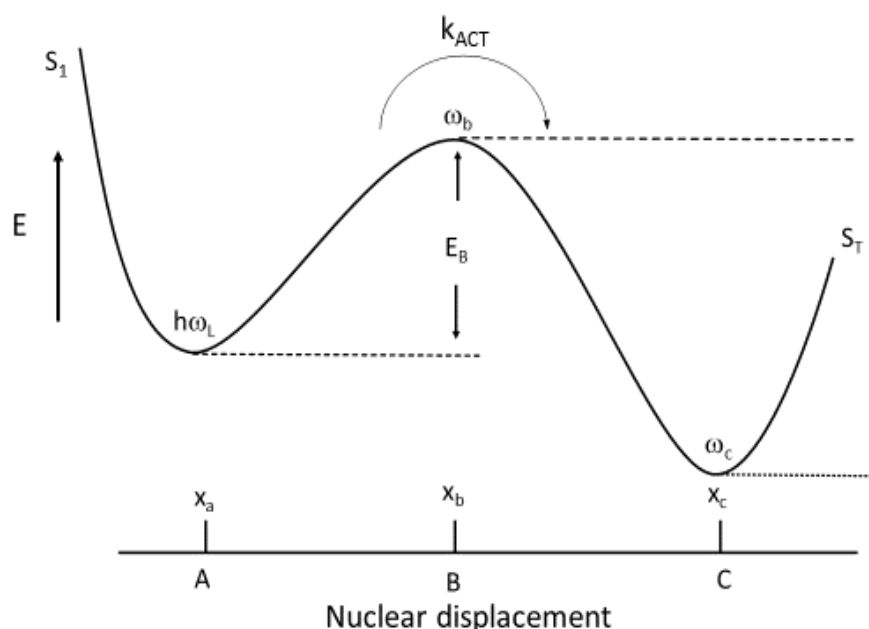


Figure 13. Graphical representation of the excited-state dynamics undertaken by PXX in solution according to Kramers' theory.

This type of generic behaviour can be considered in terms of the classical theory elaborated by Kramers⁴³ whereby k_{ACT} can be expressed in the form of Equation 2.6. Here, the friction coefficient ξ is related to the shear viscosity (η) of the solvent according to Equation 2.7, but it is necessary to accept that the pure slip boundary condition holds,⁴⁴ and the accompanying partition coefficient is taken to be unity. The total rotational friction (I_{ROT}) is given by the sum of translational friction coefficients for each coordinate associated with the oscillatory motion.⁴⁵ A limit on this model is that the barrier height, E_B , exceeds $2RT$ so as to ensure that energy equilibration occurs within the reactant potential energy well. As a starting point, we can equate E_B with E_{ACT} . The key parameters, ω and ω^\ddagger , refer respectively to the frequency of the well and of the barrier (Figure 13). Again, to simplify the calculation we can set ω ($= 15 \text{ ps}^{-1}$) to be equivalent to the low-frequency vibronic mode identified in the Gaussian curve fitting operation as explained earlier in the chapter. It is more difficult to determine precise values for the radius of gyration (r) and the radius (d) of the rotor approximated as a sphere. From molecular dynamics simulations, the hindered rotation around the ether linkages can be roughly

considered as twisting of a naphthalene residue (Figure 14). On this basis, we estimate values for d and r as being 3.5 and 1.5 Å, respectively.

$$k_{ACT} = Z \frac{\omega}{2\pi\omega^\#} \left\{ \left(\sqrt{\frac{\beta^2}{4} + \omega^{\#2}} \right) - \frac{\beta}{2} \right\} e^{-\frac{E_B}{RT}} \quad \text{Equation 2.6}$$

$$\beta = \frac{4\pi\eta dr^2}{I_{ROT}} \quad \text{Equation 2.7}$$

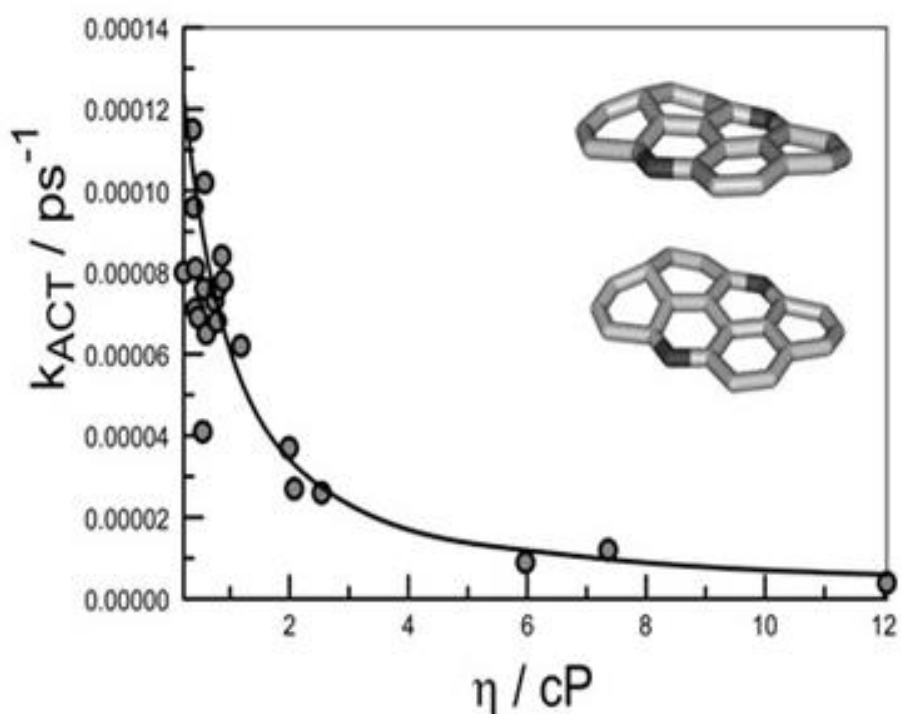


Figure 14. Fit of the experimental data collected for PXX in different solvents at 20 °C in accordance with Kramers' theory for barrier crossing at the excited-state level.

The experimental data fit well to one of the limits of Kramers' theory⁴²⁻⁴⁵ (Figure 14), giving rise to estimates for $\omega^\#$ and E_B of 2.5 ps⁻¹ and 23.5 kJ/mol. The derived barrier height is in excellent agreement with E_{ACT} and comparable to values found for other internal geometrical changes.⁴⁶ The structural change can be described as a small oscillation around the energy-minimized geometry, like a dampened pendulum. The barrier is sufficiently high to account for the observation that radiationless decay is quite slow and essentially eliminated at low temperature. The calculated frequency of the barrier is small in comparison to isomerization of cyanine dyes⁴⁷ and related compounds. Most likely,

the low value found for the potential curvature at the top of the barrier represents this modest structural change. Indeed, in most cases where Kramers' theory has been applied to well understand phototropic processes, a largescale torsional motion, such as excimer formation,⁴⁸ has been involved. We have treated the twisting motion of the molecular backbone in terms of translational diffusion against the solvent as being the cause of the friction. There are few other cases where Kramers' theory has been applied to such trivial geometry perturbations.

2.3 Conclusion

In this chapter we have examined the photophysical properties of an O-doped aryl polycycle^{18,19} under carefully controlled experimental conditions. Such compounds are looking attractive candidates for inclusion in organic opto-electronic devices as replacements for conventional aryl hydrocarbons. In our hands, PXX shows little tendency for aggregation or excimer formation in fluid solution or in thin plastic films. The compound is strongly fluorescence but resistant to intersystem crossing to the triplet manifold. The absence of triplet states might suggest that the compound will display good levels of stability under prolonged illumination. Somewhat surprisingly, we have found that PXX appears to undergo a minor structural fluctuation at the excited-state level, although the X-ray structure and DFT calculations are consistent with a planar geometry. These structural oscillations about a mean equilibrium geometry are facilitated by the two ether linkages. This situation opens a new channel for radiationless decay of the excited-singlet state in fluid solution that competes with fluorescence under ambient conditions. We have considered the dynamics of these geometry changes in terms of Kramers' theory but mathematical fitting of the experimental data needs assistance from the input of certain parameters. Nonetheless, the indications are that the excited-singlet state of PXX is involved in some type of barrier crossing process that is moderated by solvent viscosity and/or temperature. These geometry fluctuations can be dampened in viscous media. It remains to be seen if similar dynamical structural oscillations are significant for larger analogues.

One interesting observation to emerge from this study relates to the lack of significant self-quenching of fluorescence. It appears that PXX is free from self-association at moderate concentrations and when attached to microbeads at high loading. We have also demonstrated that PXX can function as a luminescent agent when incorporated into plastic LSCs. Unfortunately, there are issues with self absorption within the plastic film. These arise because the 0,0 absorption and fluorescence transitions are quite strong and the accompanying Stokes shift is small. As such, despite the good photostability of PXX under broadband illumination, this compound does not look promising as a sensitizer for solar cells.

2.4 References

1. Birks, J. B. *Photophysics of Aromatic Molecules*; Wiley - Interscience: London, **1970**.
2. Malkin, J. *Photophysical and Photochemical Properties of Aromatic Compounds*; CRC Press, Inc.: Boca Raton, Florida, **1992**.
3. Smith, M. B.; Michl, J. *Chem. Rev.* **2010**, 110, 6891.
4. Zhang, Q.; Li, J.; Shizu, K.; Huang, S.; Hirata, S.; Miyazaki, H.; Adachi, C. *J. Am. Chem. Soc.* **2012**, 134, 14706.
5. Kulkarni, A. P.; Tonzola, C. J.; Babel, A.; Jenekhe, S. A. *Chem. Mater.* **2004**, 16, 4556.
6. Anthony, J. E. *Chem. Rev.* **2006**, 106, 5028.
7. Gellman, S. H. *Acc. Chem. Res.* **1998**, 31, 173; Hill, D. J.; Mio, M. J.; Prince, R. B.; Hughes, T. S.; Moore, J. S. *Chem. Rev.* **2001**, 101, 3893.
8. Moroni, M.; Moigne, J. L.; Luzzati, S. *Macromolecules.* **1994**, 27, 562.
9. Müller, M.; Morgenroth, F.; Scherf, U.; Soczka - Guth, T.; Klärner, G.; Müllen, K. *Phil. Trans. R. Soc. Lond. A.* **1997**, 355, 715.
10. Carpenter, D. O.; Arcaro, K.; Spink, D. C. *Environ. Health Perspect.* **2002**, 110, 25.
11. Hahn, M. E. *Chemico - Biol. Inter.* **2002**, 141, 131.
12. Murov, S. L.; Carmichael, I.; Hug, G. L. *Handbook of Photochemistry*; 2nd ed.; Marcel Dekker, Inc.: New York, NY, **1993**.
13. Queguiner, G.; Marsais, F.; Snieckus, V.; Epszajn, J. *Adv. Heterocycl. Chem.* **1991**, 52, 187; Riehm, T.; Paoli, G. D.; Konradsson, A. E.; Cola, L. D.; Wadepohl, H.; Gade, L. H. *Chem. Eur. J.* **2007**, 13, 7317; Pieterse, K.; Lauritsen, A.; Schenning, A. P. H. J.; Vekemans, J. A. J. M.; Meijer, E. W. *Chem. Eur. J.* **2003**, 9, 5597.
14. Achelle, S.; Baudequin, C.; Plé, N. *Dyes Pigm.* **2013**, 98, 575; Goel, A.; Kumar, V.; Singh, S. P.; Sharma, A.; Prakash, S.; Singh, C.; Anand, R. S. *J. Mater. Chem.* **2012**, 22, 14880; Upadhyay, G. M.; Talele, H. R.; Bedekar, A. V. *J. Org. Chem.* **2016**, 81, 7751.
15. Gońka, E.; Chmielewski, P. J.; Lis, T.; Stępień, M. *J. Am. Chem. Soc.* **2014**, 136, 16399; Stępień, M.; Gońka, E.; Żyła, M.; Sprutta, N. *Chem. Rev.* **2017**, 117, 3479.
16. Brütting, W. *Physics of Organic Semiconductors*; Wiley - VCH Verlag GmbH & Co. KGaA: Weinheim, Germany, **2005**; Pope, M.; Swenberg, C. E. *Electronic Processes in Organic Crystals and Polymers*; 2nd ed.; Oxford University Press: Oxford, **1999**; Samuel, I. D. W.; Turnbull, G. A. *Chem. Rev.* **2007**, 107, 1272.
17. Lv, N.; Xie, M.; Gu, W.; Ruan, H.; Qiu, S.; Zhou, C.; Cui, Z. *Org. Lett.* **2013**, 15, 2382; Wang, L.; Duan, G.; Ji, Y.; Zhang, H. *J. Phys. Chem. C.* **2012**, 116, 22679; Kobayashi, N.; Sasaki, M.; Nomoto, K. *Chem. Mater.* **2009**, 21, 552.

18. Stassen, D.; Demitri, N.; Bonifazi, D. *Angew. Chem. Int. Ed.* **2016**, 55, 5947; *Angew. Chem.* **2016**, 128, 6051.
19. Al- Aqar, R.; Benniston, A. C.; Harriman, A.; Perks, T. *ChemPhotoChem.* **2017**, 1, 198.
20. Renge, I. *J. Phys. Chem. A.* **2000**, 104, 7452.
21. Jong, M. D.; Seijo, L.; Meijerink, A.; Rabouw, F. T. *Phys. Chem. Chem. Phys.* **2015**, 17, 16959.
22. Bovey, F. A.; Yanari, S. S. *Nature.* **1960**, 186, 1042.
23. Seko, T.; Ogura, K.; Kawakami, Y.; Sugino, H.; Toyotama, H.; Tanaka, J. *Chem. Phys. Lett.* **1998**, 291, 438.
24. Gupta, S.; Matyushov, D. V. *J. Phys. Chem. A.* **2004**, 108, 2087.
25. Markvart, T.; Greef, R. *J. Chem. Phys.* **2004**, 121, 6401; Marletta, A.; Guimarães, F. E. G.; Faria, R. M. *Braz. J. Phys.* **2002**, 32, 570; Lavrentiev, M. Y.; Barford, W. *J. Chem. Phys.* **1999**, 111, 11177.
26. Tanner, P. A. *Chem. Soc. Rev.* **2013**, 42, 5090.
27. Spano, F. C.; Clark, J.; Silva, C.; Friend, R. H. *J. Chem. Phys.* **2009**, 130, 074904-1; Liess, M.; Jeglinski, S.; Vardeny, Z. V.; Ozaki, M.; Yoshino, K.; Ding, Y.; Barton, T. *Phys. Rev. B.* **1997**, 56, 15712; Grimme, J.; Kreyenschmidt, M.; Uckert, F.; Müllen, K.; Scherf, U. *Adv. Mater.* **1995**, 7, 292; Baughman, R. H.; Shacklette, L. W. *Phys. Rev. B.* **1989**, 39, 5872.
28. Klaerner, G.; Miller, R. D. *Macromolecules.* **1998**, 31, 2007; Padmanaban, G.; Ramakrishnan, S. *J. Am. Chem. Soc.* **2000**, 122, 2244; Wohlgenannt, M.; Jiang, X. M.; Vardeny, Z. V. *Phys. Rev. B.* **2004**, 69, 241204-1; Monkman, A. P.; Burrows, H. D.; Hamblett, I.; Navarathnam, S.; Svensson, M.; Andersson, M. R. *J. Chem. Phys.* **2001**, 115, 9046.
29. Christensen, R. L.; Faksh, A.; Meyers, J. A.; Samuel, I. D. W.; Wood, P.; Schrock, R. R.; Hultzs, K. C. *J. Phys. Chem. A.* **2004**, 108, 8229.
30. Yu, Z.; Barbara, P. F. *J. Phys. Chem. B.* **2004**, 108, 11321; Padmanaban, G.; Ramakrishnan, S. *J. Phys. Chem. B.* **2004**, 108, 14933.
31. Li, J.; Liao, L.; Pang, Y. *Tetrahedron Lett.* **2002**, 43, 391; Wang, S.; Jr, W. J. O.; Jr, R. A. H.; Bazan, G. C. *J. Am. Chem. Soc.* **2000**, 122, 5695.
32. Chang, R.; Hsu, J. H.; Fann, W.S.; Liang, K.K.; Chang, C.H.; Hayashi, M.; Yu, J.; Lin, S. H.; Chang, E.C.; Chuang, K.R.; Chen, S.A. *Chem. Phys. Lett.* **2000**, 317, 142.
33. Silva, M. A. T. D.; Dias, I. F. L.; Duarte, J. L.; Laureto, E.; Silvestre, I.; Cury, L. A.; Guimarães, P. S. *J. Chem. Phys.* **2008**, 128, 094902-1; Oliveira, F. A. C.; Cury, L. A.; Righi, A.; Moreira, R. L.; Guimarães, P. S. S.; Matinaga, F. M.; Pimenta, M. A.; Nogueira, R. A. *J. Chem. Phys.* **2003**, 119, 9777.
34. Smilowitz, L.; Heeger, A. J. *Synth. Met.* **1992**, 48, 193.

35. Morgan, B.; Dadmun, M. D. *Macromolecules*. **2016**, 49, 3490; Chang, J.- F.; Sirringhaus, H.; Giles, M.; Heeney, M.; McCulloch, I. *Phys. Rev. B*. **2007**, 76, 205204 -1; Sirringhaus, H.; Tessler, N.; Friend, R. H. *Science*. **1998**, 280, 1741; Traiphol, R.; Charoenthai, N. *Synth. Met.* **2008**, 158, 135.
36. McGlynn, S. P.; Azumi, T.; Kinoshita, M. *Molecular Spectroscopy of the Triplet state*; Prentice - Hall, Inc.: Englewood Cliffs, N.J., New Jersey, **1969**.
37. Strickler, S. J.; Berg, R. A. *J. Chem. Phys.* **1962**, 37, 814.
38. Lampert, R. A.; Meech, S. R.; Metcalfe, J.; Phillips, D.; Schaap, A. P. *Chem. Phys. Lett.* **1983**, 94, 137.
39. Englman, R.; Jortner, J. *Mol. Phys.* **1970**, 18, 145.
40. Warman, J. M.; Haas, M. P. D.; Paddon - Row, M. N.; Cotsaris, E.; Hush, N. S.; Oevering, H.; Verhoeven, J. W. *Nature*. **1986**, 320, 615.
41. Zhao, Y.; Wang, J.; Xuan, X.; Lu, J. *J. Chem. Eng. Data*. **2000**, 45, 440.
42. Bowman, R. M.; Eisenthal, K. B.; Millar, D. P. *J. Chem. Phys.* **1988**, 89, 762.
43. Kramers, H. A. *Physica*. **1940**, 7, 284; Hänggi, P.; Talkner, P.; Borkovec, M. *Rev. Mod. Phys.* **1990**, 62, 251.
44. Velsko, S. P.; Fleming, G. R. *J. Chem. Phys.* **1982**, 76, 3553.
45. Hara, K.; Kiyotani, H.; Bulgarevich, D. S. *Chem. Phys. Lett.* **1995**, 242, 455.
46. Figueiras, T. S.; Neves- Petersen, M. T.; Petersen, S. B. *J. Fluoresc.* **2011**, 21, 1897; Sundström, V.; Gillbro, T. *J. Phys. Chem.* **1982**, 86, 1788; Ponterini, G.; Caselli, M. *Ber. Bunsenges. Phys. Chem.* **1992**, 96, 564.
47. Velsko, S. P.; Waldeck, D. H.; Fleming, G. R. *J. Chem. Phys.* **1983**, 78, 249; Velsko, S. P.; Fleming, G. R. *Chem. Phys.* **1982**, 65, 59; Korppi- Tommola, J. E. I.; Hakkarainen, A.; Hukka, T.; Subbi, J. *J. Phys. Chem.* **1991**, 95, 8482; Vauthey, E. *Chem. Phys.* **1995**, 196, 569; Dandapat, M.; Ghosh, D.; Mandal, D. *J. Photochem. Photobiol. A: Chem.* **2014**, 276, 41.
48. Hara, K.; Akimoto, S.; Suzuki, H. *Chem. Phys. Lett.* **1990**, 175, 493.

Table 1. Compilation of the main spectroscopic parameters recorded for PXX in a range of organic solvents at room temperature.

Solvent	$F_N^{[r]}$	$F_P^{[s]}$	λ_{ABS} [nm]	ν_{ABS} [cm^{-1}]	λ_{FLU} [nm]	ν_{FLU} [cm^{-1}]	Φ_F	τ_s [ns]
CHX ^[a]	0.341	0.000	442	22635	448	22320	0.61	4.95
CH ₃ CN	0.287	0.306	439	22760	451	22195	0.51	4.30
THF ^[b]	0.328	0.210	442	22635	451	22185	0.65	5.05
ACE ^[c]	0.298	0.284	440	22735	450	22250	0.56	4.60
BuOH ^[d]	0.324	0.264	441	22665	449	22280	0.83	6.65
BENZ ^[e]	0.385	0.002	444	22510	454	22040	0.68	5.00
BuCN ^[f]	0.313	0.276	441	22700	451	22210	0.54	4.50
2MTHF	0.329	0.202	441	22650	450	22195	0.59	4.85
CHCl ₃	0.353	0.148	443	22540	454	22020	0.65	4.60
Bu ₂ O ^[g]	0.323	0.097	442	22640	449	22285	0.64	4.90
DCE ^[h]	0.352	0.221	443	22570	453	22065	0.65	5.25
CH ₂ Cl ₂	0.339	0.217	442	22585	453	22065	0.66	4.75
Et ₂ O ^[i]	0.293	0.167	440	22720	448	22335	0.60	5.00
DIOX ^[j]	0.338	0.025	442	22630	452	22150	0.66	5.45
EtOAc ^[k]	0.306	0.200	440	22720	449	22290	0.60	4.95
CH ₃ OH	0.276	0.309	439	22775	448	22335	0.76	5.85
OcOH ^[l]	0.343	0.226	443	22595	450	22225	0.91	7.65
PC ^[m]	0.338	0.286	440	22710	452	22150	0.82	6.90
TOL ^[n]	0.383	0.013	444	22495	454	22030	0.60	5.25
HpOH ^[o]	0.339	0.206	442	22610	450	22235	0.93	7.55
DcOH ^[p]	0.346	0.237	443	22570	450	22215	0.97	7.55
DMSO ^[q]	0.372	0.263	443	22545	455	22000	0.75	6.80

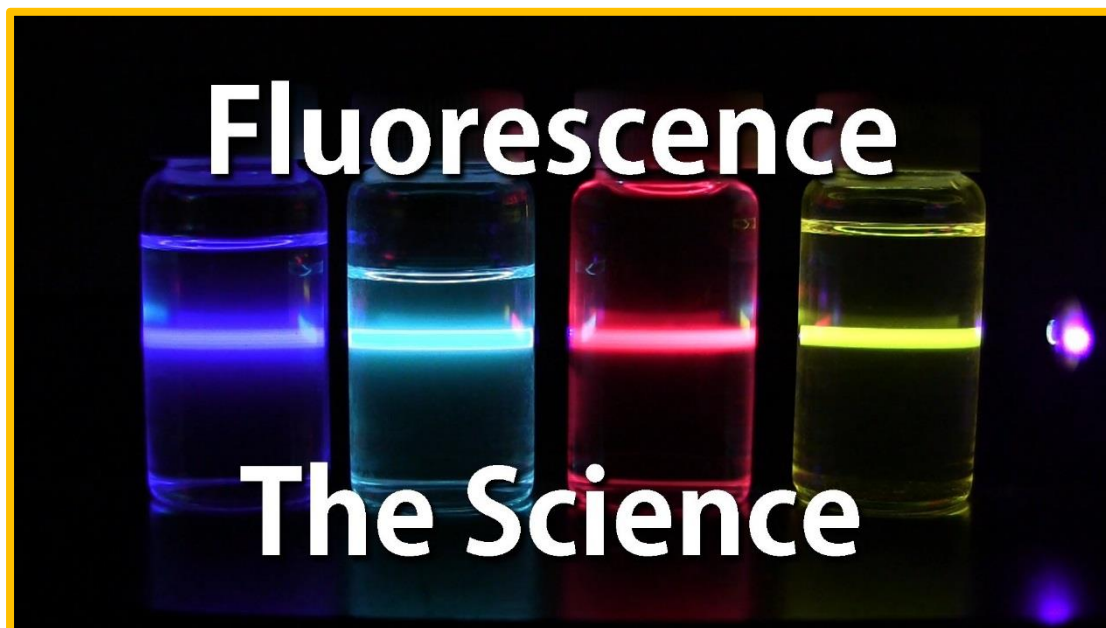
[a] Cyclohexane. [b] Tetrahydrofuran. [c] Acetone. [d] Butan-1-ol. [e] Benzene. [f] Butyronitrile. [g] Di-n-butyl ether. [h] 1,2- Dichloroethane. [i] Diethyl ether. [j] 1,4- Dioxane. [k] Ethyl acetate. [l] Octan-1-ol. [m] Propylene carbonate. [n] Toluene. [o] Heptan- 1-ol. [p] Decan- 1- ol. [q] Dimethyl sulfoxide. [r] Polarizability indices. [s] Pekar function.

Table 2. Compilation of the parameters derived from the photophysical and spectroscopic properties recorded for PXX in a range of organic solvents at room temperature.

Solvent	$K_{\text{RAD}} [10^8 \text{ s}^{-1}]$	$K_{\text{NR}} [10^8 \text{ s}^{-1}]$	$\Delta_{\text{SS}} [\text{ cm}^{-1}]$	$h\omega_{\text{L}} [\text{ cm}^{-1}]$	$h\omega_{\text{M}} [\text{ cm}^{-1}]$	S_{L}	S_{M}
CHX	1.24	0.78	320	470	1355	0.41	0.59
CH ₃ CN	1.18	1.15	570	570	1340	0.35	0.69
THF	1.29	0.69	450	525	1460	0.36	0.66
ACE	1.22	0.96	480	515	1450	0.38	0.64
BuOH	1.25	0.26	385	460	1365	0.40	0.58
BENZ	1.35	0.65	470	535	1495	0.33	0.57
BuCN	1.20	1.02	490	520	1460	0.37	0.62
2MTHF	1.22	0.84	455	600	1390	0.31	0.79
CHCl ₃	1.42	0.76	520	545	1305	0.34	0.49
Bu ₂ O	1.30	0.73	355	510	1450	0.35	0.68
DCE	1.23	0.68	500	550	1275	0.34	0.44
CH ₂ Cl ₂	1.38	0.71	515	550	1290	0.34	0.48
Et ₂ O	1.20	0.80	385	495	1420	0.36	0.69
DIOX	1.21	0.62	470	525	1470	0.34	0.60
EtOAc	1.22	0.81	425	500	1445	0.34	0.62
CH ₃ OH	1.30	0.41	440	490	1415	0.40	0.70
OcOH	1.19	0.12	370	505	1445	0.37	0.69
PC	1.18	0.27	555	520	1475	0.38	0.59
TOL	1.15	0.76	465	510	1430	0.35	0.67
HpOH	1.24	0.09	375	505	1450	0.35	0.64
DcOH	1.29	0.04	355	525	1480	0.37	0.68
DMSO	1.10	0.37	550	550	1355	0.35	0.66

Chapter 3.

The quest for highly fluorescent chromophores: Evaluation of 1*H*,3*H*-isochromeno [6,5,4-*mna*] xanthene-1,3-dione (CXD)



THERE IS A NEVER ENDING SEARCH FOR NEW ORGANIC COMPOUNDS HAVING INTERESTING FLUORESCENCE PROPERTIES, PARTICULARLY IN THE SOLID STATE. SUCH SUBSTANCES ARE ESPECIALLY ATTRACTIVE AS ANTI-COUNTERFEIT REAGENTS.

3.1 Introduction

As every chemist knows, molecules have a distinct size, shape and dimensionality instilled by the unique composition and arrangement of their constituent atoms. From birth, molecules have an identity, a name and a character. The latter leads to a set of properties which evolve as the molecule moves from isolation in a supersonic jet stream, to a dilute solution, to accretion into a microscopic cluster and finally to condensation into a solid. For some molecules, these properties are highly sensitive to the local environment and the molecule responds to changes in temperature, pressure, rheology, etc. They also respond to the presence of certain reagents. Other molecules remain indifferent to their surroundings and are therefore able to act as control or reference materials. The most interesting molecules are those that change their properties on forming a mixture, either with like molecules or with adventitious reagents. This leads to the creation of structure-reactivity criteria.¹ The beauty of the molecular world is its predictability once a set of underlying rules has been established.

No matter how wondrous might be the molecular world, it moves to a whole new dimension when the target molecule absorbs a photon of light. The resultant excited state takes on a new set of properties that might differ dramatically from those of the ground state. Molecules that are benign in the dark can become spontaneously reactive under exposure to light. Many molecules return to the ground state by way of emitting a photon of light at a slightly different frequency to that of the excitation beam. These molecules are of great interest and applicability.² Fluorescence allows visualization of the molecule and, in certain circumstances, can operate at the single molecule level.³ Few other experimental techniques can offer such high levels of sensitivity. The excited-state molecule possesses what is loosely referred to as a "lifetime", which itself might be sensitive to the environment. This offers a new protocol for monitoring the presence of secondary species or physical parameters such as temperature. This realization has not been lost on medicinal chemists and a wealth of non-intrusive diagnostic tools has been introduced in recent years.⁴ Fluorescence is the method of choice for anti-counterfeit strategies, for monitoring pollution streams and for *in situ* detection in remote or hazardous conditions. Perhaps the most dramatic feature of molecular fluorescence stems from the fact that it is not necessary for the emitting molecule to absorb the photon from the excitation beam. Indirect population of the emitting state can be engineered by way of intermolecular energy transfer.⁵ For fluorescent molecules, energy transfer can be highly effective even when the reactant pair is separated⁶ by as much as 10 nm. This is a truly remarkable occurrence, probably unrivalled in any area of natural science.

Advances in the science of fluorescence have been most apparent of late in the fields of super-resolution microscopy⁷ and in organic light-emitting devices (OLEDs).⁸ Both techniques require access to fluorescent molecules possessing certain properties. In OLED development, for example, the emitting state is accessed via charge recombination of the initially formed radical cation and radical anion species that emerge at the electrodes.⁹ Charge recombination forms both singlet and triplet excited states and the process known nowadays as thermally-activated delayed fluorescence¹⁰ (previously called E-type delayed fluorescence¹⁰) allows the fluorescent state to be reached via reverse intersystem crossing. This is an active area of research at the present time. Also under active scrutiny is the concept of a white light emitter.¹¹ Here, the OLED generates white light, often by combining three separate emitters into a bundle. There are few single molecules capable of producing white light at any reasonable efficiency. To be successful, the emitters need to be stable, insensitive to their surroundings, cheap to produce, non-toxic and strongly fluorescent. It would be useful if the target compound did not degrade under continuous exposure to light – at a recent research seminar held at Newcastle University, Professor Ifor Samuel (St Andrews University) told the audience that the emitter should survive for in excess of 50,000 hours operation. The search for suitable materials continues...

In this chapter, we describe the photophysical properties of a promising fluorescent material known to us as CXD (Figure 1). This compound, correctly called benzo-(k,l)-xanthene -3,4-dicarboxylic anhydride, is synthesized¹² in a few steps as outlined below in Scheme 1. It is recovered as a light yellow solid that easily crystallizes. The compound can be prepared in large quantities and it is stable over prolonged storage in the dark. Because of the anhydride group, there is a pronounced intramolecular dipole moment and this helps to keep the molecule in a planar orientation. We are interested to see if the compound has valuable properties for possible applications in the optoelectronics field. It absorbs at 408 nm, which is a convenient excitation wavelength because of the ready availability of cheap, high-intensity LED sources for this spectral region.

The sample of CXD was synthesized and characterized by Daniel Avis of the Molecular Photonics Laboratory (Scheme 1). He was able to obtain the crystal structure to authenticate the identity of the compound. The photophysical properties were determined as part of this thesis, as were all the results described here. A joint publication describing this system has appeared in the scientific literature.¹³

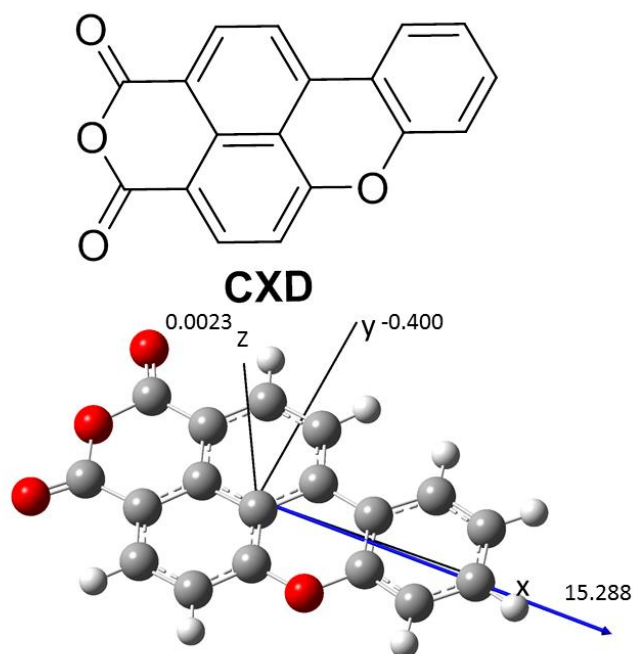
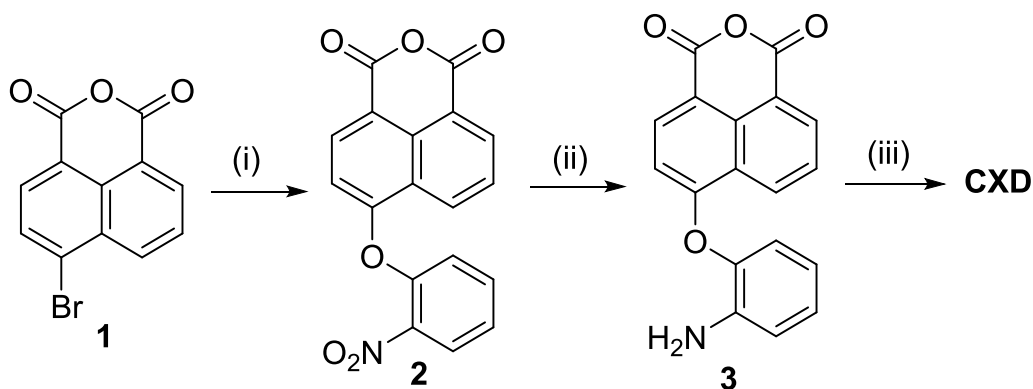


Figure 1. Molecular formula for CXD (top) and its energy-minimized structure computed for the solute in acetonitrile showing the direction and value of the ground-state dipole moment vectors (bottom).



Scheme 1. Reagents and Conditions: (i) *o*-Nitrophenol, NaOH, DMF, Cu, reflux 1h. (ii) Fe, acetic acid, reflux 1h. (iii) Hydrochloric acid, acetic acid, NaNO₂, 0-5 °C, CuSO₄, HOAc, H₂O.

3.2 Background

Prior work has reported the synthesis¹² of CXD and several closely related derivatives, but very little photophysical data were given. The structure of CXD in the gas phase, as determined by DFT using the B3LYP functional with the 6-311G⁺⁺ basis set (Figure 1), established CXD as being planar. The same situation arises for the molecule placed in a solvent reservoir. The computed bond lengths and angles appear reasonable for an aromatic compound (see later) and are in good agreement with those found by X-ray crystallography. The spatial location and identification of the HOMO and LUMO are in line with chemical anticipation, while the energy difference, $E_{\text{HOMO}} - E_{\text{LUMO}}$, for the gas-phase is calculated

to be 3.33 eV for the energy-minimized geometry. Table 1 shows the energies of the HOMO and LUMO in the case where a solvent continuum model was used. It is normal that a solvent causes a small increase in energy for both HOMO and LUMO relative to vacuum, with the effect becoming larger in more polar solvents. Figure 2A shows the electron density map computed for CXD in a pool of polar solvent molecules. The distribution indicates that considerable electron density has been moved from the aromatic core to the naphthalic anhydride residue. It is this type of intramolecular charge transfer that renders the molecule polar. The calculation also indicates that for CXD the ground-state dipole moment is long-axis polarized (Figure 1). The dipole moments are increased slightly in more polar solvents. The energy-minimized structure of the CXD radical anion is similar to that of the ground state. The main differences in bond length are restricted to the naphthalic anhydride residue (Figure 2B), thereby indicating that the added electron is essentially localized here. The same calculation performed for the corresponding radical cation, CXD⁺, predicts a planar geometry with positive charge located at the phenoxy-like subunit (Figure 2C).

Table 1. DFT computer calculated parameters using Gaussian 09 and an IEPCFM solvent model.^a

Solvent	E _{HOMO} / eV	E _{LUMO} / eV	Dipole Moment / D
None	-6.523	-3.193	10.8
THF	-6.391	-3.151	14.5
DMSO	-6.366	-3.148	15.3
MeCN	-6.368	-3.148	15.3
Toluene	-6.440	-3.159	12.8
MeOH	-6.369	-3.149	15.3
Benzene	-6.444	-3.161	12.7

^a B3LYP 6-311G⁺⁺ basis set

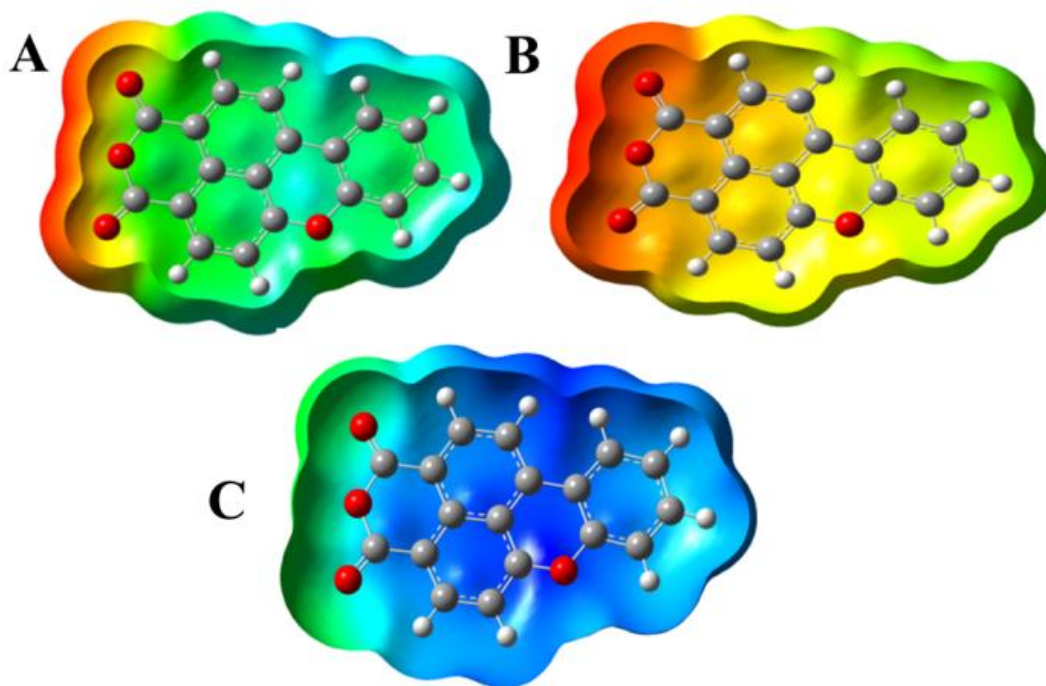


Figure 2. DFT calculated electron density distribution for CXD (A), $\text{CXD}^{\cdot-}$ (B) and $\text{CXD}^{\cdot+}$ (C) in a reservoir of acetonitrile molecules computed at the continuum model.

Cyclic voltammetry was used to study the redox chemistry of CXD in dried tetrahydrofuran (THF) containing tetra-*N*-butylammonium tetrafluoroborate as background electrolyte. On oxidative scans, an electrochemically irreversible wave was observed at a peak potential of 1.65 V vs SCE. This wave corresponds to one-electron oxidation of CXD to form the corresponding π -radical cation. This species is unstable, even on fast scan rates, and, in common with other xanthene compounds, is expected to lose a proton.¹⁴ On reductive scans, a reversible wave was observed with a half-wave potential of -1.21 V vs SCE. This particular process is attributed to formation of the π -radical anion, as identified by computational studies. No other waves were apparent in the cyclic voltammograms.

3.3 Optical spectroscopy

The absorption spectrum recorded for CXD in THF is shown as Figure 3. The spectrum is somewhat red-shifted compared to benzo[*k*]xanthene and possesses features that might be reminiscent of naphthalic anhydride.¹⁵ Two peaks stand out in the spectrum, these appearing at 420 nm ($\epsilon_{\text{MAX}} = 17,600 \text{ M}^{-1} \text{ cm}^{-1}$) and 441 nm ($\epsilon_{\text{MAX}} = 14,500 \text{ M}^{-1} \text{ cm}^{-1}$). A small shoulder is evident on the high-energy side of the 420 nm band, indicating the existence of a vibrational progression. The absorption profile below 350 nm comprises a narrow, intense band centred at 270 nm and a weaker broad, but slightly

structured, band centred at around 320 nm. A TD-DFT calculated absorption spectrum for CXD in THF matches reasonably well with the experimental spectrum (Figure 4) and indicates that the first-allowed absorption transition appears at 413 nm. The computed oscillator strength is 0.47, compared to an experimental value of 0.41. Essentially, the lowest-energy absorption transition arises from promotion of an electron from the HOMO to the LUMO. There is a notable $n-\pi^*$ contribution to the high energy band centred at 270 nm. Spectral deconstruction of the reduced absorption envelope into Gaussian-shaped components indicates the lowest-energy absorption transition has an accompanying vibronic mode corresponding to a group of vibrations centred at around $1,230\text{ cm}^{-1}$. Absorption is considered to correspond to Franck–Condon excitation, for which the 0,0 transition is located at $22\,545\text{ cm}^{-1}$, as identified by the Gaussian band-shape analysis.

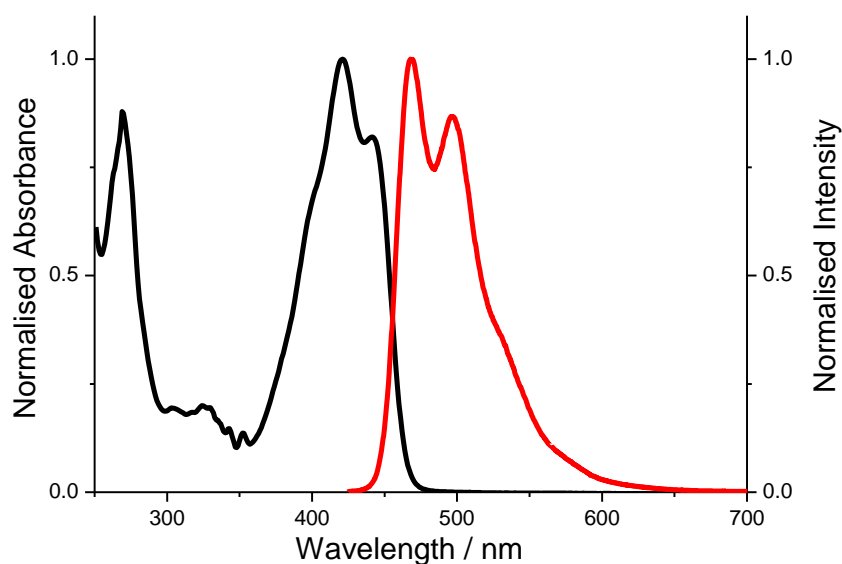


Figure 3. Room temperature normalized absorption (black) and fluorescence (red) spectra recorded for CXD in THF.

Intense emission is observed for an air-equilibrated THF solution of CXD (Figure 3), the fluorescence quantum yield (Φ_F) being 0.96 and the excited-singlet state lifetime (τ_S) being 7.4 ns. The quantum yield was measured relative to perylene in dilute methylcyclohexane solution.¹⁶ Similar spectral deconstruction of the reduced fluorescence spectral profile involves two overlapping vibronic modes. These correspond to averaged values of $1,145$ and $1,815\text{ cm}^{-1}$. This leads to poor mirror symmetry between absorption and fluorescence spectra. Even so, there is good agreement between the radiative rate constant ($k_{\text{RAD}} = 1.2 \times 10^8\text{ s}^{-1}$) calculated from the Strickler–Berg expression¹⁷ and the experimental value ($k_{\text{RAD}} = \Phi_F / \tau_S$) (Table 2). The 0,0 fluorescence band is located at $21,365\text{ cm}^{-1}$, thereby allowing calculation of the accurate Stokes' shift as being $1,180\text{ cm}^{-1}$.

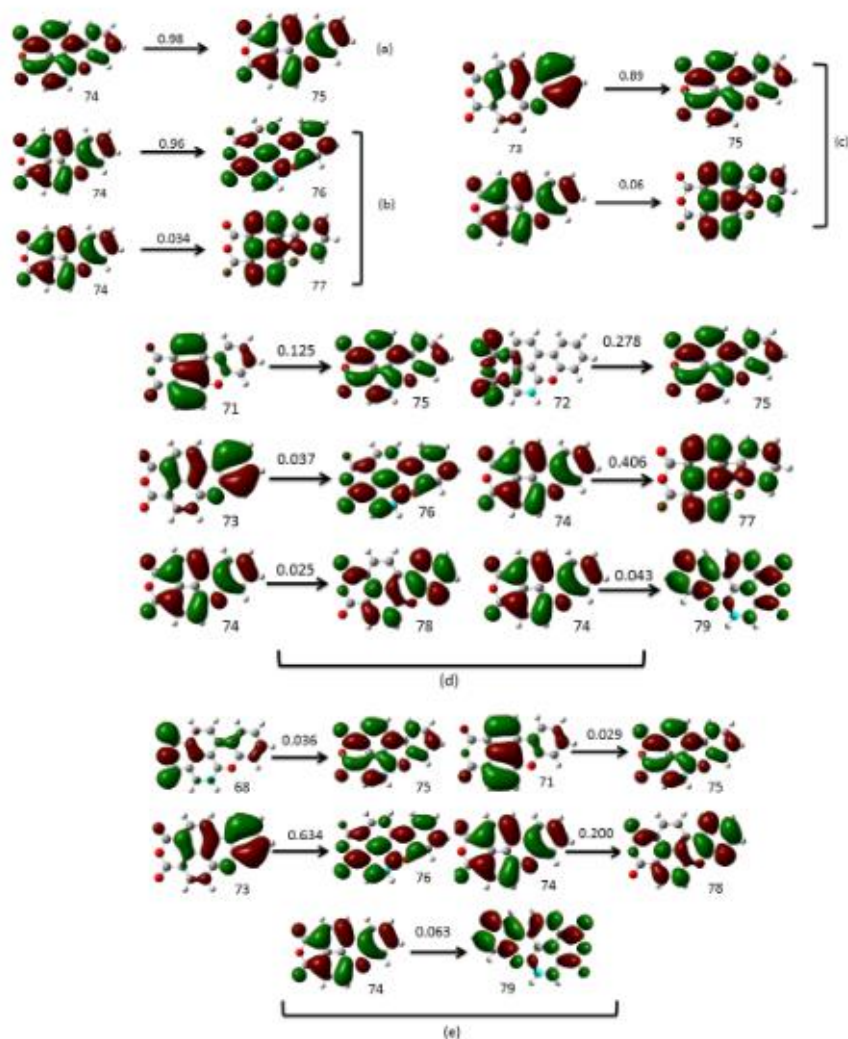
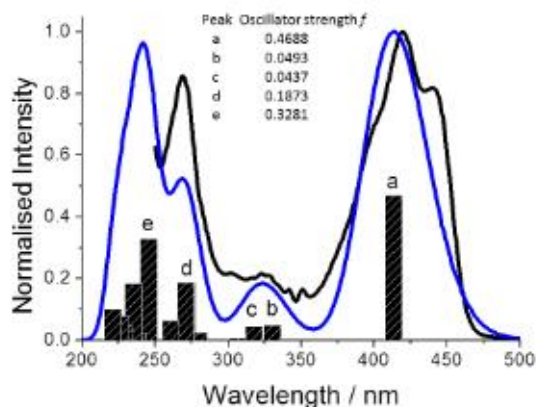


Figure 4. Comparison of recorded absorption spectrum for CXD in THF (black) and calculated (blue) spectrum using TD-DFT (B3LYP, 6-31G(d)) in a THF solvent continuum. Bars depict calculated electronic transitions with selected molecular orbitals shown for (a) to (e). The number of the molecular orbital is shown and the square of the coefficient multiplied by two is given above the arrow.

Photophysical properties measured for CXD in several solvents are collected in Table 2. Despite the subtle alterations to the shape of the emission profile with changing solvent, the lack of any

correlation between the emission peak maximum (λ_{FLU}) and a solvent polarity function is consistent with the excited state possessing a dipole moment comparable to that of the ground state. Furthermore, fluorescence quantum yields are close to unity and more-or-less constant across the range of solvents used; the small variations in the excited-state lifetimes are attributed to perturbations in the non-radiative rate constants ($k_{\text{NR}} = (1-\Phi_{\text{F}}) / \tau_{\text{S}}$). There is no obvious correlation between k_{NR} and, for example, the polarity of the solvent (cf THF vs. PC). The important point from this study is that emission is almost quantitative in solution at room temperature. See Figures 5 and 6 for the effects of solvent polarity on the absorption and fluorescence spectra of CXD in dilute solution. It might be noted that CXD is readily soluble in these solvents and shows no tendency for aggregation.

Table 2. Collected photophysical parameters recorded for CXD in a small range of solvents at room temperature.

Solvent	λ_{ABS} [nm]	$\epsilon_{\text{MAX}} / \text{M}^{-1} \text{cm}^{-1}$	λ_{FLU} [nm]	Φ_{F}	τ_{S} [ns]	$K_{\text{RAD}} [10^8 \text{ s}^{-1}]$	$K_{\text{NR}} [10^6 \text{ s}^{-1}]$
THF ^a	420	17,600	467	0.96	7.4	1.3	5.1
	441	14,500	497				
MeCN	423	14,900	474	0.94	8.1	1.1	7.4
	443	12,800	500				
Toluene	424	16,200	467	0.95	7.7	1.2	6.8
	447	13,200	497				
DEE ^b	418	14,900	460	0.96	8.7	1.1	4.9
	440	12,000	490				
PC ^c	427	17,600	476	0.96	7.4	1.3	5.1
	445	17,200	503				

^aTetrahydrofuran, ^bDiethyl ether, ^cPropylene carbonate.

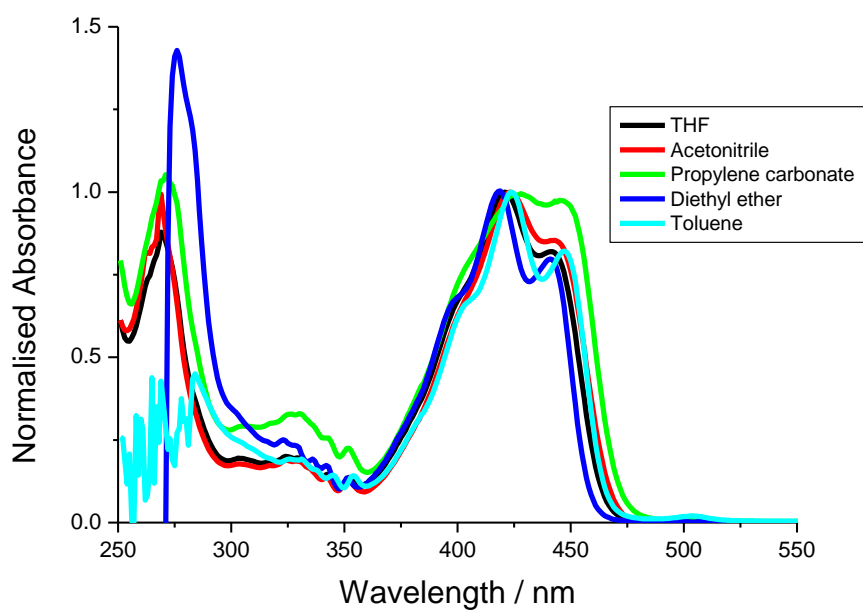


Figure 5. Room temperature normalized absorption spectra recorded for CXD in different solvents.

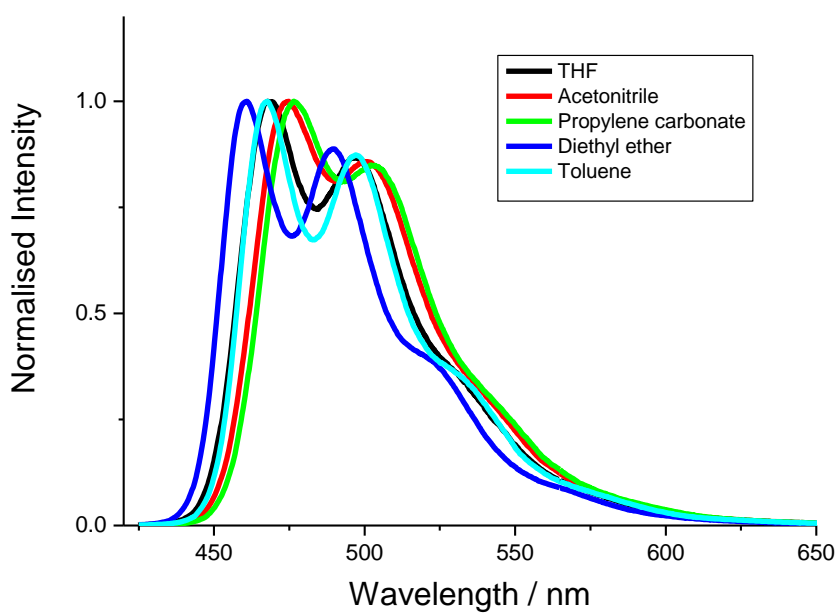


Figure 6. Room temperature normalized fluorescence spectra recorded for CXD in different solvents.

Unsurprisingly in view of the high fluorescence quantum yield, it was not possible to detect phosphorescence from CXD in an optical glass formed by freezing 2-methyltetrahydrofuran to 77 K. Likewise, it was not possible to detect the transient formation of the CXD triplet-excited state by laser

flash photolysis in deoxygenated THF at room temperature. Adding iodoethane as an external heavy-atom perturber¹⁸ to the low-temperature glass failed to switch on phosphorescence from CXD. In passing, it was found that iodoethane quenched the fluorescence from CXD in THF solution but the resulting Stern-Volmer plot showed positive deviation from linearity (Figure 7). In contrast, the Stern-Volmer plot generated using the excited-singlet state lifetime was linear, corresponding to a bimolecular quenching rate constant of ca. $3 \times 10^6 \text{ M}^{-1} \text{ s}^{-1}$. This latter value is well below the diffusion-controlled rate limit. The nonlinear Stern-Volmer plot observed for the quantum yields can be explained in terms of fluorescence quenching occurring via a combination of dynamic and static effects.¹⁹ The latter is a consequence of iodoethane forming a non-fluorescent complex with CXD. Because of the absence of phosphorescence, we were unable to establish the triplet energy for CXD.

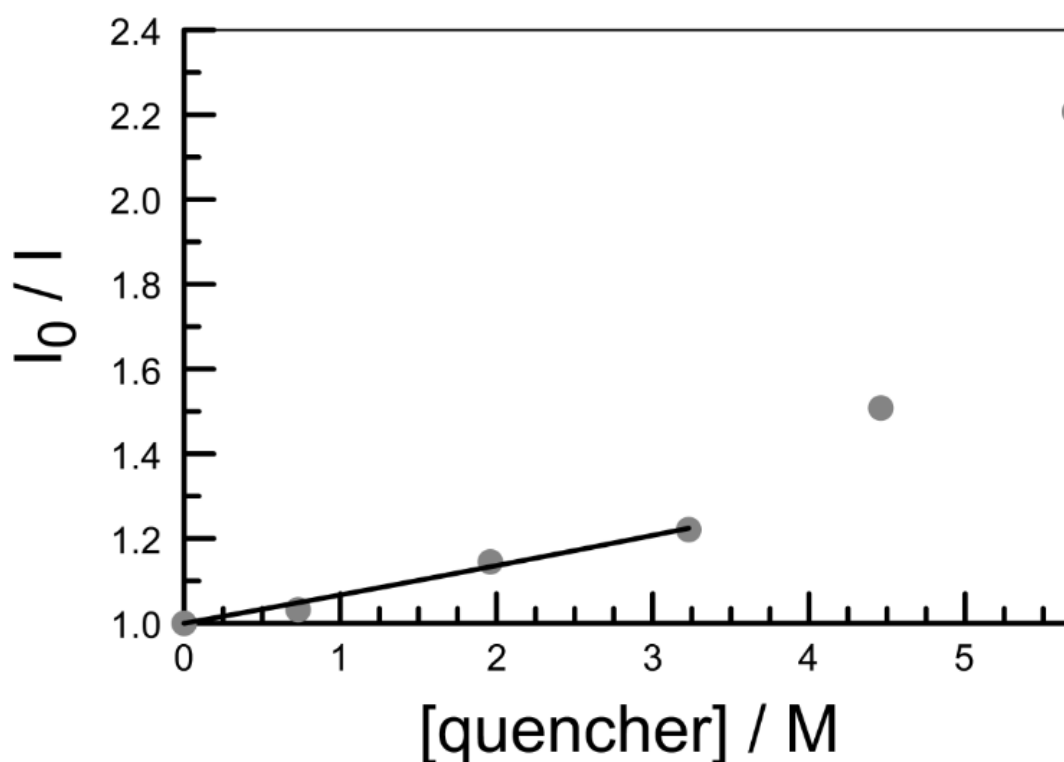


Figure 7. Stern-Volmer plot constructed for the addition of iodoethane to a solution of CXD in THF. The solid line represents a fit to a combination of dynamic quenching and formation of a 1:1 non-fluorescent complex.

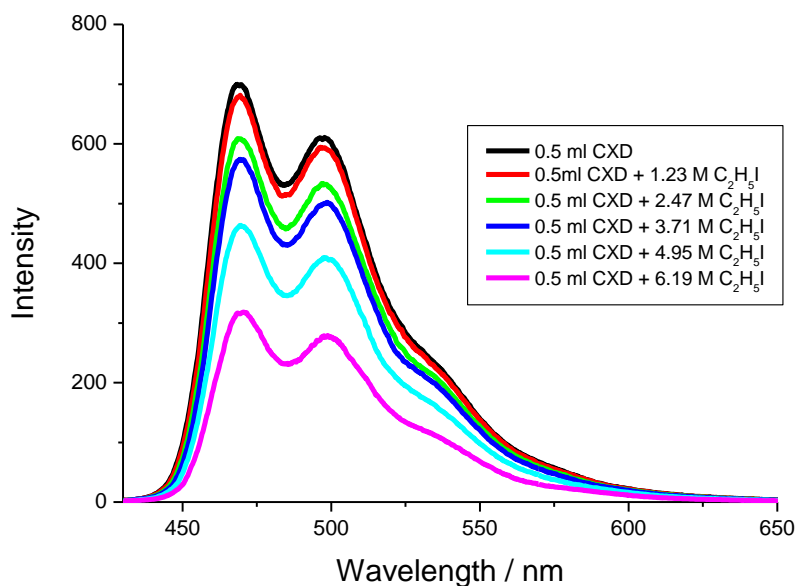
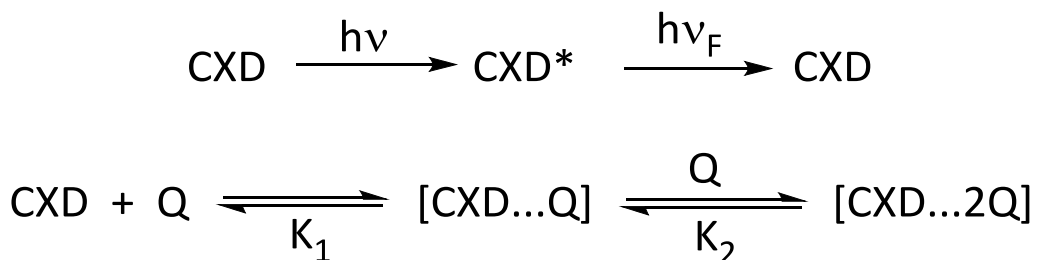


Figure 8. Effect of increasing concentrations of iodoethane on the fluorescence spectral profile of CXD in THF solution.

It might be noted that many aromatic hydrocarbons form a ground-state complex with iodo-compounds in non-polar solvents. This situation was first investigated in detail by Nemzek and Ware,²⁰ who developed a theoretical analysis for 1:1 and 1:2 complexation. A characteristic feature of such systems is the upwards curvature of the Stern-Volmer plot, as is evident from (Figure 7). It is also clear that the fluorescence spectral profile does not change in the presence of a large excess of iodoethane (Figure 8), only the intensity falls. It is difficult to say that the resultant complex is non-fluorescent because there is always some free CXD in the system and this, of course, is strongly fluorescent. Analyzing the fluorescence yield in terms of the Scheme 2, and taking the dynamic quenching rate constant as being $3 \times 10^6 \text{ M}^{-1} \text{ s}^{-1}$, we can obtain estimates²⁰ for the complexation constants, K_1 and K_2 (Scheme 2); note it is not possible to fit the entire curve to a single complexation step. Under our experimental conditions, we find $K_1 = 0.03 \pm 0.01 \text{ M}^{-1}$ for formation of a 1:1 complex. Fitting to the second complexation step is much less accurate but gives a very rough value for K_2 of $1.5 \pm 0.7 \text{ M}^{-2}$. According to Nemzek and Ware, the occurrence of 1:2 complexes is quite common.



Scheme 2. Illustration of the effect of adding high concentrations of iodoethane to a solution of CXD in THF. Only the non-complexed solute is fluorescent. Formation of both 1:1 and 2:1 complexes is considered.

3.4 Photochemical stability

The insignificant population of the triplet-excited state via intersystem crossing might be used to argue that CXD will be stable against photochemical degradation. The logic for this suggestion comes from the realization that the most common cause of photobleaching arises from intermediate formation of singlet molecular oxygen.²¹ This latter species is formed by way of electronic energy transfer²² from a high-energy triplet state to ground-state oxygen. Singlet oxygen, although short lived in most solvents,²³ is highly reactive towards unsaturated bonds and readily forms hydroperoxide species that can enter into chain reactions.²⁴ To have any practical application, it is necessary for new emitters to be photo-stable and therefore we set out to examine the performance of CXD under continuous illumination.

The experiment involved preparing a solution of CXD in an organic solvent and saturating the solution with air. The sample was sealed in an air-tight cuvette before recording the absorption spectrum. The absorbance at the lowest-energy absorption maximum was adjusted before sealing the cuvette to have a value of around unity. The sample was exposed to white light delivered from a 400W quartz halogen lamp, filtered to remove UV and IR radiation. After pre-determined times, the cuvette was removed and the absorption spectrum recorded. This procedure was repeated for many cycles. Unfortunately, it proved impossible to prevent the evaporation of diethyl ether from the cuvette and, in this experiment, the absorbance climbed gradually with exposure time. Even without the light source, the absorbance increased slightly but steadily with time. This experiment was abandoned.

In other solvents, notably THF, acetonitrile, propylene carbonate and toluene there was no significant change in absorbance over short (i.e., 100 minutes) irradiations. Loss of compound was restricted to less than 1%. In the case of propylene carbonate, for example, this corresponds to the approximate absorption of 30,000 photons per molecule without loss (Figure 9). Even in direct sunlight, CXD was found to remain unaffected by prolonged illumination. Some loss was observed when the compound in THF was irradiated with a high-power (i.e., 5 mW) LED emitting at 408 nm.

Here, we could estimate a crude quantum yield for photobleaching as being in the region of 10^{-5} . Obviously, with such a low rate of photobleaching, it is not possible to make meaningful comments about the reaction mechanism.

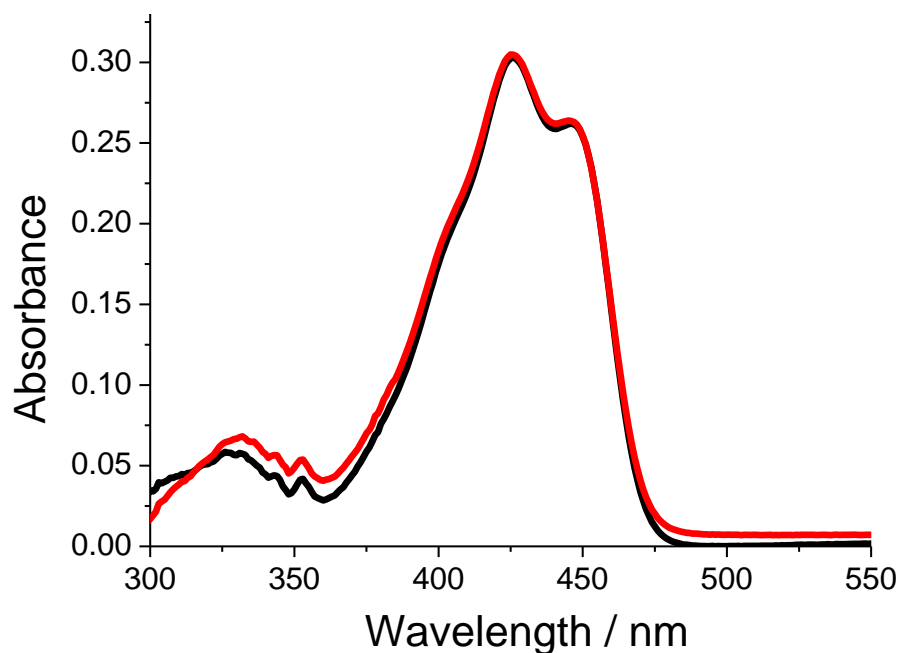


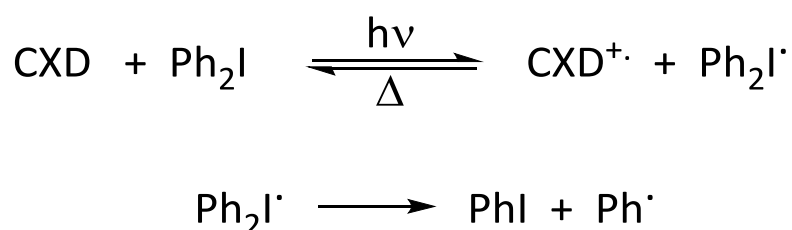
Figure 9. Absorption spectra recorded for CXD in air-equilibrated propylene carbonate following irradiation with an unfiltered 400 W halogen lamp before (black curve) and after 3 hours (red curve).

3.5 Photo-induced polymerization

We are now able to add CXD to the burgeoning library of known fluorescent compounds. This compound is relatively small, easily purified and well characterized. It is relatively stable and can be stored in the solid state or as a solution for prolonged periods, especially at low temperature. The compound does not suffer unduly from issues relating to aggregation or poor solubility. Although there are no ionic groups, the molecule has a high dipole moment that assists solubility in polar organic solvents but not water. A useful attribute of this compound is the strong absorption at 408 nm, which is ideal for excitation with a violet LED. We foresee CXD being one component of a white emitter, with excitation at 408 nm. To be practical, any material for use with OLEDs needs to be fully compatible with the polymer matrix. We found that CXD could be dispersed in PMMA and cast into a film to give a strongly fluorescent layer of variable thickness. Because CXD is redox active, it was decided to test

its ability to initiate light-induced polymerization. Here, the important point is to use light to activate the monomer via free radical reactions but to leave no residual colouration in the resultant polymer film.

As a starting point, we examined the electron-transfer chemistry between CXD and diphenyliodonium chloride (DPI), the latter being a well-known initiator²⁵ for free radical polymerizations. In methanol solution, addition of DPI to CXD in the dark had little effect but once exposed to light the yellow colour of the CXD faded rapidly. Within a few minutes, the solution was colourless. This suggests that the excited-singlet state of CXD is able to enter into electron-transfer reactions with DPI so as to form free radicals, which subsequently attack CXD. An outline for this proposed system is shown below (Scheme 3).



Scheme 3. Proposed sequence of reactions covering the photochemical bleaching of CXD in the presence of the free-radical generator. NB Ph = phenyl

To provide some quantitative data, a Stern-Volmer plot was established for quenching of the excited-singlet state of CXD by DPI in methanol solution (Figures 10 and 11). It was observed that DPI reduced the fluorescence quantum yield but did not affect the spectral shape. The resultant Stern-Volmer plot was linear, passing through the origin, with a Stern-Volmer constant (K_{SV}) of 30 M^{-1} . At higher concentrations of quencher, the Stern-Volmer plot shows negative deviation from linearity but this was found to be an artefact. The problem was caused by leaving the solution in room light. Using the excited-singlet state lifetime (τ_s) for CXD of 7.4 ns, the bimolecular quenching rate constant ($k_Q = K_{SV} / \tau_s$) can be calculated as being $4 \times 10^9 \text{ M}^{-1} \text{ s}^{-1}$. This can be compared to the diffusional limit²⁶ of $2 \times 10^{10} \text{ M}^{-1} \text{ s}^{-1}$ for methanol at 20 °C. Thus, light-induced electron transfer is quite efficient in this system. It is known that DPI can be reduced²⁷ with a reduction potential of -0.7 V vs SCE. Now, according to our cyclic voltammetry studies, CXD shows an irreversible one-electron oxidation peak at +1.65 V vs SCE. The excited-state energy for CXD is approximately 2.72 eV. From this information, we can estimate the oxidation potential for the excited-singlet state of CXD as being ca. -1.0 V vs SCE. As such, a crude estimate for the thermodynamic driving force for light-induced electron transfer in this system is -0.3 eV. This appears to be fully consistent with the high quenching rate constant. Indeed,

the Rehm-Weller relationship²⁸ would predict that fluorescence quenching is efficient but less than diffusional limited in this case.

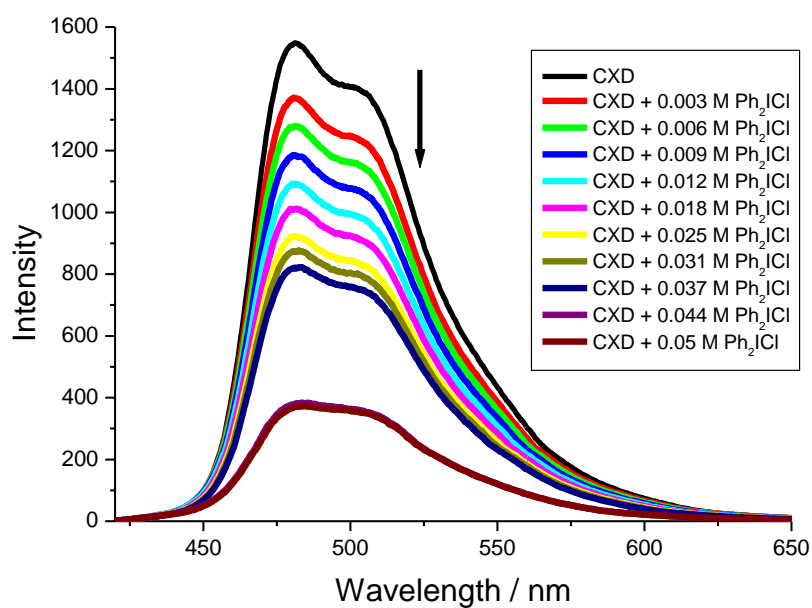


Figure 10. Effect of increasing concentrations of DPI on the fluorescence spectral profile of CXD in methanol solution.

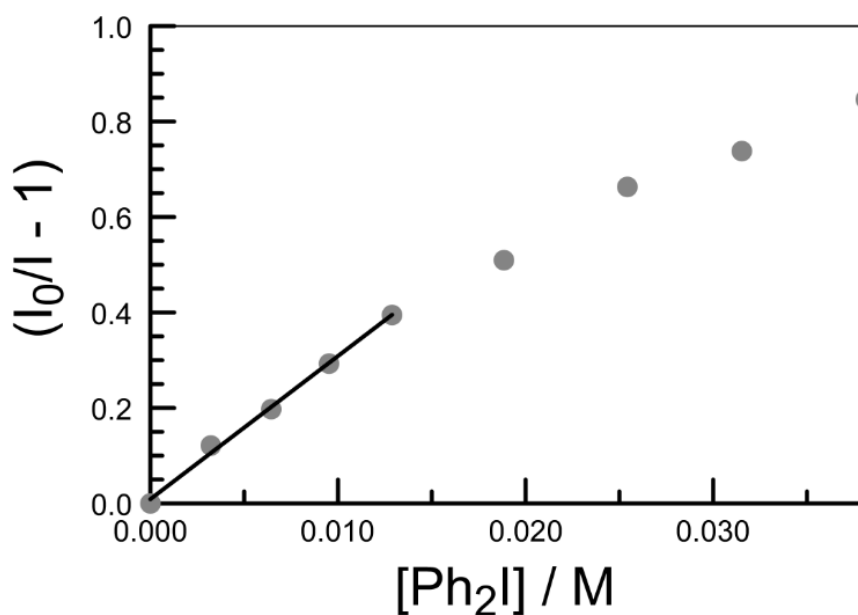


Figure 11. Stern-Volmer plot constructed for the addition of DPI to a solution of CXD in methanol. Data points correspond to fluorescence quantum yields and the line drawn through the points is a best fit to the Stern-Volmer relationship.

In continuation of these experiments, a solution of PDI (0.015 M) and freshly distilled methyl methacrylate (6.2 M) in methanol was deoxygenated with a dry N₂ stream. The mixture was exposed to white light ($\lambda > 360$ nm) but polymerization did not occur, even on long times. Then, CXD (20 μ M) was added to the solution under anaerobic conditions. This caused the solution to appear yellow in colour and to display strong fluorescence. Polymerization did not take place in the dark. However, switching on the light source had the effect of increasing the viscosity of the solution. There was the concomitant loss of both the yellow colour and the fluorescence. After a few minutes illumination, the solution had turned solid and the yellow colouration had disappeared completely (Figure 12).

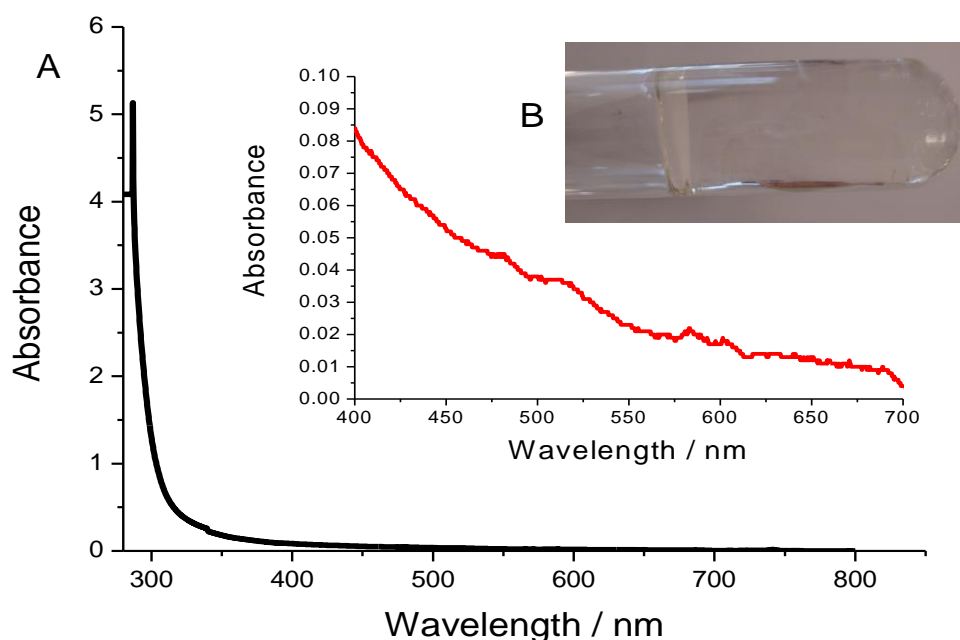


Figure 12. Absorption spectrum for PMMA showing the Rayleigh scattering effect from the polymer (A). The inset shows a picture of the PMMA polymer in a glass tube.

Because of the presence of methanol, photo-polymerization leads to the development of a soft organo-gel,²⁹ although the viscosity is very high relative to solution. In order to investigate the molecular environment within the gel, the polarity-sensitive probe JBD³⁰ was adsorbed into the matrix of the polymer (Figure 13). The absorption maximum of this latter dye depends on the polarity of the solvent. The absorption spectra measured for JBD in a small range of solvents of differing polarity are shown in Figure 13. The static dielectric constant (ϵ_s) for PMMA at room temperature is 3.5,³¹ which is not dissimilar to that in dibutyl ether ($\epsilon_s = 3.1$). However, the observed spectrum for JBD dispersed in the organo-gel is inconsistent with that of dibutyl ether. The spectrum, in fact, is more closely related to that of dichloromethane, where ϵ_s is 8.93. The presence of methanol in the organo-gel could help explain this result.

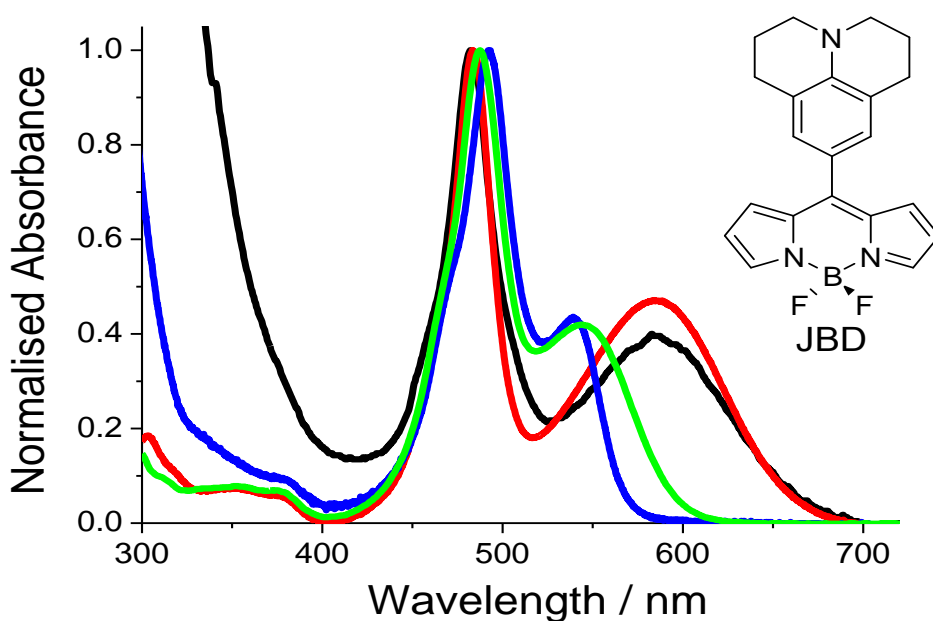


Figure 13. Absorption spectra for the proton/polarity sensitive probe JBD in CH_2Cl_2 (red), dibutyl ether (green) and methylcyclohexane (blue), and when absorbed into the PMMA polymer (black).

3.6 Afterthought

It was noted earlier that CXD is a dipolar molecule because of the occurrence of intramolecular charge-transfer interactions. In general, the anhydride group serves the purpose of being the charge acceptor while the aromatic core functions as charge donor. The actual dipole moment is kept modest by the short charge separations; for example, our computed value of 14.5 D in THF can be compared to that found for the giant porphyrin-carotene-fullerene triad described by Gust et al.³² where the dipole moment is 150 D. We have not been able to provide an experimental estimate for the dipole moment but we note that CXD is asymmetric and as such the charge will be distributed unevenly around the molecule. Indeed, the computed charges were shown earlier as part of Figure 2. Because of this intramolecular charge transfer, the various bond lengths differ from those expected from classical molecular groupings where the molecule is essentially nonpolar. The bond lengths computed for CXD are shown below in Table 3. This information is interesting because Dr. P. G. Waddell of the Newcastle Crystallography Laboratory has described³³ a procedure for determining the relative contributions of dipolar resonance forms on the basis of the bond lengths determined by X-ray crystallography. This procedure is a marked upgrade on the protocol used by Harriman et al.³⁴ to determine resonance structures for merocyanine dyes. The latter is actually an extension of a procedure reported originally by Linus Pauling.³⁵ Because of the interest in dipolar molecules as charge carriers,³⁶ it might be instructive to see if a similar analysis can be made for CXD. Rather than use the crystal structure, which

was determined by a member of the Molecular Photonics Laboratory and will be part of his PhD thesis, we prefer to use the results from the DFT calculation made in a reservoir of THF molecules.

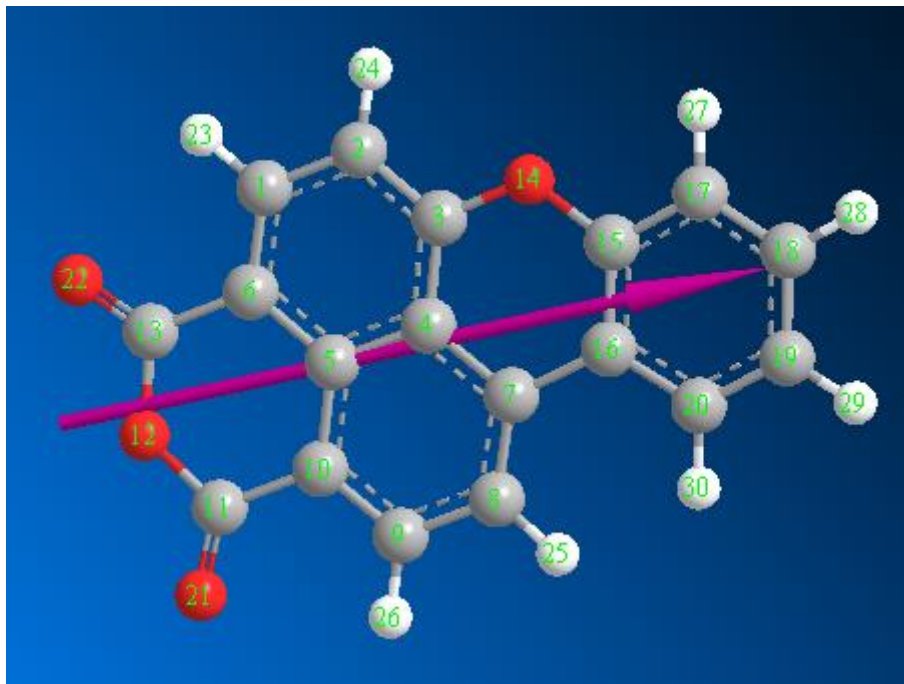


Figure 14. Molecular structure for CXD as computed by DFT (B3LYP) using GAMESS at the 6.311(G)d level with the PCM solvent model and the Mennucci / Tomasi compensation model. The direction of the dipole is indicated by the arrow and the atom labels are shown.

The computed structure (Figure 14) was used to obtain the bond lengths for the important C-C and C-O bonds (Table 3). These were used as input for the subsequent HOSE calculation. Calculating the Harmonic Oscillator Stabilisation Energy (HOSE) can provide a quantitative measure of the contribution of individual resonance structures to the overall bond length pattern of an aromatic ring.³⁷ This can be useful for estimating the extent of and likely pathways of charge transfer across the molecule. The seven different bond length patterns for the aromatic ring for which HOSE is to be calculated (denoted by the label in the scheme below), as derived from the nine resonance forms, are the two Kekulé resonance forms (K1 and K2), three *ortho*-quinoidal motifs (oQ1, oQ2 and oQ3), a *para*-quinoidal motif (pQ) and a rhodizoidal motif (R2). Charge-separated resonance forms are indicated in red (Figure 15).

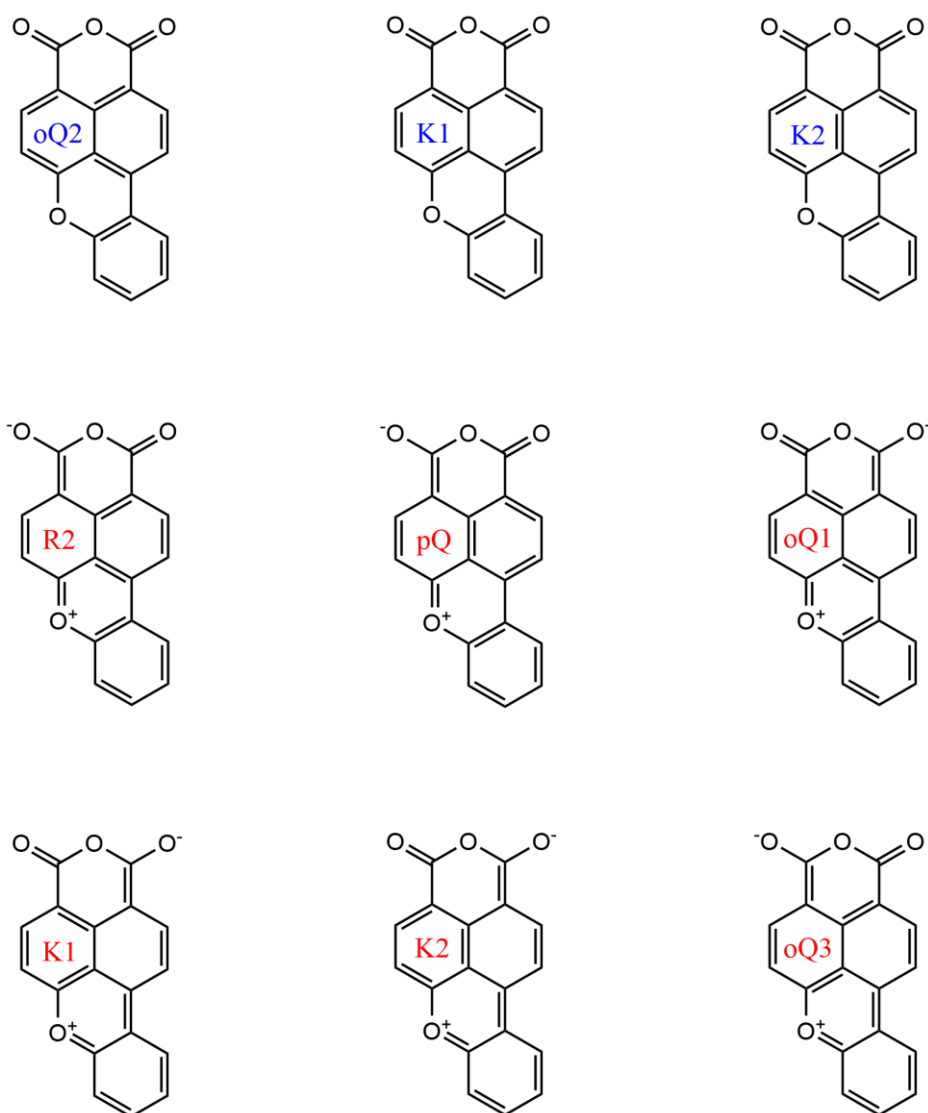


Figure 15. Illustration of the important resonance forms projected for CXD.

The HOSE calculation for each resonance form yields the following values (in kJ/mol) and the percentage contributions of each resonance form are as follows:

K1/K1	K2/K2	pQ	oQ1	oQ2	oQ3	R2
80.25	36.78	77.51	78.07	38.45	81.35	79.18
10.72	23.38	11.09	11.01	22.37	10.57	10.86

Analysing the HOSE and percentage contributions shows there is a general trend for the charge-separated forms to be associated with high energies and hence low overall contributions to the structure. The two resonance forms that exhibit a contribution of over 20% are oQ2, which is not charge-separated, and K2, for which there are both charge-separated and ground-state resonance forms. The charge-separated form of K2 is associated with the pQ motif in the adjacent ring for which an energy of 79.25 kJ/mol and a contribution of 10.18% were calculated and hence the greater

contribution to this K2 motif is the ground-state resonance form. As the change from oQ2 to K2 requires only that the adjacent ring flip between the two low energy Kekulé resonance forms, this can be rationalised fairly intuitively. From this analysis it can be concluded that the structure of CXD exhibits minimal charge-transfer character.

Table 3. Compilation of the important bond lengths calculated for CXD and the corresponding optimum values listed in the database.

Atoms	Calculated bond lengths	Optimum bond lengths
C(9)-C(8)	1.407	1.420
C(10)-C(11)	1.477	1.517
C(10)-C(9)	1.364	1.420
C(18)-C(17)	1.376	1.420
C(19)-C(18)	1.393	1.420
C(20)-C(19)	1.372	1.420
C(15)-C(17)	1.387	1.420
C(16)-C(20)	1.398	1.420
C(16)-C(15)	1.389	1.420
C(7)-C(16)	1.473	1.503
C(7)-C(8)	1.373	1.420
C(5)-C(10)	1.410	1.420
C(6)-C(13)	1.474	1.517
C(6)-C(5)	1.406	1.420
C(1)-C(6)	1.371	1.420
C(2)-C(1)	1.399	1.420
C(3)-C(2)	1.371	1.420
C(4)-C(7)	1.420	1.420
C(4)-C(5)	1.405	1.420
C(4)-C(3)	1.412	1.420
O(14)-C(3)	1.338	1.355

Table 3. Continued.

O(14)-C(15)	1.357	1.355
O(12)-C(13)	1.360	1.338
O(12)-C(11)	1.355	1.338
C(13)-O(22)	1.171	1.208
C(11)-O(21)	1.176	1.208

3.7 Conclusion

In this chapter, we have reported some photophysical properties for the target compound CXD. This compound is strongly fluorescent, possesses a relatively long-lived excited-singlet state and is resistant towards intersystem crossing to the triplet manifold. The compound has a large dipole moment due to intramolecular charge transfer from the aromatic core to the anhydride residue. Despite this charge vector, CXD does not display the features considered characteristic of compounds showing significant amounts of intramolecular charge transfer. Elsewhere in this thesis, we report on MBIC³⁸ which shows charge-recombination fluorescence. Here, the fluorescence quantum yield and excited-state lifetime decrease dramatically as the polarity of the solvent increases. There is also an important lowering of the energy of the fluorescence spectral maximum as the solvent dielectric constant augments. We see none of these features with CXD.

It is interesting to compare the molecular formulae for CXD and MBIC (Figure 16). The only real difference seems to be that whereas CXD spreads charge all around the molecule, this charge is more localized for MBIC. This might be an important point for the design of new compounds showing charge-recombination fluorescence and/or absorption. Our understanding for CXD is that the absorption and emission transitions are primarily of π,π^* character.

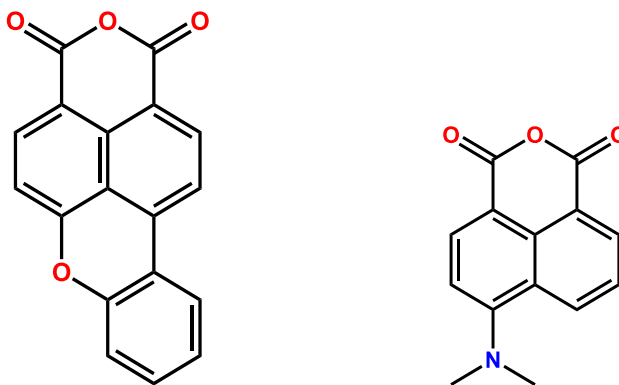


Figure 16. Comparison of the molecular formulae for CXD (left-hand side) and MBIC (right-hand side).

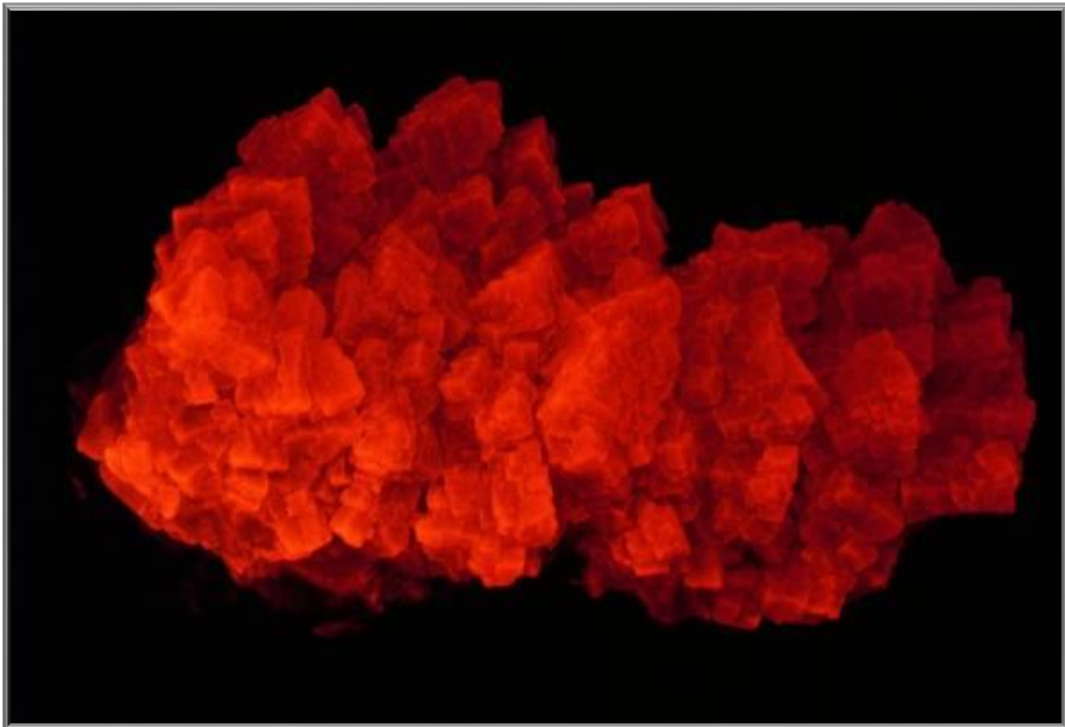
3.8 References

1. Atkins, P.; Jones, L. *Chemical Principles: The Quest for Insight*; 2nd ed.; W. H. Freeman and Company: New York, NY, **2002**.
2. Lakowicz, J. R. *Principles of Fluorescence Spectroscopy*; 2nd ed.; Springer Science: New York, USA, **2004**.
3. Peterman, E. J. G.; Sosa, H.; Moerner, W. E. *Annu. Rev. Phys. Chem.* **2004**, 55, 79.
4. Yao, J.; Yang, M.; Duan, Y. *Chem. Rev.* **2014**, 114, 6130.
5. Shu, T.; Wu, J.; Lu, M.; Chen, L.; Yi, T.; Li, F.; Huang, C. *J. Mater. Chem.* **2008**, 18, 886.
6. Govorov, A.; Martínez, P. L. H.; Demir, H. V. *Understanding and Modeling Förster - type Resonance Energy Transfer (FRET) Introduction to FRET*; Vol. 1; Springer Science: Singapore, **2016**.
7. Huang, B.; Bates, M.; Zhuang, X. *Annu. Rev. Biochem.* **2009**, 78, 993.
8. Scholz, S.; Kondakov, D.; Lüssem, B.; Leo, K. *Chem. Rev.* **2015**, 115, 8449.
9. Bässler, H. *Polym. Adv. Technol.* **1998**, 9, 402.
10. Dias, F. B.; Penfold, T. J.; Monkman, A. P. *Methods Appl. Fluoresc.* **2017**, 5, 012001.
11. Andrade, B. W. D'; Forrest, S. R. *Adv. Mater.* **2004**, 16, 1585.
12. Yin, H.; Zhu, W.; Xu, Y.; Dai, M.; Qian, X.; Li, Y.; Liu, J. *Eur. J. Med. Chem.* **2011**, 46, 3030.
13. Al-Aqar, R.; Avis, D.; Benniston, A. C.; Harriman, A. *RSC Adv.* **2014**, 4, 53072.
14. Marcinek, A.; Rogowski, J.; Adamus, J.; Gębicki, J.; Platz, M. S. *J. Phys. Chem.* **1996**, 100, 13539.
15. Alexiou, M. S.; Tychopoulos, V.; Ghorbanian, S.; Tyman, J. H. P.; Brown, R. G.; Brittain, P. I. *J. Chem. Soc., Perkin Trans.2.* **1990**, 837.
16. Berlman, I. B. *Handbook of Fluorescence Spectra of Aromatic Molecules*; Academic Press: New York, NY, **1965**.
17. Strickler, S. J.; Berg, R. A. *J. Chem. Phys.* **1962**, 37, 814.
18. McGlynn, S. P.; Daigre, J.; Smith, F. J. *J. Chem. Phys.* **1963**, 39, 675.
19. Keizer, J. *J. Am. Chem. Soc.* **1983**, 105, 1494.
20. Nemzek, T. L.; Ware, W. R. *J. Chem. Phys.* **1975**, 62, 477.
21. Zhang, L.; Huang, Z.; Dai, D.; Xiao, Y.; Lei, K.; Tan, S.; Cheng, J.; Xu, Y.; Liu, J.; Qian, X. *Org. Lett.* **2016**, 18, 5664.
22. DeRosa, M. C.; Crutchley, R. J. *Coord. Chem. Rev.* **2002**, 233-234, 351.
23. Salokhiddinov, K. I.; Byteva, I. M.; Gurinovich, G. P. *J. Appl. Spectrosc.* **1981**, 34, 561.
24. Ghogare, A. A.; Greer, A. *Chem. Rev.* **2016**, 116, 9994.

25. Xiao, P.; Dumur, F.; Graff, B.; Gignes, D.; Fouassier, J. P.; Lalevée, J. *Macromolecules*. **2014**, *47*, 601.
26. Murov, S. L.; Carmichael, I.; Hug, G. L. *Handbook of Photochemistry*; 2nd ed.; Marcel Dekker, Inc.: New York, NY, **1993**.
27. Gómez, M. L.; Montejano, H. A.; Previtali, C. M. *J. Photochem. Photobiol. A: Chem.* **2008**, *197*, 18.
28. Rehm, V. D.; Weller, A. *Ber. Bunsen - Ges. Phys. Chem.* **1969**, *73*, 834.
29. Cao, X.; Zhang, T.; Gao, A.; Li, K.; Cheng, Q.; Song, L.; Zhang, M. *Org. Biomol. Chem.* **2014**, *12*, 6399.
30. Benniston, A. C.; Clift, S.; Harriman, A. *J. Mol. Struct.* **2011**, *985*, 346.
31. Frahn, M. S.; Luthjens, L. H.; Warman, J. M. *J. Phys. Chem. B.* **2004**, *108*, 2839.
32. Smirnov, S. N.; Liddell, P. A.; Vlasiouk, I. V.; Teslja, A.; Kuciauskas, D.; Braun, C. L.; Moore, A. L.; Moore, T. A.; Gust, D. *J. Phys. Chem. A.* **2003**, *107*, 7567.
33. Liu, X.; Cole, J. M.; Waddell, P. G.; Lin, T.-C.; Radia, J.; Zeidler, A. *J. Phys. Chem. A.* **2012**, *116*, 727.
34. Benniston, A. C.; Harriman, A. *J. Chem. Soc., Faraday Trans.* **1998**, *94*, 1841.
35. Pauling, L. *The Nature of the Chemical Bond and the Structure of Molecules and Crystals: An Introduction to Modern Structural Chemistry*; 3rd ed.; Cornell University Press: Ithaca, New York, **1960**.
36. Proctor, C. M.; Kuik, M.; Nguyen, T.-Q. *Prog. Polym. Sci.* **2013**, *38*, 1941.
37. Krygowski, T. M.; Anulewicz, R.; Kruszewski, J. *Acta Cryst.* **1983**, *B39*, 732.
38. Al-Aqar, R.; Atahan, A.; Benniston, A. C.; Perks, T.; Waddell, P. G.; Harriman, A. *Chem. Eur. J.* **2016**, *22*, 15420.

Chapter 4.

Cresyl Violet: A Convenient Fluorescence Standard for the Red Spectral Region?



AN INORGANIC MINERAL DISPLAYING BRIGHT RED LUMINESCENCE UNDER NEAR-UV ILLUMINATION.

4.1 Introduction

Fluorescence spectroscopy, which has been a mainstay of optical spectroscopy for almost one hundred years, continues to expand at an astonishing rate. New techniques, such as super-resolution microscopy,¹ provide new opportunities to explore biological and molecular materials in ever-greater detail. Improved excitation sources, such as high power light-emitting diodes with narrow wavelength dispersion,² increase spectral sensitivity while time-resolved emission spectroscopy underpins further important applications such as fluorescence lifetime imaging spectroscopy.³ As the diversity of fluorescence spectroscopy grows so does the need to work with more complex systems. With biological or biomedical organisms, for example, there is a requirement to employ fluorophores that absorb and emit in the red region of the electromagnetic spectrum. This apparently simple requirement brings substantial challenges, especially in respect to accurate determination of the fluorescence quantum yield. Although the ready availability of integrating spheres⁴ has simplified measurement of emission quantum yields, most determinations continue to be made by the ratiometric method⁵ where the emission yield is compared to that of a well established reference compound. There are numerous classical standard materials⁶ for the near-UV, yellow, blue and orange regions but less so for the red region. Popular standards for the red region include chlorophyll-a,⁷ aluminium(III) phthalocyanine-tetrasulfonate,⁸ zinc(II)⁹ and free-base *meso*-tetraphenylporphyrin,¹⁰ and certain dyes with extended π -systems.¹¹ Such compounds are often limited in terms of solubility and stability. Other fluorophores, notably various derivatives of cyanine dyes, are available but quantum yield data are often unconfirmed or highly sensitive to the local environment because of competing light-induced isomerisation.¹²

Considerable attention has been given to the use of cresyl violet perchlorate (CV) as a possible fluorescence standard for the red region.¹³⁻¹⁵ Cresyl violet is a member of the oxazine family of dyes, a class of organic compounds with long history as stains for use in biology and histology.¹⁶ These dyes are built around a planar aromatic core that is susceptible to aggregation in certain solvents (Figure 1). Cresyl violet shows strong fluorescence in ethanol solution under ambient conditions¹³⁻¹⁵ and displays a relatively broad absorption band with a maximum located at 609 nm. The corresponding fluorescence maximum lies at 627 nm in ethanol, corresponding to a crude Stokes shift of ca. 460 cm^{-1} . The emission band is significantly less broad and shows poor mirror symmetry with what appears to be the lowest-energy absorption transition. The fluorescence quantum yield (Φ_F) in dilute methanol solution was originally reported¹³ to be 0.54 on the basis of detailed thermal blooming studies. Overall, these properties make for a useful fluorescence standard and there have been many reports where the emission properties of new fluorophores have been compared to those

of cresyl violet. There are, however, concerns¹⁷ about the reliability of the primary Φ_F determinations because of possible issues relating to aggregation and polarity effects. Here, we re-examine the fluorescence properties of cresyl violet in fluid solution in order to assess any important limitations for this compound as a secondary fluorescence standard.

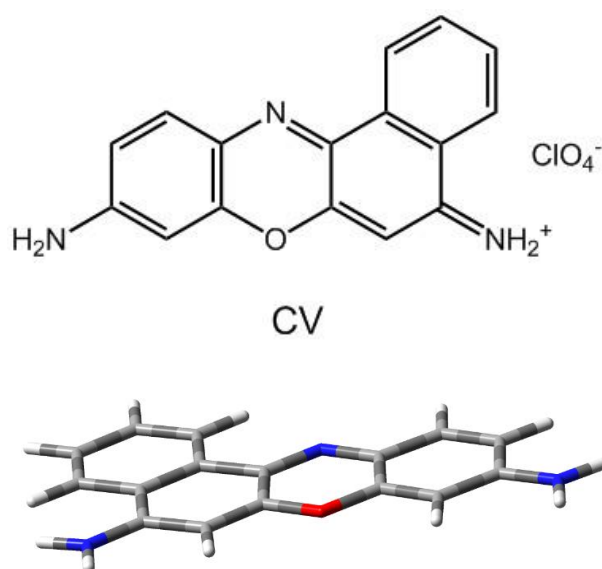


Figure 1. Molecular structure of cresyl violet showing one of the main resonance forms, and including the perchlorate anion. The lower panel shows the DFT computed molecular geometry and emphasizes the planarity of the molecule.

The original studies made by Magde *et al.*¹³ established that Φ_F for cresyl violet in methanol was 0.54. This work used thermal blooming spectroscopy to measure the absolute quantum yield and is therefore free of possible errors from inappropriate secondary standards. Almost immediately, Olmsted¹⁴ confirmed the Φ_F in methanol as being 0.55 by using calorimetric techniques. Similar values were reported by other authors,¹⁵ but with some significant variation and some surprising differences between Φ_F measured in methanol and ethanol. In particular, Isak and Eyring reported¹⁸ a significantly higher Φ_F for cresyl violet in dilute methanol, the value reaching 0.65 at very low concentration, using photothermal spectroscopic studies. A somewhat similar value ($\Phi_F = 0.70$) was reported by Drexhage.¹⁹ Several authors²⁰ have indicated that Φ_F for cresyl violet might be highly sensitive to concentration but this is most likely an artefact arising from self-absorption at higher concentration. This level of uncertainty is a concern for the application of the fluorophore as an important reference compound and we have endeavoured to re-examine the fluorescence spectral properties of cresyl violet in alcohol solvents. Our work is extended to include the effects of other polar solvents, including water. It is also clear from reading the earlier literature^{13-15,18,19} that, whereas much attention has been

given to determining Φ_F , few reports have attempted to analyse the optical spectra, notably the lack of mirror symmetry.

4.2 Absorption and fluorescence spectral measurements in absolute ethanol

Cresyl violet (Figure 1) is a mono-cationic dye, used here as the perchlorate salt, that is reasonably soluble in polar solvents such as methanol. The molecule is planar and therefore highly susceptible to self-association in solution, despite the positive charge. This is a known problem under certain experimental conditions but most of the literature supports the notion that the monomer will persist in methanol solution at low concentration. The absorption and fluorescence spectra recorded in dilute ethanol solution (Figure 2) are in agreement with this situation; we prefer to use ethanol for fluorescence measurements because of its somewhat lower volatility. Absorption (λ_{ABS}) and fluorescence (λ_{FLU}) maxima are readily identified (Table 1), there is poor mirror symmetry between the transitions but the excitation spectrum is in good agreement with the absorption spectrum recorded for the lowest-energy transition. Spectral deconstruction of the reduced fluorescence spectrum (Figure 3a) requires five Gaussian components (FWHM = 530 cm^{-1}) to reproduce the entire spectral envelope and indicates that the 0,0 transition is centred at 15,940 cm^{-1} . This analysis allows calculation²¹ of the Huang-Rhys factor as being 0.48 in ethanol. For the emission transition, the accompanying low-frequency vibronic mode is determined²² to be 500 cm^{-1} from the deconstructed spectrum (Figure 3a). The reduced absorption spectrum could not be deconstructed into a meaningful series of Gaussian components of common half-width (Figure 3b). Indeed, the most consistent analysis involves superposition of a Gaussian profile (FWHM = 600 cm^{-1}) on top of a broad absorption transition that bears the hallmark of a charge-transfer band (FWHM = 2,950 cm^{-1}). It is this underlying charge-transfer transition ($E_{00} = 17,455 \text{ cm}^{-1}$ or 573 nm) that obscures mirror symmetry between absorption and emission profiles. For the π, π^* transition, the E_{00} band is located at 16,430 cm^{-1} (i.e., 609 nm). This allows estimation of the Stokes shift (Δ_{SS}) as being only 490 cm^{-1} ; a value that indicates minor geometry change on relaxation to the excited-singlet state. Finally, the π, π^* transition is associated with a low-frequency vibronic mode of 540 cm^{-1} . Overall, the properties deduced for the π, π^* absorption transition are in reasonable agreement with those observed for the corresponding emission profile. This suggests that the emitting state is primarily π, π^* in nature, although the Huang-Rhys factor is a little high and might reflect the involvement of some charge-transfer character.

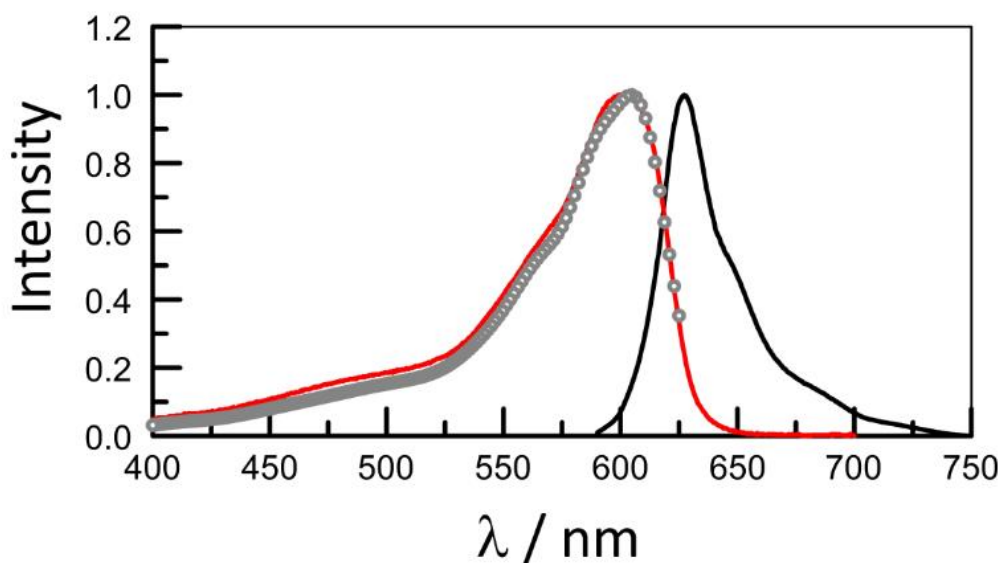


Figure 2. Overlay of absorption (red curve), fluorescence (black curve) and excitation (grey circles) spectra recorded for cresyl violet in dilute ethanol (i.e., sub- μM) solution at room temperature.

Table 1. Summary of key photophysical properties determined for cresyl violet in dilute ethanol solution at ambient temperature.

$\lambda_{\text{ABS}} / \text{nm}$	$\lambda_{\text{FLU}} / \text{nm}$	$\Delta_{\text{SS}} / \text{cm}^{-1}$	$\epsilon_{\text{MAX}} / \text{M}^{-1} \text{cm}^{-1}$	Φ_{F}	$\tau_{\text{S}} / \text{ns}$	$k_{\text{RAD}} / 10^8 \text{s}^{-1}$	S
609	627	490	85,115	0.52	3.8	1.4	0.48

In ethanol at 20 °C, cresyl violet exhibits a linear Beers' law plot, at least over concentrations less than 33 μM (Figure 4), giving rise to a molar absorption coefficient of 85,115 $\text{M}^{-1} \text{cm}^{-1}$ at the absorption maximum. The radiative rate constant (k_{RAD}) calculated from the Strickler-Berg expression²³ is $2.7 \times 10^8 \text{ s}^{-1}$, while integration of the absorption spectrum gives an oscillator strength²⁴ of 0.97 for the lowest-energy absorption band. These derived values are based on the lowest-energy absorption band being due to a single transition but our spectral deconstruction procedure indicates that the π, π^* transition overlaps with a more intense charge-transfer manifold (Figure 3b). Integration of these deconstructed transitions indicates an oscillator strength for the π, π^* transition of 0.49 and a subsequent k_{RAD} value of $1.4 \times 10^8 \text{ s}^{-1}$. In dilute ethanol solution, time-resolved fluorescence spectral measurements with laser excitation at 525 nm indicate that the fluorescence lifetime (τ_{S}) is 3.8 ± 0.1 ns. The decay profile was mono-exponential ($\chi^2 = 1.07$) and the derived lifetime was found to be independent of both concentration and detection wavelength. Using the latter lifetime in conjunction with k_{RAD} determined from the Strickler-Berg expression,²³ we reach an estimate for the fluorescence quantum yield ($\Phi_{\text{F}} = k_{\text{RAD}} \cdot \tau_{\text{S}}$) of 0.53 ± 0.04 . This estimate seems a little low in comparison to many

literature values, possibly reflecting the difficulty in assessing k_{RAD} for the π, π^* transition, but agreement is remarkably close to the Φ_F value of 0.54 measured in methanol by thermal blooming spectroscopy as reported originally by Magde *et al.*¹³

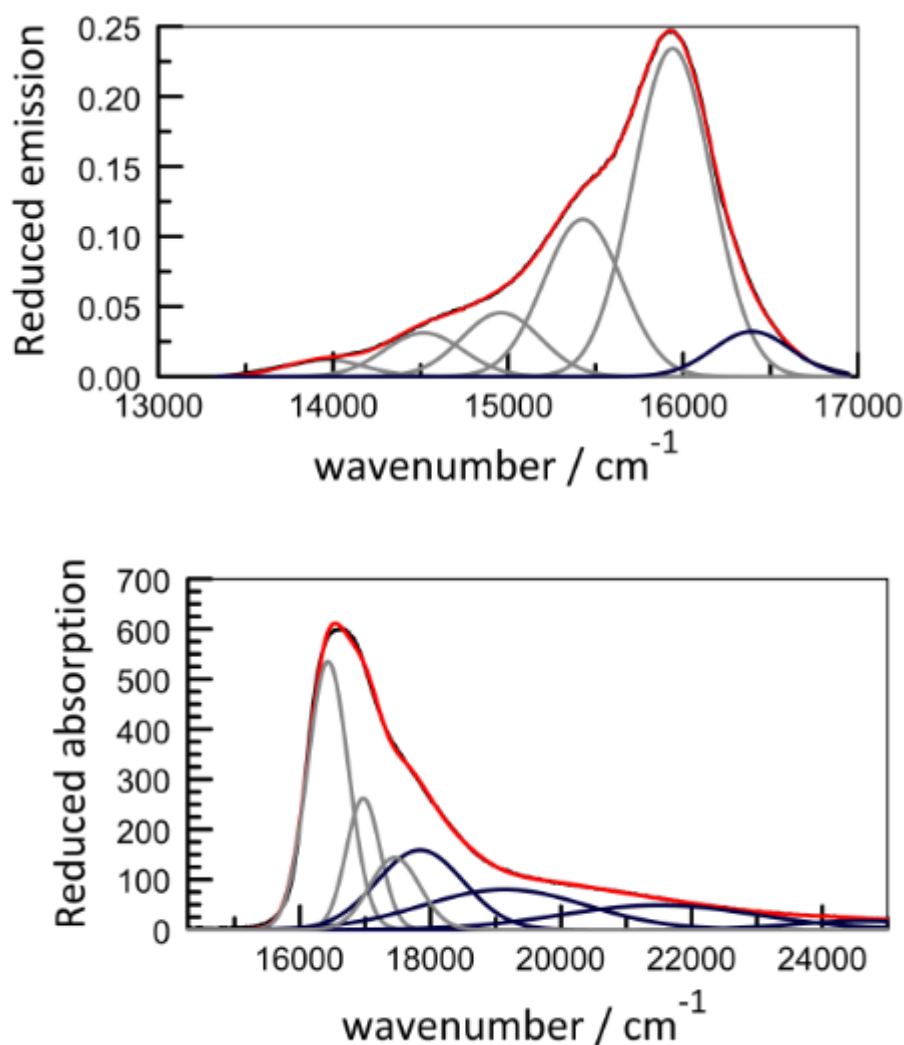


Figure 3. (a) Upper panel shows the reduced fluorescence spectrum in ethanol and the underlying series of Gaussian components. The experimental curve is in black and the reconstructed spectrum is in red. The Gaussian components are in grey. Also shown is the hot emission band needed to fully reconstitute the spectrum. (b) The lower panel shows the same deconstruction for the corresponding absorption spectrum. The grey curves refer to the π, π^* transition while the dark blue curves are associated with the intramolecular charge-transfer state.

A direct estimate for Φ_F was made using an integrating sphere with excitation being provided by a collimated beam from a high-power LED emitting at 523 nm. Output from the integrating sphere

was collected at the exit port and directed to a Zolix Omni- λ -1509 monochromator before being detected with an ABET Digital Light Detector. The optical system was calibrated for wavelength response using a standard quartz halogen lamp. Several concentrations (0.2-2 μM) of cresyl violet in deaerated absolute ethanol were used. Using the procedure developed by Beeby *et al.*,²⁵ Φ_F for cresyl violet in ethanol was determined to be 0.52 at room temperature. This value is very slightly higher than the value ($\Phi_F = 0.50$ in ethanol) reported by Olmsted¹⁴ on the basis of calorimetric measurements. Notably, our value is significantly smaller than Φ_F values reported in ethanol by Drexhage¹⁹ ($\Phi_F = 0.70$) and Petukhov *et al.*²⁶ ($\Phi_F = 0.57$). It might be noted that our fluorescence spectra indicate the presence of some hot fluorescence (Figure 3a). This latter band is situated some 455 cm^{-1} above the 0,0 vibronic band of the emitting state. Hot emission contributes $<7\%$ to the total emission spectrum and, in certain cases, could contribute to the uncertainty in establishing a completely reliable Φ_F for cresyl violet.

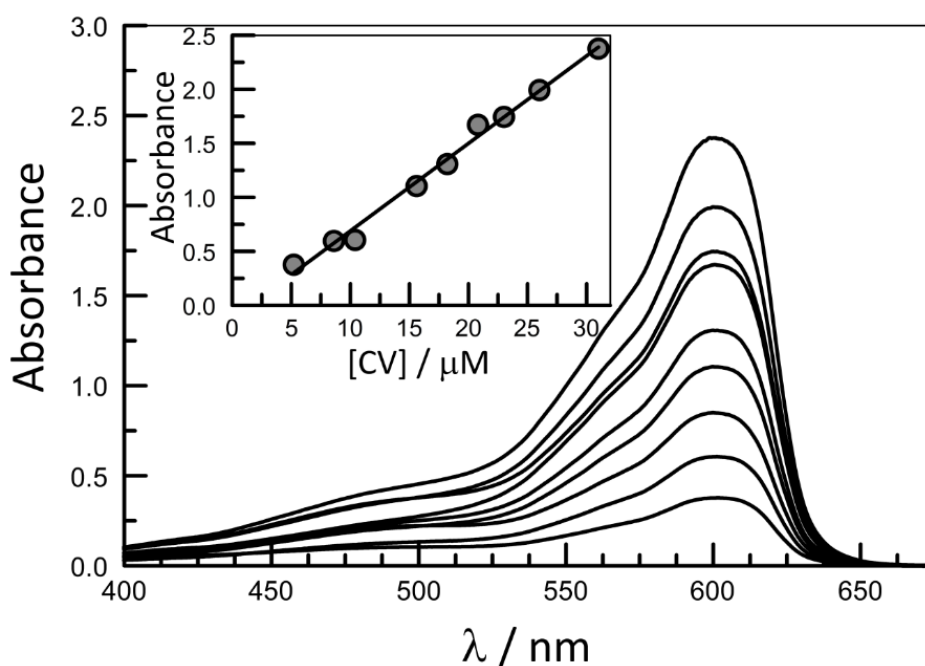


Figure 4. Concentration (5-32 μM) dependence for cresyl violet in absolute ethanol at room temperature. The inset shows the absorbance measured at the peak maximum and converted to a path length of 1 cm.

An indirect consequence of the derived Φ_F is that almost 40% of the combined avenues available for deactivation of the excited-singlet state involve nonradiative channels. In contrast to radiative decay, nonradiative pathways are often highly sensitive to changes in the local environment and this can be problematic for a fluorescence standard. With cresyl violet in ethanol, the corresponding rate constant for nonradiative decay, k_{NR} , has a value of ca. $1 \times 10^8\text{ s}^{-1}$ at room temperature. The Engman-

Jortner energy-gap law²⁷ for nonradiative decay in polycyclic compounds has recognized the importance of high-energy vibronic modes, such as N-H stretching vibrations, as being especially significant for promoting nonradiative deactivation. This is likely to be the case for cresyl violet; later it will be shown that exchange of the labile hydrogen atoms with deuterium atoms leads to a marked increase in Φ_f . This is precisely what might be expected on the basis of the energy-gap law.²⁷

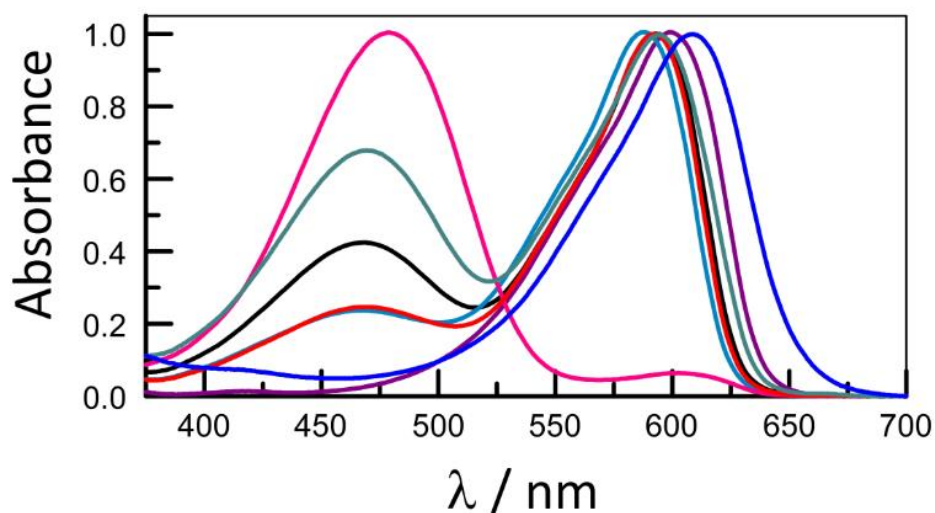


Figure 5. Comparison of normalized absorption spectra recorded for cresyl violet in a series of organic solvents at room temperature: acetone (black), acetonitrile (red), tetrahydrofuran (mauve), butyronitrile (cyan), formamide (plum), N,N-dimethylformamide (rose) and dimethylsulfoxide (blue).

4.3 Effect of solvent

Our analysis of the optical spectra recorded for cresyl violet in ethanol indicates an overlapping mixture of charge-transfer and π,π^* transitions. The energy of the charge-transfer state is likely to be affected by the polarity of the solvent while the heteroatoms might be expected to participate in hydrogen bonding interactions with certain solvents. Although no evidence for aggregation was found in ethanol, the planar structure could favour dimerization in other solvents where solvophobic effects are introduced. Prior work¹³ has recommended methanol as a suitable solvent for cresyl violet but, in our opinion, this otherwise excellent solvent is too volatile for convenient use with a fluorescence standard. In looking for alternative solvents as a means to generalize the use of cresyl violet for ratiometric fluorescence measurements, we have considered a few polar organic solvents as alternatives to alcohols. No attempt was made to exchange the perchlorate counterion as this is the most common commercially available salt. The use of water as a solvent is described separately.

Firstly, we consider the absorption spectra recorded for cresyl violet in a small series of organic solvents at room temperature (Figure 5). These solvents include both hydrogen-bond donors (e.g., formamide, butanol) and hydrogen-bond acceptors (e.g., acetone, dimethylsulfoxide) and cover a modest range of polarities. Numerous protocols exist by which to express the properties of an organic solvent and listed in Table 2 are the Pekar function²⁸ (P_S) and the Catalan solvent index function²⁹ (SP). The result of replacing ethanol as solvent is unexpectedly complex! The spectral pattern observed in ethanol is not preserved in any other solvent on our list, including butan-1-ol. In the longer alcohol solvents, the absorption spectra indicate the presence of significant transitions at higher energy than the π, π^* transition while in organic nitriles and N,N-dimethylformamide the regular π, π^* transition is replaced with a pair of broad, featureless transitions. Such behaviour is characteristic of dimerization of the solute, presumably driven by the need to minimize contact with the surrounding solvent. Dimerisation is evident in these various solvents by the appearance of a pair of fairly broad Gaussian-shaped absorption bands that displace the regular π, π^* transitions seen in ethanol (Figure 5). The location and energy splitting of this pair of Gaussian components depend markedly on the nature of the solvent.

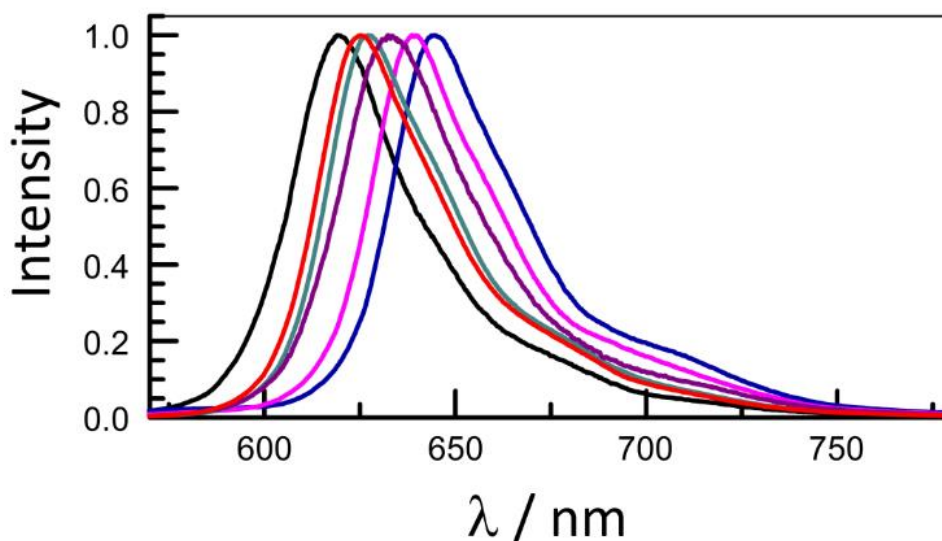


Figure 6. Comparison of normalized fluorescence spectra recorded for cresyl violet in a series of organic solvents at room temperature: acetone (black), acetonitrile (red), butyronitrile (cyan), formamide (plum), N,N-dimethylformamide (rose) and dimethylsulfoxide (blue).

Before attempting to analyse these absorption spectral effects, we turn attention to the corresponding fluorescence spectra recorded in the same solvents at room temperature (Figure 6). For all fluorescence measurements, the absorbance at the excitation wavelength was kept below 0.06 and care was taken to avoid artefacts arising from the inner-filter effect.³⁰ Solutions were filtered through a microporous frit and prepared fresh to avoid problems of aggregation. It is apparent that the fluorescence spectra are greatly simplified relative to the corresponding absorption spectra and, in each case, remain reminiscent of the situation observed in ethanol. Although the emission maximum shifts in response to changes in solvent, the basic shape does not change significantly (Figure 6). This situation might be explained in terms of emission arising only from the residual monomeric form of the dye but this simple explanation does not account for the substantial solvent-induced shifts of the emission maximum (Table 2). Instead, we consider that, in certain solvents, notably N,N-dimethylformamide, acetonitrile and acetone, fluorescence occurs from a dimer species.

Table 2. Compilation of the primary spectroscopic parameters recorded for cresyl violet in a range of organic solvents at room temperature.

Solvent	SP ^[h]	P _S ^[i]	λ_{ABS} [nm]	λ_{FLU} [nm]	Φ_{F}	τ_{s} [ns]
ACE ^[a]	0.65	0.61	469 , 592	619	0.91	4.5
DMSO ^[b]	0.83	0.59	608	645	0.54	3.8
Formamide	0.81	0.62	598	632	0.52	3.5
EtOH ^[c]	0.63	0.62	609	627	0.52	3.8
CH ₃ CN	0.64	0.66	468 , 586	625	1.0	4.5
OcOH ^[d]	0.71	0.48	615	631	0.49	4.1
BuOH ^[e]	0.67	0.32	612	622	0.71	3.4
DMF	0.75	0.6	478, 602	639	0.64	3.9
BuCN ^[f]	0.68	0.61	469 , 591	627	0.82	3.8
THF ^[g]	0.71	0.44	469 , 594	627	0.79	4.2

[a] Acetone. [b] Dimethyl sulfoxide. [c] Ethanol. [d] Octan-1-ol. [e] Butan-1-ol. [f] Butyronitrile. [g] Tetrahydrofuran. [h] Catalan solvent polarizability parameter. [i] Solvent Pekar function.

While the fluorescence spectra recorded for cresyl violet in different solvents remain comparable to those found in ethanol, the same is not true for the corresponding absorption spectra (Figures 5 and 6). Furthermore, the derived photophysical properties also remain similar to those found for cresyl violet in ethanol (Table 2). Analysis of the spectroscopic data allows the determination of secondary properties, such as the Huang-Rhys factor (S), the Stokes shift (Δ_{SS}) and the accompanying low-frequency vibronic mode ($h\omega_{\text{L}}$) coupled to the optical transition, and these values are collected in Table 3. Again, the various parameters are not too dissimilar to those found in ethanol solution. This situation is surprising because of the obvious indication for dimerization in certain

solvents. The strong implication, therefore, is the dimer emits under these conditions with quite high probability.

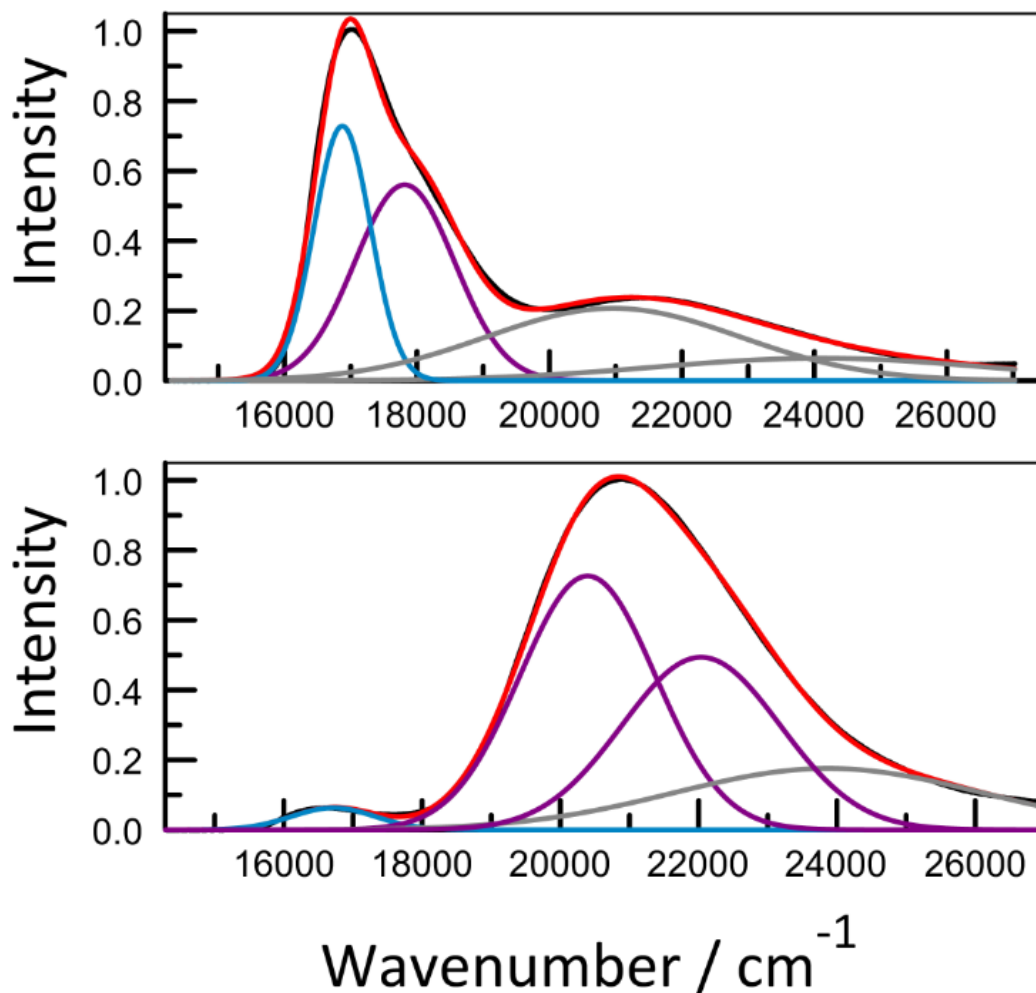


Figure 7. (a) Upper panel shows the deconstructed absorption spectrum recorded for cresyl violet in acetonitrile, with the charge-transfer transitions being coloured grey. The cyan and plum components refer to the transition for the dimer that arise from excitonic splitting. (b) Lower panel shows the same patterns derived for N,N-dimethylformamide solution.

In some solvents, notably alkane nitriles and acetone, the absorption profile for cresyl violet at low concentration exhibits two pronounced bands (Figure 7), with the lower-energy transition being dominant. In fact, the absorption spectrum also exhibits the charge-transfer absorption bands reported earlier for cresyl violet in ethanol solution such that analysis is somewhat hazardous. Nonetheless, a meaningful deconstruction of the low-energy absorption envelope can be made

(Figure 7a). N,N-Dimethylformamide (DMF), on the other hand, favours the higher-energy absorption transition, regardless of concentration (Figure 7b). It is noticeable that both absorption bands are relatively broad and featureless but can be analysed readily in terms of Gaussian-shaped components. These bands are regarded as being characteristic of a dimeric form of cresyl violet. In support of this assignment, it might be noted that addition of DMF to a dilute solution of cresyl violet in ethanol caused the appearance of the absorption spectrum considered representative of the dimer (Figure 8). Strong fluorescence ($\Phi_F = 0.64$) is observed for cresyl violet in dilute DMF solution, with the emission maximum ($\lambda_{\text{FLU}} = 639 \text{ nm}$) being the most red shifted of the solvents considered here. Excitation spectra confirm that emission arises from the dimer while time-resolved fluorescence decay profiles were mono-exponential with the lifetimes listed in Table 2. Fluorescence quantum yields are surprisingly high for a dimer species and approach unity in acetonitrile solution. Again, detailed analysis of these spectroscopic profiles permits derivation of the relevant secondary properties (Table 3) which can now be compared in terms of the nature of the surrounding solvent.

Table 3. Compilation of the parameters derived from the photophysical and spectroscopic properties recorded for cresyl violet in a range of organic solvents at room temperature.^[a]

Solvent	$E_{00} \text{ (abs)}$ / cm^{-1}	$E_{00} \text{ (flu)}$ / cm^{-1}	k_{RAD} / 10^8 s^{-1}	k_{NR} / 10^8 s^{-1}	Δ_{SS} / cm^{-1}	$h\omega_{\text{L}}$ / cm^{-1} [b]	S [b]
ACE	16,730	16,160	2.0	0.20	570	645	0.37
DMSO	16,300	16,020	1.4	1.2	280	565	0.46
Formamide	16,470	16,115	1.5	1.4	355	630	0.39
EtOH	16,430	15,940	1.4	1.3	490	490	0.48
CH ₃ CN	16,875	15,670	2.2	NA	1,205	555	0.46
OcOH	17,075	15,535	1.2	1.2	1,540	550	0.46
BuOH	17,155	15,975	2.1	0.85	1,180	550	0.48
DMF	16,715	15,825	1.6	0.92	890	625	0.39
BuCN	16,870	15,850	2.2	0.47	1,020	565	0.50
THF	16,655	15,950	1.9	0.50	705	630	0.39

[a] See footnote to Table 2 for an explanation of the abbreviations used to specify particular solvents. [b] Calculated from the reduced fluorescence spectrum on the basis of Gaussian deconstruction.

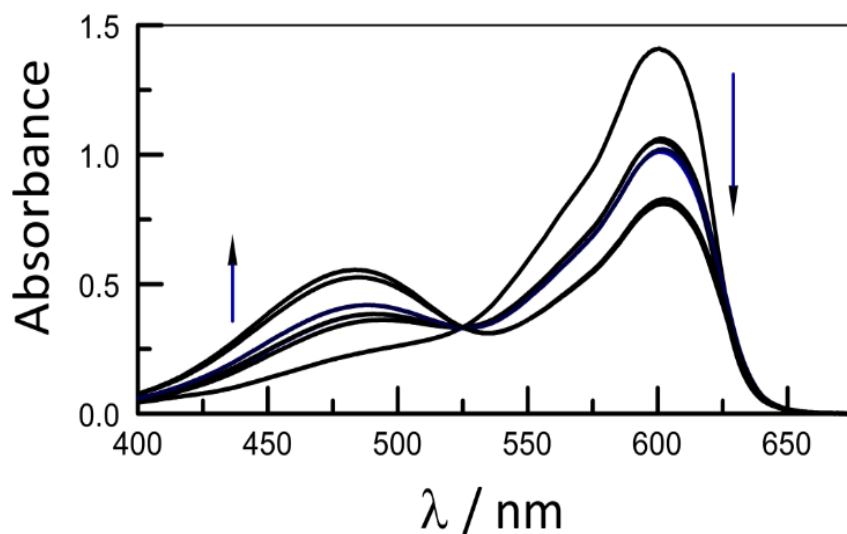
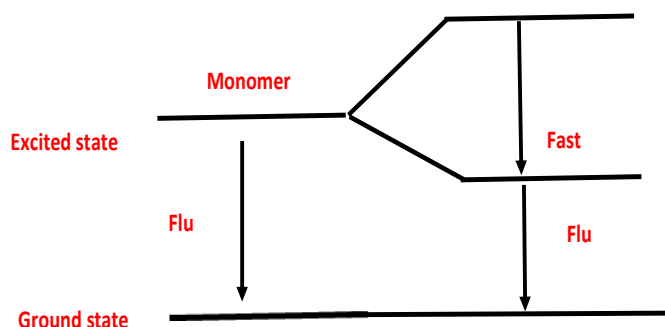


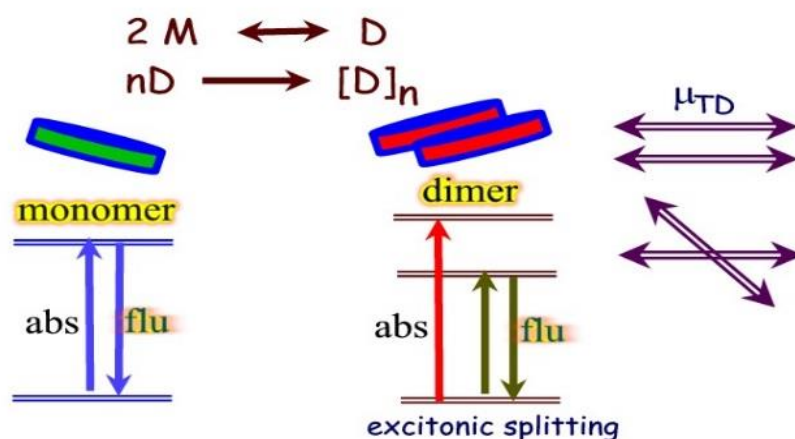
Figure 8. Representative absorption spectra recorded for cresyl violet in mixtures of ethanol and DMF. The arrows indicate the progression of increasing mole fractions of DMF.

The split absorption spectra noted especially for alkane nitriles, acetone, DMF and tetrahydrofuran are reminiscent of the dimer systems described originally by Kasha,³¹ where excitonic coupling between the monomers causes the absorption transition to split into two well-resolved bands (Scheme 1). The relative intensities of the integrated absorption transitions for the dimer can be used to estimate the mutual angle between the two transition dipole moment vectors.³² In fact, according to Kasha's model³¹ for a parallel pair, the higher energy transition (μ_u) is preferred when these dipole vectors are aligned whereas the lower energy transition (μ_l) is favoured by the corresponding perpendicular alignment. For the dimers formed by cresyl violet in organic solvents, both transitions are observed and the excitonic splitting is best considered in terms of an oblique geometry. On the basis of Equation 4.1, where ϕ is the angle between the transition dipole moment vectors resident on the paired monomers and μ is the relative integrated absorption transition including any vibronic satellites,³² the mutual angle can be estimated (Table 4).

$$N = \frac{\mu_1}{\mu_2} = \frac{\sin\phi}{\cos\phi}$$

Equation 4.1





Scheme 1. The upper panel shows the excitonic coupling proposed by Kasha to split the absorption spectrum of the monomer (M) into two components. Only the lower-energy transition gives rise to fluorescence. The lower panel illustrates how the alignment of the transition dipole moment vectors (μ_{TD}) on the paired monomers comprising the dimer are associated with the upper-lower and lower-energy excitonic states.

Table 4. Summary of spectroscopic properties derived for cresyl violet in a range of organic solvents at room temperature.^(a)

Solvent	$\nu_L^{(b)}$ / cm^{-1}	$\nu_U^{(c)}$ / cm^{-1}	N	ϕ / $^\circ$	V_{AB} / cm^{-1}	DN ^(d)	AN ^(e)
ACE	16,730	21,275	0.9	47	4,545	17.0	12.5
DMSO	18,410	20,070	0.8	45	1,660	29.8	19.3
Formamide	16,470	17,245	2.0	71	775	24.0	39.8
CH ₃ CN	16,875	17,815	1.4	60	940	14.1	18.9
OcOH	17,075	18,220	0.43	26	1,145		
BuOH	17,155	18,210	0.94	48	1,060	23.0	36.8
DMF	16,715	20,215	33.3	98	3,500	27.0	32.1
BuCN	16,870	17,810	1.4	60	940	16.1	
THF	16,655	21,190	1.2	56	4,535	20	8

(a) See footnote to Table 2 for an explanation of the abbreviations used for the solvents. (b) Absorption maximum derived by Gaussian deconstruction for the lower energy dimer absorption band. (c) Corresponding absorption maximum for the higher energy transition. (d) Gutmann donor number for the solvent. (e) Gutmann acceptor number for the solvent.

For cresyl violet in DMF solution, analysis of the absorption spectrum (Figure 7b) shows that the splitting (V_{AB}) of the absorption band because of excitonic coupling amounts to $3,500 \text{ cm}^{-1}$ while the ratio of integrated absorption bands for upper-lying ($\mu_1 = 74.87$) and lower-lying ($\mu_2 = 2.25$) absorption transitions is 33.3. From Equation 4.1, we can estimate the angle (ϕ) between the two transition dipole moment vectors as being 98° . The same analysis carried out for cresyl violet in acetonitrile (Figure 7a) gives $\phi = 60^\circ$. The nature of the solvent, therefore, has a profound effect on the mutual alignment of the transition dipole moment vectors in the resultant dimer. For monomeric cresyl violet, quantum chemical calculations made at the DFT level indicate that the transition dipole moment vector runs down the long molecular axis, from N to N. In acetonitrile solution, the extent of excitonic splitting of the absorption band ($V_{AB} = 940 \text{ cm}^{-1}$) is significantly smaller than that found in DMF. According to the model developed by Kasha for obliquely paired monomers,³¹ this excitonic splitting energy can be expressed in terms of Equation 4.2. Here, κ is an orientation factor given by Equation 4.3, R_{AB} is the average separation distance between the centres of the vectors, α is the angle subtended between the vectors and the molecular axis, n is the solvent refractive index and μ_{TD} is the transition dipole moment calculated³³ for the isolated monomer in the same solvent. We are unable to make a direct measurement for this latter term because cresyl violet does not exist in a monomeric form in these solvents. As such, μ_{TD} ($= 3.25 \text{ D}$) was measured in ethanol solution (Equation 4.4 where f refers to the Onsager cavity factor), where the monomer abounds, and used for both DMF and CH_3CN .

$$V_{AB} = \frac{2|\mu_{TD}|^2}{4\pi\epsilon_0 R_{AB}^3} \kappa \quad \text{Equation 4.2}$$

$$\kappa = (\cos\alpha + 3\cos^2\phi) \quad \text{Equation 4.3}$$

$$\mu_{TD}^2 = \frac{3000 \ln 10 \hbar c}{8\pi^3 N_A} \frac{n}{f^2} \int \frac{\epsilon}{\nu} d\nu \quad \text{Equation 4.4}$$

The two factors that might be affected by changes in the nature of the surrounding solvent are the molecular orientation (κ) and the mutual separation distance (R_{AB}). These terms are associated with the degree of excitonic coupling between the paired monomers by way of Equation 4.2. It is not possible to resolve these two terms without inputting some structural information. Before attempting to do so, we note that cresyl violet in methanol, ethanol, butan-1-ol and octan-1-ol exists as a mixture of monomer and dimer, with the fraction of dimer increasing as the molecular mass of the solvent increases. NMR studies carried out in d_4 -methanol and d_6 -ethanol are consistent with the monomer dominating the solution species. The same situation arises for cresyl violet in dimethylsulfoxide

solution and here NMR studies indicate spectra similar to those recorded in d_4 -methanol. We omit these solvents from the analysis because of the complexity of the spectral deconstruction. In all other solvents studied here, cresyl violet prefers to exist in solution as the dimer. The derived information for these dimers is listed in Table 4, where it can be seen that the hydrogen-bond donating solvents (i.e., DMF and formamide) align the transition dipole moment vectors in an almost orthogonal manner. Hydrogen-bond accepting solvents tend to arrange these vectors in a less extreme geometry, with ϕ values between 45 and 60°. Part of this effect might be attributed to electrostatic repulsion between the two chromophores. Regarding the degree of excitonic coupling, it appears that strong coupling occurs in the better hydrogen-bond donors and acceptors. There is, however, no obvious correlation between V_{AB} and the Gutmann donor or acceptor number for the solvent. Instead, it appears the excitonic splitting is driven by the solvophobic effect.

According to the Strickler-Berg expression,²³ given as Equation 4.5, the radiative rate constant depends on the refractive index (n) of the solvent and on the mean energy of the fluorescence profile (ν_{FLU}). This latter term is equivalent to E_{00} as listed in Table 3. There is, in fact, only a small variation in the derived k_{RAD} values and this is consistent with the minor differences in the emission maxima. Some doubt exists as to the exact form that the refractive index correction term should adopt but, in reality, there is not much difference in the refractive index of organic liquids at room temperature. The main driver, therefore, in controlling k_{RAD} is the amount of energy to be dissipated during deactivation of the excited state. The Stokes shift is likewise insensitive to changes in the nature of the solvent.

$$k_{RAD} = 2.88 \times 10^{-9} n^2 \langle \nu_{FLU}^3 \rangle \int \epsilon d \ln \nu \quad \text{Equation 4.5}$$

There is somewhat more variation in the rates of nonradiative decay of the excited state among the different solvents (Table 3). According to the Englman-Jortner²⁷ energy-gap law, k_{NR} should increase as the excited-state energy decreases. The latter term is conveniently expressed in terms of ν_{FLU} . There is, however, no obvious correlation between k_{NR} and the amount of energy that has to be dissipated. Perhaps, this is because some solvents favour monomers and other give rise to dimers. There is also the possibility of hydrogen bonding between solvent and cresyl violet and, should this take place, there is every chance that this would promote nonradiative decay. Such an effect has been recognized¹¹ for azaBodipy derivatives in alcohol solvents. In fact, there is a crude relationship here in as much as those solvents likely to function as hydrogen-bond donors tend to give the higher k_{NR} values. Hydrogen-bond accepting solvents tend to decrease the magnitude of k_{NR} . Superimposed on this generic effect is some kind of polarity function because more polar solvents tend to exaggerate the effects of hydrogen bonding between solute and the solvent.

4.4 Optical properties for cresyl violet in water

Cresyl violet dissolves in water at room temperature, even as the perchlorate salt, and exhibits an easily detected fluorescence signal. The absorption spectrum displays two pronounced bands, centred at around 560 and 580 nm, respectively, of comparable intensity. In fact, the ratio of these two absorption bands in water evolves somewhat in favour of the lower-energy transition as the sample is diluted and as the temperature is raised (Figure 9). This situation might be explained in terms of partial dimerization of cresyl violet in water, with the monomer being favoured at low concentration and high temperature. In support of this idea is the observation that the addition of small amounts of the neutral surfactant Triton X-100 causes the appearance of an absorption spectrum that can be considered to represent the monomeric form of cresyl violet. In fact, both absorption and emission maxima are subject to significant red shifts on addition of the surfactant at concentrations above the critical micelle concentration. This suggests that the monomer form of cresyl violet is associated with the surface of the micelle. It is most unlikely that cresyl violet will penetrate into the centre of the micelle because of the electronic charge and, in any case, the dye is somewhat soluble in water. The surfactant serves the purpose of breaking the dimer.

In dilute aqueous solution ($[CV] = <5 \mu\text{M}$) at room temperature, the fluorescence quantum yield is 0.66 and the excited-singlet lifetime is 2.4 ns. These values are surprisingly high, being comparable to those found for cresyl violet in ethanol. Time-resolved fluorescence decay profiles remained mono-exponential while the Stokes shift was kept fairly small at ca. $1,350 \text{ cm}^{-1}$. In D_2O , under otherwise identical conditions, Φ_F approaches unity and τ_s is increased to 6.6 ns. This is the longest excited-singlet state lifetime recorded for cresyl violet and indicates that, under these conditions, non-radiative decay has been curtailed.²⁷ The observed lifetime is also the radiative lifetime.²³ It is concluded that in D_2O , labile protons on the amino groups are exchanged for deuterons and this causes a sharp decrease in the frequency of the relevant vibrations. If these N-H vibrations promote non-radiative decay in accordance with the Englman-Jortner energy-gap law,²⁷ then we would expect to see a major increase in Φ_F and τ_s on replacing H_2O with D_2O . Comparison of the data collected in these two solvents is available by way of (Table 5). NMR spectra recorded for cresyl violet in D_2O are consistent with extensive dimerization at room temperature.

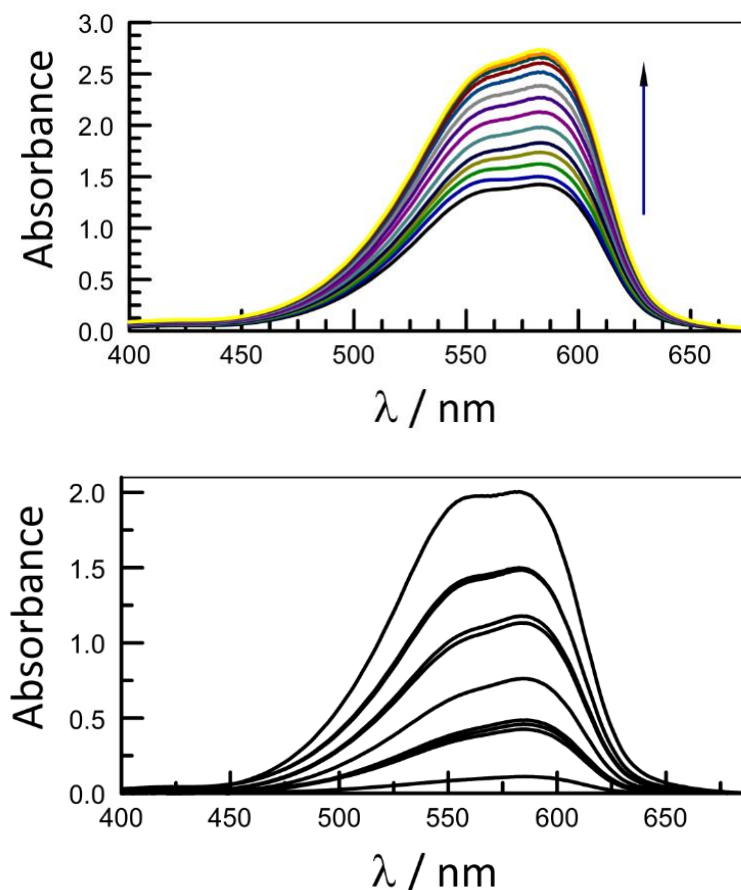


Figure 9. The upper panel shows the effect of increasing temperature (from 10 to 70 °C) on the absorption spectrum recorded for cresyl violet in water while the lower panel shows the effect of solute concentration over the range 1 to 25 μM in water at room temperature. Higher concentration and lower temperature favour dimerization of cresyl violet, with the dimer absorbing preferentially at wavelengths around 550 nm.

The fluorescence spectra recorded in both D_2O and H_2O are relatively narrow and show slight signs of fine structure (Figure 10). This allows deconstruction into Gaussian components (FWHM = 850 cm^{-1} and 930 cm^{-1} respectively for H_2O and D_2O) and subsequent assessment of the low-frequency vibronic mode coupled to decay and the Huang-Rhys factor (Table 5). There are slight variations in these properties and also in the 0,0 energies which are found at 15,855 and 15,940 cm^{-1} , respectively, for H_2O and D_2O . In marked contrast, the corresponding absorption spectra are relative broad and appear as an intense doublet with overlapping weaker transitions lying at higher energy (Figure 10). These absorption spectra are more difficult to deconstruct into Gaussian components in a fully convincing manner but, making use of the spectra recorded in organic solvents, a satisfactory analysis has been reached.

Table 5. Compilation of spectroscopic and photophysical data determined for cresyl violet perchlorate in water and deuterium oxide at room temperature. The concentration of solute was kept below 5 μM .

Property	H ₂ O	D ₂ O
$\lambda_{\text{ABS}} / \text{nm}$	582	578
$\lambda_{\text{FLU}} / \text{nm}$	631	627
Φ_{F}	0.66	1.0
$\tau_{\text{S}} / \text{ns}$	2.4	6.6
$k_{\text{RAD}} / 10^8 \text{ s}^{-1}$	2.8	1.5
$k_{\text{NR}} / 10^8 \text{ s}^{-1}$	1.4	NA
$\Delta_{\text{SS}} / \text{cm}^{-1}$	1,335	1,350
$h\omega_{\text{L}} / \text{cm}^{-1}$	710	800
S	0.32	0.26

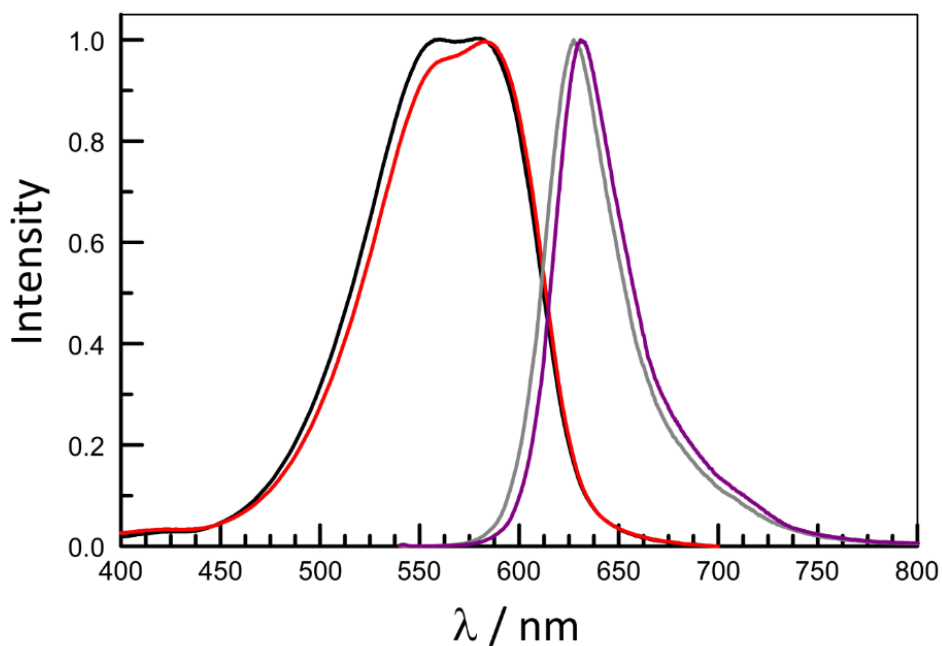


Figure 10. Comparison of the normalized absorption spectra recorded for cresyl violet in H₂O (red curve) and D₂O (black curve) at room temperature. Also shown are the corresponding normalized fluorescence spectra recorded in H₂O (plum curve) and D₂O (cyan curve).

The spectral deconstructions carried out for the fluorescence spectra recorded for cresyl violet are shown in (Figure 11). The analysis indicates a progression of four vibronic modes coupled to excited-state deactivation, with neglect of any hot fluorescence. These vibronic modes are subject to anharmonic distortion. There are slight differences between the derived vibrational energies ($h\omega_{\text{L}}$), as

indicated by the entries in Table 5, and also in the Huang-Rhys factors. It is noted that these small variations are preserved throughout the spectral properties and we take this to indicate that there are minor differences between the structures of cresyl violet in H₂O and D₂O. The absorption spectral deconstructions are shown as Figure 12. We consider that these spectra refer to a dimeric form of cresyl violet, even at low concentration. This conclusion is reached as follows: (1) The spectra, and underlying vibronic components, are broad, (2) surfactant dissociates the dimer into monomers possessing regular features, and (3) time-resolved emission profiles are consistent with the presence of a single emitting species that must exist in high proportion. On this basis, the excitonic splitting (V_{AB}) amounts to 1,075 and 1,160 cm⁻¹, respectively, in H₂O and D₂O while the corresponding 0,0 transitions are located at 16,870 and 16,935 cm⁻¹. From the relative integrated absorption bands, it appears that both dimers position the transition dipole moment vectors at a mutual angle of 65°.

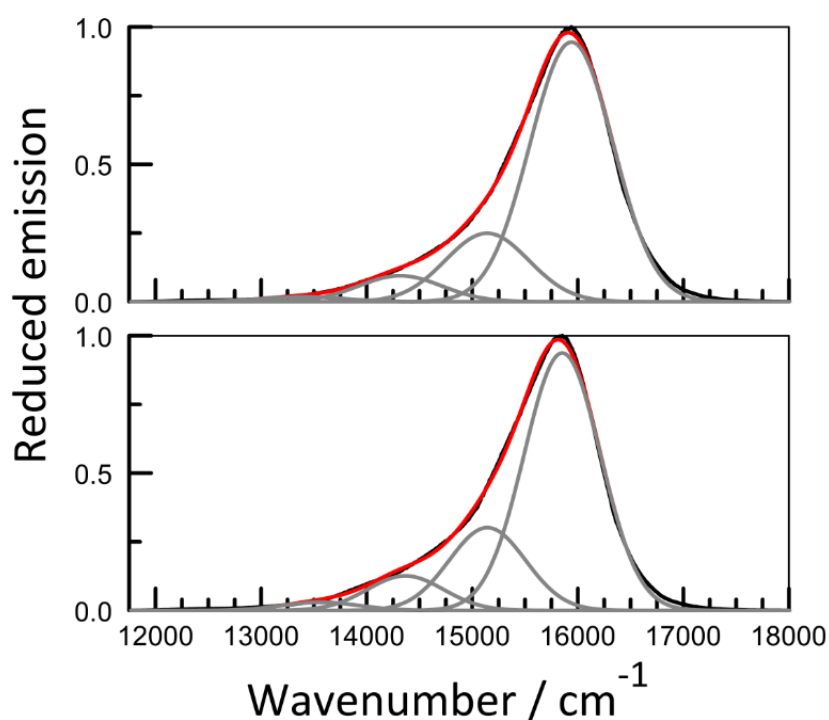


Figure 11. Deconstructed emission spectra recorded for cresyl violet in D₂O (upper panel) and H₂O (lower panel). The experimental profile is shown in black with the reconstituted spectrum being shown in red. The corresponding Gaussian components intended to simulate the underlying vibronic components are shown in grey. Note that any hot fluorescence was omitted from this particular deconstruction.

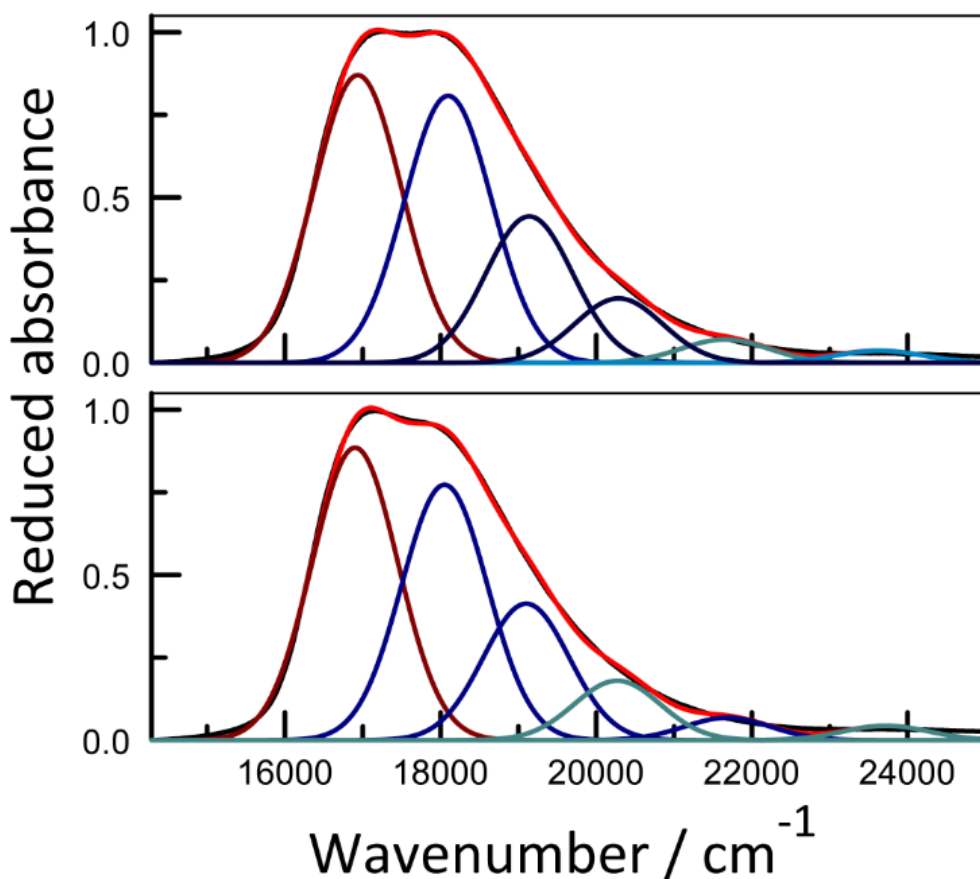


Figure 12. Deconstruction of the absorption spectrum recorded for cresyl violet in D₂O (upper panel) and H₂O (lower panel) on the basis of Gaussian components. The black curve is the experimental spectrum and the overlaid red curve is the reconstituted spectrum. The brown and blue curves represent the upper- and lower-energy dimer transitions while the cyan curves complete the spectrum.

The absorption ($E_{00} = 16,920 \pm 50 \text{ cm}^{-1}$), and indeed the NMR, spectra indicate that cresyl violet aggregates in aqueous solution, with the effect of added surfactant confirming this situation. It is remarkable that the dimer emits so strongly and switching off nonradiative decay by replacing the promoting N-H bonds with N-D bonds increases the emission quantum probability to unity. The optical spectra remain very similar in both D₂O and H₂O and allow estimation of V_{AB} as being $1,155 \pm 150 \text{ cm}^{-1}$. This value is comparable to that found in the longer alcohol solvents and in formamide. The mutual transition dipole moment vectors align at an approximate angle (ϕ) of $64 \pm 3^\circ$, again quite similar to the value found for formamide solutions. Perhaps this geometry is the most appropriate for hydrogen-bond donor solvents. On the assumption that symmetrical dimers are formed in aqueous solutions, we can set α as being equal to 57.5° . We can now determine the orientation factor in Equation 4.3 as being 1.07. Inputting this information into Equation 4.2 allows estimation of the distance separating the two oxazine rings as being $4.6 \pm 0.5 \text{ \AA}$. This seems to be a reasonable estimate.

4.5 Structure of the dimer

In order to probe further into the dimerization process, a series of high-resolution NMR spectral studies were made with cresyl violet dissolved in certain organic solvents. The solute concentration is significantly higher for NMR spectroscopy than was used for the optical spectroscopic studies described above. These spectra were recorded by Dr. Corinne Wills and interpreted with the aid of Prof. William McFarlane. ^1H -NMR spectra were recorded at 700 MHz and were supported by a limited number of COSY experiments. The main results can be summarized as follows: In all of the solvents except D_2O the spectra show sharp, well resolved peaks. In D_2O , the spectrum is broadened (Figure 13) even at elevated temperatures. As the sample was heated the peaks continued to broaden. An enlarged spectrum is shown as Figure 14. Figure 15 shows the spectrum obtained in methanol which is attributed to the monomer.

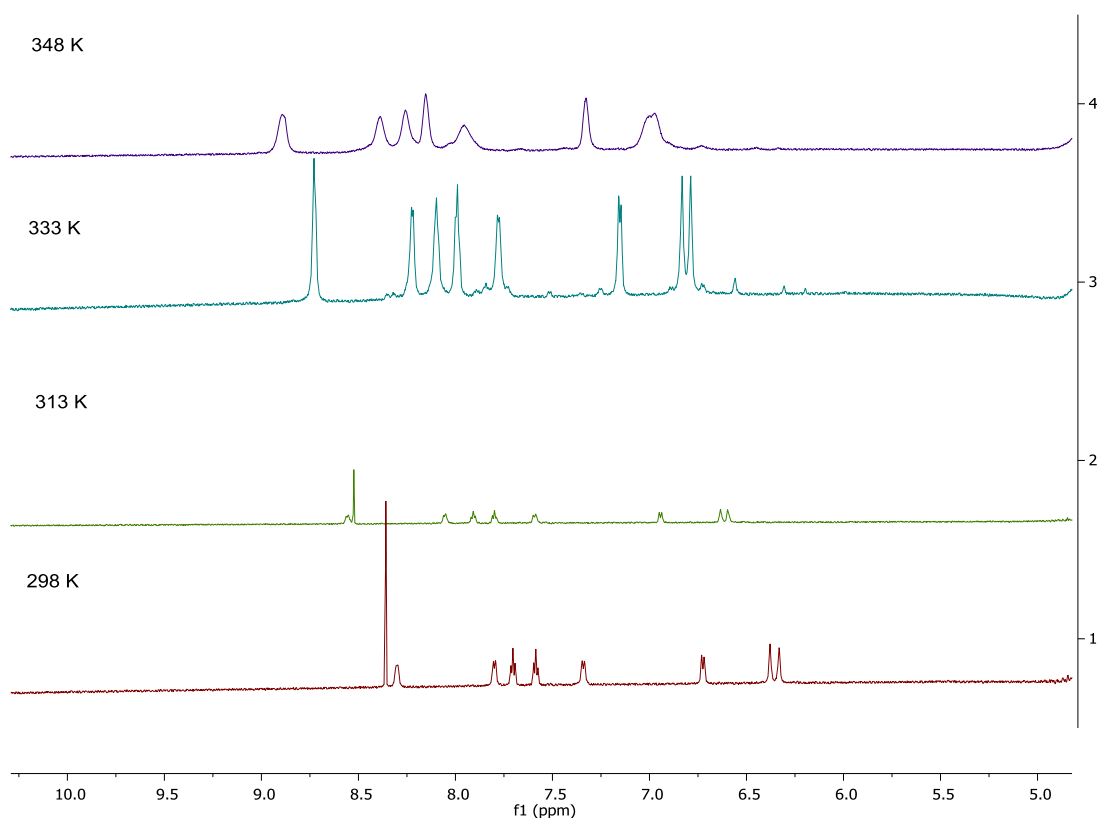


Figure 13. The ^1H -NMR spectrum recorded for cresyl violet at different temperatures in D_2O .

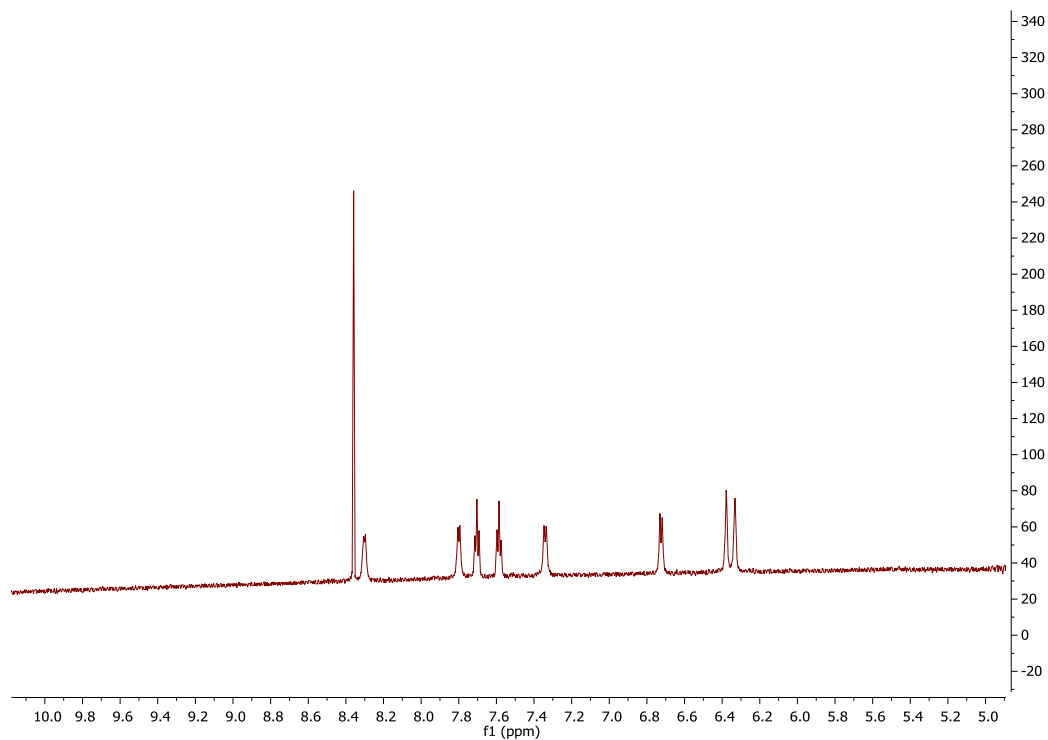


Figure 14. The ^1H -NMR spectrum recorded for cresyl violet in D_2O .

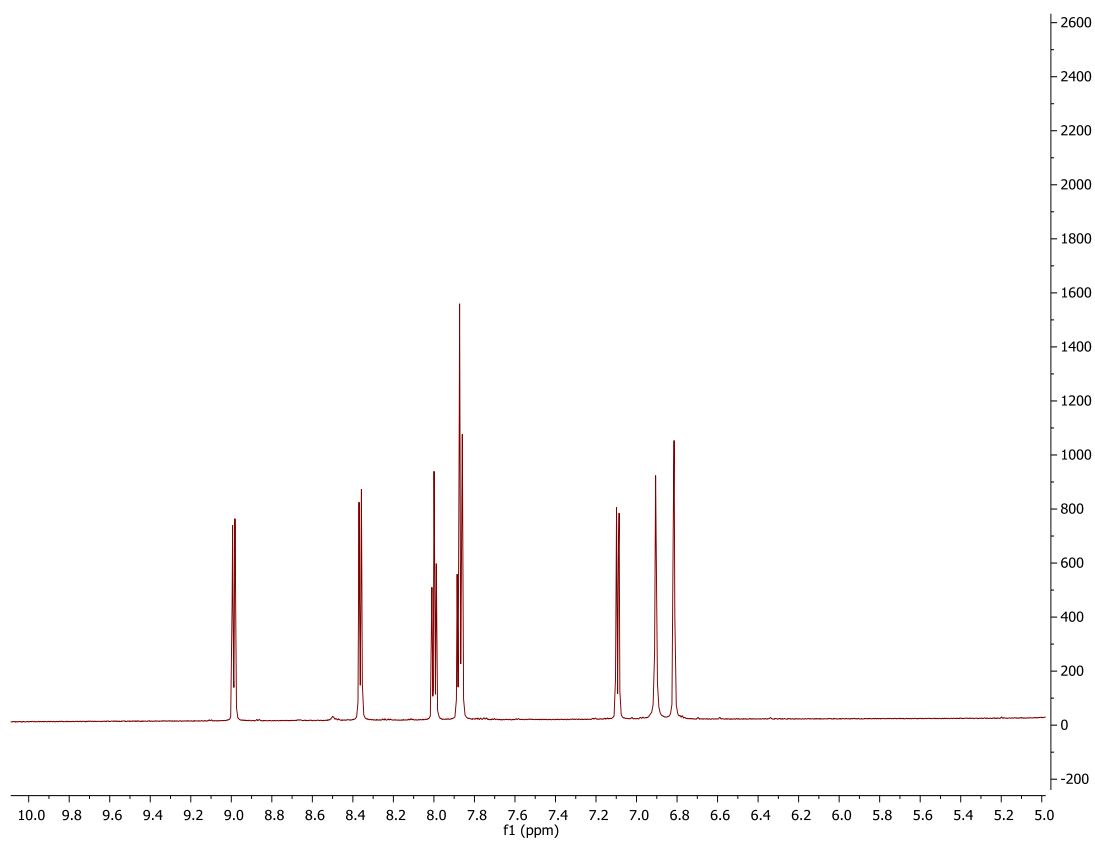


Figure 15. The ^1H -NMR spectrum recorded for cresyl violet in D_4 -methanol.

4.6 Conclusion

In this chapter, we have examined fluorescence from cresyl violet in fluid solution. This compound behaves well in ethanol and could form the basis of a convenient standard for ratiometric fluorescence quantum yield measurements. Aggregation, or possibly dimerization, of cresyl violet occurs in water and, although fluorescence remains strong, we cannot recommend these conditions for fluorescence spectroscopy. Interestingly, replacing the N-H bonds with N-D bonds leads to a marked reduction in the rate of nonradiative decay of the excited state. This is a nice illustration of the Englman-Jortner energy-gap law.²⁷ We encounter a certain dilemma in other solvents. Our spectroscopic analysis implies that cresyl violet dimerises in most non-alcohol organic solvents but NMR spectroscopy indicates that the compound appears to be present as a monomer. It is possible that the different timescales inherent to these techniques masks the situation. Alternatively, the dimer might be too weak or too poorly coupled in electronic terms to perturb the NMR spectrum. The result, however, is that we do not recommend any solvent other than ethanol (or methanol) for cresyl violet.

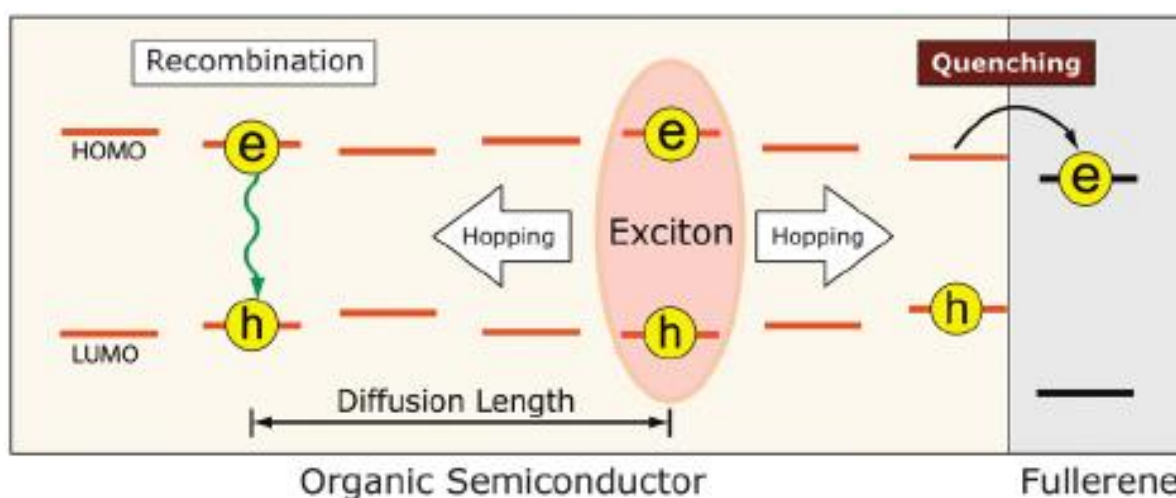
4.7 References

1. Sydor, A. M.; Czymmek, K. J.; Puchner, E. M.; Mennella, V. *Trends Cell Biol.* **2015**, *25*, 730.
2. Kuo, J. S.; Kuyper, C. L.; Allen, P. B.; Fiorini, G. S.; Chiu, D. T. *Electrophoresis.* **2004**, *25*, 3796.
3. Lakowicz, J. R. *Principles of Fluorescence Spectroscopy*; 3rd ed.; Springer Science: New York, USA, **2006**.
4. Gaigalas, A. K.; Wang, L. *J. Res. Natl. Inst. Stand. Technol.* **2008**, *113*, 17.
5. Haidekker, M. A.; Theodorakis, E. A. *J. Mater. Chem. C.* **2016**, *4*, 2707.
6. Rurack, K.; Spieles, M. *Anal. Chem.* **2011**, *83*, 1232.
7. Forster, L. S.; Livingston, R. *J. Chem. Phys.* **1952**, *20*, 1315.
8. Ambroz, M.; Beeby, A.; MacRobert, A. J.; Simpson, M. S. C.; Svensen, R. K.; Phillips, D. J. *Photochem. Photobiol. B: Biol.* **1991**, *9*, 87.
9. Harriman, A. *J. Chem. Soc. Faraday Trans. I.* **1980**, *76*, 1978.
10. Fonda, H. N.; Gilbert, J. V.; Cormier, R. A.; Sprague, J. R.; Kamioka, K.; Connolly, J. S. *J. Phys. Chem.* **1993**, *97*, 7024.
11. Karlsson, J. K. G.; Harriman, A. *J. Phys. Chem. A.* **2016**, *120*, 2537.
12. Benniston, A. C.; Harriman, A. *J. Chem. Soc. Faraday Trans.* **1998**, *94*, 1841.
13. Magde, D.; Brannon, J. H.; Cremers, T. L.; III, J. O. *J. Phys. Chem.* **1979**, *83*, 696.
14. III, J. O. *J. Phys. Chem.* **1979**, *83*, 2581.
15. Sens, R.; Drexhage, K. H. *J. Lumin.* **1981**, *24/25*, 709.
16. Urrutia, M. N.; Ortiz, C. S. *New J. Chem.* **2016**, *40*, 10161.
17. Würth, C.; González, M. G.; Niessner, R.; Panne, U.; Haisch, C.; Genger, U. R. *Talanta.* **2012**, *90*, 30.
18. Isak, S. J.; Eyring, E. M. *J. Phys. Chem.* **1992**, *96*, 1738.
19. Drexhage, K. H. *Laser Focus.* **1973**, *9*, 35.
20. Sabol, J. E.; Rockley, M. G. *J. Photochem. Photobiol. A: Chem.* **1987**, *40*, 245.
21. Jong, M. D.; Seijo, L.; Meijerink, A.; Rabouw, F. T. *Phys. Chem. Chem. Phys.* **2015**, *17*, 16959.
22. Al-Aqar, R.; Benniston, A. C.; Harriman, A.; Perks, T. *ChemPhotoChem.* **2017**, *1*, 198.
23. Strickler, S. J.; Berg, R. A. *J. Chem. Phys.* **1962**, *37*, 814.
24. Sauer, M.; Hofkens, J.; Enderlein, J. *Handbook of Fluorescence Spectroscopy and Imaging*; Wiley - VCH Verlag GmbH & Co. KGaA: Weinheim, Germany, **2011**.
25. Porrès, L.; Holland, A.; Pålsson, L.-O.; Monkman, A. P.; Kemp, C.; Beeby, A. *J. Fluoresc.* **2006**, *16*, 267.
26. Petukhov, V. A.; Popov, M. B.; Krymova, A. I. *Sov. J. Quantum Electron.* **1986**, *16*, 503.
27. Englman, R.; Jortner, J. *Mol. Phys.* **1970**, *18*, 145.

28. Abboud, J.-L. M.; Notario, R. *Pure Appl. Chem.* **1999**, 71, 645.
29. Catalán, J. *J. Phys. Chem. B.* **2009**, 113, 5951.
30. Zeng, L.-H.; Wang, C.; Wang, T.; Li, D.-L. *Analyst.* **2016**, 141, 5339.
31. Kasha, M.; Rawls, H. R.; El-Bayoumi, M. A. *Pure Appl. Chem.* **1965**, 11, 371.
32. Thorley, K. J.; Würthner, F. *Org. Lett.* **2012**, 14, 6190.
33. Stachelek, P.; Harriman, A. *J. Phys. Chem. A.* **2016**, 120, 8104.

Chapter 5.

A Small Organic Molecule Displaying Charge-Recombination Fluorescence in Liquid and Solid Phases



CHARGE RECOMBINATION CAN LEAD TO FLUORESCENCE IN CERTAIN CASES AND IS ONE OF THE MAIN PROCESSES UNDERPINNING ORGANIC LIGHT-EMITTING DIODES.

5.1 Introduction

In Chapter 3, we described the photophysical properties of an organic compound, namely CXD, where intramolecular charge transfer served to augment the internal dipole moment. The nature of this compound was such that the molecule retained a modest dipole moment that did not change substantially on promotion to the first-excited singlet state. The net result of this situation was that the excited-state showed only weak sensitivity to changes in solvent polarity. It is known¹ that other compounds offer far greater response to changes in the nature of the surrounding solvent and many systems have been reported² to function as fluorescent probes for solvent polarity. A common type of such probes is based on the so-called TICT (twisted intramolecular charge-transfer) phenomenon³ whereby excitation causes charge transfer to occur across the molecule. In turn, this event causes a largescale geometrical change that helps to isolate the electronic charges. Now, according to the nature of the donor and acceptor units, a high dipole moment can arise for the excited state. If this dipole moment exceeds that of the ground state by a reasonable amount, the fluorescence yield and spectral maximum will be set by interactions between solute and solvent. In general, polar solvents help to stabilize the polar resonance forms by lowering the energy of the emitting state.⁴ The emission maximum moves to lower energy and, because of the Englman-Jortner energy gap law,⁵ there is a decrease in both the fluorescence quantum yield and the corresponding excited-state lifetime. Many such cases have been reported⁶ in the literature, although it has to be noted that the fluorescence quantum yields tend to be rather small in polar media. It can also be stressed that we did not see this type of behaviour with CXD, probably because the donor unit is not sufficiently powerful to effect strong charge transfer across the molecule. We decided to explore this possibility in detail by moving to a new molecule, referred to here as MBIC, where a more potent donor is in place.

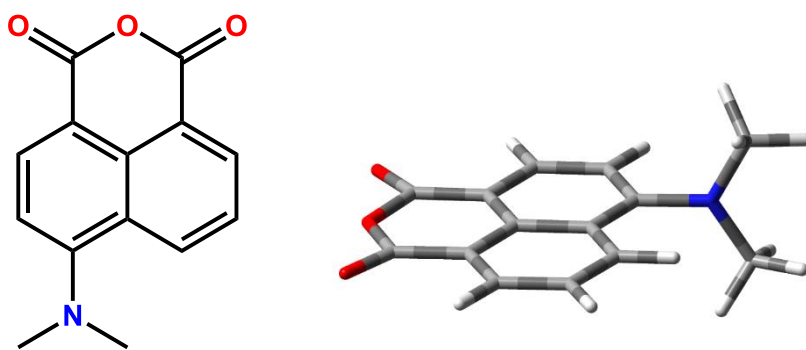


Figure 1. Molecular formula for MBIC and the energy-minimized geometry computed by TD-DFT methods for the excited-singlet state in a solvent reservoir with dielectric constant equal to 20.

Figure 1 shows the molecular formula for MBIC – more correctly called 4-N,N dimethyl-1,8-naphthalic anhydride – together with the computed molecular structure for the excited state. This

compound was synthesized⁷ by Dr. Alparslan Atahan of the Molecular Photonics Laboratory. It is a small molecule that can be prepared easily by amination of the corresponding naphthalic anhydride and crystallized from chloroform and hexane mixtures. Alternatively, MBIC is prepared by the conversion of 4-bromo-1,8-naphthalic anhydride into the N,N-4-dimethyl analogue in the presence of copper sulfate in DMF. The product is obtained as a yellow solid with 78% overall yield. Our sample was fully characterized by NMR and MS methods before recording the crystal structure. The latter, determined by Dr. P. G. Waddell of the Newcastle Crystallography Unit, shows the molecule to be planar. During routine handling of the sample, it was noted that crystals of MBIC were strongly fluorescent under exposure to near-UV light. This behaviour is unusual but not unknown.⁸ Indeed, most organic crystals formed from strongly fluorescent monomers are non-fluorescent in the solid state due to π,π -interactions that promote nonradiative decay to the ground state. This is the case with popular fluorophores like pyrene and anthracene. Light-induced dimerization happens in the crystalline phase, leading to formation of what are known as “photo-dimers”.⁹ This effect is illustrated in Figure 2 for anthracene. At the other extreme, excitation of pentacene in the crystalline state leads to singlet fission¹⁰ – a protocol that has now been exploited to increase the concentration of charge carriers in certain organic solar cells.¹¹ The exercise of singlet exciton fission is illustrated by way of Figure 3 and has been recognized for a few other aryl hydrocarbons, such as tetracene.¹² It requires the special condition that the triplet state energy must be less than one-half of the corresponding singlet state energy. This situation arises for the longer linear polyacenes.

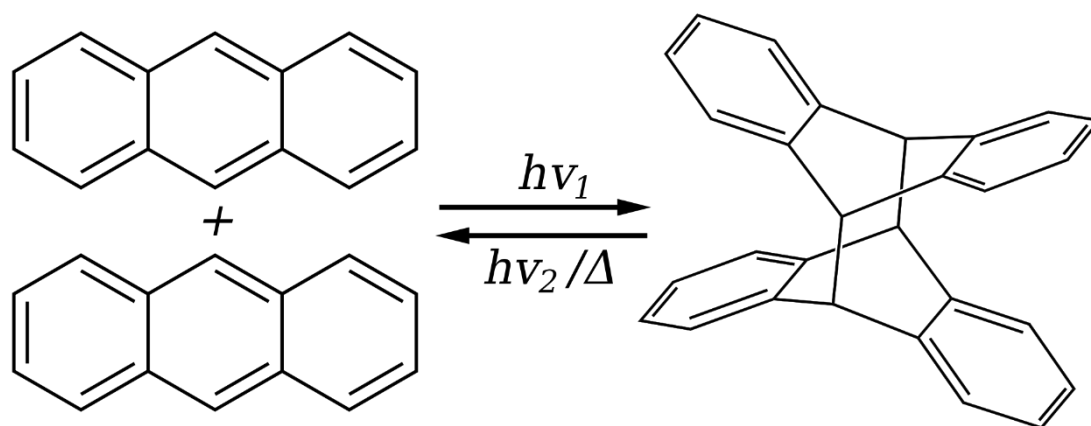


Figure 2. Photodimer formation proposed for crystalline anthracene under UV illumination.

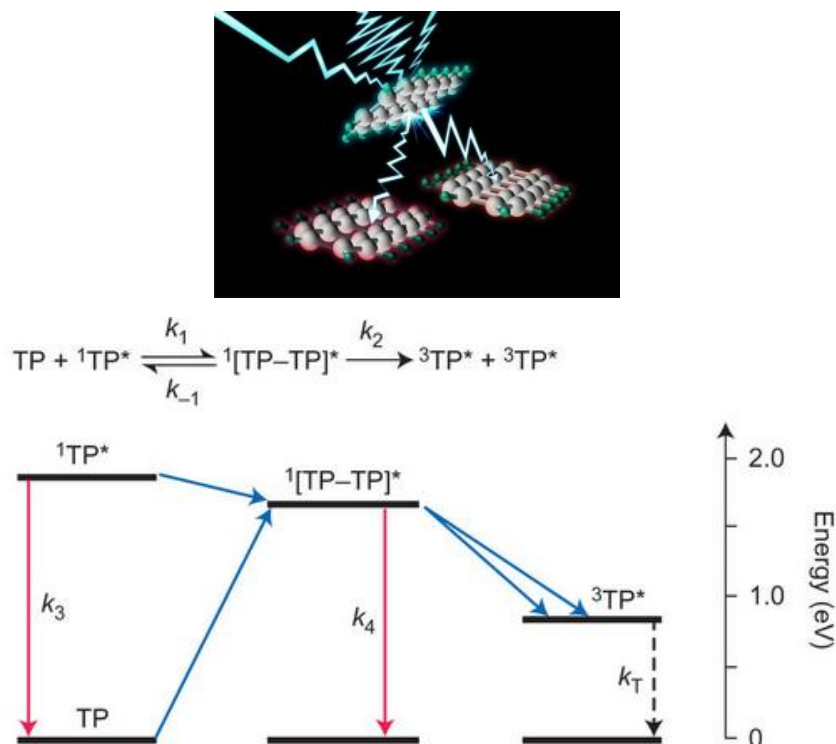


Figure 3. Illustration (upper panel) and reaction pathway (lower panel) proposed for singlet exciton fission in pentacene derivatives.

5.2 Electrochemistry

The electrochemical properties of MBIC were investigated by way of cyclic voltammetry in acetonitrile solution containing tetra-N-butylammonium tetrafluoroborate (0.2 M) as background electrolyte (Figure 4). The working electrode was a highly polished glassy carbon disk, freshly cleaned for each run. The counter electrode was a thin platinum wire and the reference electrode was made from a saturated calomel electrode. The circuit was calibrated by adding ferrocene at the end of the experiment. For MBIC, it was found that the compound exhibited a quasi-reversible one-electron reduction wave with a half-wave potential of -1.66 V vs SCE. On oxidation, the compound gave an irreversible wave with a peak potential at 0.85 V vs SCE. This peak remained electrochemically irreversible at all accessible scan rates. It is our understanding that the amino group operates as electron donor and therefore this unit will be oxidized preferentially. The naphthalic anhydride residue is the most likely electron acceptor¹³ and it is on this group that the added electron will reside. The difference between the two electrochemical peak potentials equates to 2.5 eV, which can be compared to the absorption energy of 2.6 eV found for MBIC in acetonitrile solution. Thus, the lowest-energy transition seen in the absorption spectrum can be assigned to a transition from the HOMO to the LUMO.

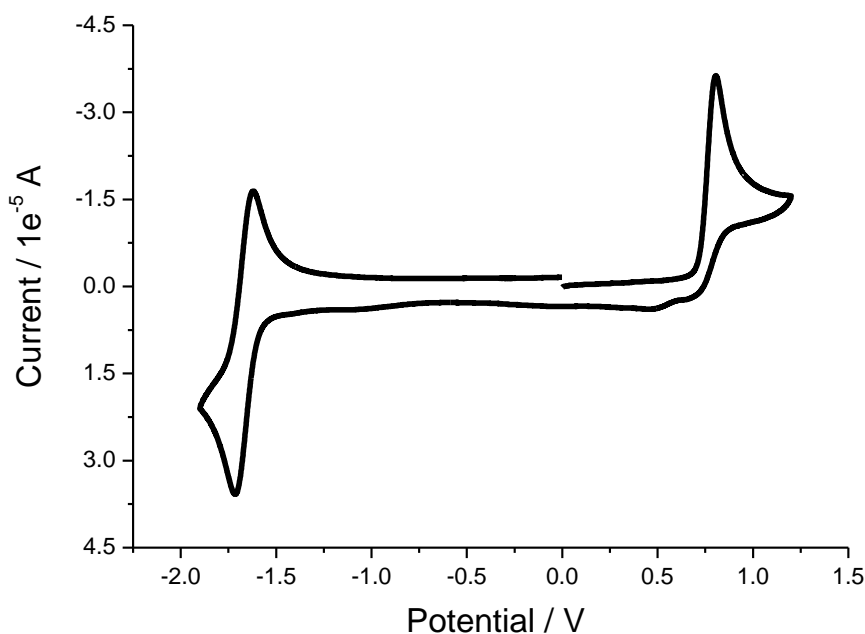


Figure 4. Example of a cyclic voltammogram recorded for MBIC in deoxygenated acetonitrile containing background electrolyte. The scan rate was 100 mV per second and the substrate concentration was ca. 2 mM. The potential scale is referenced to the standard SCE and was calibrated by addition of ferrocene.

5.3 Photophysical properties in the solution

In liquid solution, MBIC shows a broad and essentially featureless absorption spectral profile with a peak (λ_{MAX}) at 420 nm in chloroform. The molar absorption coefficient at the peak (ϵ_{MAX}) is $10,720 \text{ M}^{-1} \text{ cm}^{-1}$ and the oscillator strength for the lowest-energy transition is 0.20. On changing the solvent, there is a general red shift for the absorption maximum with increasing dielectric constant of the solvent, as will be discussed later. These various features can be used to argue that the lowest-energy absorption transition for MBIC is essentially of charge-transfer character.^{14,15} Simply looking at the molecular formula (Figure 1), it appears that the amino group will function as a powerful electron donor while the naphthalic anhydride unit will act as the complimentary electron acceptor. In a way, this represents a continuation of the case described earlier with CXD but now the donor is more potent.

Absorption spectra were measured for MBIC in a series of twenty five organic solvents and the main properties are summarized in Table 1. It can be observed that the longest-wavelength absorption band undergoes a modest red-shift in polar solvents. This effect can be explained through the charge-transfer resonance forms being stabilized in the more polar solvent. The spectral profile

remains broad and featureless in all solvents, including cyclohexane (Figure 5). There is no sign of a corresponding π,π^* absorption transition at wavelengths longer than 300 nm. The absorption maximum, converted into wavenumbers, shows a crude correlation with the $E_T(30)$ solvent parameter.¹⁶ This effect is illustrated in Figure 6. It serves to illustrate the ability of the polar solvent to stabilize the ground state by way of specific alignment around the dipole. Compared to CXD, it appears that the dimethylamino group acts as a much improved charge donor.

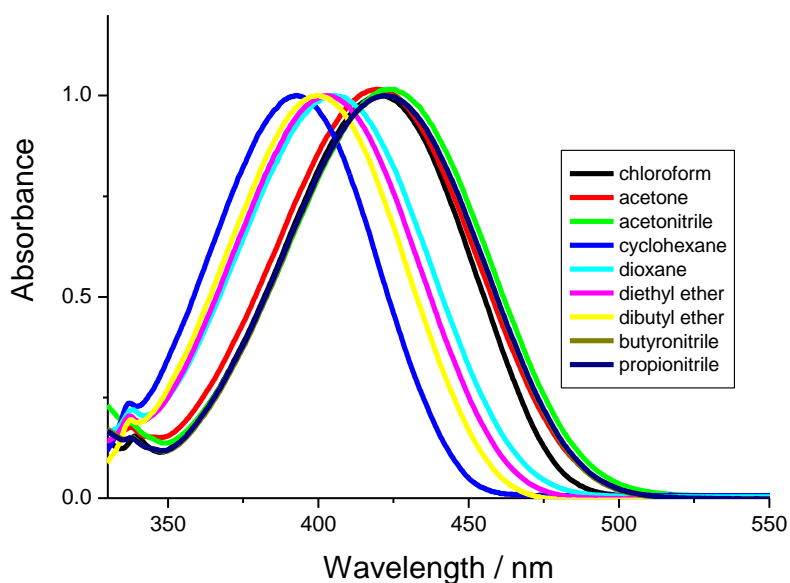


Figure 5. Absorption spectra recorded for MBIC in a range of organic solvents. Individual spectra have been normalized to the peak seen around 420 nm and details are listed in Table 1.

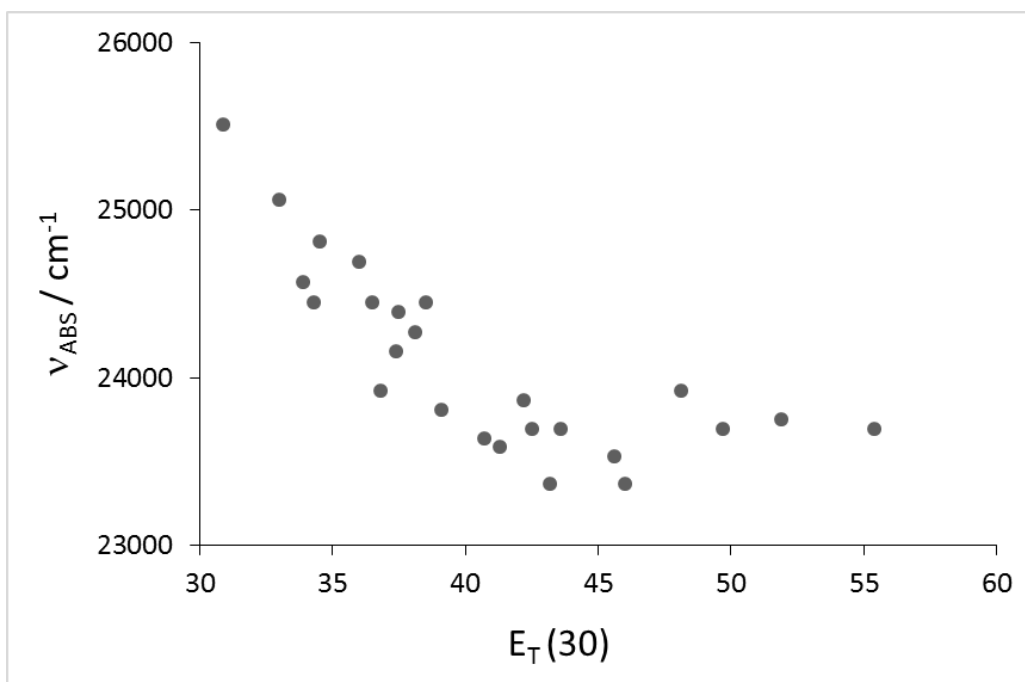


Figure 6. Effect of solvent polarity, measured in terms of the empirical $E_T(30)$ parameter, on the absorption maximum recorded for MBIC in a series of organic solvents.

It can be seen that the absorption maximum moves progressively towards lower energy with increasing polarity. The effect is non-linear in terms of representing the polarity function by the empirical $E_T(30)$ parameter.¹⁷ This particular solvent parameter is based on the experimental measurement of a solvent-sensitive dye in a wide range of solvents. For MBIC, however, the presence of carbonyl and amino groups might introduce specific solvation effects, such as hydrogen bonding, which might obscure other effects. There is no obvious reason why there should be a linear relationship between the energy of the absorption peak and the $E_T(30)$ parameter. This would happen only if the same factors affect the absorption maximum for the two dyes. With MBIC, the key property is likely associated with intramolecular charge transfer. Nonetheless, it is clear that the nature of the solvent has an important effect on the position, but not the shape, of the absorption band.

Fluorescence is readily observed in fluid solution but the spectral profile is broad and featureless (Figure 7). There is quite good mirror symmetry with the lowest-energy absorption band and a relatively large Stokes' shift. These features suggest that the emitting state retains strong intramolecular charge-transfer character. In non-polar solvents, like cyclohexane, the fluorescence spectrum shows some structure. We compare the energy of the fluorescence maximum (ν_{FLU}) with the solvent $E_T(30)$ parameter in Figure 8. It is seen that this effect closely resembles that found for the absorption maximum.

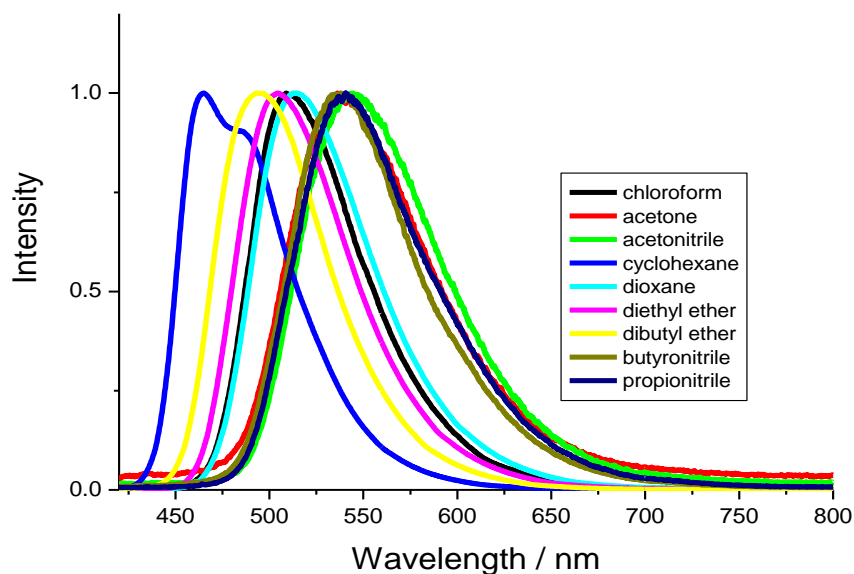


Figure 7. Effect of solvent on the fluorescence spectrum recorded for MBIC at room temperature.

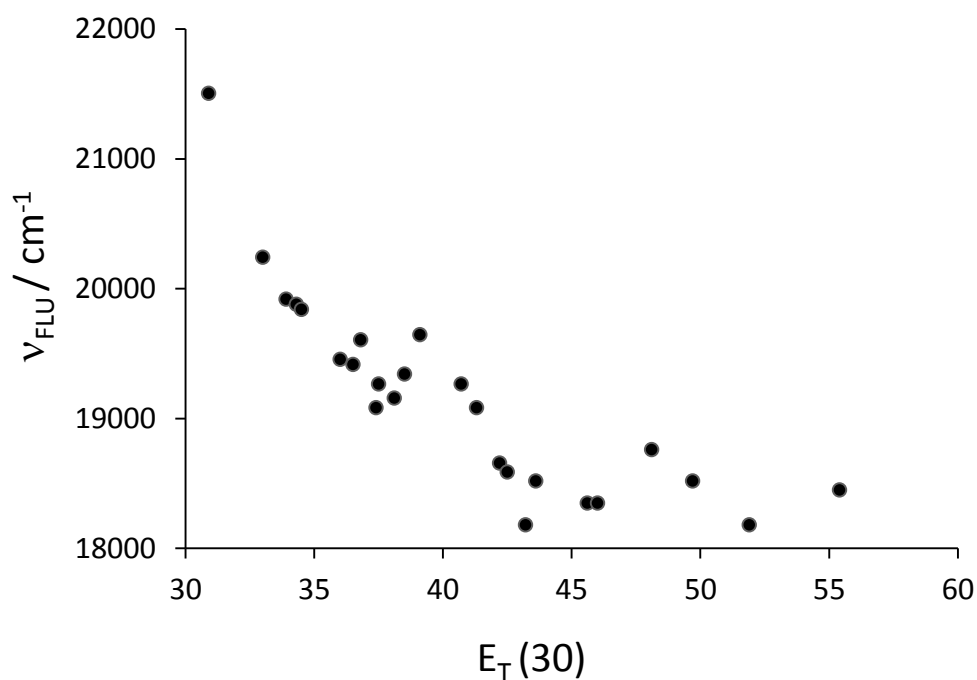


Figure 8. Effect of solvent polarity, measured in terms of the empirical $E_T(30)$ parameter, on the fluorescence maximum recorded for MBIC in a series of organic solvents.

We can perhaps better represent the solvent polarity function by way of the static dielectric constant (ϵ_s). As this term increases in magnitude, the fluorescence peak moves towards lower energy (Figure 9) and the Stokes' shift increases (Table 1). These features tell us that the excited-singlet state has a larger dipole moment than does the ground state. Now, using the Lippert-Mataga expression¹⁸

Equation 5.1 it is possible to estimate the size of this increase in dipole moment provided a plot between the Stokes' shift and the solvent Pekar factor is linear. From Figure 10, we see that this relationship is generally true but certain solvents do not follow the generic trend. This might be expected since hydrogen bonding will disrupt the solvent-solute interactions. From the general expression, it can be concluded that the dipole moment of the excited state exceeds that of the ground state by around 5 D.

Table 1 is provided at the end of this chapter for ease of printing.

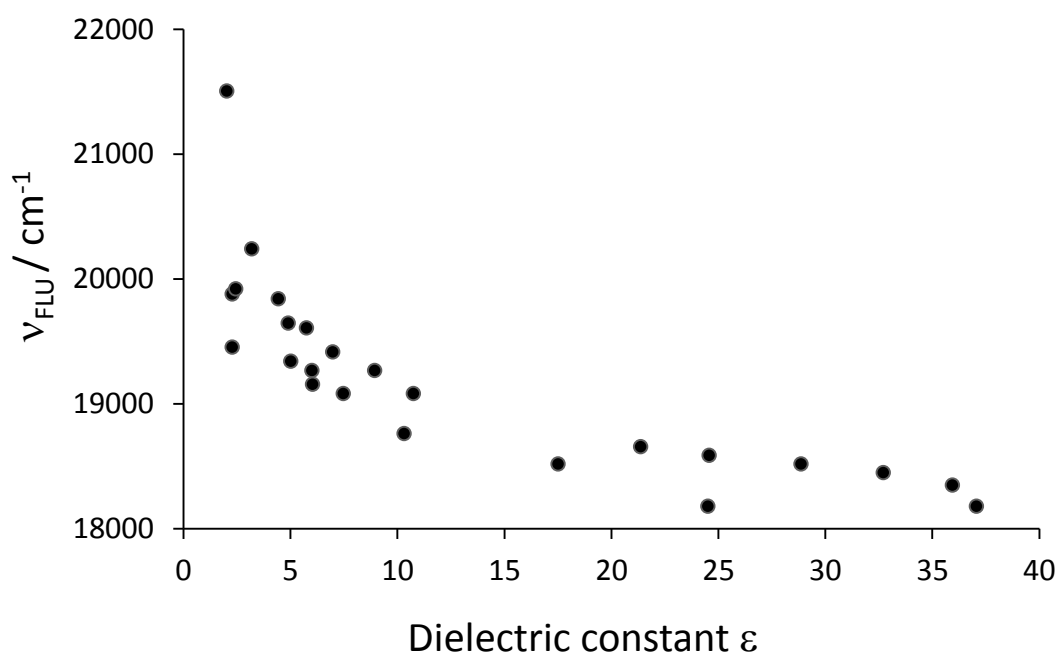


Figure 9. Relationship between the emission maximum and the solvent dielectric constant.

$$\bar{\nu}_A - \bar{\nu}_F = \frac{2}{hc} \left[\frac{\epsilon-1}{2\epsilon+1} - \frac{n^2-1}{2n^2+1} \right] \frac{(\mu_E - \mu_G)^2}{a^3} + \text{constant} \quad \text{Equation 5.1}$$

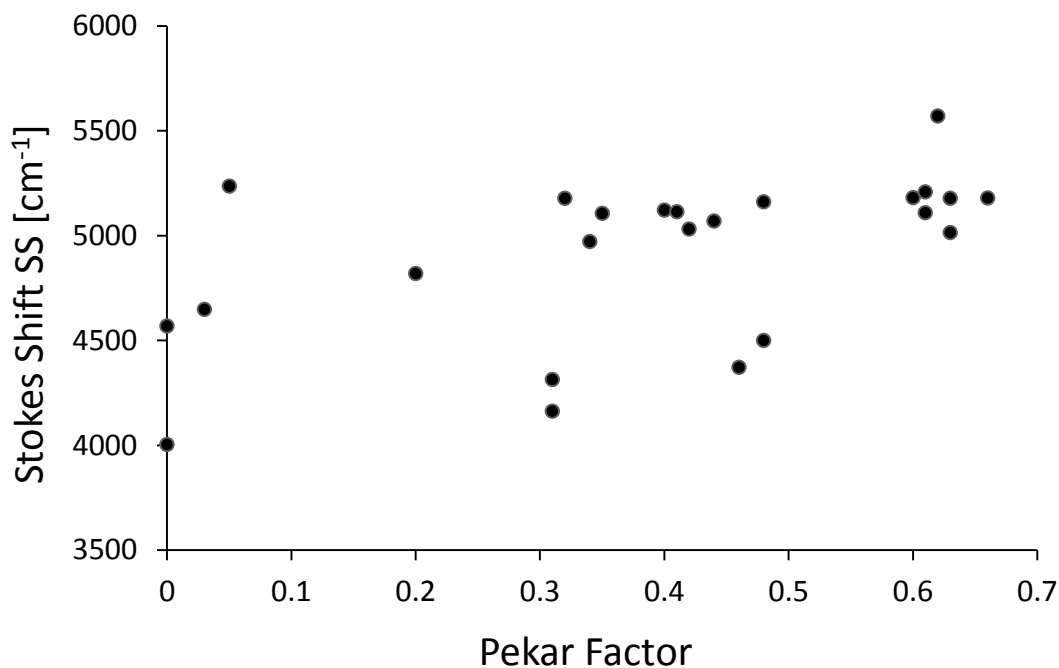


Figure 10. Plot of the Stokes' shift versus solvent polarity function according to the Lippert-Mataga expression.

Certain derivatives of 1,8-naphthalimide have been reported¹⁹ to exhibit room temperature phosphorescence. This was not the case for MBIC but, after addition of 20% v/v iodoethane to a solution in 2-methyltetrahydrofuran (MTHF), it was possible to detect phosphorescence at 77K. The spectrum so derived is shown in Figure 11 and indicates the presence of a certain degree of fine structure. Indeed, the emission is more related to phosphorescence from a π,π^* state than from a charge-transfer state. The phosphorescence maximum occurs at 548 nm, while the maximum fluorescence wavelength is located at 515 nm. This enables us to estimate the singlet-triplet energy gap as being $1,170\text{ cm}^{-1}$ (i.e., 0.15 eV). This is a relatively small splitting but is probably too large to promote E-type delayed fluorescence.²⁰

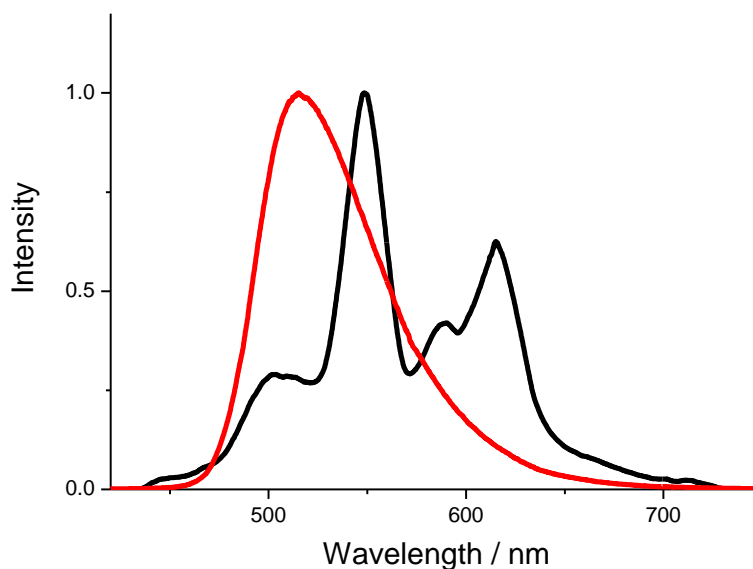


Figure 11. Comparison of the phosphorescence (black curve) and fluorescence (red curve) spectra recorded for MBIC in MTHF containing 20% v/v iodoethane at 77K. The phosphorescence spectrum was isolated using a 10 μ s chopper.

In order to confirm formation of the excited-triplet state, MBIC was studied by laser flash photolysis with excitation at 360 nm. The sample was prepared in deoxygenated MTHF solution and was excited with a 4-ns laser pulse. A weak signal was observed with an absorption maximum centred at around 360 nm and with bleaching of the ground-state band in the region around 410 nm (Figure 12). The triplet lifetime was found to be 25 μ s under these conditions. Addition of molecular oxygen resulted in a serious decrease in the triplet lifetime. The signal increased on addition of iodoethane but, at the same time, the lifetime was seen to decrease. Such behaviour is fully consistent with expectations based on the external spin-orbit coupling mechanism.²¹

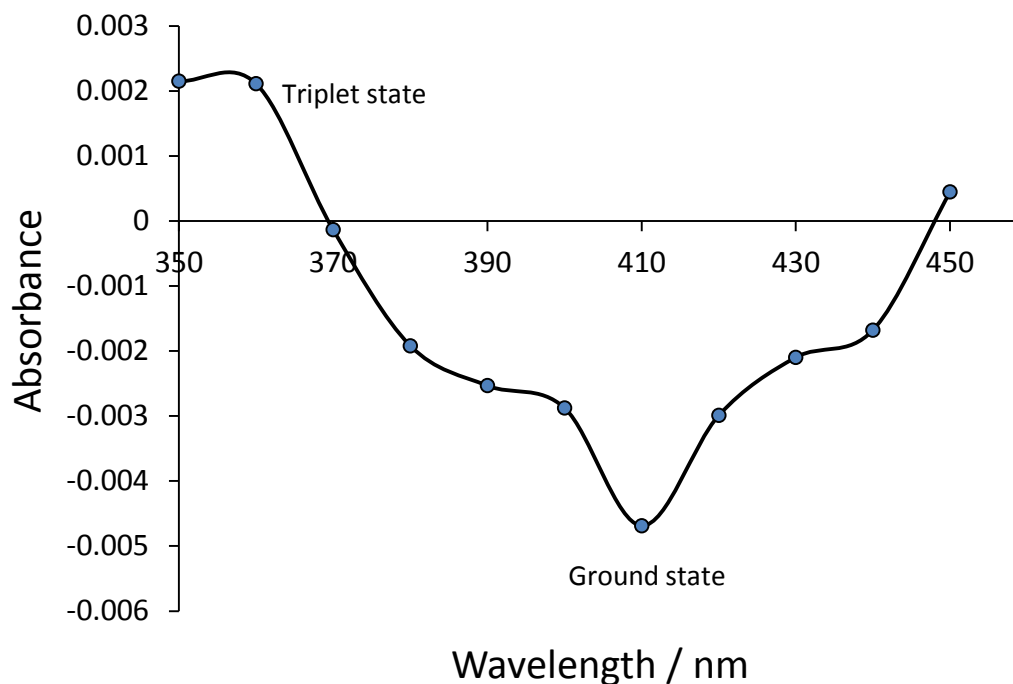


Figure 12. The transient differential absorption spectrum recorded for MBIC in deoxygenated MTHF after excitation with a 4-ns laser pulse at 360 nm.

Table 1 includes the photophysical properties recorded for MBIC in a wide range of organic solvents at room temperature. These solvents, which were of spectroscopic standard and were checked for fluorescent impurities before use, include both aprotic and protic solvents. As mentioned elsewhere in this chapter, we have some concerns that certain solvents will form hydrogen bonds with the donor and/or acceptor units associated with the solute. Nonetheless, some general comments can be made about the experimental data. Thus, polar solvents stabilize both ground and excited states because of the pronounced intramolecular charge-transfer character. This effect is seen as a lowering of the absorption and fluorescence maxima with increasing polarity of the solvent. Fluorescence is more affected than is the corresponding absorption transition, with the effect that the Stokes' shift increases in the more polar solvents. One problem with expressing results in terms of solvent polarity is the realization that the effect is non-linear and many stabilization issues reach saturation at a dielectric constant of around 10 or so. There is no reason to expect linear correlations between spectral maxima and solvent properties. One generic exception to this behaviour comes from the Lippert-Mataga relationship¹⁸ which addresses the effect of solvent polarity on the Stokes' shift. Now, in a series of solvents showing comparable levels of interaction with the solute, we can expect a linear correlation with the solvent Pekar function (Δf). The latter is defined in Equation 5.2 and includes terms for both the polarizability of the solvent, this being related to the refractive index (n), and the polarity, this being measured by the Onsager principle.²² A linear relationship, together with an

estimate of the molecular dimensions, allows estimation of the change in dipole moment on excitation to the emitting state.

$$\Delta f = [(\epsilon_S - 1)/(2\epsilon_S + 1)] - [(n^2 - 1)/(2n^2 + 1)] \quad \text{Equation 5.2}$$

The data listed in Table 1 indicate that polar solvents decrease both the fluorescence quantum yield and the corresponding excited-singlet state lifetime. These two parameters can be used to extract values for the radiative (k_{RAD}) and nonradiative (k_{NR}) rate constants covering deactivation of the emitting state. The nonradiative rate constant includes contributions from both internal conversion to recover the ground state and intersystem crossing to the triplet manifold. The S_1 - T_1 energy gap appears to be quite small and, because the T_1 state appears to be primarily of π, π^* character while the S_1 state has appreciable charge-transfer character, the actual gap is probably sensitive to changes in solvent polarity. We can represent these various processes by way of a simple potential energy diagram of the type displayed in Figure 13. Equations 5.3 and 5.4 allow us to determine values for both k_{RAD} and k_{NR} from the measured quantum yields and lifetimes (Table 1); it might be noted that the time-resolved fluorescence decay records could be analysed satisfactorily in terms of a single-exponential function. We can now consider the effects of solvent on the two global rate constants.

$$k_{RAD} = \Phi_F/\tau_S \quad \text{Equation 5.3}$$

$$k_{NR} = (1 - \Phi_F)/\tau_S \quad \text{Equation 5.4}$$

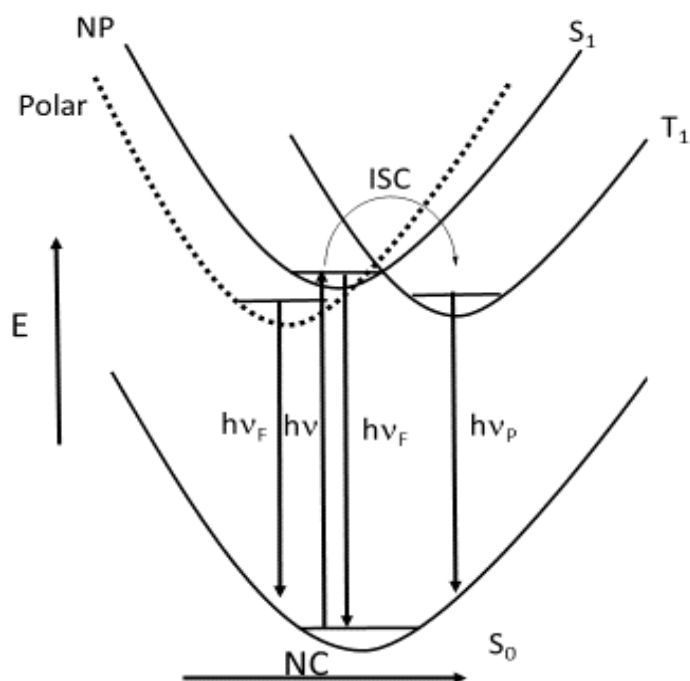


Figure 13. Potential energy level diagram proposed for MBIC, showing the ground, excited- singlet and excited-triplet levels in a relatively non- polar (NP) solvent. The effect of solvent polarity is to lower the relative energy of S_1 , thereby leading to a red shift for the fluorescence profile.

Firstly, it should be stressed that the solvent sensitivity is quite large. For example, the fluorescence quantum yield falls from 0.95 to 0.004 on moving from benzene to N,N-dimethylformamide. At the same time, the excited-state lifetime decreases from 10.5 ns to 170 ps. These changes are well outside experimental error! There are several alternative expressions by which to consider the solvent effects on the main decay rates but, in line with Figure 13, we prefer to restrict attention to the relationship between the rates and the corresponding energy gaps. Let us first address how k_{NR} responds to changes in the energy of the emitting state as induced by solvent polarity. This can be done most conveniently in terms of the Englman-Jortner energy gap law.⁵ The Englman-Jortner energy-gap law⁵ relates the rate constant (k_{NR}) for nonradiative deactivation of an excited state to the energy gap (ΔE) between the excited state and the acceptor state Equation 5.5. The latter is usually the corresponding ground state of the molecule but might be the triplet-excited state or, in certain cases, an isomer. It is highly likely that in the case of MBIC both the triplet and ground state function as the acceptor state. Passage from donor to acceptor is conducted by way of an averaged vibronic mode of energy $h\omega$. Alternative forms of the expression²³ have been developed to include several internal vibrations of different frequency but, since we lack precise information on this parameter, we use the simplest form. Also included in Equation 5.5 is an electronic-vibronic coupling constant, C , that

enables mixing between the excited state and hot vibronic levels of the acceptor state. The scaling factor, γ , is often referred to as the coefficient and is defined by way of Equation 5.6. Here, Δ describes the displacement in terms of geometry of the two potential energy surfaces and d is the number of degenerate vibrational modes coupled to the nonradiative process. The expression as written is restricted to nonradiative processes between weakly coupled systems and is often simplified to Equation 5.7 where all the pre-exponential terms are grouped into a single factor, F . This form of the energy-gap law, usually referred to as the exponential energy-gap law,⁵ is useful for homologous series of emitters or for a single compound in a series of different environments.

$$k_{NR} = \frac{c^2 \sqrt{2\pi}}{\hbar \sqrt{\Delta E} \hbar \omega} \exp\left(\frac{-\gamma \Delta E}{\hbar \omega}\right) \quad \text{Equation 5.5}$$

$$\gamma = \ln\left(\frac{2\Delta E}{d\Delta^2 \hbar \omega}\right) - 1 \quad \text{Equation 5.6}$$

$$k_{NR} \propto F \exp\left(\frac{-\gamma \Delta E}{\hbar \omega}\right) \quad \text{Equation 5.7}$$

As can be seen from Figure 14, k_{NR} for MBIC in a range of solvents appears to fit reasonably well to the exponential energy-gap law, despite several important simplifications. We know that k_{NR} contains contributions from internal conversion and intersystem crossing while there is no reason to suppose that a single vibronic mode is involved. We should also question the use of a single coefficient, γ , for a case where the degree of internal charge transfer is changing. Nonetheless, the experimental data give a satisfactory fit to Equation 5.7. In fitting the experimental data, we have replaced the energy gap, ΔE , with the emission maximum, ν_{FLU} . It is seen that there is a reasonable fit over the entire series of solvents. This suggests that the important vibronic mode arises from an internal geometrical change and is not over-ruled by hydrogen bonding. It is also evident that the choice of a single coefficient is valid for this system. However, the fact that we do not know the magnitude of the energy gap, because of the likely involvement of triplet-excited states, means that we cannot evaluate the expression in order to estimate a value for γ .

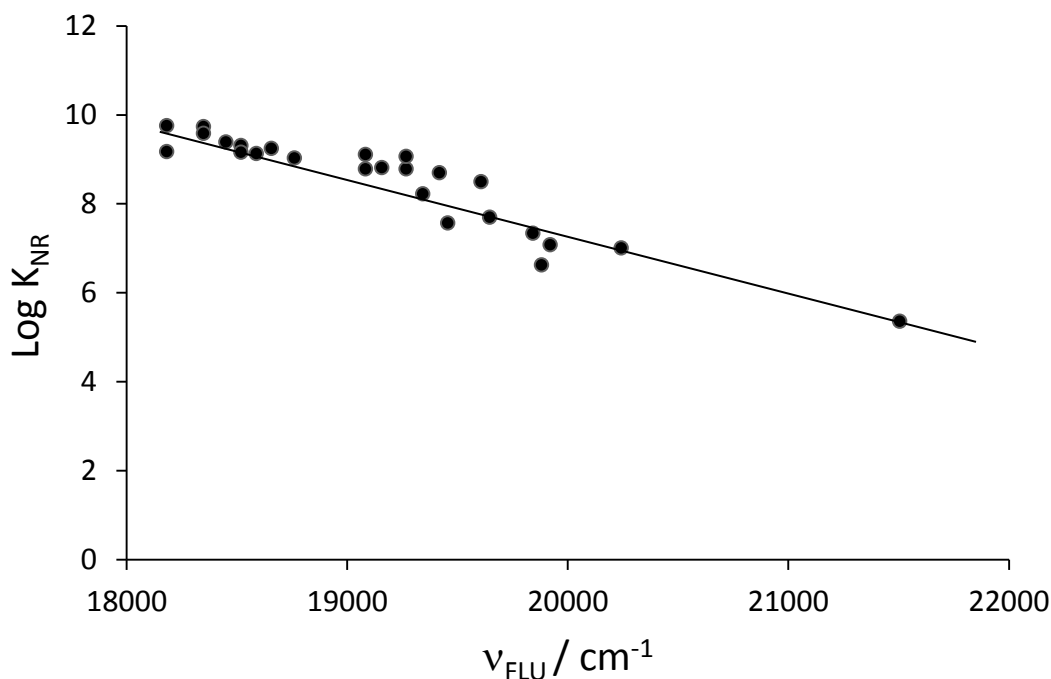


Figure 14. Fit of the experimental data for the non-radiative decay rate constant to the simplified form of the Englman-Jortner energy gap law Equation 5.7.

In contrast to k_{NR} , there is a progressive decrease in the magnitude of the radiative rate constant (k_{RAD}) as the energy gap decreases. This situation is the opposite of the situation found for k_{NR} . The net result is the probability for fluorescence increases as the energy of the emitting state increases. For k_{RAD} , there is a good linear relationship between the emission maximum and k_{RAD} (Figure 15). This correlation is to be expected on the basis of the equation derived by Jortner and Verhoeven²⁴ for an excited state characterized by strong intramolecular charge transfer. The expression is shown as Equation 5.8. There is some discussion as to the exact form of the energy gap but our results appear to fit to the simplest case. Linearity is observed over a wide range of solvents, including aprotic and protic media, showing that the relationship is quite robust.

$$k_{\text{rad}}(\nu) = \frac{32\pi^3 n^3}{3h} \nu |\mu_{\nu}(\nu)|^2 \quad \text{Equation 5.8}$$

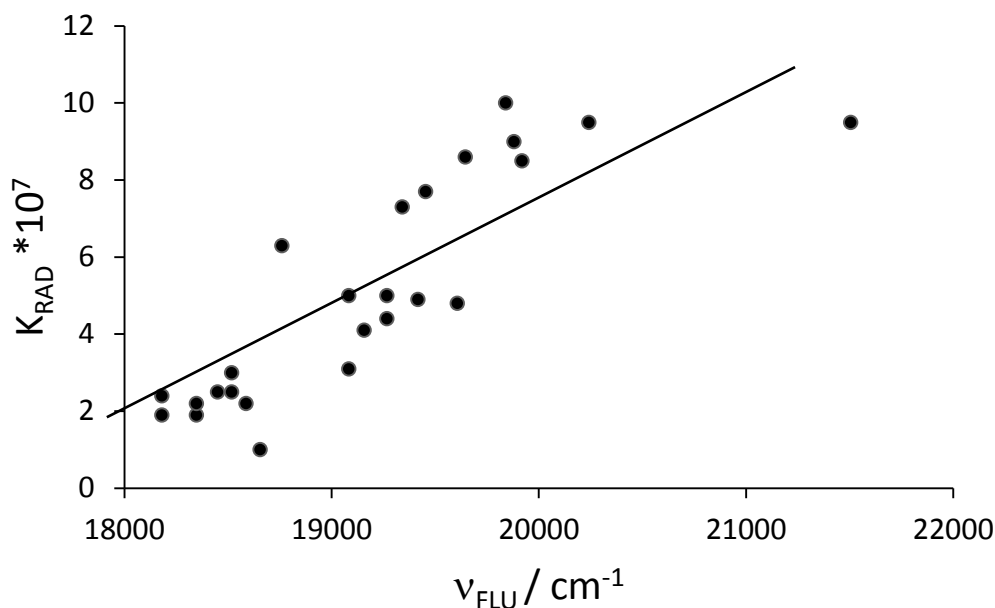


Figure 15. Effect of the energy gap on the rate constant for radiative decay of the intramolecular charge-transfer excited state. The solid line drawn through the data points represents a fit to Equation 5.8. Improvement could be attained by using the cube of the emission energy.

To further probe the importance of the nonradiative decay channel, a series of temperature-dependence studies was made. Firstly, solutions of MBIC were prepared in different solvents, for example cyclohexane and butyronitrile, and fluorescence spectra were recorded after equilibration at different temperatures over the range 20 to 70 °C. However, it proved difficult to prevent evaporation of the solvent. To overcome this problem, MBIC was dispersed in dried KBr and pressed into transparent disks under pressure. The resultant disks were used to record fluorescence spectra over a wide temperature range (i.e. 25 to 200 °C). It should be noted that MBIC remains strongly fluorescent under these conditions, with the emission profile resembling that found in solution (Figure 16). It appears, therefore, that charge recombination fluorescence occurs in the KBr matrix. During the temperature change, there is no real shift in the emission maximum which remains at ca. 560 nm. There is, however, a general decrease in emission intensity with increasing temperature. This effect is non-linear and quenching becomes more pronounced at elevated temperature (Figure 17). Temperature also affects the band half-width (FWHM), with the band broadening as the temperature increases. This latter effect is consistent with the emission being essentially of charge-recombination character. For such emission, the reorganization energy accompanying charge recombination (λ_{τ}) can be expressed in the form of Equation 5.9. Here, we might expect a linear correlation between the square of the band half-width and temperature, as observed by the experiment (Figure 18).

$$\lambda_T = \frac{(FWHM)^2}{16 \ln 2 K_B T} \quad \text{Equation 5.9}$$

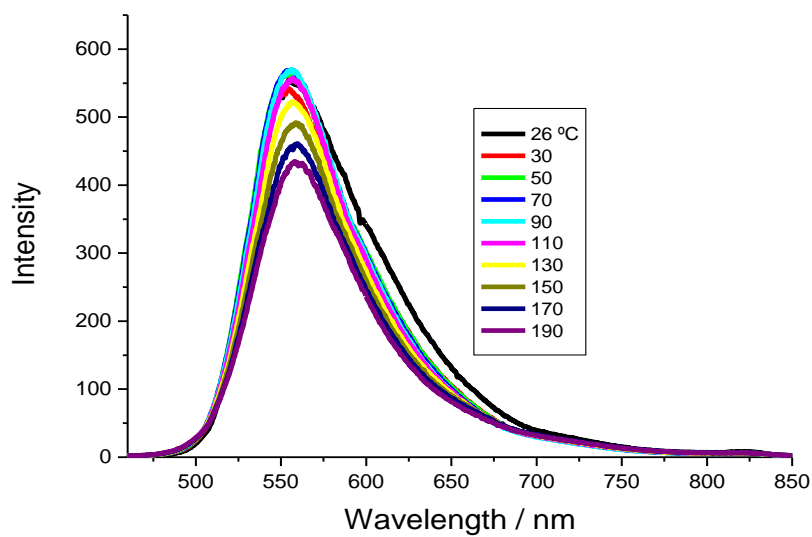


Figure 16. The effect of temperature on the fluorescence spectral profile for MBIC dispersed in a dried KBr disc.

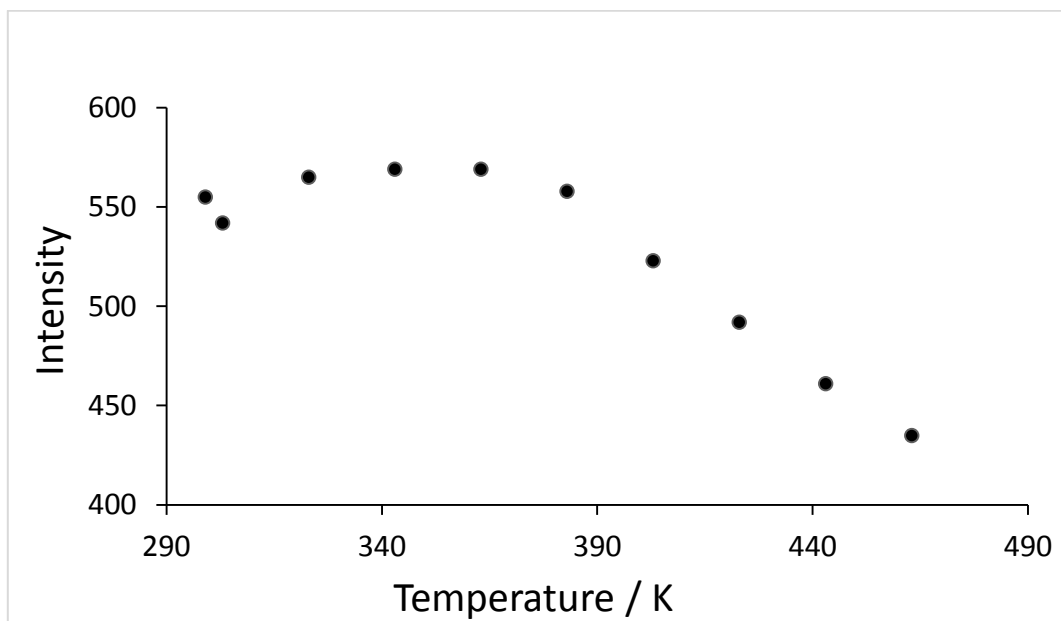


Figure 17. The effect of temperature on the integrated emission intensity recorded for MBIC dispersed in a transparent KBr disc.

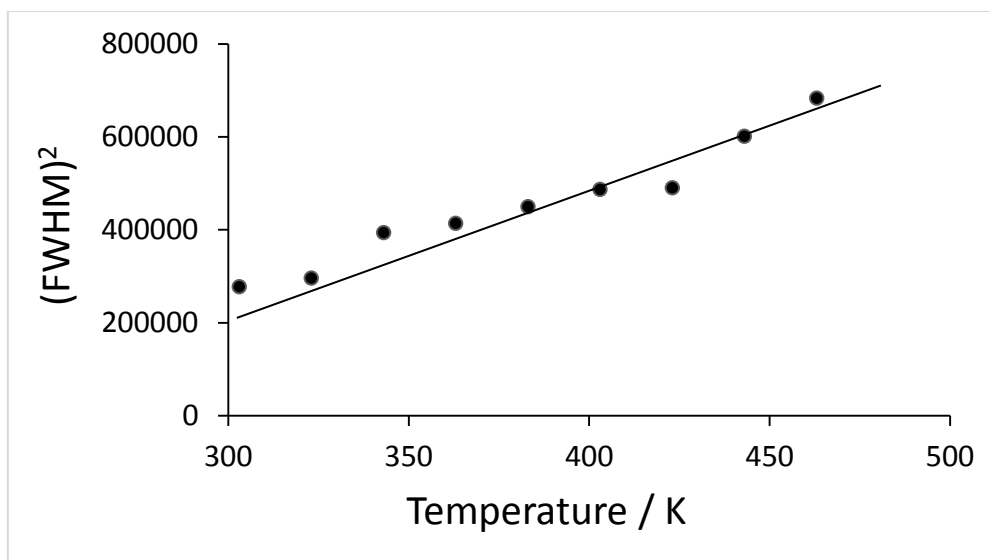


Figure 18. Relationship between the fluorescence spectral band half-width and temperature for MBIC dispersed in a KBr disk. The solid line drawn through the data points represents a fit to Equation 5.9.

Returning now to the temperature effect on the integrated fluorescence intensity, we can propose that there must be a high-lying trap that deactivates the excited state under these conditions. The trap is strongly coupled to the ground state but can only be reached at higher temperature. This situation, which is well known²⁵ for luminescent metal poly (pyridine) complexes, is illustrated in Figure 19. If we accept that there is no change in the absorption spectrum under these conditions, it becomes possible to relate the emission intensity to the corresponding quantum yield. The fluorescence quantum yield in KBr at room temperature was estimated as being 0.09 while the emission lifetime was found to be 1.25 ns. Assuming that only the non-radiative rate constant changes under these conditions, the temperature dependence for k_{NR} can be determined from the temperature-dependence studies. This allows Figure 17 above to be reformulated as a modified Arrhenius plot according to Equation 5.10. Here, k_0 refers to an activationless rate constant that controls non-radiative decay at modest temperature. The observed temperature dependence arises from the activated rate constant, k_{ACT} , and the accompanying activation energy, E_B . Fitting the data to Equation 5.10 allows estimation of k_0 and k_{ACT} , respectively, as being $6 \times 10^8 \text{ s}^{-1}$ and $1.3 \times 10^{12} \text{ s}^{-1}$ (Figure 19). The activation energy has a value of 40 kJ/mol. The significance of these values is that the trap plays an important role in the deactivation of the excited state at elevated temperature. The barrier is sufficiently high to prevent serious occupation of the trap at normal temperature.

$$k_{NR} = k_0 + k_{ACT} \exp\left(-\frac{E_B}{RT}\right) \quad \text{Equation 5.10}$$

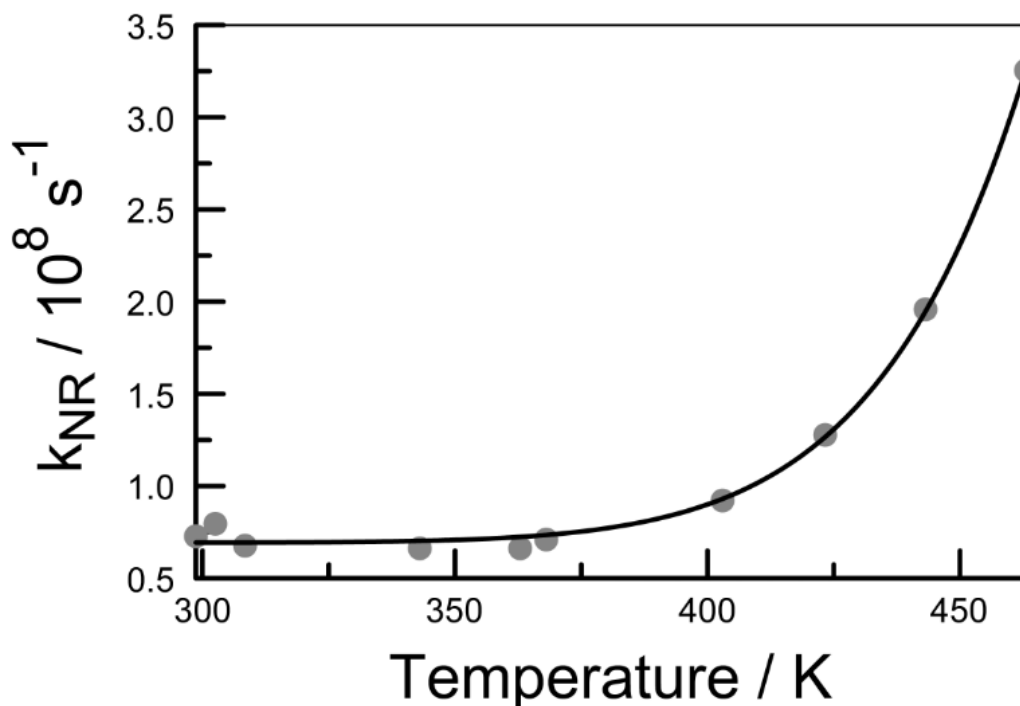


Figure 19. Modified Arrhenius plot for the temperature dependence recorded for fluorescence from MBIC in KBr.

5.4 Photochemical stability of MBIC

Any possible applications for MBIC are dependent on the chromophore being resistant to degradation under prolonged illumination, especially if the excitation source is a violet LED. To test the stability of this compound, solutions of MBIC were prepared in air-equilibrated solution and exposed to broadband illumination from a floodlight. The excitation beam was filtered to remove UV and IR radiation and the course of reaction was followed by absorption spectroscopy. It was observed that photolysis of MBIC in polar solvents caused very little loss of compound, even over quite long exposure times. Figure 20 illustrates this situation for MBIC in air-equilibrated chloroform. No new absorption bands appear and the total loss of compound is restricted to a few percent at most. Thus, under these conditions, MBIC seems to be reasonably stable towards white light. Loss of chromophore is more pronounced, however, in cyclohexane where intramolecular charge-transfer interactions are less important. Here, illumination leads to bleaching over a few hours. The inference from these studies is that the charge-separated resonance forms are stable towards photochemical destruction but the neutral forms are sensitive to degradation. This is a serious conclusion because most foreseeable applications would require the compound to be prepared in the solid state. Such materials are likely

to be relatively non-polar, such as PMMA, and will provide an environment where photodegradation might be a problem.

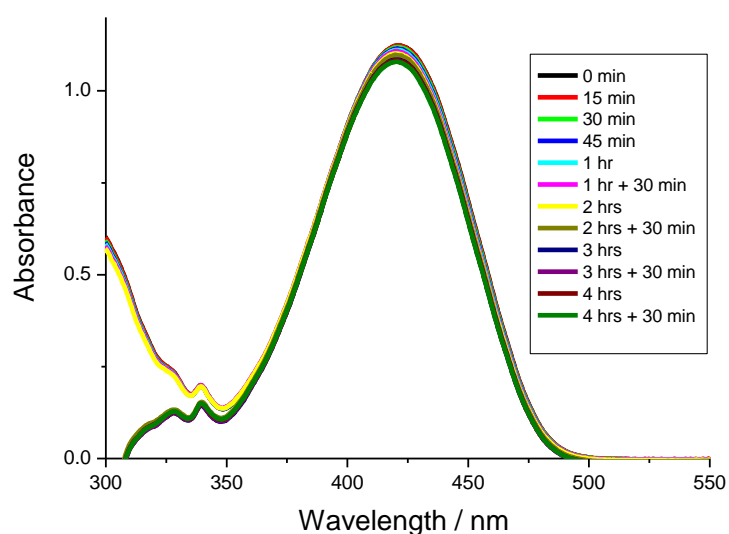


Figure 20. Absorption spectra recorded during the photochemical bleaching of MBIC in air-equilibrated chloroform. The light source was a 400W floodlight filtered to remove UV and IR radiation.

5.5 Protonation of the amino group

Samples of MBIC in dioxane solution were titrated with HCl in order to switch-off the intramolecular charge transfer by eliminating the donor potential of the amino group. As acid is added progressively, the lowest-energy absorption bands decrease in intensity and new bands appear at higher energy (Figure 21). This situation is the expected outcome of eliminating the charge-transfer effect. The new absorption transition has a maximum at around 340 nm and the absorption band shows fine structure consistent with a π, π^* transition. During the titration, fluorescence spectra were also recorded and indicate that the emerging species is fluorescent (Figure 22). The new fluorescence band appears at higher energy and gives an excitation spectrum in agreement with the π, π^* absorption transition seen in acidic solution.

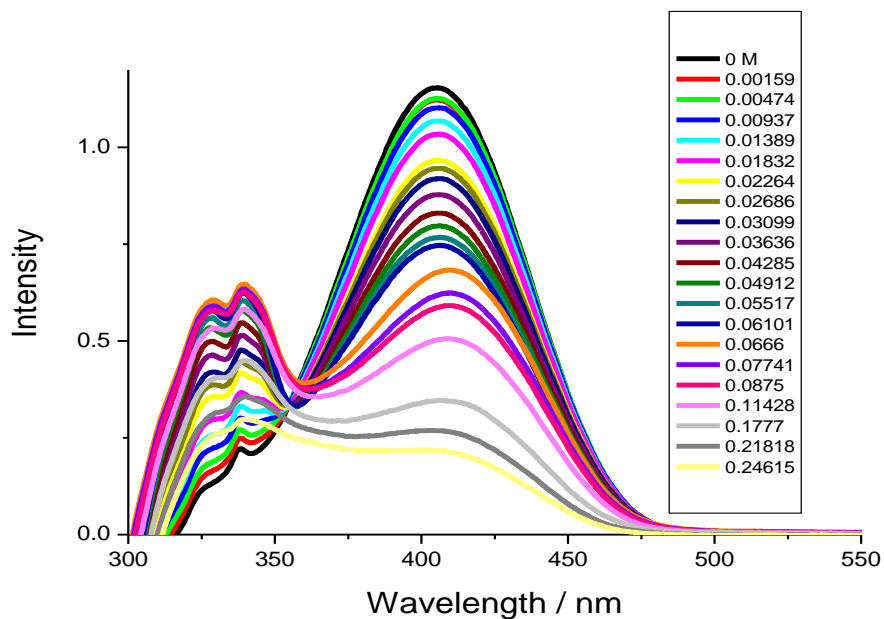


Figure 21. The absorption spectra of MBIC in different concentrations of HCl in dioxane.

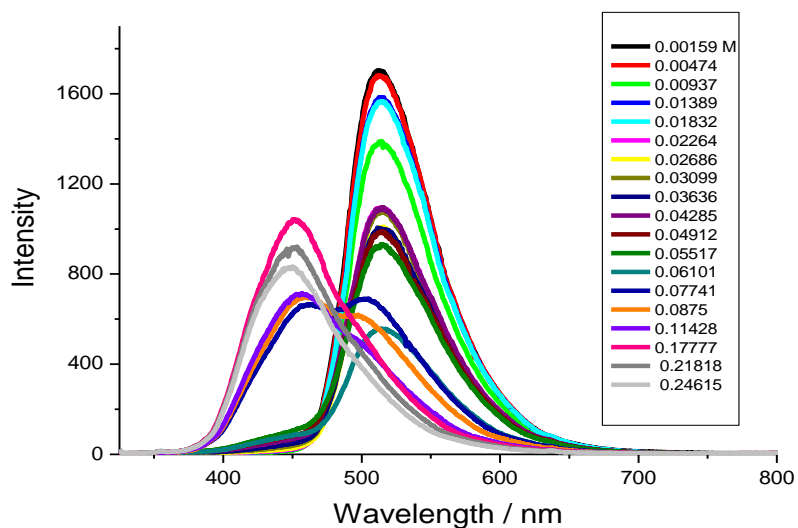


Figure 22. Fluorescence spectra of MBIC recorded in the presence of different concentrations of HCl in dioxane.

5.6 Photophysics of Crystalline MBIC

Quite similar absorption and fluorescence spectral profiles are observed from a single crystal of MBIC at room temperature when illuminated at 385 nm (Figure 23). The absorption spectrum for the

crystalline sample remains similar to that found in solution, in particular the strong intramolecular charge-transfer character is clearly evident, but a lower-energy band is seen at around 500 nm. This latter transition might be associated with Frenkel excitons,²⁶ which are often apparent with crystalline materials.²⁷ Charge-recombination fluorescence can be observed for the crystal, with a maximum centred at 557 nm. Relative to MBIC in solution, the emission profile recorded for the crystal is slightly narrower. This could be because of the absence of solvent stabilization. The fluorescence profile remains unchanged for a variety of excitation wavelengths but the spectral maximum is red-shifted compared to even the most polar solvent. Furthermore, dispersing crystals of MBIC in dried KBr powder, followed by pressing into a compact disc, gives rise to a similar spectrum. Indeed, the same profile is obtained from filter paper impregnated with micro-crystals of MBIC.

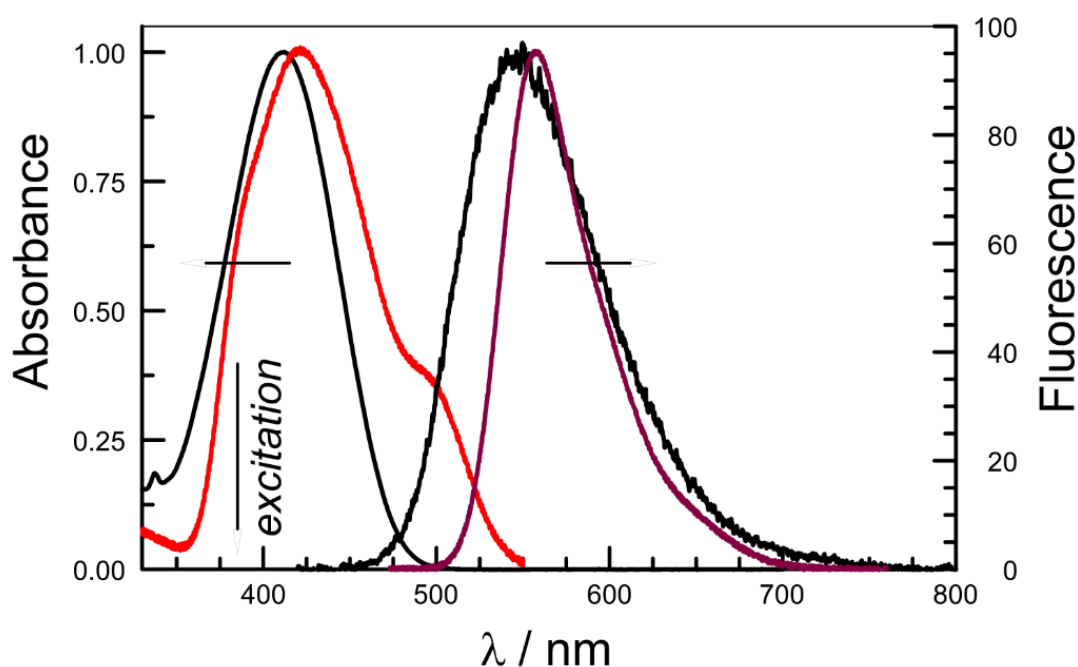


Figure 23. Comparison of the absorption and fluorescence spectra recorded for MBIC in ethanol solution (black curve) and for a single crystal of MBIC (grey curve) at room temperature. The vertical arrow represents the excitation wavelength used for emission studies.

The conclusion, therefore, is that MBIC emits charge-recombination fluorescence in the crystalline phase. While not unique,^{28,29} this behaviour is uncommon and attests to the fact that MBIC does not undergo substantial self-quenching in the solid matrix. A temperature dependence emission study carried out with a single crystal of MBIC indicates that the re-organization energy associated with charge-recombination is ca. $1,530 \text{ cm}^{-1}$ while the Huang-Rhys factor³⁰ is 0.50. The latter is fully consistent with the exciton being localized on a single molecule,³¹ rather than being spread over several aligned molecules within the lattice. The re-organization energy and Huang-Rhys factor are

small compared to typical values determined in solution but, as mentioned above, solvent stabilization is not possible in the crystal. The emission peak maximum does not change significantly (i.e., <5 nm) over a temperature variation from 20 to 200 °C.

The crystal structure exhibits stacking of the molecules via π - π interactions along the crystallographic [100] direction (a-axis). Molecules in the stack are arranged disk-like with a head-to-head orientation and are hence related to each other by a pure translation along the direction of the stack (Figure 24). A typical needle-like crystal of MBIC has a crystallographic density of 1.50 g/cm³. It is interesting to note that the alternative crystal structure, obtained by crystallization from acetic acid, has the MBIC molecules arranged in a head-to-head fashion (Figure 25). This is a remarkable variation in crystal structure, being caused solely by a change in the crystallizing medium, which is far from common in the field. It might be anticipated that, given the high molecular polarity of MBIC, the two morphologies will be subjected to quite disparate intermolecular dipole-dipole interactions. This, in turn, could lead to an unusual way to manipulate non-linear optical properties of the material.

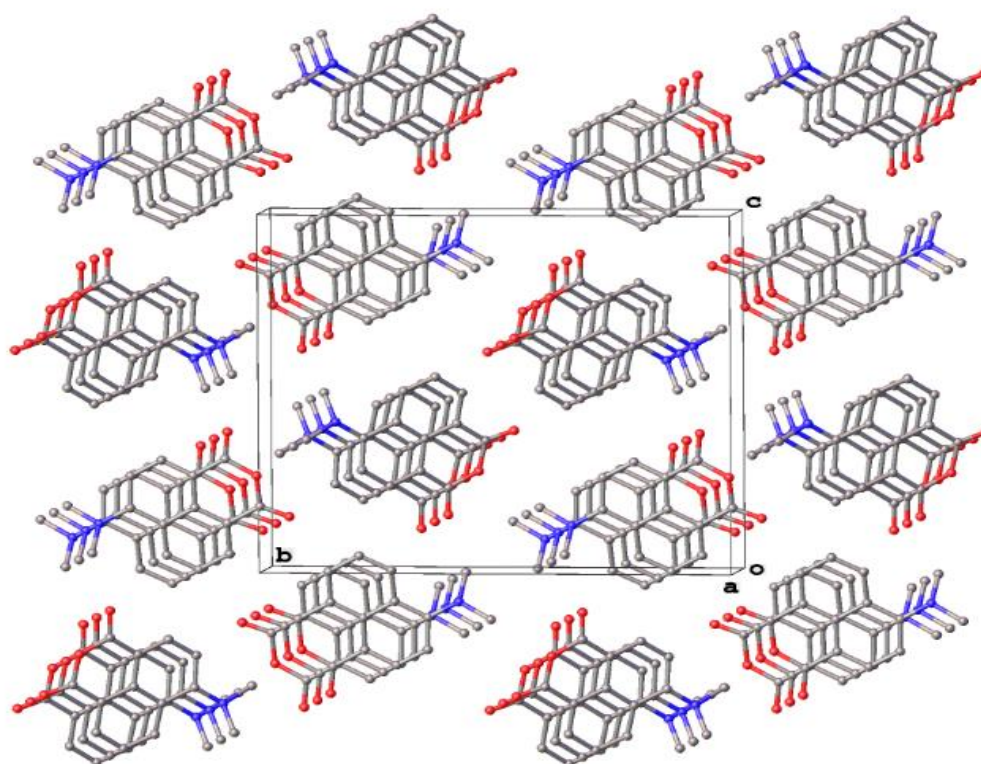




Figure 24. Crystal packing diagram determined for MBIC. The same packing is found after crystallization in the presence of Rh-B.

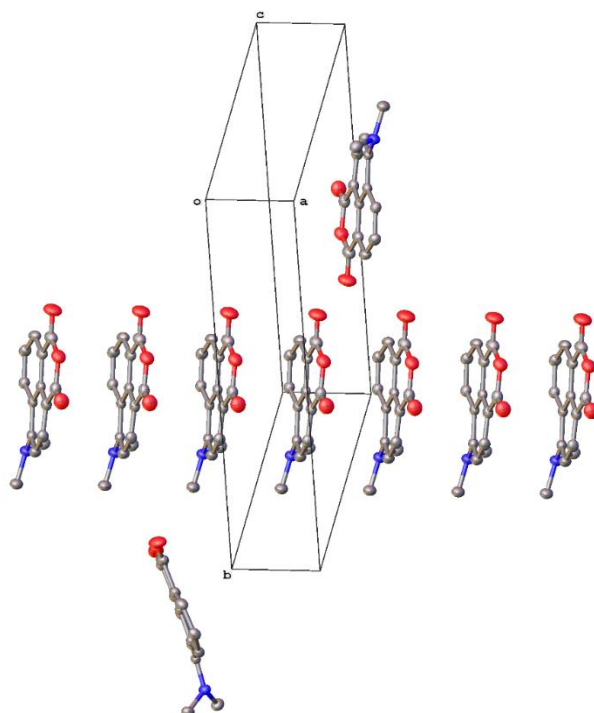


Figure 25. Crystal packing diagram for the second polymorph of MBIC, as obtained by recrystallization from acetic acid.

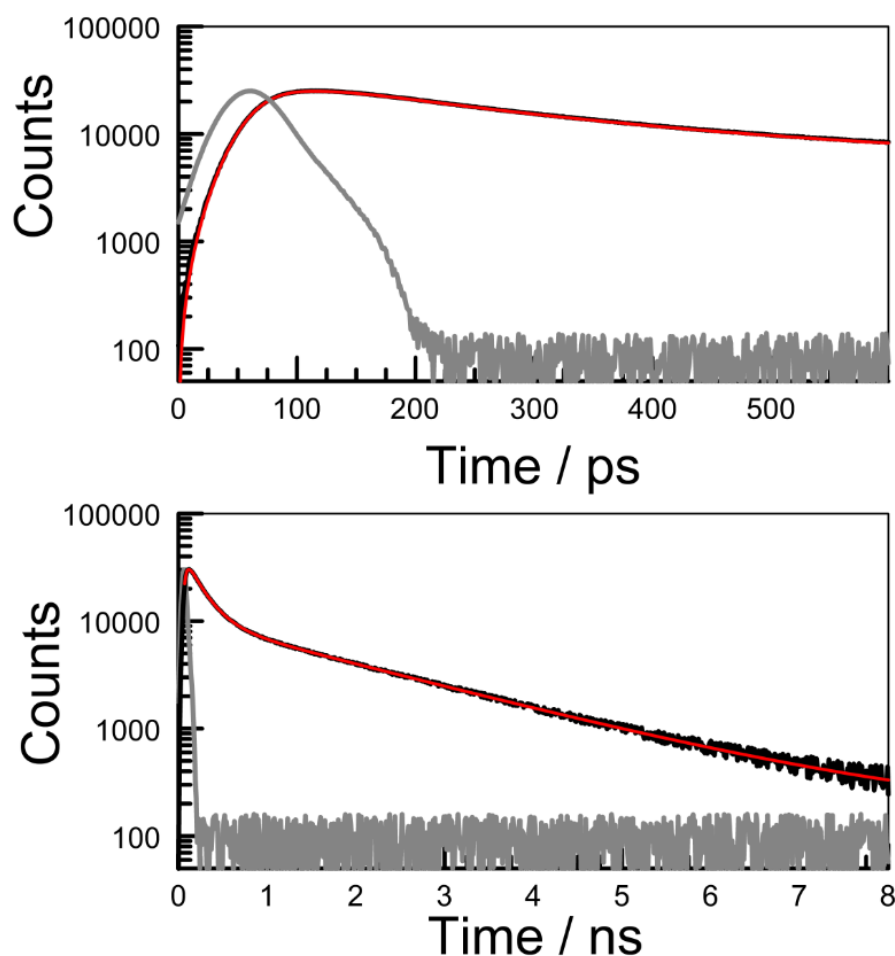


Figure 26. Examples of time-resolved fluorescence decay curves recorded for a single crystal of MBIC at room temperature. The curves refer to two different time bases. The instrument response function is shown as a grey curve while the best fit to a two-exponential decay process is shown as a light-grey curve running through the data points (black curve).

The emission quantum yield determined for a single crystal of MBIC using an integrating sphere was found to be 0.09. This is similar to the value expected for MBIC in a weakly polar environment, such as that provided by 2-MTHF. Time-resolved fluorescence studies following excitation at 370 nm with a short-duration (FWHM = 90 ps), pulsed LED are consistent with dual-exponential decay kinetics (Figure 26). The recovered lifetimes are 0.20 ± 0.08 ns (80%) and 2.0 ± 0.08 ns (20%). The fractional components do not change significantly with detection wavelength, at least over a modest range, and are independent of excitation wavelength. The longer lifetime was recovered reproducibly for different time ranges, count rates and total signal intensity. This was not the case for the short lifetime, which proved difficult to reproduce consistently, but its fractional contribution to the total signal remained around 80%. It appears that the shorter lifetime refers to a distribution of lifetimes having a mean value of around 0.2 ns. Indeed, the convoluted decay profiles

could be simulated using the maximum entropy method³² (MEM), together with the instrumental response function, to indicate a Gaussian-shaped distribution of lifetimes centred at 0.2 ns and with a variance of ± 0.05 ns together with a single lifetime of 2.0 ns. An example of this fitting routine is shown as Figure 27. The MEM analysis appears more robust than the dual-exponential model when considered over a range of time bases, although the latter gives acceptable statistical fits on a single time base.

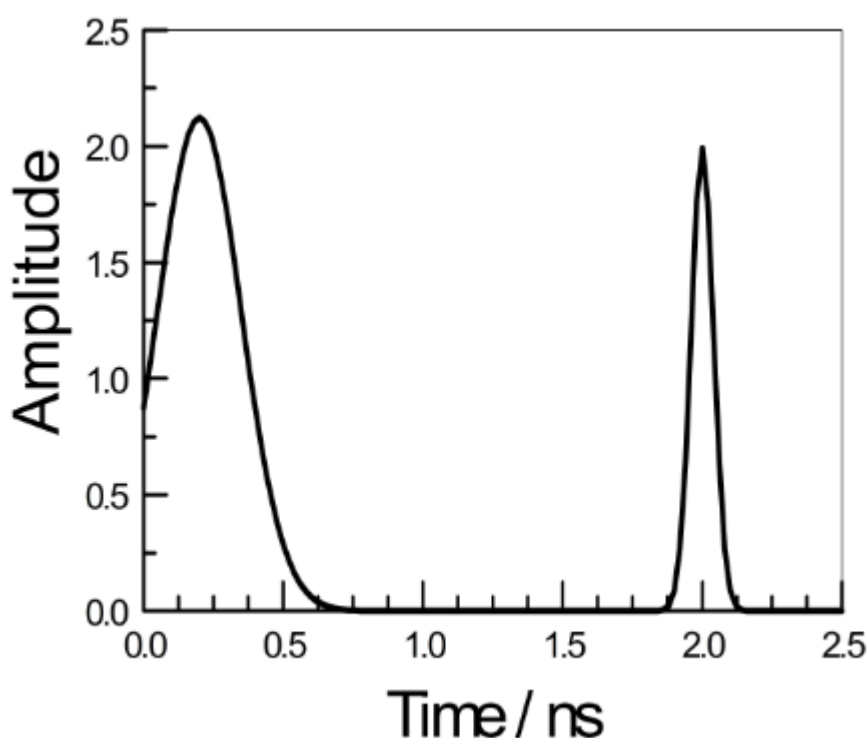


Figure 27. Maximum entropy method analysis of the time-resolved emission profile for a single crystal of MBIC. The analysis corresponds to a distribution of lifetimes centred at 0.2 ns and a single lifetime of 2.0 ns.

Our interpretation of this behaviour is that the crystal comprises MBIC molecules in two distinct environments. Since there are no obvious lattice irregularities, these two disparate localities most likely refer to bulk- and surface-bound molecules. On the basis that the longer lifetime (i.e., the smaller contribution) refers to surface states and that the radiative lifetime remains fixed for crystalline samples, it appears that most (i.e., ca. 75%) of the steady-state emission is associated with the surface. The occurrence of dual-exponential decay processes was recognized earlier for certain emissive quantum dots.^{33,34} Here, exciton migration occurs within the interior but the exciton becomes trapped as it approaches the surface, with the resultant surface-states decaying relatively slowly. We might anticipate comparable behaviour for crystalline MBIC.

Analysis of the X-ray structure denotes that the center-to-center separation between MBIC molecules aligned along the stack is only 3.8 Å. In contrast, the closest center-to-center distances between molecules in adjacent stacks are 9.0 and 9.75 Å. Because of the large Stokes' shift induced by the strong charge-transfer character, the spectral overlap integral ($J_{DA} = 3.25 \times 10^{-5} \text{ cm}$) for Förster-style excitation energy migration between neighboring MBIC molecules is relatively small.³⁵ Likewise, the transition dipole moment calculated³⁶ for MBIC in solution, computed to be 1.53 D, is kept modest by the weak oscillator strength. Nonetheless, this is offset to a large extent by the short separation distance and good dipole-dipole alignment between adjacent MBIC molecules in the stack. Indeed, it can be calculated³⁷ that the hopping time between stacked molecules is on the order of 0.3 ps. Taking the shorter of the two lifetimes as reflecting the bulk molecules, we can estimate that, on average, 50% of the excitons will undergo at least 400 hops before returning to the ground state while 10% will make at least 1,400 hops. Of course, any such migration will be incoherent and it should be stressed that the Coulombic mechanism³⁸ usually underestimates the hopping time at very short separations.³⁹ The mean time needed for an exciton to cross between stacks is 50 ± 8 ps. Thus, an exciton has only ca. 1% chance to pass to a nearby stack rather than migrate to the neighboring MBIC molecule along the same stack but, within its lifetime, we might expect the exciton to make at least four trans-stack jumps. Our observation that the shorter-lived species shows a distribution of survival times seems fully consistent with a variety of trapping rates reflecting the distance travelled prior to arrival at the surface states.

In separate experiments, MBIC was crystallized in the presence of a very small amount of Rhodamine B (Rh-B). The latter was chosen because, in solution phase, its absorption spectrum overlaps the emission profile of MBIC, it shows intense fluorescence and it has a flat shape not too dissimilar from that of MBIC. It was anticipated that Rh-B might intercalate into the MBIC stacks within the crystal. Indeed, the presence of Rh-B at very low doping levels does not perturb the crystal structure of MBIC as determined by X-ray crystallography but these studies did not define the location of the dopant. Likewise, the precise level of loading could not be defined although absorption spectroscopy carried out with dissolved crystals indicated that this was similar to that of the mixture before crystallization. The presence of Rh-B has no noticeable effect on the dimensions or colour of the crystal but does affect the emission spectral profile. At the very low loadings used here, it was not possible to detect Rh-B by optical absorption spectroscopy while the excitation spectrum recorded for emission associated with bound Rh-B corresponded to the absorption spectrum of crystalline MBIC. Washing the doped crystal with cold water before drying with warm N_2 serves the purpose of removing the fluorescence due to Rh-B. Under these conditions, the crystal remains intact and emits as described earlier while the aqueous solution shows characteristic fluorescence from Rh-B. The

impression, therefore, is that Rh-B is associated with surface-states of the emerging crystal rather than occupying a site within the MBIC stacks.

In ethanol solution, Rh-B exhibits sharp absorption ($\lambda_{\text{MAX}} = 545 \text{ nm}$) and fluorescence ($\lambda_{\text{FLU}} = 563 \text{ nm}$) spectra. The emission lifetime (τ_s) decreases with increasing concentration, as does the quantum yield, but reaches an upper limit of 2.8 ns at micro-molar concentrations. It has been reported that the absorption spectrum remains essentially unchanged⁴⁰ when Rh-B is adsorbed at sub-monolayer coverage onto ZnO crystals. In contrast, adsorption of Rh-B from water onto a quartz plate causes a modest red shift⁴¹ for both absorption ($\lambda_{\text{MAX}} = 558 \text{ nm}$) and emission ($\lambda_{\text{FLU}} = 576 \text{ nm}$) maxima while τ_s increases to 3.1 ns. Adsorption of Rh-B from aqueous solution onto the outer surface of a MBIC crystal gives rise to a broad fluorescence spectrum superimposed over the usual emission profile characterised for MBIC. This broad spectrum, the maximum for which moves progressively towards the blue with increasing contact time between Rh-B solution and the MBIC crystal, is assigned to aggregated dye on the surface of the crystal.⁴²

Doped crystals were illuminated at 385 nm, where Rh-B is unlikely to contribute to the absorption profile. The resultant fluorescence spectrum differs, albeit slightly, from that characterized for crystalline MBIC (Figure 28). In fact, the new spectrum can be reproduced reasonably well by a mixture of emission profiles for crystalline MBIC and for Rh-B adsorbed onto a quartz plate (Figure 28). For example, at a Rh-B loading of 5 ppm (i.e., 10 mols of Rh-B per million mols of MBIC or a molar ratio of 100,000 in favour of MBIC), the emission spectrum is nicely reproduced by allowing for 40% MBIC and 60% Rh-B (Figure 28). Furthermore, exact agreement between compiled and observed fluorescence spectra can be reached by slight shifting (i.e., 2-3 nm) of the Rh-B maximum wavelength but retaining an equivalent profile. The same situation is found for other loadings of Rh-B; in each case the observed spectrum being a supposition of individual spectra assigned to MBIC and Rh-B. Iterative reconstruction procedures based on global analysis data fitting⁴³ and assuming a two-component mixture allowed the fractional contribution (α) of Rh-B emission to the total spectrum to be determined (Table 2). It can be seen that there is a smooth correlation between α and the initial doping level, although saturation seems to occur at the higher loadings. Since direct excitation of Rh-B can be eliminated, the only reasonable explanation for these mixed spectra involves electronic energy transfer (EET) from MBIC to Rh-B occurring in the solid matrix.⁴⁴

Table 2. Emission properties recovered for the crystals of MBIC loaded with a minor amount of Rh-B.

Property	S0 ^[a]	S1	S2	S3	S4
Rh-B / mpm ^[b]	0	2.5	5	10	15
Φ_F	0.09	0.092	0.115	0.132	0.123
α [%] ^[c]	0	35	60	75	65
τ_1 (A_1) [ps]	0.20 (79.8)	0.14 (82.5)	0.18 (81.6)	0.10 (74.3)	0.18 (78.3)
τ_2 (A_2) [ns]	2.00 (20.2)	1.75 (13.7)	1.25 (10.3)	1.00 (14.7)	0.95 (12.4)
τ_3 (A_3) [ns]	NA	5.3 (3.8)	5.4 (8.1)	5.4 (11.0)	5.4 (9.3)

(a) Refers to sample number. Each sample size was 200 mg and each measurement was repeated ten times. (b) Loading of Rh-B expressed in terms of mols and converted to mols Rh-B per million mols of MBIC. (c) Fraction of emission yield assigned to Rh-B on the basis of spectral deconstruction into two overlapping spectra. (d) Excited-state lifetimes derived from the time-resolved emission decay curves following excitation at 370 nm. The fractional contribution at 575 nm, A , is given in parenthesis. For τ_1 , the quoted value is the mean of the distribution obtained from MEM analysis.

For the same samples, time-resolved fluorescence decay profiles required analysis as the sum of three-exponential terms (Figure 28); such analysis has to be undertaken with caution!⁴⁵ However, in the present case, a logical account of the complex kinetics could be reached as follows: One lifetime (τ_3) was found to be 5.4 ± 0.1 ns, which is somewhat longer than that ($\tau_5 = 3$ -4 ns) determined for Rh-B in a small range of solid samples.⁴¹ Furthermore, the fractional amplitude (A_3) for this particular component increased with increasing loading of Rh-B, until attaining a saturation level (Table 2). Thus, we assign the longest-lived component to emission from Rh-B, which we believe to be predominantly associated with the surface structure of the crystal. Support for this identification is nicely derived by comparison of time-resolved emission profiles recorded at early (i.e., 0.4-0.5 ns) and late (i.e., 4-5 ns) gate times after the excitation pulse (Figure 29). The early-gated spectrum resembles emission characteristic of the MBIC crystal while the late-gated profile closely resembles the spectrum recorded for Rh-B adsorbed onto quartz at sub-monolayer coverage.

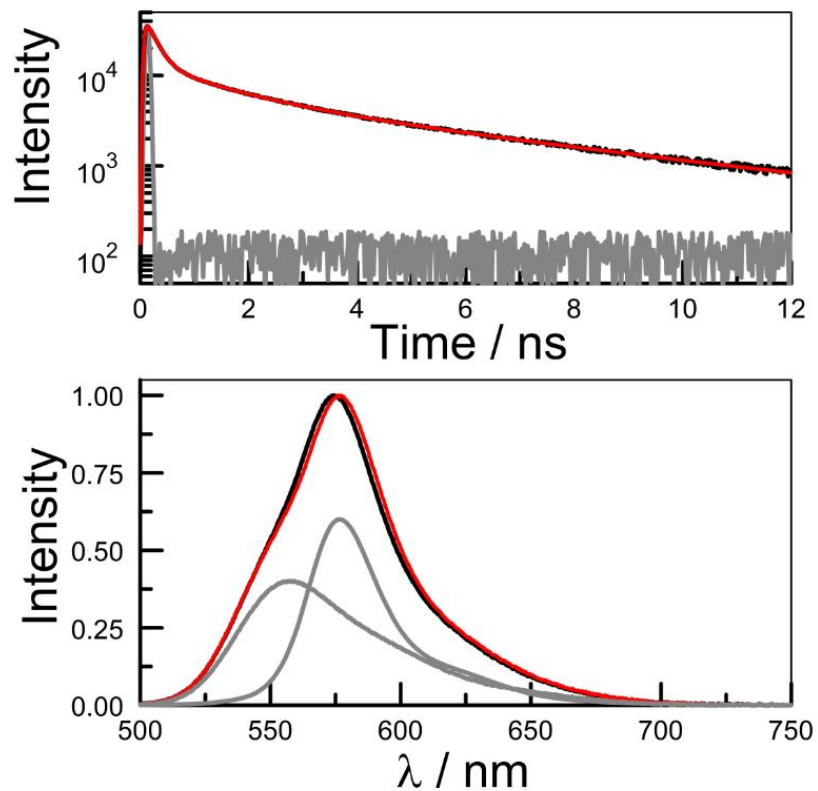


Figure 28. The lower panel shows the fluorescence spectrum recorded for a crystal of MBIC doped with Rh-B, at a loading of 5 mpmm, (black curve) and the reconstruction (light-grey curve) from components associated with crystalline MBIC (grey curve) and Rh-B adsorbed onto a quartz plate at sub-monolayer coverage (grey curve). The upper panel shows the time-resolved fluorescence decay profile recorded at 575 nm with the instrumental response function in grey, the experimental data as a black curve and the fit to the sum of three exponentials as a red curve.

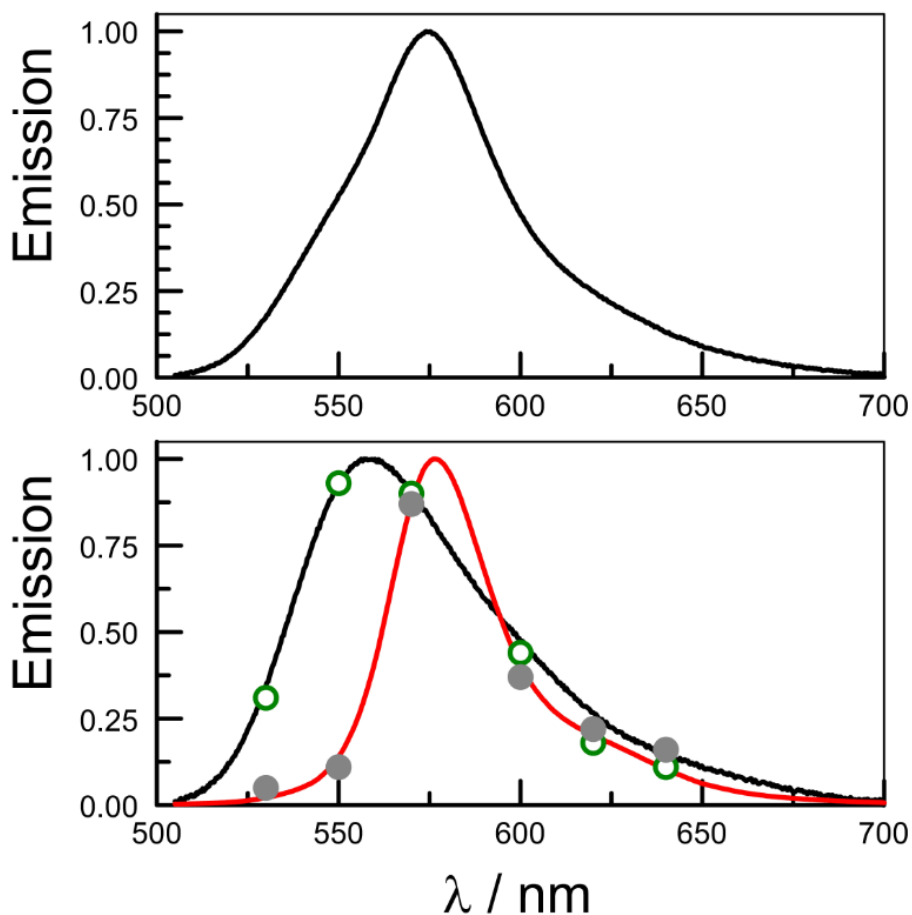


Figure 29. The upper panel shows the emission profile recorded for a single crystal of MBIC doped with Rh-B at a level of 5 mpm. The lower panel shows normalized time-resolved emission spectra recorded at 0.4-0.5 ns (open circles) and 4-5 ns (filled circles) gate times. The solid lines correspond to simulated spectra for pure MBIC (black curve) and a mixture of (15%) MBIC and (85%) Rh-B (grey curve).

The shortest lifetime (τ_1) shows the largest fractional contribution (A_1) and remains closely comparable to that assigned to MBIC molecules comprising aligned stacks within the interior of the crystal. As before, it proved difficult to obtain unique solutions for this lifetime when varying the count rate or the total signal accumulation. This behaviour is considered characteristic of a distribution of lifetimes⁴⁶ and is better reflected by the MEM analysis.⁴⁷ Fast exciton hopping between neighbouring MBIC molecules and across stacks appears to be unaffected by the presence of Rh-B. Again, this seems in keeping with the suggestion that most of the Rh-B resides in an amorphous region near the surface of the crystal.

The remaining lifetime (τ_2) is the only one that varies from sample to sample, decreasing progressively with increasing loading of Rh-B (Table 2). The ratio of fractional contributions made by τ_1 and τ_2 remains reasonably constant across the series while the magnitude of τ_2 is not too far removed from that attributed to surface-localized MBIC in the pure crystal. On this basis, we assign τ_2

to MBIC molecules comprising the surface layer and attribute the shortening of the lifetime to EET to Rh-B molecules also localized at the surface. This leads to the overall scheme illustrated by (Chart 1). Excitons generated within the interior of the crystal oscillate incoherently along the aligned stacks until approaching the surface states. Trapping occurs near to the surface so as to generate a longer-lived excited state of MBIC, presumably existing as a somewhat amorphous phase. Loading the MBIC crystal with Rh-B tends to localize the dopant at the surface, where it acts as an acceptor for excitons migrating slowly around the surface layer of MBIC. The model considers exciton trapping by surface-bound MBIC and surface-mediated EET to Rh-B to be irreversible steps.

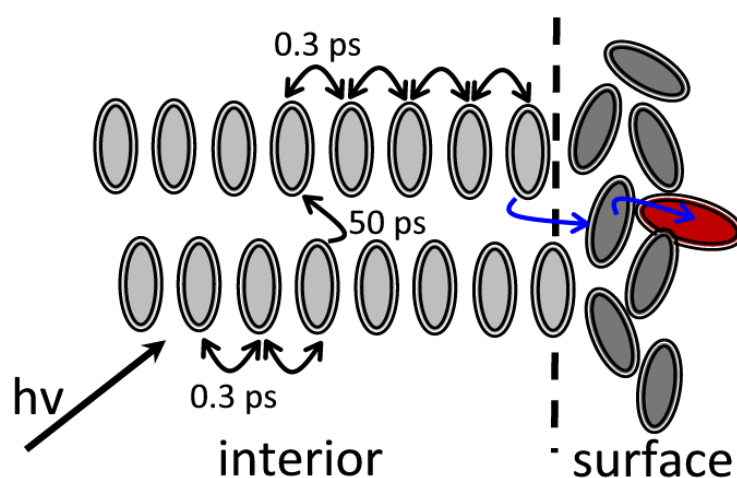


Chart 1. Pictorial representation of rapid exciton migration along and between stacks within the MBIC crystal (grey disk), followed by exciton trapping at surface-bound MBIC molecules (dark grey disk) and EET to the Rh-B dopant (light-grey disk with dark surround).

On the basis of this model, fluorescence from Rh-B is the consequence of energy migration within the MBIC stacks, trapping by surface-bound MBIC molecules and EET to ground-state Rh-B. The excitation spectrum recorded at an emission wavelength where Rh-B is expected to dominate the fluorescence profile, namely 580 nm (Figure 28), corresponds to absorption by MBIC but does not feature direct absorption by the dye. The time-resolved emission spectra recorded at early and late time gates provide further support for the notion that Rh-B fluorescence arises from secondary events. Using this information, it becomes clear that the derived lifetime of 5.4 ns for the Rh-B dopant is too long. Convolution of τ_3 with an exponential function with a lifetime corresponding to τ_2 , shortens the effective singlet-state lifetime of the dye to around 4 ns. This brings it more into expectation with an isolated Rh-B molecule in the solid state.

Even at the very low loadings of Rh-B employed here, there is the impression that saturation has been reached in as much as both the total emission and the fractional contribution attributed to Rh-B reach a maximum at around 10 ppm (Table 2). It is likely that self-association of Rh-B, or self-quenching, becomes important at the highest loading.⁴⁸ Under optimum conditions, about 50% of the MBIC fluorescence is quenched by the presence of a very low concentration of Rh-B. There is a compromise between increasing the level of quenching and avoiding self-association in the surface region but, under appropriate conditions, loading the crystal with Rh-B leads to a modest (i.e., ca. 50%) increase in the fluorescence quantum yield. This was not the case when Rh-B was replaced with Cresyl Violet;⁴⁹ here, there was no indication for association of the dye with the MBIC crystal and no EET from MBIC to Cresyl Violet.

The concept of multiple, linear EET events followed by trapping at a terminal is not new and was introduced successfully by Calzaferri⁵⁰ in the form of doped zeolites. Related theoretical studies^{51,52} have developed Monte-Carlo modelling algorithms to describe exciton migration and trapping in crystals and on the outer surfaces of micro-heterogeneous media.⁵³ Similar, but more spatially restricted, processes are known to occur with certain dendrimers⁵⁴ and organic clusters.^{55,56} Of course, exciton migration in photosynthetic light-harvesting antennae has been subjected to considerable experimental⁵⁷ and theoretical⁵⁸ investigation over many decades. For crystalline MBIC, our illumination studies were carried out at low irradiance such that only a single exciton is present on the crystal at any given moment. Allowing for a common radiative rate constant for both bulk and surface-bound MBIC, we can estimate that the latter accounts for about 2% of the total MBIC.

5.7 Conclusion

In conclusion, we have described a new type of photonic crystal that might have useful applications in the field of photon concentrators. By making use of an intramolecular charge-transfer system, we ensure a substantial Stokes' shift which minimizes self-absorption. The effective Stokes' shift is further extended by way of EET to the dopant, present at very low concentrations. By growing the crystal in the presence of dopant, as opposed to coating the surface of a fully grown crystal with dye, it becomes possible to increase the loading without aggregation. Even so, saturation is reached at a relatively low concentration of dopant. A further drawback of the present system concerns the modest spectral overlap integral⁵⁹ between absorption by Rh-B and emission from MBIC. This term needs to be increased markedly in order to optimize exciton trapping by the dopant.

5.8 References

1. Islam, A.; Cheng, C.-C.; Chi, S.- H.; Lee, S. J.; Hela, P. G.; Chen, I.- C.; Cheng, C.- H. *J. Phys. Chem. B*. **2005**, 109, 5509.
2. Hrdlovič, P.; Chmela, Š.; Danko, M. *J. Photochem. Photobiol. A: Chem.* **1998**, 112, 197.
3. Sasaki, S.; Drummen, G. P. C.; Konishi, G.-I. *J. Mater. Chem. C*. **2016**, 4, 2731.
4. Grabowski, Z. R.; Rotkiewicz, K. *Chem. Rev.* **2003**, 103, 3899; Johnson, G. E.; Limburg, W. *J. Phys. Chem.* **1984**, 88, 2211; Rotkiewicz, K.; Grellmann, K.H.; Grabowski, Z. R. *Chem. Phys. Lett.* **1973**, 19, 315.
5. Englman, R.; Jortner, J. *Mol. Phys.* **1970**, 18, 145.
6. Brun, A. M.; Harriman, A.; Tsuboi, Y.; Okada, T.; Mataga, N. *J. Chem. Soc. Faraday Trans.* **1995**, 91, 4047; Hu, R.; Lager, E.; Aguilar- Aguilar, A.; Liu, J.; Lam, J. W. Y.; Sung, H. H. Y.; Williams, I. D.; Zhong, Y.; Wong, K. S.; Pěna- Cabrera, E.; Tang, B. Z. *J. Phys. Chem. C*. **2009**, 113, 15845.
7. Banerjee, S.; Kitchen, J. A.; Gunnlaugsson, T.; Kelly, J. M. *Org. Biomol. Chem.* **2013**, 11, 5642; Kilpin, K. J.; Clavel, C. M.; Edafe, F.; Dyson, P. J. *Organometallics*. **2012**, 31, 7031.
8. Zhang, Y.- Q.; Wang, J.- X.; Ji, Z.- Y.; Hu, W.- P.; Jiang, L.; Song, Y.- L.; Zhu, D.- B. *J. Mater. Chem.* **2007**, 17, 90.
9. Moré, R.; Busse, G.; Hallmann, J.; Paulmann, C.; Scholz, M.; Techert, S. *J. Phys. Chem. C*. **2010**, 114, 4142; Kihara, H.; Yoshida, M. *IOP Conf. Ser.: Mater. Sci. Eng.* **2014**, 54, 012020.
10. Smith, M. B.; Michl, J. *Chem. Rev.* **2010**, 110, 6891.
11. Zimmerman, P. M.; Zhang, Z.; Musgrave, C. B. *Nat. Chem.* **2010**, 2, 648.
12. Wilson, M. W. B.; Rao, A.; Johnson, K.; Gélinas, S.; Pietro, R. D.; Clark, J.; Friend, R. H. *J. Am. Chem. Soc.* **2013**, 135, 16680.
13. Ghosh, S.; Biswas, S.; Mondal, M.; Basu, S. *J. Lumin.* **2014**, 145, 410.
14. Schuddeboom, W.; Jonker, S. A.; Warman, J. M.; Leinhos, U.; Kühnle, W.; Zachariasse, K. *J. Phys. Chem.* **1992**, 96, 10809.
15. Harriman, A.; Hissler, M.; Zissel, R. *Phys. Chem. Chem. Phys.* **1999**, 1, 4203.
16. Rauf, M. A.; Soliman, A. A.; Khattab, M. *Chem. Cent. J.* **2008**, 2, 1.
17. Saha, S.; Samanta, A. *J. Phys. Chem. A*. **2002**, 106, 4763; Dhar, S.; Roy, S. S.; Rana, D. K.; Bhattacharya, S.; Bhattacharya, S.; Bhattacharya, S. C. *J. Phys. Chem. A*. **2011**, 115, 2216; Patra, D.; Barakat, C. *Spectrochim. Acta, Part A*. **2011**, 79, 1034.
18. Lippert, V. E. *Z. Naturforsch. Sect. A*. **1955**, 10a, 541; Mataga, N.; Kaifu, Y.; Koizumi, M. *Bull. Chem. Soc. Jpn.* **1956**, 29, 465.

19. Ventura, B.; Bertocco, A.; Braga, D.; Catalano, L.; Agostino, S. D'; Grepioni, F.; Taddei, P. *J. Phys. Chem. C* **2014**, 118, 18646.
20. Dias, F. B.; Penfold, T. J.; Monkman, A. P. *Methods Appl. Fluoresc.* **2017**, 5, 012001.
21. McGlynn, S. P.; Reynolds, M. J.; Daigre, G. W.; Christodouleas, N. D. *J. Phys. Chem.* **1962**, 66, 2499.
22. Milischuk, A.; Matyushov, D. V. *J. Phys. Chem. A* **2002**, 106, 2146; Onsager, L. *J. Phys. Chem.* **1939**, 43, 189; Wilson, J. N. *Chem. Rev.* **1939**, 25, 377.
23. Bixon, M.; Jortner, J.; Cortes, J.; Heitele, H.; Michel-Beyerle, M. E. *J. Phys. Chem.* **1994**, 98, 7289.
24. Bixon, M.; Jortner, J.; Verhoeven, J. W. *J. Am. Chem. Soc.* **1994**, 116, 7349.
25. Kober, E. M.; Caspar, J. V.; Lumpkin, R. S.; Meyer, T. J. *J. Phys. Chem.* **1986**, 90, 3722.
26. Hoffmann, M.; Schmidt, K.; Fritz, T.; Hasche, T.; Agranovich, V. M.; Leo, K. *Chem. Phys.* **2000**, 258, 73.
27. Plötz, P.- A.; Niehaus, T.; Kühn, O. *J. Chem. Phys.* **2014**, 140, 174101-1; Liao, Y.; Génot, V.; Méallet-Renault, R.; Vu, T. T.; Audibert, J.- F.; Lemaistre, J.- P.; Clavier, G.; Retailleau, P.; Pansu, R. B. *Phys. Chem. Chem. Phys.* **2013**, 15, 3186.
28. Miniewicz, A.; Palewska, K.; Sznitko, L.; Lipinski, J. *J. Phys. Chem. A* **2011**, 115, 10689.
29. He, X.; Benniston, A. C.; Saarenpää, H.; Lemmetyinen, H.; Tkachenko, N. V.; Baisch, U. *Chem. Sci.* **2015**, 6, 3525.
30. Jong, M. D.; Seijo, L.; Meijerink, A.; Rabouw, F. T. *Phys. Chem. Chem. Phys.* **2015**, 17, 16959.
31. Baderschneider, S.; Scherf, U.; Köhler, J.; Hildner, R. *J. Phys. Chem. A* **2016**, 120, 233.
32. Vinogradov, S. A.; Fernandez-Searra, M. A.; Dugan, B. W.; Wilson, D. F. *Rev. Sci. Instrum.* **2001**, 72, 3396.
33. Wuister, S. F.; Donegá, C. D. M.; Meijerink, A. *J. Phys. Chem. B* **2004**, 108, 17393.
34. Tang, J.; Marcus, R. A. *J. Chem. Phys.* **2005**, 123, 204511-1.
35. Harriman, A.; Alamiry, M. A. H.; Hagon, J. P.; Hablot, D.; Ziessel, R. *Angew. Chem. Int. Ed.* **2013**, 52, 6611; *Angew. Chem.* **2013**, 125, 6743.
36. Alden, R. G.; Johnson, E.; Nagarajan, V.; Parson, W. W.; Law, C. J.; Cogdell, R. G. *J. Phys. Chem. B* **1997**, 101, 4667.
37. Förster, V. T. *Ann. Phys.* **1948**, 437, 55.
38. Saini, S.; Singh, H.; Bagchi, B. *J. Chem. Sci.* **2006**, 118, 23; Ziessel, R.; Alamiry, M. A. H.; Elliott, K. J.; Harriman, A. *Angew. Chem. Int. Ed.* **2009**, 48, 2772; *Angew. Chem.* **2009**, 121, 2810; Krueger, B. P.; Scholes, G. D.; Fleming, G. R. *J. Phys. Chem. B* **1998**, 102, 5378.

39. Hedley, G. J.; Ruseckas, A.; Benniston, A. C.; Harriman, A.; Samuel, I. D. W. *J. Phys. Chem. A*. **2015**, 119, 12665.
40. Spitler, M.; Calvin, M. *J. Chem. Phys.* **1977**, 67, 5193.
41. Kemnitz, K.; Tamai, N.; Yamazaki, I.; Nakashima, N.; Yoshihara, K. *J. Phys. Chem.* **1986**, 90, 5094.
42. Fujii, T.; Nishikiori, H.; Tamura, T. *Chem. Phys. Lett.* **1995**, 233, 424.
43. Laurence, T. A.; Chromy, B. A. *Nat. Methods*. **2010**, 7, 338.
44. Nichols, J. W.; Pagano, R. E. *Biochemistry*. **1982**, 21, 1720.
45. Istratov, A. A.; Vyvenko, O. F. *Rev. Sci. Instrum.* **1999**, 70, 1233.
46. Siemiarczuk, A.; Wagner, B. D.; Ware, W. R. *J. Phys. Chem.* **1990**, 94, 1661.
47. Vincent, M.; Gallay, J.; Demchenko, A. P. *J. Phys. Chem.* **1995**, 99, 14931.
48. Arbeloa, F. L.; Ojeda, P. R.; Arbeloa, I. L. *J. Lumin.* **1989**, 44, 105.
49. Magde, D.; Brannon, J. H.; Cremers, T. L.; III, J. O. *J. Phys. Chem.* **1979**, 83, 696.
50. Calzaferri, G.; Huber, S.; Maas, H.; Minkowski, C. *Angew. Chem. Int. Ed.* **2003**, 42, 3732; *Angew. Chem.* **2003**, 115, 3860.
51. Singh, J.; Bittner, E. R.; Beljonne, D.; Scholes, G. D. *J. Chem. Phys.* **2009**, 131, 194905-1; Stehr, V.; Engels, B.; Deibel, C.; Fink, R. F. *J. Chem. Phys.* **2014**, 140, 024503-1.
52. Minkowski, C.; Pansu, R.; Takano, M.; Calzaferri, G. *Adv. Funct. Mater.* **2006**, 16, 273; Sigal, H.; Markovitsi, D.; Gallos, L. K.; Argyrakis, P. *J. Phys. Chem.* **1996**, 100, 10999.
53. Thompson, W. H. *J. Chem. Phys.* **2002**, 117, 6618.
54. Adronov, A.; Gilat, S. L.; Fréchet, J. M. J.; Ohta, K.; Neuwahl, F. V. R.; Fleming, G. R. *J. Am. Chem. Soc.* **2000**, 122, 1175.
55. Nakamura, Y.; Aratani, N.; Osuka, A. *Chem. Soc. Rev.* **2007**, 36, 831; Li, J.; Ambroise, A.; Yang, S. I.; Diers, J. R.; Seth, J.; Wack, C. R.; Bocian, D. F.; Holten, D.; Lindsey, J. S. *J. Am. Chem. Soc.* **1999**, 121, 8927; Giacalone, F.; Segura, J. L.; Martín, N.; Ramey, J.; Guldi, D. M. *Chem. Eur. J.* **2005**, 11, 4819.
56. Ziessel, R.; Harriman, A. *Chem. Commun.* **2011**, 47, 611; Harriman, A.; Mallon, L. J.; Elliot, K. J.; Haefele, A.; Ulrich, G.; Ziessel, R. *J. Am. Chem. Soc.* **2009**, 131, 13375; Wagner, R. W.; Johnson, T. E.; Lindsey, J. S. *J. Am. Chem. Soc.* **1996**, 118, 11166.
57. Grondelle, R. V.; Novoderezhkin, V. I. *Phys. Chem. Chem. Phys.* **2006**, 8, 793; Chachisvilis, M.; Kühn, O.; Pullerits, T.; Sundström, V. *J. Phys. Chem. B*. **1997**, 101, 7275; Tiwari, V.; Peters, W. K.; Jonas, D. M. *Proc. Natl. Acad. Sci. USA*. **2013**, 110, 1203.

58. Ishizaki, A.; Fleming, G. R. *Proc. Natl. Acad. Sci. USA*. **2009**, 106, 17255; Adolphs, J.; Renger, T. *Biophys. J.* **2006**, 91, 2778; Beljonne, D.; Curutchet, C.; Scholes, G. D.; Silbey, R. J. *J. Phys. Chem. B*. **2009**, 113, 6583.
59. Sumi, H. *J. Phys. Chem. B*. **1999**, 103, 252.

Table 1. Summary of the photo-physical properties determined for MBIC in a range of organic solvents at room temperature.

Solvent	$\epsilon_s^{[a]}$	λ_{ABS} [nm]	ν_{ABS} [cm ⁻¹]	λ_{FLU} [nm]	ν_{FLU} [cm ⁻¹]	Φ_F	τ_s [ns]	K_{RAD} [10 ⁷ s ⁻¹] ^[b]	K_{NR} [10 ⁷ s ⁻¹] ^[c]	Δ_{SS} [cm ⁻¹]
CHX ^[d]	2.02	392	25510	465	21505	1.00	10.5	9.5	0.02	4004
BENZ ^[e]	2.27	409	24449	503	19880	0.95	10.6	9.0	0.43	4569
DIOX ^[f]	2.27	405	24691	514	19455	0.67	8.7	7.7	3.79	5236
TOL ^[g]	2.43	407	24570	502	19920	0.87	10.3	8.5	1.20	4649
Bu ₂ O ^[h]	3.18	399	25062	494	20242	0.90	9.5	9.5	1.02	4819
Et ₂ O ^[i]	4.42	403	24813	504	19841	0.95	8.2	10.0	2.19	4972
CHCl ₃	4.89	420	23809	509	19646	0.63	7.3	8.6	5.09	4163
BuOAc ^[j]	5.01	409	24449	517	19342	0.30	4.1	7.3	17.09	5107
PhCl ^[k]	5.74	418	23923	510	19607	0.13	2.7	4.8	32.23	4315
PrOAc ^[l]	6.00	410	24390	519	19267	0.066	1.5	4.4	62.26	5122
EtOAc ^[m]	6.03	412	24271	522	19157	0.057	1.4	4.1	67.32	5114
2MTHF ^[n]	6.97	409	24449	515	19417	0.088	1.8	4.9	50.65	5032
THF ^[o]	7.47	414	24154	524	19083	0.075	1.5	5.0	61.66	5070
DCM ^[p]	8.93	423	23640	519	19267	0.040	0.80	5.0	120.0	4372
OcOH ^[q]	10.30	418	23923	533	18761	0.055	0.88	6.3	107.33	5161
1,2- DCE ^[r]	10.74	424	23584	524	19083	0.023	0.75	3.1	130.23	4500
BuOH ^[s]	17.5	422	23696	540	18518	0.020	0.67	3.0	146.25	5178
ACE ^[t]	21.36	419	23866	536	18656	0.0055	0.55	1.0	180.81	5209
EtOH ^[u]	24.50	421	23752	550	18181	0.012	0.64	1.9	154.35	5571
BuCN ^[v]	24.56	422	23696	538	18587	0.016	0.72	2.2	136.68	5109
CH ₃ CH ₂ CN	28.86	422	23696	540	18518	0.012	0.48	2.5	205.83	5178
CH ₃ OH	32.7	422	23696	542	18450	0.010	0.40	2.5	247.50	5246
CH ₃ CN	35.94	425	23529	545	18348	0.0055	0.25	2.2	397.80	5180
DMF ^[w]	37.06	428	23364	550	18181	0.0040	0.17	2.4	585.83	5182
PC ^[x]	62.93	428	23364	545	18348	0.0035	0.18	1.9	553.65	5015

[a] Static dielectric constant, taken from literature compilations. [b] Radiative rate constant. [c] Nonradiative rate constant. [d] Cyclohexane. [e] Benzene. [f] 1,4- Dioxane. [g] Toluene. [h] Di-n-butyl ether. [i] Diethyl ether. [j] Butyl acetate. [k] Chloro benzene. [l] Propyl acetate. [m] Ethyl acetate. [n]. 2-Methyltetrahydrofuran. [o] Tetrahydrofuran. [p] Dichloro methane. [q] Octan-1-ol.[r] 1,2-Dichloroethane.[s] Butan-1-ol. [t] Acetone. [u] Ethanol. [v] Butyronitrile. [w] Dimethyl formamide. [x] Propylene carbonate.

Chapter 6.

Photochemical Bleaching of Certain Non-toxic Dyes in Aqueous Solution



SUPPOSEDLY NON-TOXIC DYES ARE COMMONLY ADDED TO FOODSTUFFS TO MAKE THE PRODUCTS APPEAR MORE ATTRACTIVE.

6.1 Introduction

Organic dyes^{1,2} are useful colourants for a variety of applications, ranging from cosmetics to printing inks and to anti-counterfeit devices. Historically, such dyes were selected for the strength and range of their colours and many, for example indigo, have played an important role in shaping our lifestyle.³ More recently there has been a move towards identifying non-toxic dyes that dissolve readily in water.^{4,5} These latter compounds are highly attractive to the food industry⁶ and are popular with artists, while being valuable agents for bio-conjugation.^{7,8} A major concern for all organic dyes relates to their likely instability under prolonged exposure to visible light. Indeed, photo-degradation can be a serious limitation for certain classes of dye,⁹ although engineering (e.g., the omission of molecular oxygen and introduction of screens or filters) can provide important levels of relief. Despite the practical inconvenience of dye photo-fading, there have been relatively few detailed studies describing the kinetics of light-induced degradation under controlled conditions.¹⁰⁻¹⁵ Such studies might be complicated by auto-catalysis¹⁶ and invariably require multiple numbers of photons for complete bleaching of an individual molecule. Mechanistic studies are especially difficult in those cases where the quantum yields are very low. It might be mentioned that the photo-fading process is used routinely for measuring diffusion coefficients via Fluorescence Recovery After Photo-bleaching (FRAP).¹⁷

Here, we report on the photochemical degradation of some well-known non-toxic dyes in aqueous solution. Erythrosine is a water-soluble, cherry-pink dye with a long tradition as a food colourant.¹⁸ It is commonly used in fruit cocktails but has additional applications in printing ink, as a sensitizer for orthochromic photographic plates, and as a biological stain.¹⁹ Phloxine-B is quite similar to Erythrosine but provides a different colour when dissolved in water. Our interest in these two compounds stems from their known ability to function as a triplet state photo-sensitizer in water. Indeed, Xanthene dyes^{20,21} in general are promising sensitizers for antimicrobial studies^{22,23} because of their relatively low toxicity, high triplet energies, high triplet state quantum yields and relatively long triplet lifetimes. The interest in killing bacteria by way of photodynamic therapy²⁴ has led to further development of new sensitizers. Some of these reagents look highly promising but would be subject to lengthy clinical and legislative regulation. More immediate benefits could arise from the employment of compounds, such as Erythrosine, already used routinely in the food industry. To complete the series, we consider the photodegradation of Riboflavin. This latter compound is non-toxic and therefore could be a useful photosensitizer for systems where the safety of the operators is an issue.

One aspect of these photosensitizers, often overlooked in the search for optimum performance, is the need to eliminate the compound from the system at the conclusion of the process. This can be done most conveniently by photochemical means since the system is already under illumination. In turn, this situation demands a detailed understanding of the photo-fading kinetics such that destruction of the sensitizer occurs only on completion of the desired photochemistry. Optimization of the sensitizer concentration is a key requisite in the challenge to achieve optimal performance in terms of product yield and dye depletion. When sunlight is used to drive the reactions, this being the only sustainable way to promote largescale photochemistry, the temperature of the aqueous reservoir will increase markedly during the reaction. Hence the need to measure activation parameters for the photo-fading processes. Such studies are rare.

6.2 Erythrosine

6.2.1 Background

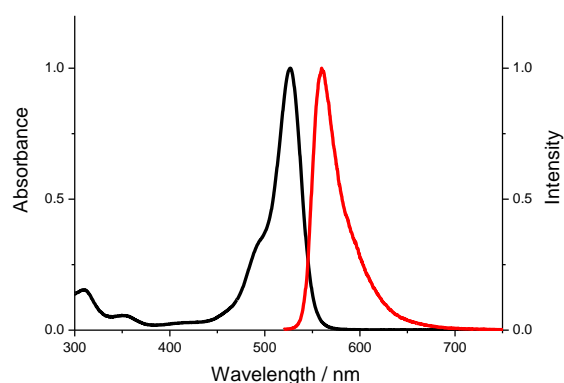
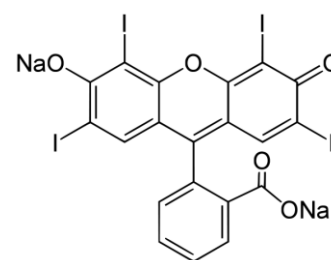


Figure 1. Absorption (black curve) and fluorescence (red curve) spectra recorded for Erythrosine in aqueous solution.



This study is part of a collaboration with Joshua Karlsson and Owen Woodford of the Molecular Photonics Laboratory. A paper has been prepared for publication and is given at the end of the chapter. Here, we present only a brief summary before moving to other compounds.

In water, Erythrosine exhibits an absorption maximum at 530 nm, with a molar absorption coefficient at the peak of $75,000 \text{ M}^{-1} \text{ cm}^{-1}$, and shows weak fluorescence centred at 550 nm (Figure 1). The compound follows Beer's law over a wide concentration range, covering that relevant to this work, in water. The fluorescence quantum yield in dilute aqueous solution is 3% while the excited-singlet state lifetime is $0.25 \pm 0.05 \text{ ns}$. The corresponding triplet-excited state can be detected readily by transient absorption spectroscopy following laser excitation at around 520 nm (see later). At low laser intensity, the triplet state decays via first-order kinetics with a lifetime of ca. $150 \mu\text{s}$ in the absence of molecular oxygen. This latter species shortens the triplet lifetime, the

corresponding bimolecular rate constant being $1.4 \times 10^9 \text{ M}^{-1} \text{ s}^{-1}$ for aqueous solution at 20°C . The product of this interaction is singlet molecular oxygen ($\text{O}_2(^1\Delta_g)$), formed via electronic energy transfer, although superoxide ions might also be formed in low yield under some conditions.

The quantum yield²⁵ for formation of $\text{O}_2(^1\Delta_g)$ in air-saturated D_2O is 0.68 at 20°C under conditions where the triplet quantum yield ($\Phi_T = 0.97$) is close to unity. Singlet molecular oxygen, which has a lifetime of ca. $4 \mu\text{s}$ in H_2O ,²⁶ can attack Erythrosine to initiate the bleaching process.²⁷ Here, we address the kinetics of the photo-fading reaction and, in particular, consider the effects of temperature and chromophore concentration on the rate of dye degradation. To the best of our knowledge, there are no reports in the scientific literature describing the activation parameters associated with photo-bleaching of an organic dye.

There have been several earlier reports²⁸⁻³¹ of the photo-bleaching of Xanthene dyes in water but few quantitative details are available. Consequently, preliminary studies were made to assess the significance of photo-bleaching by exposing an air-equilibrated, aqueous solution of Erythrosine to white light. Under such conditions, the main absorption transition centred at 530 nm bleaches. There are no coloured products but absorption spectroscopy indicates the build-up of one or more species absorbing in the near-UV region (Figure 2). These latter products, which are either formed in low yield or possess a weak molar absorption coefficient, are relatively stable towards further illumination. After saturating the solution with N_2 , the photo-bleaching process is much less evident but still proceeds at a measurable rate (Figure 3). Laser flash photolysis studies carried out in deaerated aqueous solution have shown³² that the rate of decay of the triplet-excited state increases with increasing concentration of Erythrosine. The bimolecular rate constant for this reaction, which is a type of self-quenching process, is $4 \times 10^8 \text{ M}^{-1} \text{ s}^{-1}$. This situation is far from uncommon³³ and could be the reason why photo-fading occurs in the absence of molecular oxygen. In air-equilibrated solution at the highest substrate concentration used here, self-quenching will account for less than 3% of the total triplet-state population.

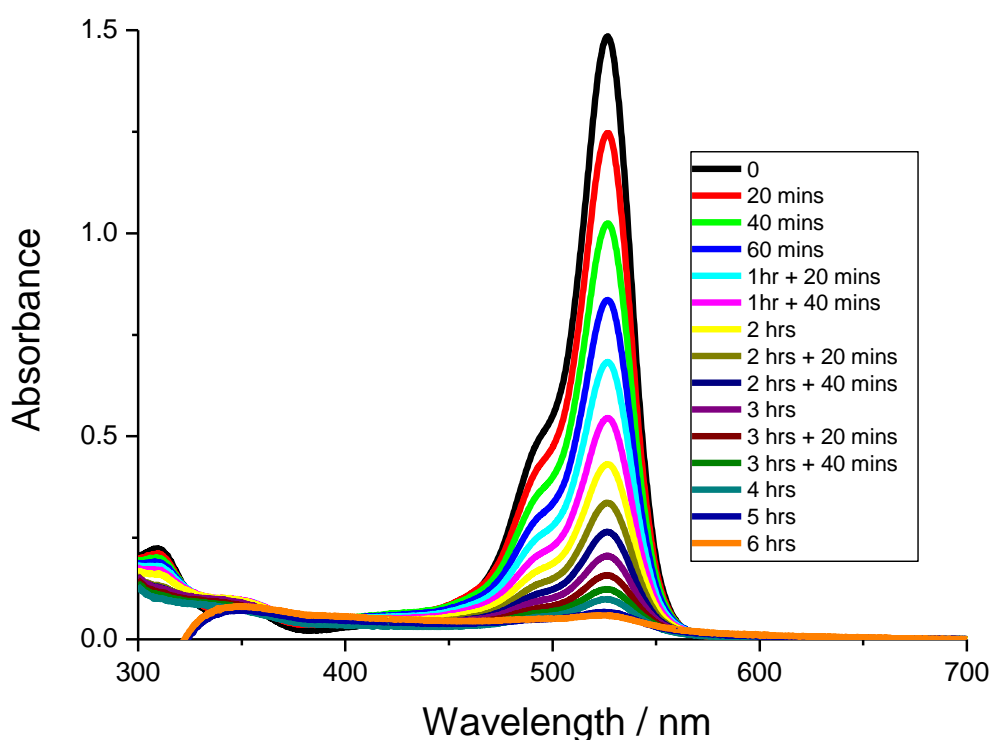


Figure 2. Absorption spectra recorded during the broadband (i.e., white light) steady-state irradiation of a solution of Erythrosine in air-equilibrated water. The chromophore undergoes stepwise bleaching.

The usual consequence of attack by $O_2(^1\Delta_g)$ on an aryl heterocycle in solution is an endoperoxide.³⁴ In water, this latter species will re-arrange to form stable products derived from substitution at the hydroperoxide group.^{35,36} For Erythrosine, it was found that a partially bleached solution formed an instantaneous precipitate on treatment with $AgNO_3$ solution. It was observed, however, that the addition of KI (ca. 1 mM) to a solution of Erythrosine in aerated H_2O has essentially no effect on the rate of photo-bleaching, although iodide is known to quench singlet molecular oxygen.^{37,38} Examination of partially bleached solutions of Erythrosine in D_2O by 1H - and ^{13}C -NMR spectroscopy did not provide conclusive information regarding the site of attack. We thank Dr Corinne Wills and Prof William McFarlane for making these NMR measurements.

In the absence of molecular oxygen, Erythrosine bleaches slowly under broadband illumination (Figure 3). The same kind of fading of the absorption spectral profile occurs and there are no obvious coloured products. Although it is impossible to eliminate traces amounts of oxygen from the system, it seems unlikely that bleaching under these conditions can be attributed to reactions of singlet oxygen. The relative rates of photo-bleaching are compared in Figure 4 for aerated and deaerated aqueous solutions.

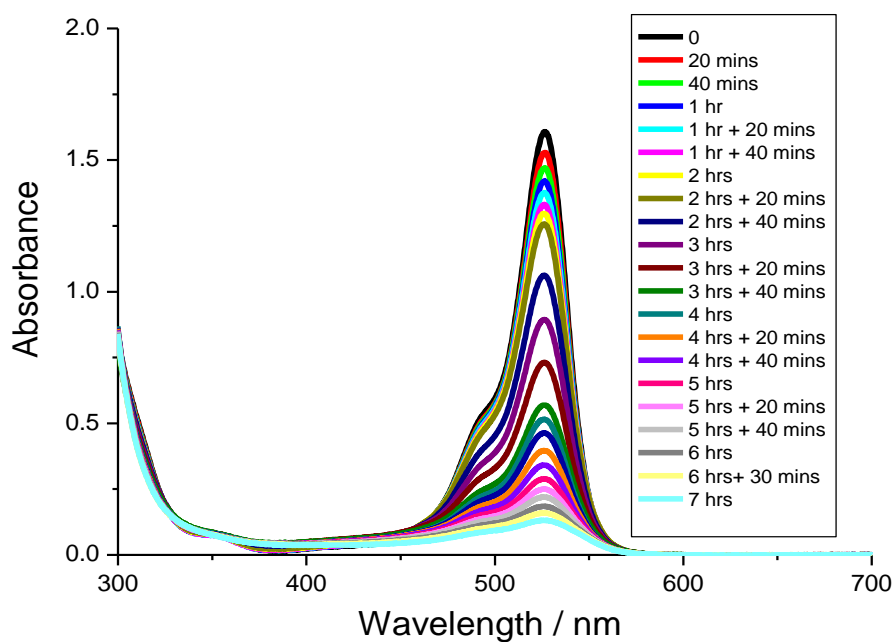


Figure 3. Progressive photo-bleaching of Erythrosine in deaerated water under broadband illumination.

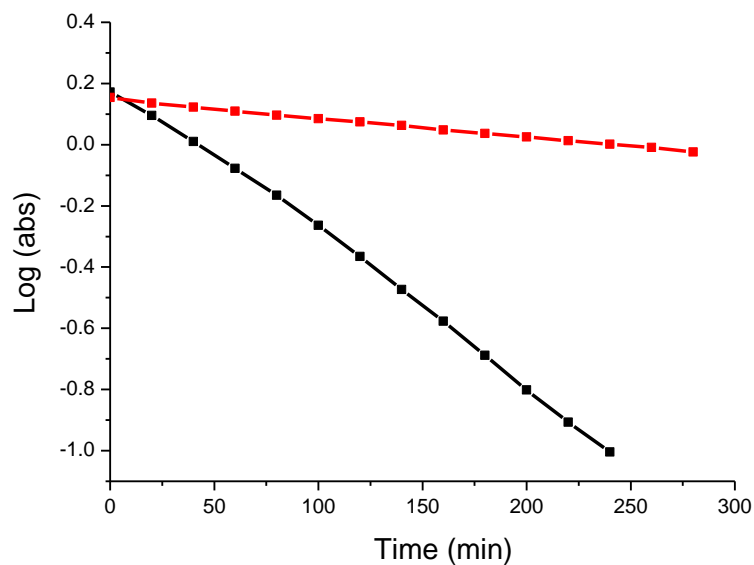


Figure 4. Comparison of the rates of photo-bleaching of Erythrosine in aerated (black points) and deaerated (red points) water under broadband illumination.

In deaerated water, photo-bleaching of Erythrosine occurs by way of first-order kinetics according to Equation 6.1. Here, $[ER]$ and $[ER]_0$ refer, respectively to Erythrosine concentrations at time t and before starting illumination. However, the apparent first-order rate constant, k_F , derived from Equation 6.1 depends on the initial concentration of Erythrosine. This situation might

reflect differences in penetration depth and other non-homogeneous illumination issues or, more likely, point to a complex mechanism. In fact, both the initial rate of bleaching and k_F depend on the number of absorbed photons, which in turn depends on the incident light intensity and on the fraction of light absorbed by the chromophore. This latter parameter is expressed by way of Equation 6.2 with A being the absorbance at any wavelength where Erythrosine absorbs. The net result is that changing $[ER]$ also affects I_{ABS} and has a direct effect on the rate of bleaching.

$$[ER] = [ER]_0 - k_F t \quad \text{Equation 6.1}$$

$$I_{ABS} = 1 - 10^{-A} \quad \text{Equation 6.2}$$

In air-equilibrated water, the rate of photo-bleaching of Erythrosine shows the characteristic “S-shaped” time dependence attributable to auto-catalysis. We will return to this process later but it means that a product formed during the early stages of reaction causes further bleaching of Erythrosine. According to this model, the kinetic data can be analysed in terms of Equation 6.3, which allows for self-catalysis.³⁹ Here, ω refers to the observed rate of reaction, k_1 is the first-order rate constant for primary (i.e., inherent) photo-bleaching and k_2 is the corresponding bimolecular rate constant for self-catalysis.⁴⁰

$$\frac{\omega}{[ER]} = (k_1 + k_2[ER]_0) - k_2[ER] \quad \text{Equation 6.3}$$

Analysis of the photo-bleaching data in terms of Equation 6.3 allows determination of the two rate constants (Figure 5). The apparent first-order rate constant, ($k_1 = 0.0069 \text{ min}^{-1}$) can be equated with k_F considered at lower concentrations, although different incident light intensities were used for the different experiments. The rate constant for self-catalysis, k_2 , at 20 °C was found to be 0.46 $\text{nM}^{-1} \text{ min}^{-1}$ at an initial Erythrosine concentration of 20 μM . Similar values were recovered at lower (i.e., 8 μM) concentration and at different incident light intensities.

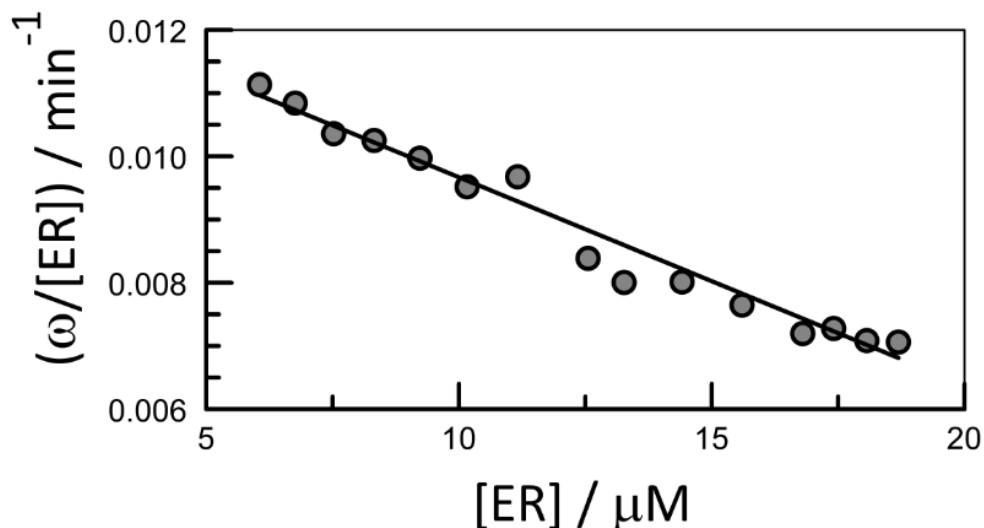


Figure 5. Example of kinetic analysis in terms of inherent and auto-catalytic bleaching reactions, with the solid line drawn through the data points representing a fit to Equation 6.3. The initial concentration of Erythrosine was 20 μM .

We consider that the bleaching reaction occurs primarily via the triplet excited state of Erythrosine. This triplet-excited state can be detected by way of transient absorption spectroscopy following laser excitation at around 520 nm (Figure 6). The differential absorption spectrum shows bleaching of the visible band of the ground state ($\lambda = 528 \text{ nm}$) while the absorption from ca. 575 nm onwards is assigned solely to the triplet state. The triplet state decays via first-order kinetics with a lifetime of ca. 150 μs in the absence of molecular oxygen at low laser intensity (Figure 7). This latter species shortens the triplet lifetime, the bimolecular rate constant is $1.4 \times 10^9 \text{ M}^{-1} \text{ s}^{-1}$. The product is singlet molecular oxygen which is formed by electronic energy transfer.⁴¹

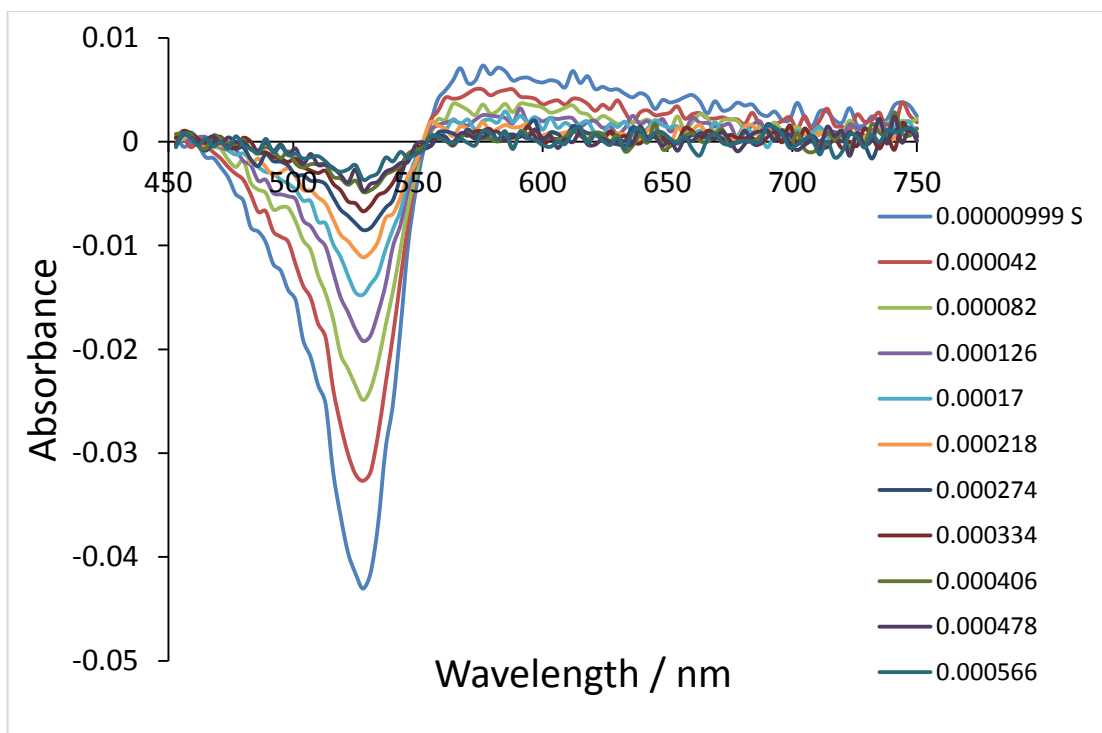


Figure 6. The transient differential absorption spectrum recorded for Erythrosine in de-oxygenated water.

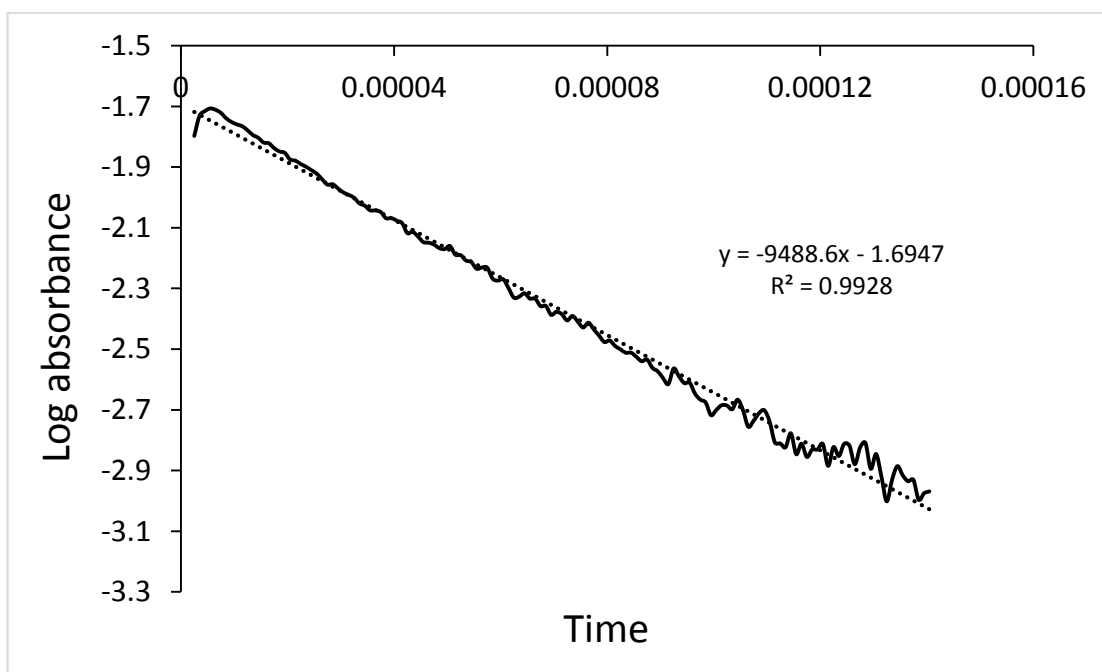


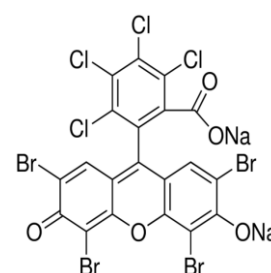
Figure 7. The relationship between log absorbance versus time for decay of the triplet-excited state of Erythrosine in water in the absence of oxygen.

The experiment was repeated and the lifetime of the triplet state was calculated after purging the solution with mixtures of N_2 and O_2 in order to monitor triplet quenching by molecular oxygen. This is a well-known reaction that has been studied for a great number of chromophores. In non-

polar solvents, quenching of the triplet state occurs at exactly one-ninth the diffusion controlled rate limit. This situation is imposed by spin-statistical factors associated with the formation of singlet oxygen. In more polar solvents, triplet energy transfer is not the only process leading to catalyzed deactivation of the triplet state and the corresponding bimolecular quenching rate constant tends to increase closer to the diffusional limit. For Erythrosine in water, we find $k_Q = 1.4 \times 10^9 \text{ M}^{-1} \text{ s}^{-1}$ which can be compared to the diffusional rate limit of $6 \times 10^9 \text{ M}^{-1} \text{ s}^{-1}$. The triplet lifetime is slightly shortened at higher concentrations of Erythrosine, which points to some kind of self-quenching, while formation of superoxide ions is a possibility in water. These latter reactions tend to be reversible but might play a minor role in the photo-bleaching process.

6.3 Phloxine B

This section continues our interest in the use of non-toxic dyes as disposable photosensitizers by looking at the properties of Phloxine B. It is known that Phloxine B is a colour additive for drugs, foods, and cosmetics and can be used as a bacterial stain. Phloxine B is used also as a stain for many branches of microscopy.⁴² It is soluble in water and most common organic solvents. One interesting application of Phloxine B is the



proposal to use it as a photochemical insecticide because of its ability to form singlet oxygen when exposed to light. The presence of heavy atoms ensures that intersystem crossing to the triplet state is highly efficient and indeed the triplet yield is formed in excess of 95%. Phloxine B has low toxicity and is described as a hydrophilic dye that does not suffer unduly from problems of aggregation.⁴³ In water at room temperature, Phloxine B displays a linear Beer-Lambert plot at concentrations from 0.22 to 33.2 μM and gives a molar absorption coefficient at the peak maximum of $80,205 \text{ M}^{-1} \text{ cm}^{-1}$ (Figures 8 and 9). The absorption maximum in water can be found at 539 nm.

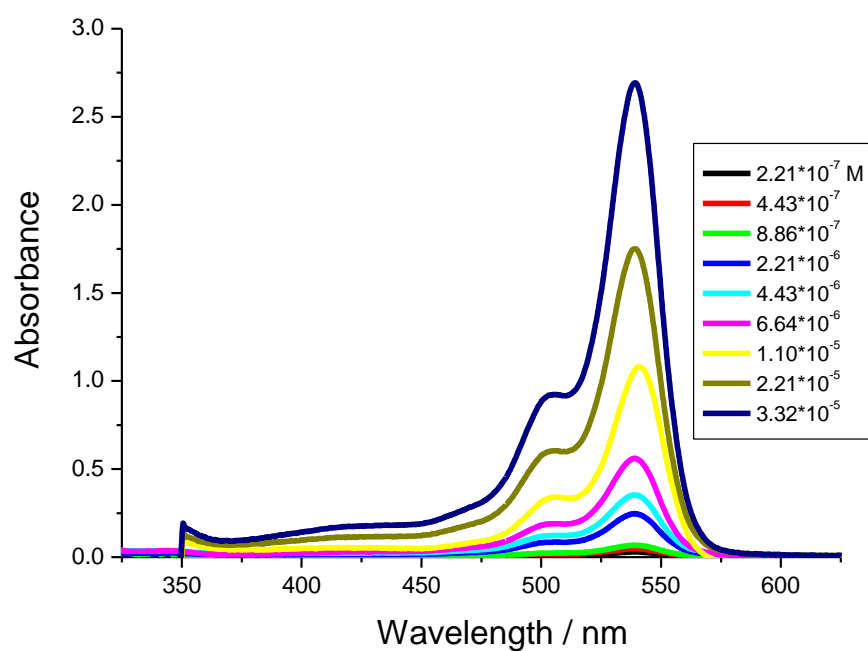


Figure 8. Overlaid absorption spectra recorded for Phloxine B as a function of concentration in water.

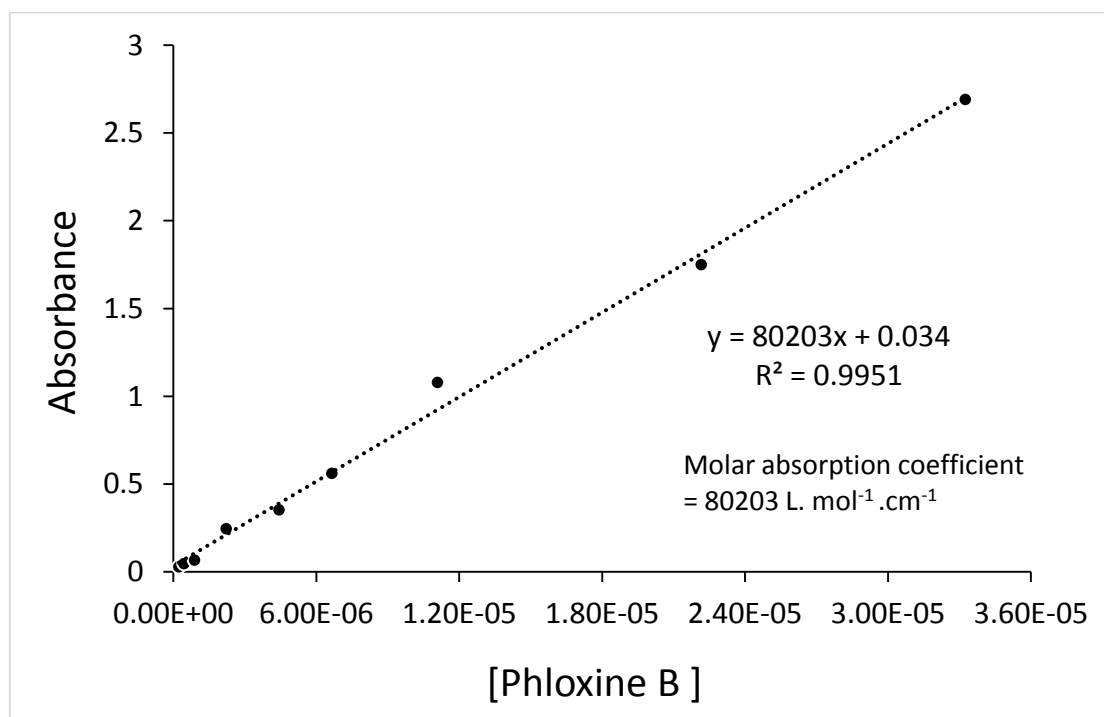


Figure 9. Beer-Lambert plot made for Phloxine B in water using absorbance values measured for the peak.

The absorption maximum shows a modest dependence on the nature of the solvent (Figure 10), although the spectral shape does not change significantly. Weak fluorescence can be detected

but this is most likely the result of E-type delayed fluorescence caused by the small singlet-triplet energy gap.

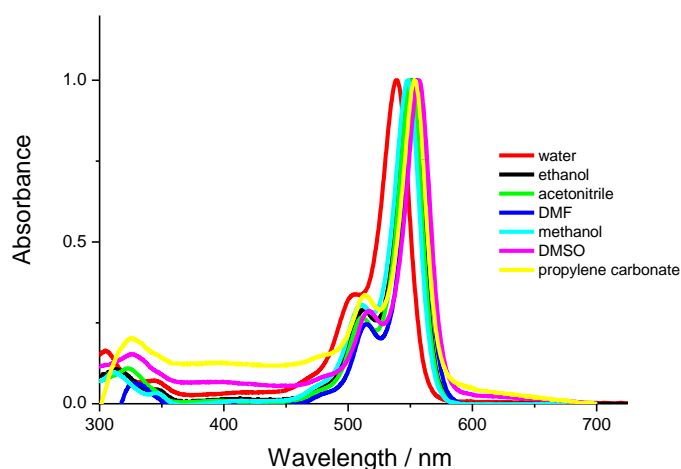


Figure 10. Normalised absorption spectra recorded for Phloxine B in different organic solvents.

Phloxine B is commercially available and is generally regarded as a safe food dye. There have been a few reports of its photodegradation in solution, where singlet oxygen is usually considered to be the species responsible for chemical breakdown. We have investigated the kinetics for photo-bleaching under broadband illumination in aerated water. Some early work has indicated that exposure to sunlight causes breakdown to form 2',4',5'-tribromo-4,5,6,7-tetrachlorofluorescein and 4',5'-dibromo-4,5,6,7-tetrachloro-fluorescein, with the release of bromide ions into the solution. The photolysis of Phloxine B may be complicated at high concentrations through self-sensitization.⁴⁴

Under broadband illumination of Phloxine B in air-equilibrated water, the absorption band centred at 539 nm slowly bleaches. A new product evolves, the absorption maximum lying at 433 nm, and slowly fades as illumination continues. These spectral changes are illustrated by way of Figure 11. Bleaching is slower than was observed for Erythrosine under similar conditions. However, after purging the solution with N₂, it was seen that similar bleaching of the lowest-energy absorption band occurred. In the absence of O₂, quenching is somewhat slower but still highly significant (Figure 12). It appears that the primary product absorbing at 433 nm does not form in the absence of O₂.

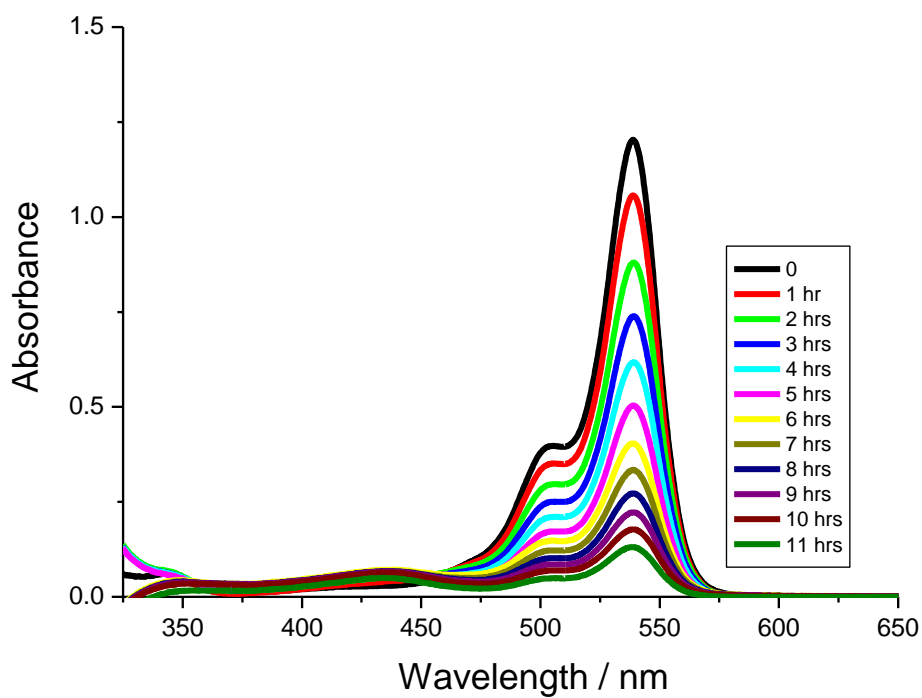


Figure 11. Stepwise bleaching of Phloxine B in aerated water under broadband illumination.

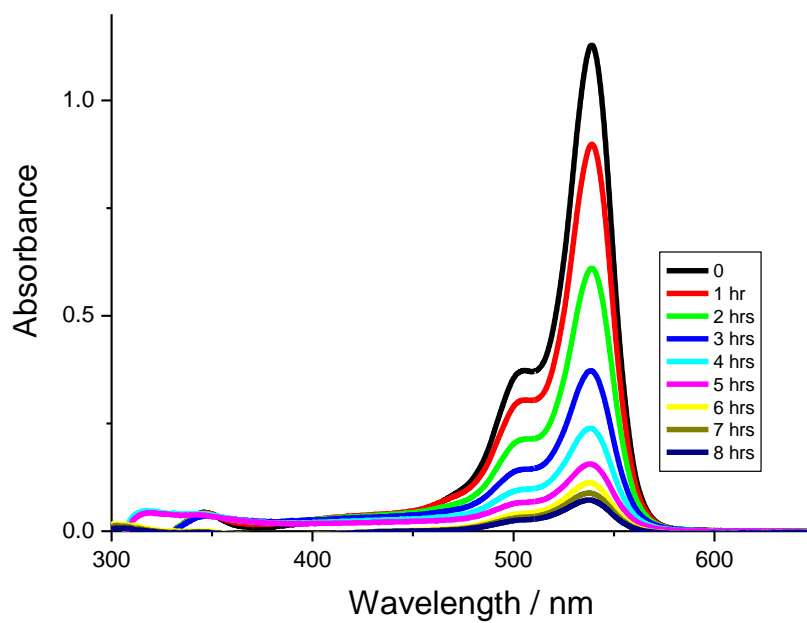


Figure 12. Stepwise bleaching of Phloxine B in water under broadband illumination, in the absence of oxygen. Conditions are otherwise identical to those used for the experiment described by Figure 11.

It was found that bleaching of Phloxine B in the presence of molecular oxygen followed a kinetic pathway where the rate of reaction increased slightly with illumination time. The primary product absorbing at 433 nm was seen to accumulate in solution but, at the end of the experiment, this species began to disappear (Figure 13). This product builds up on the same timescale as found for bleaching of the original species so it seems safe to assume that the 433-nm species does indeed arise from initial breakdown of Phloxine B. It is specific to reactions involving molecular oxygen. The same experiment carried out after purging the solution with N₂ did not form the 433-nm species while bleaching of the starting compound exhibits the sigmoidal kinetic trace considered characteristic of an auto-catalytic reaction (Figure 14). Bleaching is still efficient, it appears to be faster than that found in the presence of oxygen, and leads to loss of bromide ions since a precipitate forms when silver nitrate is added.

In deoxygenated solution, the experimental bleaching data can be described in terms of Equation 6.3 but only over early times. Again, this situation is to be expected for an auto-catalytic reaction. From the fit, it is possible to derive rate constants for auto-catalysis (k_{AC}) and for the inherent first-order bleaching step (k_1). The derived values are collected in Table 1 below. The first-order reaction starts the bleaching process but, under these conditions, auto-catalysis quickly takes over and begins to dominate the reaction. In the presence of molecular oxygen, the bleaching reaction is slower but the experimental data are well explained by Equation 6.3. Here, the inherent first-order bleaching step is somewhat slower than found in the absence of oxygen while k_{AC} is markedly reduced (Table 1). By monitoring reaction at 433 nm, it is clear that this primary product is not responsible for auto-catalysis. Instead, it appears that triplet energy transfer to molecular oxygen, and any subsequent chemical reactions, is in competition to photo-bleaching. This is an unusual stabilization effect by oxygen.

Table 1. Summary of parameters derived for the photo-bleaching of Phloxine B in water under auto-catalytic conditions.

Conditions	k_1 / min^{-1}	$k_{AC} / \text{nM}^{-1} \text{min}^{-1}$
N ₂	0.0034	0.54
Air	0.0023	0.16

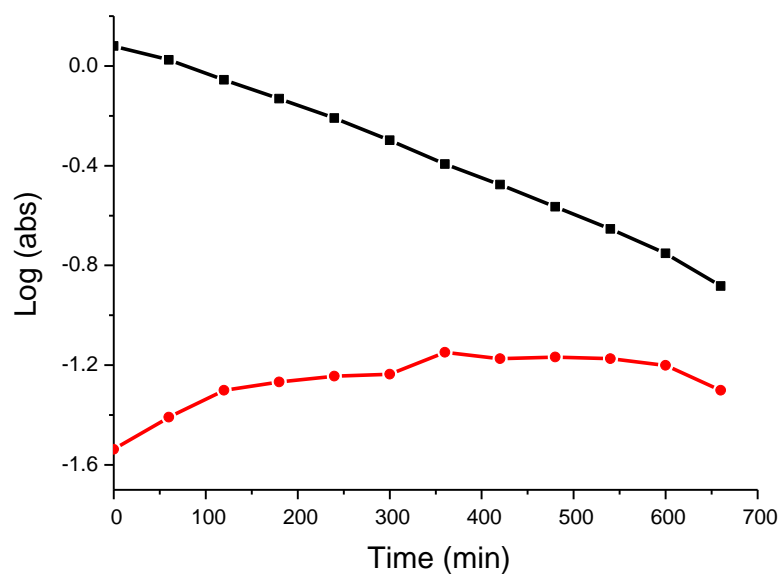


Figure 13. Photobleaching kinetics recorded for Phloxine B in air-equilibrated water at 539 nm (black circles) and at 433 nm (red circles).

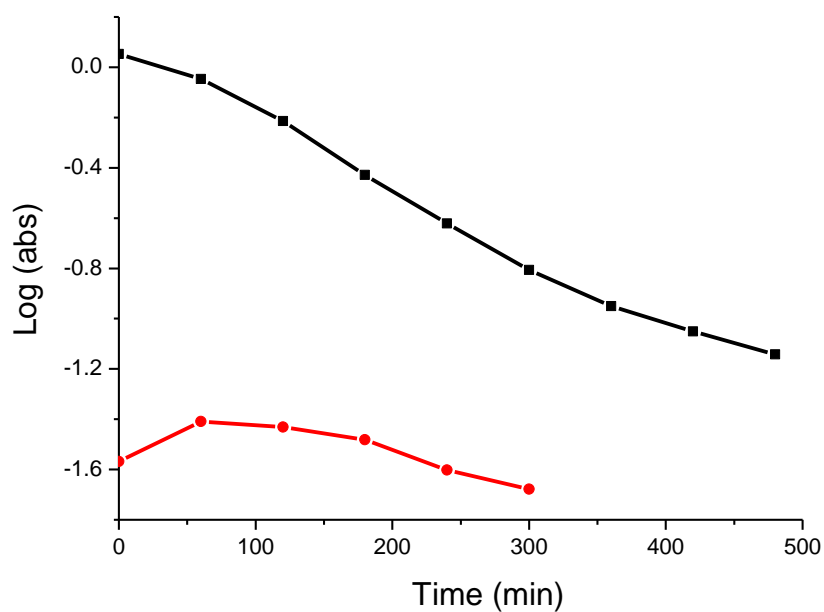
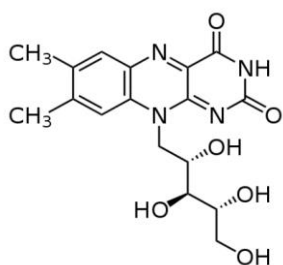


Figure 14. Photobleaching kinetics recorded for Phloxine B in deaerated water at 539 nm (black circles) and at 433 nm (red circles).

6.4 Riboflavin



Riboflavin, more often referred to as vitamin B₂, is a water-soluble chromophore found in food products. This compound is known to participate in electron-transfer processes.⁴⁵ Riboflavin is associated with the coenzymes of flavin mononucleotide (FMN) and flavin-adenine dinucleotide (FAD) and is therefore an important component in biological systems. The absorption spectrum recorded for Riboflavin in water (Figure 15) shows pronounced peaks at 373 nm and 444 nm

nm, the 444-nm peak involves a $\pi - \pi^*$ transition while the 373-nm peak appears to involve a mixture of $n - \pi^*$ and $\pi - \pi^*$ transitions.⁴⁶ In ethanol solution, Riboflavin exhibits absorption maxima at 365 nm and 449 nm. In water, Riboflavin shows quite strong fluorescence with a maximum at 531 nm (Figure 16). The fluorescence quantum yield in water is 0.2 while the excited-singlet state lifetime is 5.2 ns. The compound is considered as non-toxic and has found prominent use as a sensitizer for various artificial chemical processes. Compared to most other potential sensitizers, the absorption band lies at relatively high energy and, as such, Riboflavin looks a promising candidate for promoting photochemical reactions that require a significant driving force. Here, we consider the photochemical bleaching of Riboflavin in water and compare the results with those obtained earlier in the chapter. In fact, there have been several prior studies of the photodegradation of Riboflavin and it is important to summarise these findings.

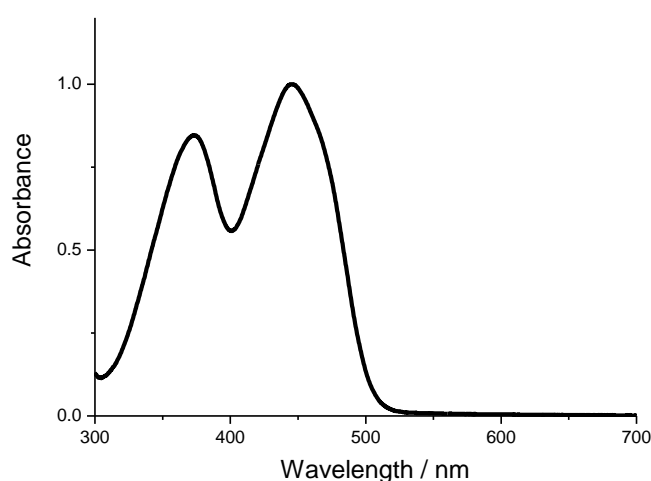


Figure 15. Absorption spectra recorded for Riboflavin in dilute aqueous solution.

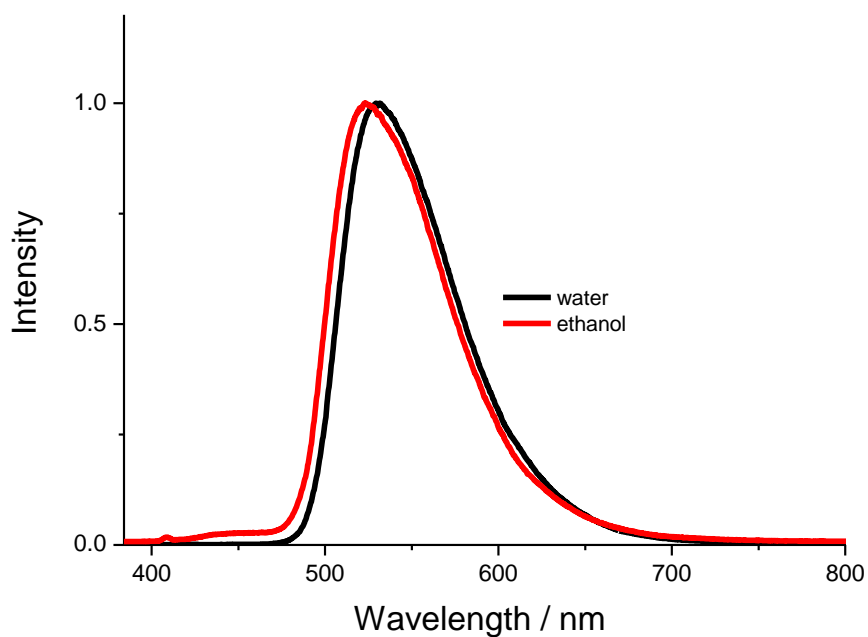


Figure 16. Fluorescence spectra recorded for Riboflavin in dilute aqueous and ethanolic solution.

Earlier work has established that Riboflavin is degraded into several photoproducts upon light exposure. These products are formyl-methylflavin (FMF), lumichrome (LC), lumiflavin (LF), carboxymethyl flavin (CMF), 2,3-butanedione, a β -keto acid and cyclodehydroriboflavin (CDRF). The structures of the main photoproducts are shown in Figure 17. It was demonstrated that the product distribution is a complex variable of temperature, concentration, pH and oxygen concentration. Further effects are noted for light intensity and wavelength. The overall picture, therefore, is highly confusing, however degradation of Riboflavin appears to take place chemically through isoalloxazine ring cleavage (Figure 18).⁴⁵ Our work relates to the kinetics of the primary photobleaching steps and we are less concerned with the product distribution.

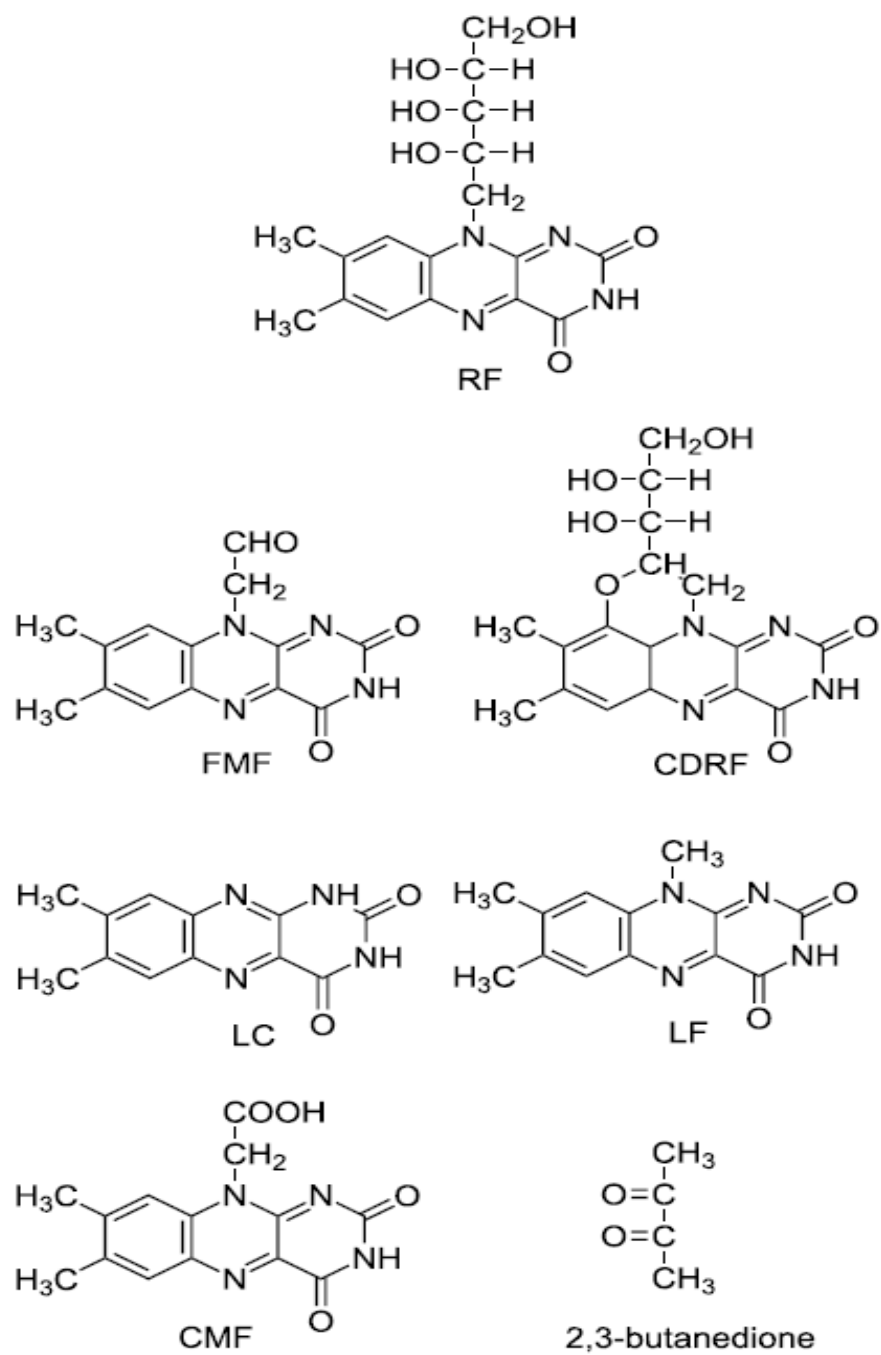


Figure 17. The molecular formulas for Riboflavin and its known photoproducts.

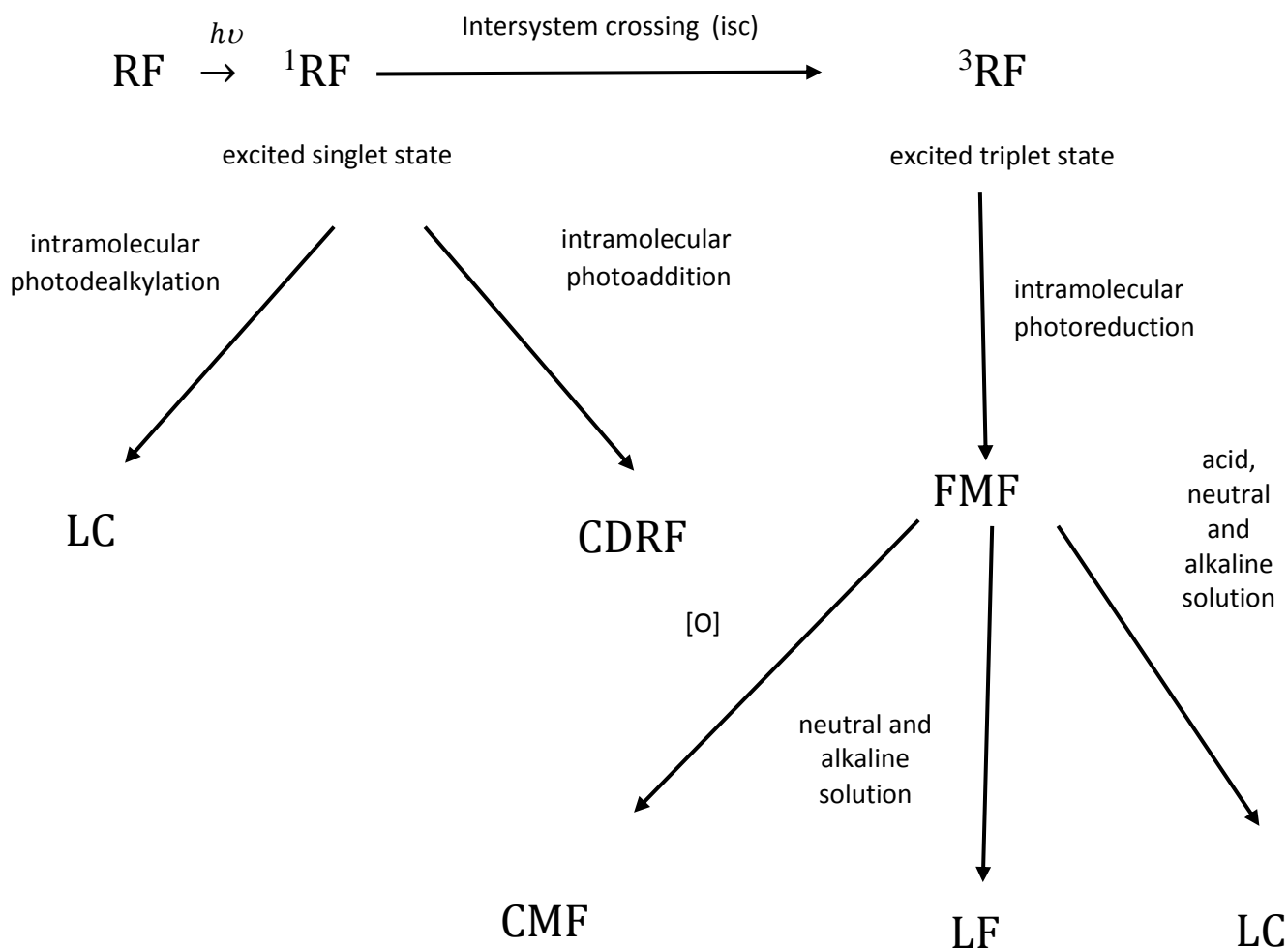


Figure 18. A general scheme for the photodegradation of Riboflavin in aqueous solution.

Figure 19 shows how the absorption spectrum of Riboflavin in aqueous solution evolves during continuous illumination with white light. At the onset, the two main absorption peaks are located at around 445 nm and 373 nm. The absorbance measured at these two wavelengths decreases during irradiation and the 373-nm peak shifts to around 354 nm. After prolonged illumination, the solution has lost its characteristic colour but, on further illumination, the absorption bands seen in the near-UV region also fade (Figure 20). This secondary photolysis is fairly slow. Figure 21 shows kinetic plots recorded in the presence of oxygen for absorbance measurements made at key wavelengths. It is seen that the lowest-energy absorption band bleaches with the profile believed to be characteristic of auto-catalysis while the band at around 350 nm bleaches very slowly via (approximately) first-order kinetics (Figure 22).

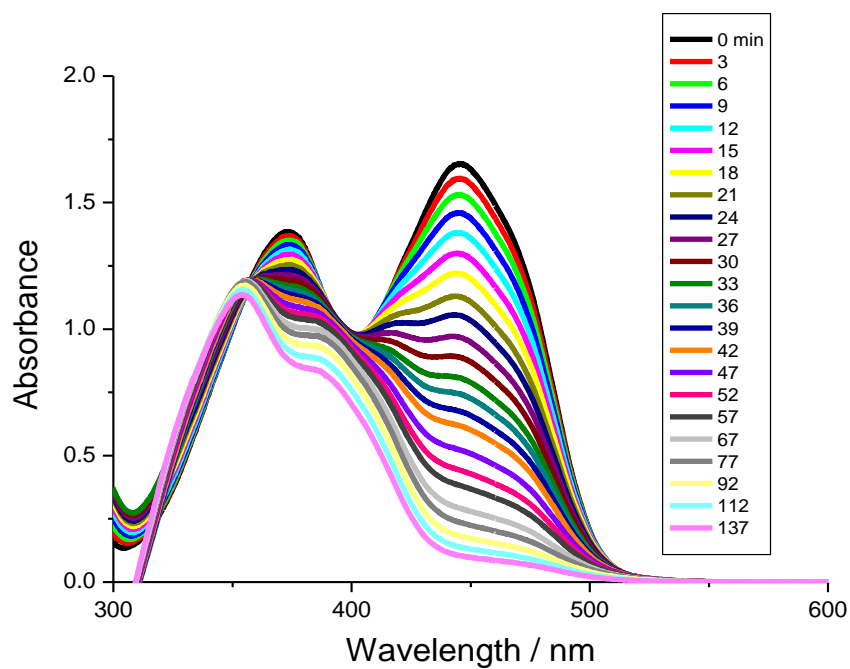


Figure 19. Stepwise bleaching of Riboflavin in air-equilibrated water under broadband illumination.

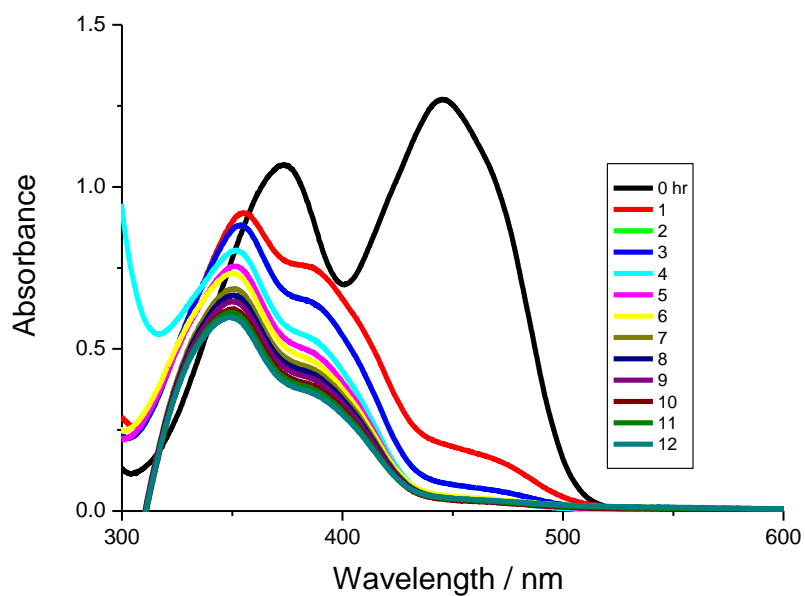


Figure 20. Effect of prolonged illumination with white light of Riboflavin in air-equilibrated water.

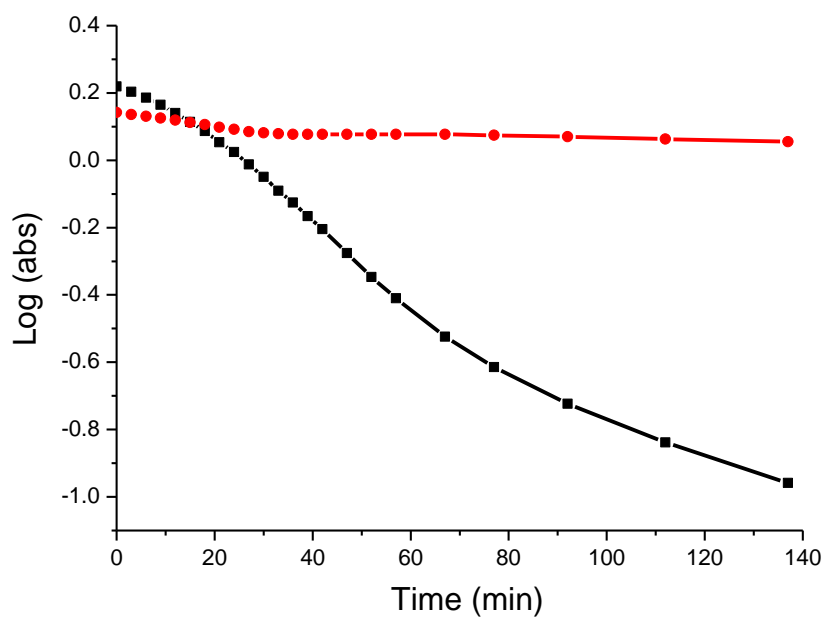


Figure 21. Typical kinetic plots for the photobleaching of Riboflavin in the presence of oxygen, the absorbance measurements are made at 443-445 nm (black circles) and at 354 -374 nm (red circles).

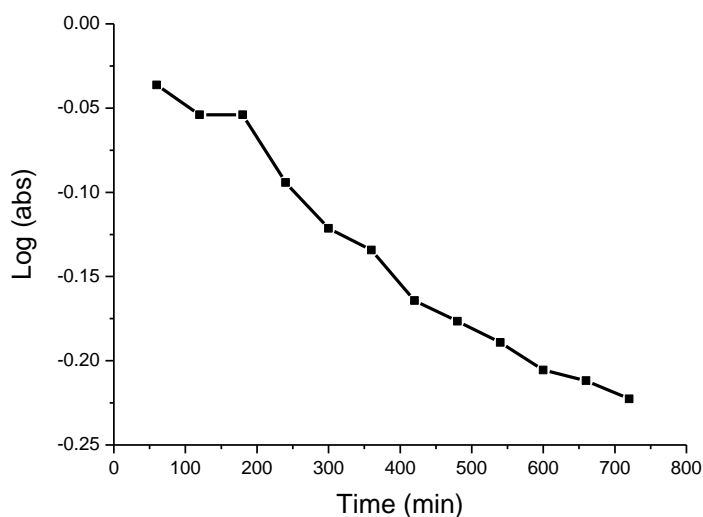


Figure 22. Kinetic plot for long-term photolysis of Riboflavin in air-equilibrated water with absorbance being followed at 349-355 nm. Note, more than one species is involved in the overall kinetic process.

Quite similar spectral profiles are observed for broadband illumination in the absence of molecular oxygen but, in this case, there is a strong growth in the absorption around 350 nm. These effects are shown below in Figures 23 and 24. We can analyze the kinetic data to derive rate

constants that might be compared with experiments made with Erythrosine and Phloxine B. In air-equilibrated solution, the primary photochemical event leads to loss of colour at around 445 nm and the concomitant build-up of a product absorbing at about 350 nm. Looking at the absorbance measured around 350 nm, we see that in the presence of oxygen there is a two-step increase in optical density. This can be analysed as two successive first-order rate constants with values of 0.0047 min^{-1} and 0.00083 min^{-1} . In the absence of oxygen, we see an increase in absorbance occurring via first-order kinetics with a rate constant of 0.0126 min^{-1} . The bleaching chemistry, therefore, is quite different in the two experiments.

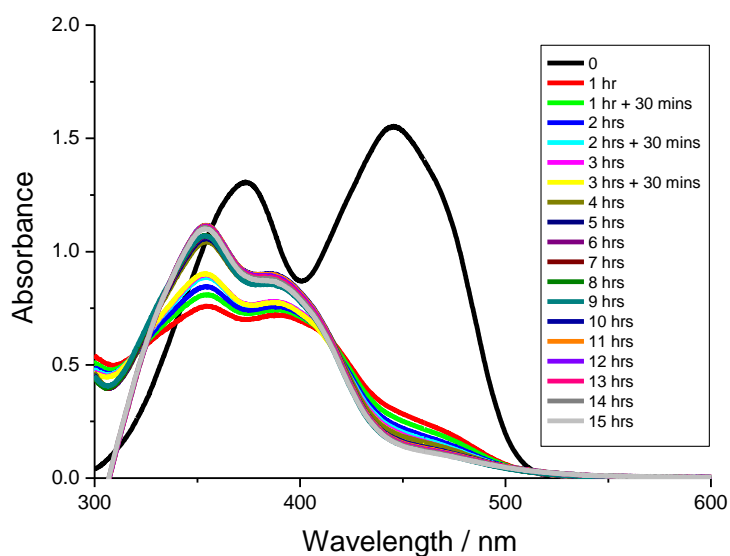


Figure 23. Stepwise bleaching of Riboflavin in deaerated water under broadband illumination.

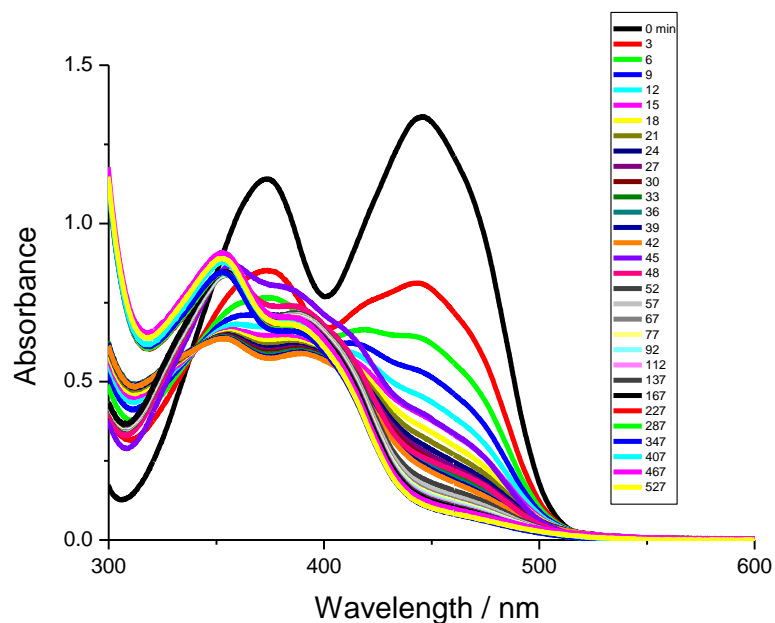


Figure 24. Stepwise bleaching of Riboflavin in deaerated water under broadband illumination, concentrating on the early stages of photolysis.

At the lowest-energy absorption band, the kinetics for photobleaching in the presence of oxygen involve auto-catalysis. Analysis of the absorbance change versus time yields estimates for the two rate constants (Figure 25). The derived values are $k_1 = 0.0021 \text{ min}^{-1}$ and $k_{AC} = 0.3 \text{ nM}^{-1} \text{ min}^{-1}$.

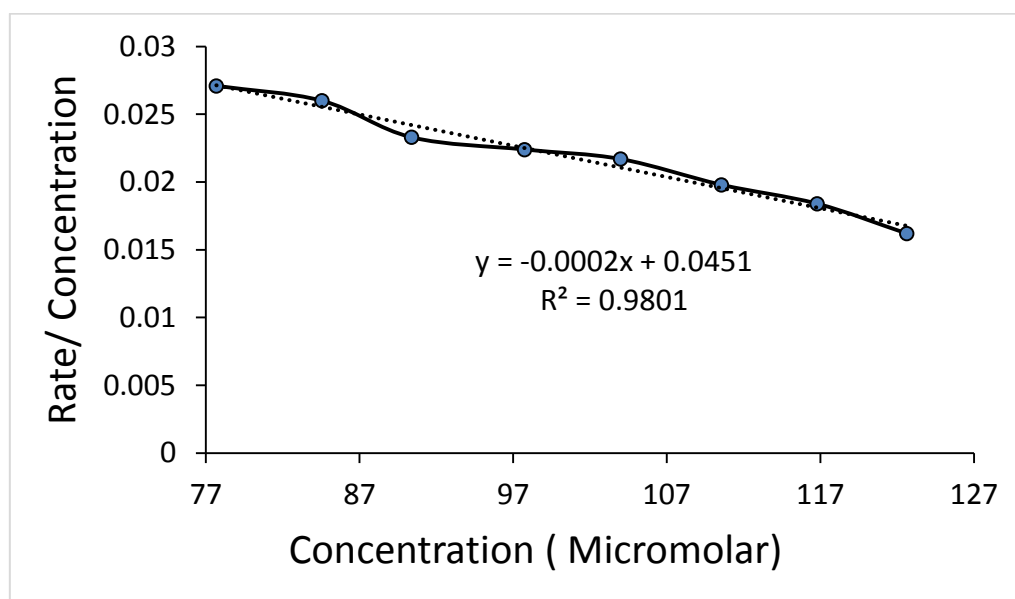


Figure 25. Stepwise bleaching of Riboflavin air-equilibrated water under broadband illumination at 443-445 nm.

6.5 Conclusion

In this chapter, we have compared the photobleaching of three food dyes in aqueous solution after equilibration with air. The three dyes show quite disparate chemistry under closely comparable conditions. The main features can be summarized as follows: *Erythrosine* bleaches from the triplet-excited state via formation of singlet molecular oxygen as a reactive intermediate. The bleaching process is auto-catalytic but does not lead to coloured intermediates. Bleaching is fast and irreversible. *Phloxine B* undergoes fast photobleaching in the absence of molecular oxygen, leading to loss of bromide ions. In this case, the presence of molecular oxygen leads to a noticeable stabilization of the chromophore. The triplet-excited state is implicated as the reactive species but no important coloured species are involved as intermediate products. *Riboflavin* shows highly complex bleaching chemistry and is the only compound of those studied here to form coloured products. These products degrade very slowly under illumination with white light. The reaction mechanism involves auto-catalysis at the primary stage but does not require the presence of molecular oxygen. In this latter case, light-induced electron transfer and bond cleavage are likely processes. The triplet-excited state has a lifetime of 30 μs in deaerated water, which is relatively short and indicates chemistry occurring from the triplet state, that is reduced to 8 μs on aeration of the solution.

Because different light-absorbing properties are associated with these compounds, it is not meaningful to attempt to compare rates of bleaching. This is especially relevant for the auto-catalytic processes since these reactions are necessarily bimolecular in nature. Auto-catalysis is a major problem because it causes the rate of bleaching to be strongly time dependent. An additional issue found with Riboflavin is that the products bleach very slowly under continuous illumination. This means that quite different behaviour will be found when different light sources are used. In principle, monochromatic light delivered at the absorption maximum should not be absorbed by these products and, in consequence, they will accumulate in the system. Of the compounds studied here, Erythrosine is the “cleanest” and we have studied this system in some detail by way of collaboration with other members of the Molecular Photonics Laboratory.

6.6 References

1. Novotný, Č.; Dias, N.; Kapanen, A.; Malachová, K.; Vándrovcová, M.; Itävaara, M.; Lima, N. *Chemosphere*. **2006**, 63, 1436.
2. Rajaguru, P.; Fairbairn, L. J.; Ashby, J.; Willington, M. A.; Turner, S.; Woolford, L. A.; Chinnasamy, N.; Rafferty, J. A. *Mutat. Res.* **1999**, 444, 175.
3. Gurr, E. *Synthetic Dyes in Biology, Medicine and Chemistry*; Academic Press Inc.: London, **1971**.
4. Robinson, T.; McMullan, G.; Marchant, R.; Nigam, P. *Bioresour. Technol.* **2001**, 77, 247.
5. Chequer, F. M. D.; Angeli, J. P. F.; Ferraz, E. R. A.; Tsuboy, M. S.; Marcarini, J. C.; Mantovani, M. S.; Oliveira, D. P. D. *Mutat. Res.* **2009**, 676, 83.
6. Yamjala, K.; Nainar, M. S.; Ramiseti, N. R. *Food Chem.* **2016**, 192, 813.
7. Johnson, I. *Histochem J.* **1998**, 30, 123.
8. Greenspan, P.; Mayer, E. P.; Fowler, S. D. *J. Cell Biol.* **1985**, 100, 965.
9. Devi, L. G.; Kumar, S. G.; Reddy, K. M.; Munikrishnappa, C. *J. Hazard. Mater.* **2009**, 164, 459.
10. Suárez- Parra, R.; Hernández- Pérez, I.; Rincón, M. E.; López- Ayala, S.; Roldán- Ahumada, M. *C. Sol. Energ. Mat. Sol. Cells.* **2003**, 76, 189.
11. Hu, C.; Hu, X.; Wang, L.; Qu, J.; Wang, A. *Environ. Sci. Technol.* **2006**, 40, 7903.
12. Stylidi, M.; Kondarides, D. I.; Verykios, X. E. *Appl. Catal. B Environ.* **2003**, 40, 271.
13. Nasr, C.; Vinodgopal, K.; Fisher, L.; Hotchandani, S.; Chattopadhyay, A. K.; Kamat, P. V. *J. Phys. Chem.* **1996**, 100, 8436.
14. Comparelli, R.; Fanizza, E.; Curri, M. L.; Cozzoli, P. D.; Mascolo, G.; Agostiano, A. *Appl. Catal. B Environ.* **2005**, 60, 1.
15. Vinodgopal, K.; Wynkoop, D. E.; Kamat, P. V. *Environ. Sci. Technol.* **1996**, 30, 1660.
16. Fazekas, T.; Nagy, A.; Treindl, L. *Collect. Czech. Chem. Commun.* **1993**, 58, 775.
17. Axelrod, D.; Koppel, D. E.; Schlessinger, J.; Elson, E.; Webb, W. W. *Biophys. J.* **1976**, 16, 1055.
18. Chequer, F. M. D.; Venâncio, V. D. P.; Bianchi, M. D. L. P.; Antunes, L. M. G. *Food Chem. Toxicol.* **2012**, 50, 3447.
19. Levitan, H. *Proc. Natl. Acad. Sci.* **1977**, 74, 2914; Krause, A. W.; Carley, W. W.; Webb, W. W. *J. Histochem. Cytochem.* **1984**, 32, 1084.
20. Odo, J.; Torimoto, S.-I.; Nakanishi, S.; Niitani, T.; Aoki, H.; Inoguchi, M.; Yamasaki, Y. *Chem. Pharm. Bull.* **2012**, 60, 846.
21. Pellosi, D. S.; Estevão, B. M.; Semensato, J.; Severino, D.; Baptista, M. S.; Politi, M. J.; Hioka, N.; Caetano, W. *J. Photochem. Photobiol. A: Chem.* **2012**, 247, 8.
22. Kim, J. R.; Michielsen, S. *Nanomaterials.* **2016**, 6, 1.
23. Hamblin, M. R.; Hasan, T. *Photochem. Photobiol. Sci.* **2004**, 3, 436.

24. Buck, S. T. G.; Bettanin, F.; Orestes, E.; Homem - de - Mello, P.; Imasato, H.; Viana, R. B.; Perussi, J. R.; Silva, A. B. F. D. *J. Chem.* **2017**, 2017, 1.
25. Usui, Y. *Chem. Lett.* **1973**, 2, 743.
26. Lindig, B. A.; Rodgers, M. A. J. *J. Phys. Chem.* **1979**, 83, 1683.
27. DeRosa, M. C.; Crutchley, R. J. *Coord. Chem. Rev.* **2002**, 233- 234, 351.
28. Manivannan, G.; Leclere, P.; Semal, S.; Changkakoti, R.; Renotte, Y.; Lion, Y.; Lessard, R. A. *Appl. Phys. B.* **1994**, 58, 73.
29. Talhavini, M.; Corradini, W.; Atvars, T. D. Z. *J. Photochem. Photobiol. A: Chem.* **2001**, 139, 187.
30. Herculano, L. S.; Lukasiewicz, G. V. B.; Sehn, E.; Caetano, W.; Pellosi, D. S.; Hioka, N.; Astrath, N. G. C.; Malacarne, L. C. *Appl. Spectrosc.* **2015**, 69, 883.
31. Epling, G. A.; Lin, C. *Chemosphere.* **2002**, 46, 561.
32. Flamigni, L. *J. Phys. Chem.* **1992**, 96, 3331.
33. Mansha, A.; Grampp, G.; Landgraf, S. *Monatsh. Chem.* **2011**, 142, 11.
34. Montagnon, T.; Kalaitzakis, D.; Triantafyllakis, M.; Stratakis, M.; Vassilikogiannakis, G. *Chem. Commun.* **2014**, 50, 15480.
35. Gorman, A. A.; Rodgers, M. A. J. *Chem. Soc. Rev.* **1981**, 10, 205.
36. Feringa, B. L. *Recl. Trav. Chim. Pays- Bas.* **1987**, 106, 469.
37. Wilkinson, F.; Farmilo, A. *J. Photochem.* **1984**, 25, 153.
38. Rohatgi- Mukherjee, K. K.; Gupta, A. K. *Chem. Phys. Lett.* **1977**, 46, 368.
39. Mata- Perez, F.; Perez- Benito, J. F. *J. Chem. Educ.* **1987**, 64, 925.
40. Perez- Benito, J. F.; Mata- Perez, F.; Brillas, E. *Can. J. Chem.* **1987**, 65, 2329.
41. Yesilgul, N.; Uyar, T. B.; Seven, O.; Akkaya, E. U. *ACS Omega.* **2017**, 2, 1367.
42. Rasooly, R. *FEMS Immunol Med Microbiol.* **2007**, 49, 261.
43. Litman, Y.; Rodríguez, H. B.; Román, E. S. *Photochem. Photobiol. Sci.* **2016**, 15, 80.
44. Keum, Y. S.; Kim, J. H.; Li, Q. X. *J. Photosci.* **2003**, 10, 219.
45. Sheraz, M. A.; Kazi, S. H.; Ahmed, S.; Anwar, Z.; Ahmad, I. *Beilstein J. Org. Chem.* **2014**, 10, 1999.
46. Saha, A.; Roy, B.; Esterrani, A.; Nandi, A. K. *Org. Biomol. Chem.* **2011**, 9, 770.

Effects of Temperature and Concentration on the Rate of Photo-bleaching of Erythrosine in Water

Joshua K. G. Karlsson,^a Owen J. Woodford,^a Roza Al-Aqar^a and Anthony Harriman^{a,*}

Molecular Photonics Laboratory, School of Chemistry, Bedson Building, Newcastle University, Newcastle upon Tyne, NE1 7RU, United Kingdom

KEYWORDS. Kinetics: Photochemistry: Self-catalysis: Singlet Molecular Oxygen: Food dye.

ABSTRACT: Erythrosine, a popular food dye and cocktail ingredient, undergoes fast O₂-sensitive bleaching in water when subjected to visible light illumination. In dilute solution, Erythrosine undergoes photo-bleaching via first-order kinetics, where the rate of bleaching depends also on the rate of photon absorption and oxygen concentration. Kinetic studies indicate that this inherent bleaching is augmented by self-catalysis at higher concentrations of Erythrosine. The limiting reaction is trapping of singlet molecular oxygen by the sensitizer. Despite the complexity of the overall photo-bleaching process, the rate constants for both inherent and self-catalytic bleaching reactions follow Arrhenius-type behavior, allowing the activation parameters to be resolved. Bleaching remains reasonably efficient in the solid state, especially if the sample is damp, and provides a convenient means by which to construct a simple chemical actinometer.

INTRODUCTION

Organic dyes^{1,2} are useful colorants for a variety of applications, ranging from cosmetics to printing inks and to anti-counterfeit devices. Historically, such dyes were selected for the strength and range of their colors and many, for example indigo, have played an important role in shaping our lifestyle.³ More recently there has been a move towards identifying non-toxic dyes that dissolve readily in water.^{4,5} These latter compounds are highly attractive to the food industry⁶ and are popular with artists, while being valuable agents for bio-conjugation.^{7,8} A major concern for all organic dyes relates to their likely instability under prolonged exposure to visible light. Indeed, photo-degradation can be a serious limitation for certain classes of dye,⁹ although engineering (e.g., the omission of molecular oxygen and introduction of screens or filters) can provide important levels of relief.¹⁰ Despite the practical inconvenience of dye photo-fading, there have been relatively few detailed studies describing the kinetics of light-induced degradation under controlled conditions.¹¹⁻¹⁶ Such studies might be complicated by auto-catalysis¹⁷ and invariably require multiple absorbed photons for complete bleaching of an individual molecule. Mechanistic studies are especially difficult in those cases where the quantum yields are very low. It might be mentioned that the photo-fading process is used routinely for measuring diffusion coefficients via Fluorescence Recovery after Photo-bleaching (FRAP).¹⁸

Here, we report on the photochemical degradation of Erythrosine in aqueous solution with particular reference to its temperature dependence. Erythrosine is a water-soluble, cherry-pink dye with a long tradition as a food colorant.¹⁹ It is commonly used in fruit cocktails but has additional applications in printing ink, as a sensitizer for orthochromic photographic plates, and as a biological stain.²⁰ Our interest in this compound stems from its known ability to function as a triplet state photo-sensitizer in water. Indeed, Xanthene dyes^{21,22} in general are promising sensitizers for antimicrobial studies^{23,24} because of their relatively low toxicity, high triplet energies, near-quantitative triplet state quantum yields and relatively long triplet lifetimes. The interest in killing bacteria by way of photodynamic therapy²⁵ has led to further development of new sensitizers. Some of these reagents look promising but would be subject to lengthy clinical and legislative regulation. More immediate benefits might arise from the use of compounds, such as Erythrosine, already used in the food industry.

One aspect of these photosensitizers, often overlooked in the search for optimum performance, is the need to eliminate the compound from the system at the conclusion of the process. This can be done most conveniently by photochemical means since the system is already under illumination. In turn, this situation demands a detailed understanding of the photo-fading kinetics such that destruction of the sensitizer occurs only on completion of the desired photochemistry. Optimization of the sensitizer concentration is a key requisite in the challenge to achieve optimal performance in

terms of product yield and dye depletion. When sunlight is used to drive the reactions, this being the only sustainable way to promote largescale photochemistry, the temperature of an aqueous reservoir will increase markedly during the reaction. Hence the need to measure activation parameters for the photo-fading processes. Such studies are rare.

RESULTS and DISCUSSION

Background

In water, Erythrosine exhibits an absorption maximum at 530 nm, with a molar absorption coefficient at the peak of $75,000 \text{ M}^{-1} \text{ cm}^{-1}$, and shows weak fluorescence centered at 550 nm (Figure S3). The compound follows Beer's law over a wide concentration range, covering that relevant to this work, in water (Figure S4). The fluorescence quantum yield in dilute aqueous solution is 3% while the excited-singlet state lifetime is 0.25 ns. The corresponding triplet-excited state can be detected readily by transient absorption spectroscopy following laser excitation at around 520 nm (Figure S20). At low laser intensity, the triplet state decays via first-order kinetics with a lifetime of ca. 150 μs in the absence of molecular oxygen. This latter species shortens the triplet lifetime (Figure S20, inset); the corresponding bimolecular rate constant being $1.4 \times 10^9 \text{ M}^{-1} \text{ s}^{-1}$ for aqueous solution at 20 °C. The product of this interaction is singlet molecular oxygen ($\text{O}_2(^1\Delta_g)$), formed via electronic energy transfer, although superoxide ions might also be formed in low yield under certain conditions.

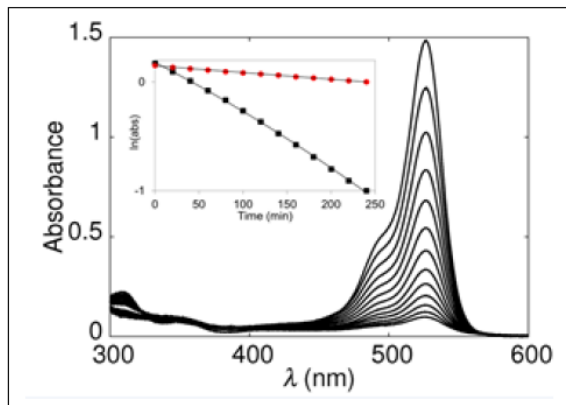


Figure 1. Stepwise bleaching of Erythrosine in aerated water under broadband illumination. The inset shows kinetic plots in the absence (red circles) and presence (black circles) of molecular oxygen.

The quantum yield²⁶ for formation of $\text{O}_2(^1\Delta_g)$ in air-saturated D_2O is 0.68 at 20 °C under conditions where the triplet quantum yield ($\Phi_T = 0.97$) is close to unity. Singlet molecular oxygen, which has a lifetime of ca. 4 μs in H_2O ,²⁷ can attack Erythrosine to initiate the bleaching process.²⁸ Here, we address the kinetics of the

photo-fading reaction and, in particular, consider the effects of temperature and chromophore concentration on the rate of dye degradation. To the best of our knowledge, there are no reports in the scientific literature describing the activation parameters associated with photo-bleaching of an organic dye.

There have been several prior records²⁹⁻³² of the photo-bleaching of Xanthene dyes in water but few quantitative details are available. Consequently, preliminary studies were made to assess the significance of photo-bleaching by exposing an air-equilibrated, aqueous solution of Erythrosine to white light. Under such conditions, the main absorption transition centered at 530 nm bleaches. There are no colored products but absorption spectroscopy indicates the build-up of one or more species absorbing in the near-UV region (Figure 1). These latter products, which are either formed in low yield or possess a weak molar absorption coefficient, are relatively stable towards further illumination. After saturating the solution with N_2 , the photo-bleaching process is much less evident but still proceeds at a measurable rate (Figure 1). Laser flash photolysis studies carried out in deaerated aqueous solution have shown³³ that the rate of decay of the triplet-excited state increases with increasing concentration of Erythrosine. The bimolecular rate constant for this reaction, which is a kind of self-quenching process, is $4 \times 10^8 \text{ M}^{-1} \text{ s}^{-1}$. This situation is far from uncommon³⁴ and could be the reason why photo-fading occurs in the absence of molecular oxygen. In air-equilibrated solution at the highest substrate concentration used here, self-quenching will account for less than 3% of the total triplet-state deactivation.

At 20 °C, monochromatic ($\lambda = 523 \text{ nm}$) illumination of Erythrosine in air-equilibrated water leads to loss of color. No change occurs in the dark and, as mentioned above, the rate of photo-bleaching is decreased significantly on removal of the dissolved oxygen. The course of reaction is insensitive to changes in pH at pH greater than 4. The initial rate of photo-bleaching increases linearly with increasing light intensity (Figure S16), as might be expected for a photo-induced reaction.

The usual consequence of attack by $\text{O}_2(^1\Delta_g)$ on an aryl heterocycle in solution is an endoperoxide.³⁵ In water, this latter species will re-arrange to form stable products derived from substitution at the hydroperoxide group.^{36,37} For Erythrosine, it was found that a partially bleached solution formed an instantaneous precipitate on treatment with AgNO_3 solution. It was observed, however, that the addition of KI (ca. 1 mM) to a solution of Erythrosine in aerated H_2O has essentially no effect on the rate of photo-bleaching, although iodide is known to quench singlet molecular oxygen.^{38,39} Examination of partially bleached solutions of Erythrosine in D_2O by ^1H -spectroscopy showed formation of a product consistent with loss of iodine from Erythrosine. Figure S7

Concentration Dependence

The absence of colored products allows kinetic measurements to be made by following absorbance changes at wavelengths around the peak maximum. This can be done most conveniently by illuminating an aqueous solution of Erythrosine with an LED emitting at 523 nm and detecting the amount of transmitted light with an appropriate photocell (see Supporting Information experimental section). At modest concentrations (i.e., 3 μM , where the dye absorbs ca. 40% of the incident light intensity at the onset of the experiment), the rate of photo-bleaching appears first-order with respect to Erythrosine (Figure 2); a similar conclusion was reached⁴⁰ earlier for photo-bleaching of Phloxine in water. First-order kinetics with respect to Erythrosine are likewise observed at all concentrations less than ca. 7 μM (Figure 2). However, the apparent first-order rate constant, k_F , derived from Equation 1 depends on the initial concentration of Erythrosine (Table 1). Here, $[\text{ER}]$ and $[\text{ER}]_0$ refer, respectively to Erythrosine concentrations at time t and before starting illumination. This situation might reflect differences in penetration depth, non-homogeneous illumination issues or, more likely, point to a complex mechanism.

$$\ln[\text{ER}] = \ln[\text{ER}]_0 - k_F t \quad (1)$$

At 20 °C under monochromatic illumination, the approximate quantum yield for photo-bleaching, measured from the absorbance change at 530 nm, is around 1×10^{-3} . This value is very much lower than the quantum yield²⁶ for formation of singlet molecular oxygen ($\Phi_\Delta = 0.68$) under comparable conditions. This indicates that the rate-limiting factors arise during attack on Erythrosine by $\text{O}_2(^1\Delta_g)$ and the subsequent chemical modifications³⁵⁻³⁷ leading to formation of the final product. With a triplet quantum yield of 0.97 and at an initial Erythrosine concentration of 3 μM , we can estimate the bimolecular rate constant for attack by $\text{O}_2(^1\Delta_g)$ in water to be ca. $8 \pm 3 \times 10^7 \text{ M}^{-1} \text{ s}^{-1}$.

$$I_{\text{ABS}} = 1 - 10^{-A} \quad (2)$$

$$P_O = \frac{k_B[\text{O}_2]}{k_B[\text{O}_2] + k_D} \quad (3)$$

$$P_\Delta = \frac{\Phi_\Delta}{P_T} \quad (4)$$

$$P_Q = \frac{k_Q[\text{ER}]}{k_Q[\text{ER}] + k_\Delta} \quad (5)$$

At an Erythrosine concentration of 3 μM , it was observed that the initial rate of photo-bleaching, ω_0 , measured over the early part of the curve, decreased linearly with decreasing light intensity, I_i (Figure S16). Apart from changing the incident light intensity, the rate of photon uptake also varies according to the fraction of light absorbed, I_{ABS} , by Erythrosine according to Equation 2. Here, A refers to the absorbance in a 1 cm cuvette at 523 nm. It was observed that ω_0 increased linearly with increasing I_{ABS} over a wide range (Figure S17). The

initial rate of photo-bleaching depends also on the concentration of dissolved oxygen. To be more precise, ω_0 depends on the probability, P_O , with which O_2 quenches the triplet state of Erythrosine under the experimental conditions. This particular term can be expressed by way of Equation 3, where k_B ($= 1.4 \times 10^9 \text{ M}^{-1} \text{ s}^{-1}$) refers to the bimolecular rate constant for quenching triplet Erythrosine by O_2 and k_D ($= 6.7 \times 10^3 \text{ s}^{-1}$) refers to the corresponding rate constant for decay of the triplet state in the absence of O_2 . Under our conditions, P_O is essentially unity. We can define the probability, P_Δ , with which interaction between the triplet state and O_2 leads to formation of singlet molecular oxygen in terms of Equation 4. Here, P_T ($= 0.97$) is the probability for formation of the triplet excited state and Φ_Δ ($= 0.68$) is the quantum yield for formation of singlet molecular oxygen.

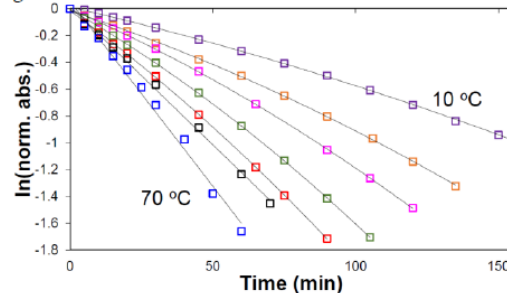


Figure 2. Effect of temperature on the kinetics for photofading of Erythrosine in aerated water in 10 °C increments.

It was observed that, at constant incident light intensity, ω_0 was sensitive to changes in the initial concentration of erythrosine (Figure 3). The effect was non-linear but indicated that ω_0 tended towards a maximum rate at high concentration. This saturation effect can be explained in terms of the effective probability with which Erythrosine traps $\text{O}_2(^1\Delta_g)$ before the latter undergoes nonradiative decay in aqueous solution. Our results do not provide a clear estimate of the saturation concentration; simulations based on the available quantitative information suggests that saturation will require around 250 μM (Figure S7). In fact, the extent of bleaching observed at low concentration of Erythrosine exceeds that anticipated on the basis of diffusional contact between chromophore and $\text{O}_2(^1\Delta_g)$, even allowing for every contact resulting in chemical modification (Equation 5). Here, k_Q is the bimolecular rate constant for chemical trapping of $\text{O}_2(^1\Delta_g)$ by Erythrosine and k_Δ ($= 2.5 \times 10^5 \text{ s}^{-1}$) is the rate constant⁴¹ for nonradiative decay of $\text{O}_2(^1\Delta_g)$ in water. This situation can be explained in terms of a certain fraction of $\text{O}_2(^1\Delta_g)$ reacting with the sensitizer immediately after excitation energy transfer. Assuming activation of O_2 occurs via the electron exchange⁴² (i.e., Dexter-type electronic energy transfer) mechanism, there must be orbital contact between

erythrosine and O₂. The geminate bleaching proposed to account for low concentrations of Erythrosine would occur before O₂(¹Δ_g) could diffuse from the contact pair.

$$\omega_0 = (I_\lambda \times I_{ABS})(P_T \times P_O \times P_\Delta \times P_Q)k_0 \quad (6)$$

These various probabilities can be combined to give a generic expression for the initial rate of photo-bleaching (Equation 6). Fitting the experimental initial rates to the starting concentration of Erythrosine, under conditions of fixed O₂ concentration and I_λ, allows refinement of k_Q as being 2.0 ± 0.5 × 10⁷ M⁻¹ s⁻¹. It now becomes clear that this is the rate-determining step at the level of Erythrosine concentrations used here. The effective zero-order rate constant, k₀, associated with Equation 6 has a value of 0.55 ± 0.08 μM min⁻¹ at 20 °C. This latter value depends on the total light intensity and, under our fixed conditions, is highly reproducible. Comparing ω₀ and k₀ indicates that, because of the relatively low concentrations of erythrosine used, our conditions are far from optimized with respect to the maximum rate of photo-bleaching.

Table 1. Summary of the kinetics parameters determined as a function of temperature.

Temp./°C	k _i /min ⁻¹	k _{AC} /nM ⁻¹ min ⁻¹	ω ₀ /μM min ⁻¹
10	0.0049	0.31	0.051
20	0.0069	0.46	0.128
30	0.0082	0.63	0.140
40	0.0091	0.82	0.192
50	0.0122	0.92	0.240
60	0.0137	1.01	0.258
70	0.0172	1.34	0.290

Self-Catalysis at Higher Concentrations

At Erythrosine concentrations above ca. 7 μM there is a marked positive deviation from first-order kinetics, even over short illumination periods (Figure 3). This suggests that a product formed during the inherent photo-bleaching reaction enters into the chemistry and augments the quenching of triplet erythrosine by O₂. According to this model (Scheme 1), the kinetic data can be analysed in terms of Equation 7, which allows for self-catalysis.⁴³ Here, ω refers to the observed rate of reaction, k_i is the first-order rate constant for primary (i.e., inherent) photo-bleaching and k_{SC} is the corresponding bimolecular rate constant for self-catalysis.⁴⁴

$$\frac{\omega}{[ER]} = (k_1 + k_{SC}[ER]_0) - k_{SC}[ER] \quad (7)$$

Analysis of the photo-bleaching data in terms of Equation 7 allows determination of the two rate constants. The apparent first-order rate constant, k_i, can be converted to a zero-order rate constant on the basis of Equation 6. The derived values (Table s1) are in accord with those obtained from the initial rates (Table 1), after due allowance for the different I_λ values. The rate constant for self-catalysis, k_{SC}, was found to be 0.46 nM⁻¹

min⁻¹ at an initial Erythrosine concentration of 10 μM. A similar value was recovered at lower concentration (Table s1). These studies were carried out at constant light intensity but comparison is possible only after adjustment for differences in I_{ABS} and P_Q.

Confirmation that auto-catalysis is likely for this reaction was obtained by illumination of Erythrosine in the presence 0.05 M furfuryl alcohol. This compound is used as a trap for singlet molecular oxygen,⁴⁵ where reaction leads to the formation of labile peroxides and hydroperoxides. The rate of photo-bleaching of Erythrosine is accelerated by the presence of the substrate (Figure S18). We interpret this result in terms of furfuryl alcohol intercepting singlet molecular oxygen generated from the triplet-excited state of Erythrosine to form highly reactive peroxy species.⁴⁶⁻⁴⁸ Subsequent dark reactions with Erythrosine leads to further bleaching of the dye. In auto-catalysis,⁴⁹⁻⁵² the primary breakdown products replace the peroxy species formed from furfuryl alcohol. There is no recovery of coloration on leaving a bleached sample in the dark.

The overall bleaching process is “collectively auto-catalytic” since one or more products form and promote further bleaching of the chromophore. The best known examples of auto-catalytic reactions are the Belousov-Zhabotinsky clock reactions, although certain hydrolysis reactions are also believed to exhibit auto-catalysis. Other well-known examples include the spontaneous degradation of aspirin to salicylic acid and DNA replication. Photochemical examples are less common but the bleaching of a dye in the presence of a reactive substrate such as furfuryl alcohol seems a likely candidate. The normal signature of auto-catalysis is a sigmoidal variation in product concentration with reaction time. It is also a basic requirement that the reaction order is nonlinear since at least one step involves the square of concentration. A complication particular to the bleaching studied here is that the number of absorbed photons changes as the reaction proceeds. This effect can disturb the shape of the product evolution profile.

It is also clear that self-catalysis serves to augment the overall bleaching but by itself provides only a modest acceleration in rate. The primary bleaching process involves attack on Erythrosine by O₂(¹Δ_g). The fact that auto-catalysis occurs only at relatively high concentration of Erythrosine is taken as being indicative of a dark reaction. The most likely scenario is that Erythrosine intercepts a peroxy species formed during primary attack by O₂(¹Δ_g) before it can undergo chemical modification to form a permanent product (Scheme 1).

Temperature Dependence

At a fixed Erythrosine concentration of 3 μM, the first-order rate constant derived from Equation 1 shows a modest dependence on temperature and increases by a factor of ca. 2-fold on raising the temperature from 20

to 60 °C. The adherence to Equation 1 can be used to argue that the mechanism remains the same over this temperature variation. Indeed, most of the terms associated with Equation 6 are essentially insensitive to temperature but this is not so for the concentration of dissolved molecular oxygen (Table 1). The probability for quenching the triplet-excited state by O₂, however, remains in excess of 0.95 at all accessible temperatures because of the long inherent triplet lifetime. This allows determination of the corresponding zero-order rate constants, *k*₀, for photochemical bleaching of Erythrosine as a function of temperature (Table 1). It can be seen that *k*₀ varies smoothly with temperature over the available range. The rate constants follow Arrhenius behavior and give rise to an effective activation energy of 9.7 ± 1.0 kJ/mol and a pre-exponential factor of 880 μM min⁻¹ (Figure 3). The latter value provides further confirmation that our standardized experimental conditions are well short of being optimal for bleaching. The derived activation energy is modest⁵³ but we could not find any meaningful comparator in the literature. In fact, Gorman et al.³⁶ have shown that addition of singlet molecular oxygen across double bonds provided by simple alkenes involves an activation energy close to zero. Such reactions are driven by entropic changes.

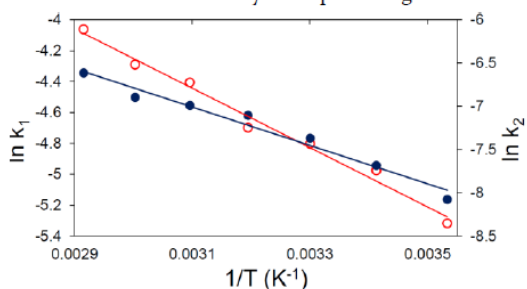


Figure 3. Arrhenius-type plots for the inherent first-order rate constant (black curve) and the auto-catalytic reaction (red curve) determined for photofading of Erythrosine in aerated water. The solid lines correspond to least-squares, non-linear fits to the Arrhenius expression.

It is reasonable to suppose that the measured activation energy is associated with addition of molecular oxygen to a molecule of Erythrosine. The resultant product (i.e., EROO in Scheme 1) is liable to hydrolyze in water and there are crude indications for the release of halide ions. The non-zero activation energy, which is sufficiently small to minimize the effects of temperature, points towards a rate-limiting step more complex than simple addition of oxygen across a double bond.

At higher concentration of Erythrosine, it was found that *k*_{sc} increased progressively with increasing temperature (Table 1). Indeed, *k*_{sc} follows Arrhenius-type behavior over the accessible temperature range, giving an activation energy of 18.5 kJ/mol while the pre-exponential factor is 0.74 μM⁻¹ min⁻¹. It is less surprising that *k*_{sc} might follow an activated route since the key reaction

must involve diffusional contact between Erythrosine and a product from its chemical breakdown. Indeed, other auto-catalytic reactions have been reported⁵⁴⁻⁵⁶ to proceed via an activated process. The activation energy derived here for Erythrosine photo-bleaching is small, although twice that for the inherent bleaching step, and indicates that the reaction is easily achieved despite the fact that the molecule is large and its breakdown might require numerous electrons. Using furfuryl alcohol as a model, we can speculate that auto-catalysis involves reactions of peroxy species with Erythrosine (Scheme 1). Such chemical processes, which are often chain reactions involving free radicals, are known to involve small activation barriers.⁵⁷

Our understanding of this self-catalysis is based on a dark reaction between Erythrosine and one of its intermediary breakdown products. It is easy to imagine that the latter (stable) intermediate (i.e., EROO in Scheme 1) will degrade faster at higher temperatures. This makes it more challenging for Erythrosine to intercept the intermediate before its conversion to a benign product (i.e., P₃ in Scheme 1). Temperature, therefore, plays a key role in the overall bleaching chemistry and it becomes essential that we extend our knowledge of such processes if we are to control the photo-fading steps.

Bleaching in the Solid State

Erythrosine is a readily available food dye with a characteristic color and, as such, could make a convenient universal standard by which to compare and contrast the photo-stability of other dyes. This situation is made possible by the realization that bleaching occurs on a relatively fast timescale, at least in aqueous solution. For a viable standard photosystem, the most convenient protocol would utilize controlled bleaching of Erythrosine in the form of solid-state samples. This, of course, has implications for the photo-bleaching of dye adsorbed on textiles, printed on paper or painted on canvas. As a demonstration of this principal, we note that filter paper soaked in aqueous Erythrosine solution and dried makes an ideal medium for recording the beam characteristics of the LED used for illumination of the samples (Figure S2). For adsorbent paper (300 g/m²) soaked in Erythrosine solution, the pink coloration disappears gradually on exposure to sunlight, leaving a progressively bleached panel. The difference is obvious to the naked eye even on short irradiations (see Table of Contents Entry). This makes for an excellent actinometer since the residual color is a marker for the integrated number of absorbed photons.

CONCLUSION

This work has advanced our general understanding of the photochemical bleaching of organic dyes by reporting activation parameters for both the inherent first-order step and the accompanying auto-catalytic process.

Such information is essential, especially for exterior applications where exposure to sunlight will lead to an inevitable increase in temperature for the system. Indeed, evermore applications are being proposed for organic chromophores but little attention is being given to their stability under operating conditions. Of particular importance is the observation that, at high concentrations of chromophore, self-catalysis becomes significant. For improved design of advanced reagents it is necessary to move away from serendipitous discovery of unusually stable dyes and to construct databases containing critical entries useful for the recognition of optimum experimental conditions. It should be noted that the onset of self-catalysis means that the rate of bleaching takes on a significant time dependence.

The bleaching reaction under consideration here is one of the simplest cases; involvement of singlet molecular oxygen was confirmed by the realisation that the rate doubles in D₂O relative to H₂O (Figure S15). This latter effect arises because the lifetime of O₂(¹Δ_g) is increased markedly in D₂O.⁴ Even so, the probable involvement of peroxy species makes it difficult to control the rate. In the absence of an activation barrier, the inherent rate constant for bleaching of Erythrosine in aerated water is 35 min⁻¹. This is relatively high; under our standard conditions, this corresponds to the loss of 0.13 μM of dye per minute illumination at 20 °C. Converting this rate to a formal quantum yield for photo-bleaching leads to a value of 0.002 at 20 °C under conditions where all incident light is absorbed at the onset. At 50 °C, a temperature easily reached under direct sunlight, the quantum yield is doubled. Auto-catalysis increases both the rate and quantum yield. A net result is that Erythrosine is too susceptible to photo-degradation to be proposed as a viable sensitizer for sustainable photochemical processes. It is ideal, however, for use as a sensitizer for any process where the final product distribution needs to be colorless. It is also apparent that a simple chemical actinometer can be formulated by impregnation of the dye onto adsorbent paper.

ASSOCIATED CONTENT

Supporting Information. Includes full experimental details, absorption/emission spectra, triplet-state differential absorption spectra, examples of kinetic profiles, light-intensity dependences, effects of furfuryl alcohol on bleaching kinetics. This material is available free of charge via the Internet at <http://pubs.acs.org>.

AUTHOR INFORMATION

Corresponding Author

* Professor Anthony Harriman: Anthony.harriman@ncl.ac.uk (tel: +44 1912088660).

Author Contributions

The manuscript was written through contributions of all authors.

Funding Sources

We thank Newcastle University and EPSRC for financial support of this work. The sample of Erythrosine was kindly donated by The Procter & Gamble Company. Ms. R. Al-Aqar acknowledges The Higher Committee for Education Development in Iraq (HCED) for the award of a research scholarship.

ACKNOWLEDGMENT

The sample of Erythrosine was kindly donated by The Procter & Gamble Company. Ms. R. Al-Aqar acknowledges The Higher Committee for Education Development in Iraq (HCED) for the award of a research scholarship. We are especially grateful to Dr. Corinne Wills and Prof. William McFarlane for recording the NMR spectra reported in this manuscript.

REFERENCES

- (1) Zollinger, H. *Color Chemistry. Syntheses, Properties and Applications of Organic Dyes and Pigments*. Third Edition. Wiley-VCH, Weinheim, 2003.
- (2) Kim, S.-H. *Functional Dyes*. Elsevier, Amsterdam, 2006.
- (3) Gurr, E. *Synthetic Dyes in Biology, Medicine and Chemistry*. Academic Press, London, 1971.
- (4) Imran, M.; Yousaf, A. B.; Zhou, X.; Liang, K.; Jiang, Y. F.; Xu, A. W. Oxygen-Deficient TiO₂(*x*)-Methylene Blue Colloids: Highly Efficient Photoreversible Intelligent Inks. *Langmuir* **2016**, *32*, 8980-8987.
- (5) Narwal, S.; Kumar, S.; Verma, P. K. Synthesis and Therapeutic Potential of Quinoline Derivatives. *Res. Chem. Intermed.* **2017**, *43*, 2765-2798.
- (6) *Colour Additives for Food and Beverages*. Scotter, M. J.: Ed.: Woodhead Publishing Series in Food Science, Technology and Nutrition. Elsevier, Amsterdam, 2015.
- (7) Johnson, I. Fluorescent Probes for Living Vells. *Histochem. J.* **1998**, *30*, 123-140.
- (8) Greenspan, P.; Mayer, E. P.; Fowler, S. D. Nile Red – A Selective Fluorescent Stain for Intracellular Lipid Droplets. *J. Cell Biol.* **1985**, *100*, 965-973.
- (9) Van Beek, H. C. A. Fading by Light of Organic Dyes on Textiles and Other Materials. *Stud. Conservation* **1966**, *11*, 123-132.
- (10) Padfield, T.; Landi, S. The Light Fastness of Natural Dyes. *Stud. Conservation* **1966**, *11*, 181-196.
- (11) Alamiry, M. A. H.; Harriman, A.; Haefele, A.; Ziesel, R. Photochemical Bleaching of an Elaborate Artificial Light-Harvesting Antenna. *ChemPhysChem* **2015**, *16*, 1867-1872.
- (12) Harriman, A.; Stachelek, P.; Sutter, A.; Ziesel, R. Stepwise Photoconversion of an Artificial Light-Harvesting Array Built from Extended BODIPY Units. *Photochem. Photobiol. Sci.* **2015**, *14*, 1100-1109.
- (13) Georgakoudi, I.; Nichols, M. G.; Foster, T. H. The Mechanism of Photofrin[®] Photobleaching and its Consequences for Photodynamic Therapy. *Photochem. Photobiol.* **1997**, *65*, 135-144.
- (14) Carretero, L.; Blaya, S.; Mallavia, R.; Madrigal, R. F.; Belendez, A.; Firmia, A. Theoretical and Experimental Study of the Bleaching of a Dye in a Film-Polymerization Process. *App. Opt.* **1998**, *37*, 4496-4499.
- (15) Huston, A. L.; Reimann, C. T. Photochemical Bleaching of Adsorbed Rhodamine 6G as a Probe of Binding Geometries on a Fused-Silica Surface. *Chem. Phys.* **1991**, *149*, 401-407.
- (16) Batchelor, S. N.; Carr, D.; Coleman, C. E.; Fairclough, L.; Jarvis, A. The Photofading Mechanism of Commercial Reactive Dyes on Cotton. *Dyes Pigm.* **2003**, *59*, 269-275.
- (17) Fazekas, T.; Nagy, A.; Treindl, L. Analysis of Asymmetric Sigmoid Kinetic Curves of Autocatalytic Reactions. *Collect. Czech. Chem. Commun.* **1993**, *58*, 775-782.

- (18) Axelrod, D.; Koppel, D.E.; Schlessinger, J.; Elson, E.; Webb, W. W. Mobility Measurement by Analysis of Fluorescence Photobleaching Recovery Kinetics. *Biophys. J.* **1976**, *16*, 1055-1069.
- (19) Chequer, F. M. D.; Venancio, V. P.; Bianchi, M. L. P.; Antunes, L. M. G. Genotoxic and Mutagenic Effects of Erythrosine B, a Xanthene Food Dye on HepG2 Cells. *Food Chem. Toxicol.* **2012**, *50*, 3447-3451.
- (20) Krause, A. W.; Carley, W. W.; and Webb, W. W. Fluorescent Erythrosine B is Preferable to Trypan Blue as a Vital Exclusion Dye for Mammalian-Cells in Monolayer-Culture. *J. Histochem. Cytochem.* **1984**, *32*, 1084-1090.
- (21) Sibrian-Vazquez, M.; Escobedo, J. O.; Lowery, M.; Fronczek, F. R.; Strongin, R. M. Field Effects Induce Bathochromic Shifts in Xanthene Dyes. *J. Am. Chem. Soc.* **2012**, *134*, 10502-10508.
- (22) Maryakhina, V. S. Nature of Phosphorescence Kinetics of Xanthene Dyes in Biological Media. *Laser Phys.* **2016**, *26*, 105603.
- (23) Pellosi, D. S.; Batistela, V. R.; De Souza, V. R.; Scarmínio, I.; Caetano, W.; Hioka, N. Evaluation of Photodynamic Activity of Xanthene Dyes on Artemia Salina Described by Chemometric Approaches. *Ann. Acad. Bras. Cienc.* **2013**, *85*, 1267-1274.
- (24) Wood, S.; Metcalf, D.; Devine, D.; Robinson, C. Erythrosine is a Potential Photosensitizer for the Photodynamic Therapy of Oral Plaque Biofilms. *Antimicrob. Chemother.* **2006**, *57*, 680-684.
- (25) Wainwright, M. Photodynamic Antimicrobial Chemotherapy (PACT). *Antimicrob. Chemother.* **1998**, *42*, 13-58.
- (26) Arakane, K.; Ryu, A.; Takarada, K.; Masunaga, T.; Shinmoto, K.; Kobayashi, R.; Mashito, S.; Hirobe, M. Measurement of 1268 nm Emission for Comparison of Singlet Oxygen ($^1\Delta(g)$) Production Efficiency of Various Dyes. *Chem. Pharm. Bull.* **1996**, *44*, 1-4.
- (27) Lindig, B. A.; Rodgers, M. A. J. Laser Photolysis Studies of Singlet Molecular Oxygen in Aqueous Micellar Dispersions. *J. Phys. Chem.* **1979**, *83*, 1683-1688.
- (28) Kanofsky, J. R.; Sima, P. D. Structural and Environmental Requirements for Quenching of Singlet Oxygen by Cyanine Dyes. *Photochem. Photobiol.* **2000**, *71*, 361-368.
- (29) Herculano, L. S.; Malacame, L. C.; Zanuto, V. S.; Lukaszewicz, G. V. B.; Capeloto, O. A.; Astrath, N. C. G. Investigation of the Photobleaching Process of Eosin Y in Aqueous Solution by Thermal Lens Spectroscopy. *J. Phys. Chem. B* **2013**, *117*, 1932-1937.
- (30) Gerola, A. P.; Semensato, J.; Pellosi, D. S.; Batistela, V. R.; Rabello, B. R.; Hioka, N.; Caetano, W. Chemical Determination of Singlet Oxygen from Photosensitizers Illuminated with LED: New Calculation Methodology Considering the Influence of Photobleaching. *J. Photochem. Photobiol. A Chem.* **2012**, *232*, 14-21.
- (31) Talhavini, M.; Corradini, W.; Alvars, T. D. Z. The Role of the Triplet State on the Photobleaching Process of Xanthene Dyes in Poly(vinyl alcohol) Matrix. *J. Photochem. Photobiol. A Chem.* **2001**, *139*, 187-197.
- (32) Dibbern-Brubelli, D.; De Oliveira, M. G. Temperature Dependence of the Photobleaching Process of Fluorescein in Poly(vinyl alcohol). *J. Photochem. Photobiol. A Chem.* **1995**, *85*, 285-289.
- (33) Brennetot, R.; Georges, J. Transient Absorption of the Probe Beam by the Erythrosine Triplet in Pulsed-Laser Thermal Lens Spectrometry: The Influence of the Solvent, Oxygen and Dye concentration. *Chem. Phys. Lett.* **1998**, *289*, 19-24.
- (34) Harriman, A.; Porter, G.; Searle, N. Reversible Photo-oxidation of Zinc Tetraphenylporphine by Benzo-1,4-quinone. *J. Chem. Soc., Faraday Trans. 2* **1979**, *75*, 1515-1521.
- (35) Gorman, A. A.; Rodgers, M. A. J. Singlet Molecular Oxygen. *Chem. Soc. Rev.* **1981**, *10*, 205-231.
- (36) Gorman, A. A.; Lovering, G.; Rodgers, M. A. J. Entropy-Controlled reactivity of Singlet Oxygen ($^1\Delta(g)$) Toward Furans and Indoles in Toluene - Variable Temperature Study by Pulse Radiolysis. *J. Am. Chem. Soc.* **1979**, *101*, 3050-3055.
- (37) Usui, Y.; Kamogawa, K. Standard System to Determine Quantum Yield of Singlet Oxygen Formation in Aqueous Solution. *Photochem. Photobiol.* **1974**, *19*, 245-247.
- (38) Li, F. H.; Kong, Q. Q.; Chen, P.; Chen, M.; Liu, G. G.; Lv, W. Y.; Yao, K. Effect of Halide Ions on the Photodegradation of Ibuprofen in Aqueous Environments. *Chemosphere* **2017**, *166*, 412-417.
- (39) Goda, Y.; Sato, K.; Hori, N.; Takeda, M.; Maitani, T. Liberation of Halide Ions from Xanthene Colours by Photoirradiation. *Chem. Pharmaceut. Bull.* **1994**, *42*, 1510-1513.
- (40) Keum, Y. S.; Kim, J. H.; Li, Q. X. Relationship Between Singlet Oxygen Formation and Photolysis of Phloxine B in Aqueous Solution. *J. Photosci.* **2003**, *10*, 219-223.
- (41) Rodgers, M. A. J.; Snowden, P. T. Lifetime of $O_2(^1\Delta(g))$ in liquid water as determined by time-resolved infrared luminescence measurements. *J. Am. Chem. Soc.* **1982**, *104*, 5541-5543.
- (42) Brun, A. M.; Harriman, A. Energy-Transfer and Electron-Transfer Processes Involving Palladium Porphyrins Bound to DNA. *J. Am. Chem. Soc.* **1994**, *116*, 10383-10393.
- (43) King, G. A. M. Auto-Catalysis. *Chem. Soc. Rev.* **1978**, *7*, 297-316.
- (44) Mata-Perez, F.; Perez-Benito, J. F. The Kinetic Rate Law for Autocatalytic Reactions. *J. Chem. Educ.*, **1987**, *64*, 925-927.
- (45) Haag, W. R.; Hoigne, J.; Gassman, E.; Braun, A. M. Singlet Oxygen in Surface Waters. 1. Furfuryl Alcohol as a Trapping Agent. *Chemosphere* **1984**, *13*, 631-640.
- (46) Tanaka, K.; Miura, T.; Urano, Y.; Kikuchi, K.; Higuchi, T.; Nagano, T. Rational Design of Fluorescein-Based Fluorescence Probes, Mechanism-Based Design of a Maximum Fluorescence Probe for Singlet Oxygen. *J. Am. Chem. Soc.* **2001**, *123*, 2530-2536.
- (47) Levitus, M.; Ranjit, S. Cyanine Dyes in Biophysical Research: the Photophysics of Polymethine Fluorescent Dyes in Biomolecular Environments. *Quart. Rev. Biophys.* **2011**, *44*, 123-151.
- (48) Ishiyama, K.; Nakamura, K.; Ikai, H.; Kanno, T.; Kohno, M.; Sasaki, K.; Niwano, Y. Bactericidal Action of Photogenerated Singlet Oxygen from Photosensitizers Used in Plaque Disclosing Agents. *PLOS ONE* **2012**, *7*, e37871.
- (49) Perez-Benito, J. F. Autocatalytic Reaction Pathway on Manganese Dioxide Colloidal Particles in the Permanganate Oxidation of Glycine. *J. Phys. Chem. C* **2009**, *113*, 15982-15991.
- (50) Perez-Benito, J. F.; Arias, C.; Amat, E. A Kinetic Study of the Reduction of Colloidal Manganese Dioxide by Oxalic Acid. *J. Colloid. Interface Sci.*, **1996**, *177*, 288-297.
- (51) d'Arlas, B. F.; Rueda, L.; Stefani, P. M.; de la Caba, K.; Mondragon, I.; Eceiza, A. Kinetic and Thermodynamic Studies of the Formation of a Polyurethane Based on 1,6-Hexamethylene diisocyanate and poly(carbonate-co-ester) diol. *Thermochim. Acta*, **2007**, *459*, 94-103.
- (52) Siani, G.; Angelini, G.; De Maria, P.; Fontana, A.; Pierini, M. Solvent Effects on the Rate of the Keto-Enol Interconversion of 2-Nitrocyclohexanone. *Org. Biomol. Chem.*, **2008**, *6*, 4236-4241.
- (53) Gottfried, V.; Kimel, S. Temperature Effects on Photosensitized Processes. *J. Photochem. Photobiol. B Biol.* **1991**, *8*, 419-430.
- (54) Wang, J.; Gu, J. D.; Nguyen, M. T.; Springsteen, G.; Leszczynski, J. From Formamide to Purine: A Self-Catalyzed Reaction Pathway Provides a Feasible Mechanism for the Entire Process. *J. Phys. Chem. B* **2013**, *117*, 9333-9342.
- (55) Mihaylov, T. T.; Parac-Vogt, T. N.; Pierloot, K. A Mechanistic Study of the Spontaneous Hydrolysis of Glycylserine as the Simplest Model for Protein Self-Cleavage. *Chem. Eur. J.* **2014**, *20*, 456-466.
- (56) Rodriguez, R.; Arroyo, R.; Salinas, P. Dynamic Light-Scattering Studies of the Stability and Growth of Silica Particles. *J. Non-Cryst. Solids* **1993**, *159*, 73-79.

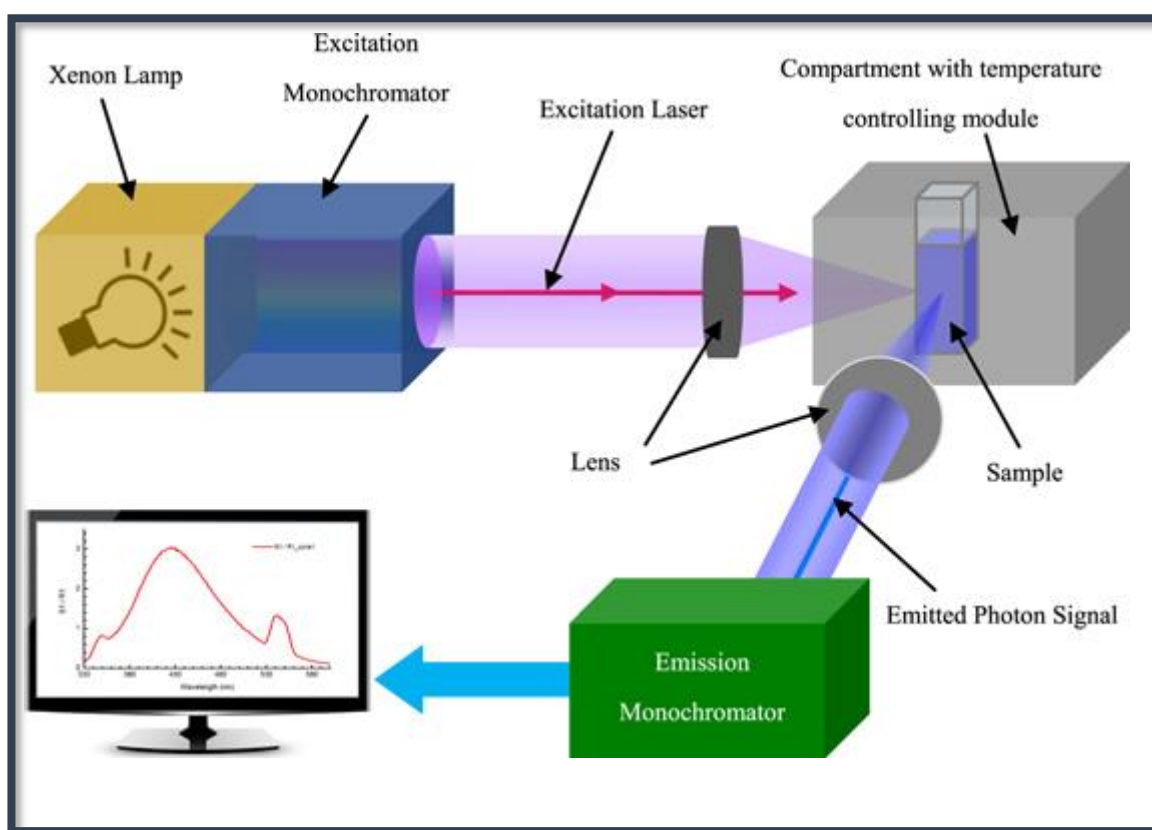
(57) Neta, P.; Huie, R. E.; Ross, A. B. Rate Constants for Reactions of Peroxyl Radicals in Fluid Solution. *J. Phys. Chem. Ref. Data* 1990, 19, 413-505.

Authors are required to submit a graphic entry for the Table of Contents (TOC) that, in conjunction with the manuscript title, should give the reader a representative idea of one of the following: A key structure, reaction, equation, concept, or theorem, etc., that is discussed in the manuscript. Consult the journal's Instructions for Authors for TOC graphic specifications.



Chapter 7.

Experimental Details



SPECTROSCOPY PLAYS A CRITICAL ROLE IN ESTABLISHING REACTIONS RATES, EFFICIENCIES AND MECHANISMS AND IS USED EXTENSIVELY IN THIS WORK.

Table 1. List of the main compounds studied in this work, giving sample abbreviation and origin.

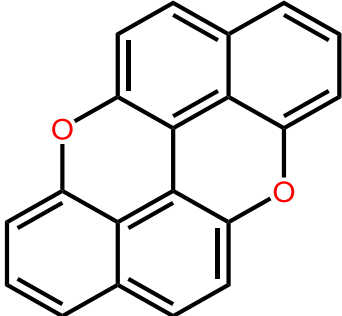
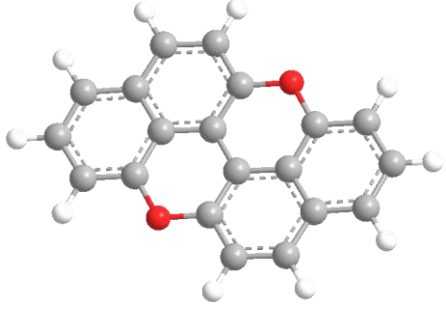
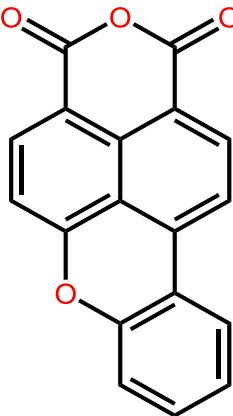
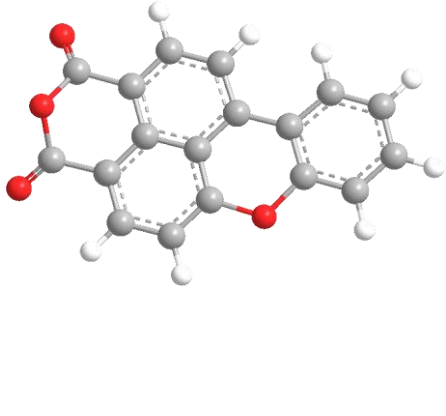
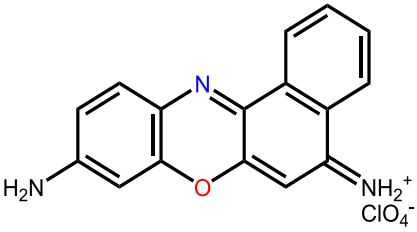
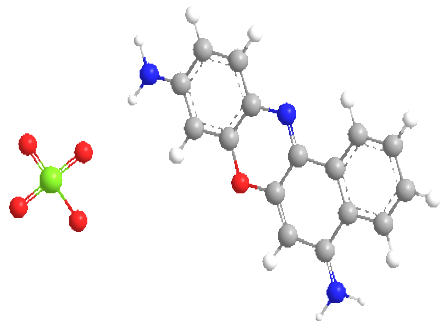
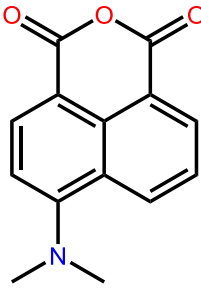
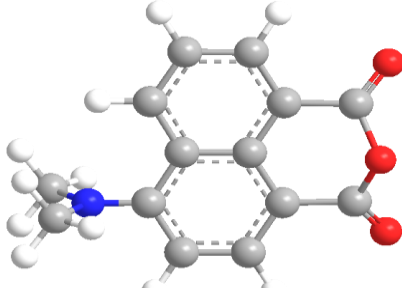
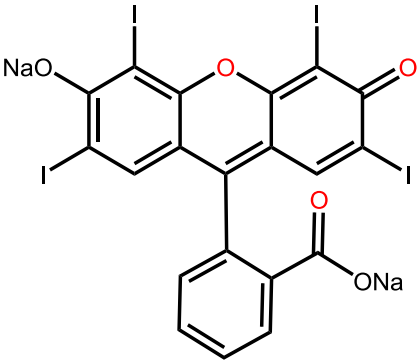
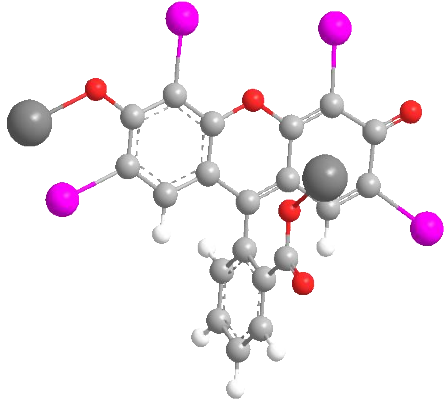
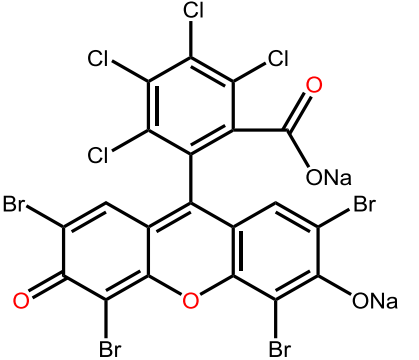
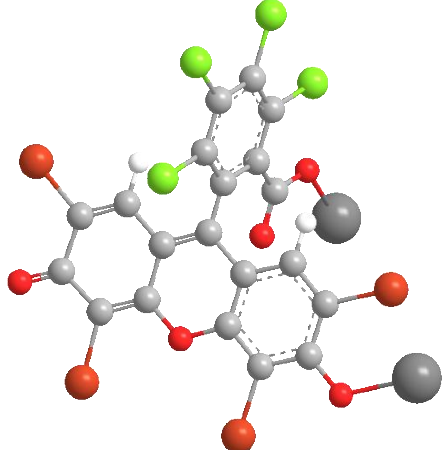
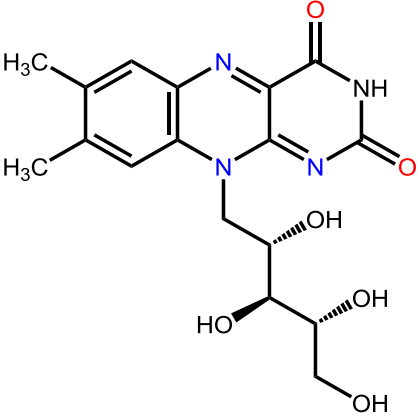
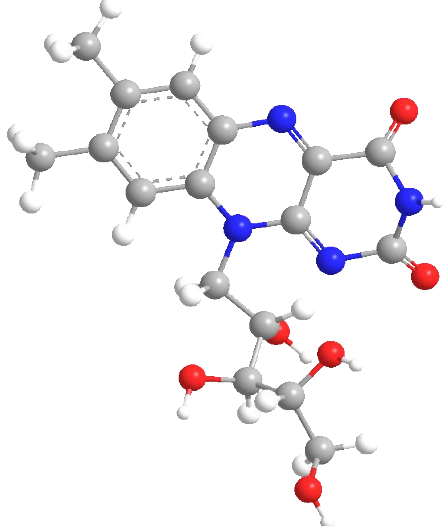
Chapter	Symbol	Origin	λ_{ABS} [nm]	λ_{FLU} [nm]	Chemical formula	Chemical structure
2	PXX	MPL ^[a]	442	451		
3	CXD	MPL ^[a]	420 441	467 497		
4	CVP	Aldrich	469 594	627		
5	MBIC	MPL ^[a]	414	524		

Table 1. Continued.

6	Ery	PGC ^[b]	527	560	 <p>Chemical structure of Erythrosine sodium salt, showing a xanthone core with iodine substituents and a sodium carboxylate group.</p>	 <p>3D ball-and-stick model of Erythrosine sodium salt, showing the spatial arrangement of atoms.</p>
6	PhB	PGC ^[b]	550	569	 <p>Chemical structure of Phloxalin B sodium salt, showing a xanthone core with chlorine and bromine substituents and a sodium carboxylate group.</p>	 <p>3D ball-and-stick model of Phloxalin B sodium salt, showing the spatial arrangement of atoms.</p>
6	RF	PGC ^[b]	365 449	523	 <p>Chemical structure of Riboflavin, showing a ribityl side chain and a dimethyl-substituted isoalloxazine ring system.</p>	 <p>3D ball-and-stick model of Riboflavin, showing the spatial arrangement of atoms.</p>

[a] Molecular Photonics Laboratory. [b] Procter & Gamble Company.

7.1 Materials

All solvents used throughout this research project were of the highest possible purity, usually spectrophotometric grade, with the exception of solvents used for electrochemical studies. The spectrophotometric grade solvents were purchased from Sigma-Aldrich and used without further purification after checking for the presence of fluorescent impurities. The purity and properties of solvents used are important here, especially when the experiment involves long-term steady-state irradiations for monitoring photo-bleaching kinetics. In some cases, several samples of a given solvent were compared or samples were further purified by colleagues working in the synthetic chemistry laboratories. Factors such as dielectric constant and polarity can affect the spectroscopic behaviour of dyes, for example peak maxima, Stokes' shifts, fluorescence quantum yields and so on. In order to be consistent, a single literature source¹ was used to identify these properties wherever possible. Solvents employed for electrochemical investigations were refluxed over appropriate drying reagents, distilled and used immediately. Tetrabutylammonium hexafluorophosphate and ammonium hexafluorophosphate were used as electrolytes, both being purchased from Sigma-Aldrich and used after recrystallisation. These materials were kept dry. Special materials, such as sucrose octaacetate, were purified by standard protocols before use and certain solvents, such as butyronitrile, were redistilled by other members of the group before use. Anhydrous solvents were purchased from Sigma-Aldrich and used by way of syringe injection techniques. Ethers, most notably 2-methyltetrahydrofuran – used extensively for low-temperature emission spectroscopy – was used fresh and kept away from contact with air. Samples were replaced at very regular intervals in order to avoid contamination by peroxides.

The majority of the compounds studied here were synthesised in the Molecular Photonics Laboratory under the supervision of Prof. A. C. Benniston. These samples were subjected to comprehensive purification procedures before being considered for spectroscopic examination. The compounds were fully characterised by a wide battery of analytical techniques. Some samples were further analysed by 700 MHz NMR spectroscopy by Dr. Corrine Wills at Newcastle University. We are grateful to both Prof. Benniston and Dr. Wills for their collaboration and for many fruitful discussions during the course of this work. Dr. Patrycja Stachelek recorded some of the electrochemical measurements on the new compounds. Sometimes, the amount of sample provided - the emphasis being placed on purity not quantity - was insufficient for electrochemistry or for determination of the molar absorption coefficient. The latter measurements were made at the end of the series of experiments, often consuming all the remaining material. Often, samples were part of a small series, with control compounds being available for comparative studies.

Additional compounds were synthesised in Strasbourg by the research group supervised by Dr. Raymond Ziessel. The water-soluble sensitizers (Phloxine B, Riboflavin and Erythrosine) were provided by the Procter & Gamble Company and were analysed by NMR spectroscopy before starting the spectroscopic studies. Certain compounds, notably Cresyl Violet, were purchased from commercial sources and tested by TLC analysis prior to use. In order to measure fluorescence quantum yields (ϕ_f), some well-known and thoroughly established reference compounds were used. These include magnesium *meso*-tetraphenylporphyrin (Mg[TPP]),² Cresyl Violet,^{3,4} Rhodamine 6G,^{5,6} Rhodamine B,^{7,8} and Nile Red.^{9,10} The fluorescence quantum yields of these standards are available from peer-reviewed literature citations. In addition, many secondary standards were employed for quantum yield measurements. Without exception, these were BODIPY-based dyes studied by other members of the MPL. Appropriate solvents were used for these studies and great care was taken to ensure that the solution was free from undissolved solid material. Some fluorescence measurements, notably those with solid samples, were undertaken with an integrating sphere. All samples were stored as solids in the dark and usually kept at low temperature.

7.2 UV-Visible Absorption Spectroscopy

All the solutions used for absorption spectroscopy were prepared using spectrophotometric grade solvents. Most spectra were recorded using a Hitachi U3310 dual-beam spectrophotometer. Cuvettes used in these experiments were fabricated from optical quality quartz. The scan rate used for routine spectra collection was usually set at 120



nm/min, slit widths at 1 nm, and the resolution was set at 0.2 nm unless specified otherwise. The possible error in wavelength position is estimated to be less than 1 nm. The concentration of solutions was kept between 10^{-7} M, for samples with very high molar absorption coefficient (over $100,000 \text{ M}^{-1} \text{ cm}^{-1}$), and 10^{-5} M. In some cases, a Perkin-Elmer Lambda 35 spectrophotometer was used due to its better stability at lower energies. Essentially, this translates to less noise at longer wavelengths. All of the settings and procedures were kept the same as for the Hitachi U3310 spectrophotometer. In order to determine the molar absorption coefficient (ϵ) of the dyes described here, the Beer-Lambert law was used Equation 7.1. The molar absorption coefficient in units of $\text{M}^{-1} \text{ cm}^{-1}$ is determined by dividing absorbance (A , no units) by molar concentration (C) multiplied by the pathlength in centimetres. As necessary, a series of cuvettes of different pathlengths was employed for improved precision and a range of concentrations was used. The limit to the accuracy of these measurements was set by the amount of material available. Solutions were filtered with a sub-micron membrane filter prior to recording the absorption spectrum. Temperature

variations were achieved with a circulating fluid bath. A homemade variable pathlength optical cell was used for certain studies where the concentration was varied over a wide range.

$$A = \epsilon Cl \quad \text{Equation 7.1}$$

7.3 Emission Spectroscopy

Fluorescence spectra were recorded using a Hitachi F-4500 fluorescence spectrophotometer, for most measurements the scan rate was kept at 60 nm/min. The excitation and emission slit widths were kept at 2.5 for most solutions. They were usually increased for solid samples as well as for microscope slides and low-temperature measurements carried out using an optical



cryostat. The response rate was kept at the auto setting but was varied for weak samples. Dilute solutions were used, the absorbance at the excitation wavelength was kept between 0.05 and 0.1. This was done in order to avoid re-absorption and inner-filter effects. The solutions used were always prepared using spectrophotometric grade solvents and recorded using quartz cuvettes. Solutions were prepared freshly and passed through a sub-micron membrane filter before making the measurement. Optical filters were always used to isolate fluorescence from scattered excitation light coming from the excitation source. As for absorption spectroscopy, the resolution of all spectra recorded was 0.2 nm. This guarantees small experimental error for the emission wavelength, approximately 1 nm. Without exception, fluorescence excitation spectra were recorded for the dyes of interest and compared with the corresponding absorption spectrum. Spectra were corrected for spectral imperfections using a calibration curve supplied by the instrument maintenance staff. At regular intervals, calibration curves were recorded using Rhodamine B solutions supplied by the instrument maker. The instrument was maintained by LAT Inc. and serviced at six-monthly intervals to ensure proper calibration of wavelength and intensity linearity. All spectral data were removed from the controlling PC and analysed separately, usually after conversion from wavelength to wavenumber. All fluorescence measurements were repeated several times to ensure self-consistency.

Low-temperature studies were performed using an Oxford Instruments Optistat DN cryostat, connected to an ITC temperature controller (Figure 1). The cryostat used here is a nitrogen cryostat, i.e. it uses liquid nitrogen to cool a sample by conduction via a stream of nitrogen gas. The nitrogen reservoir and heat exchanger are surrounded by high vacuum. The temperature is regulated using a precision controller and can be adjusted by manual nitrogen flow control. Solutions were prepared in a solvent known to form an optical glass at low temperature. The optical absorbance at the excitation wavelength was kept low, between 0.05 and 0.1. The prepared solution was then purged with nitrogen for 5 minutes. The sample was sealed into a glass cuvette and placed in the sample holder of the cryostat. Using our set up, it is possible to record absorption, emission and excitation spectra over a range from 80 to 340K.



Figure 1. Photograph of the cryostat used for low-temperature studies.

High-temperature spectroscopy was carried out on solid state samples in the form of a KBr disc. The measurements were carried out using a temperature-controlled, demountable liquid cell purchased from Harrick Scientific Products (Figure 2). This cell was used for measurements over the range from 298 to 513K (although according to the manufacturer the lowest temperature it can go to is 223K). High-temperature measurements were also carried out on liquid samples,



Figure 2. High-temperature cell and the temperature controller used in this work.

this was done using either the demountable cell or a circulating fluid bath. Using this latter technique, the available temperature range is from 273K to about 333K. At the lower temperatures, the cell windows were purged constantly with a strong flow of N₂ to avoid misting, especially on humid days.

Low-temperature phosphorescence was studied using the optical cryostat, but in most cases the sample solution was doped with around 20% w/w iodoethane to promote intersystem crossing.^{11, 12} In some cases, an optical Dewar was used in place of the cryostat. The Dewar is fitted with quartz windows at 90° to each other. A long glass tube, 1cm in diameter, holds the sample, and fits into a PTFE stopper. The Dewar is filled with liquid nitrogen to obtain a set temperature of 77K. The Dewar was mounted in the sample chamber of the Hitachi F4500 emission spectrophotometer. The slit widths were usually set at 10 nm. For each experiment, five separate spectra were averaged.

7.4 Fluorescence Lifetime Measurements

Time-resolved fluorescence spectroscopy is an essential technique needed in order to investigate the excited state of a luminescent chromophore. Factors contributing to the overall emission lifetime are solvent relaxation, interactions with surrounding molecules, and changes in macromolecular conformation. Lifetime measurements were carried out at room temperature using optically dilute samples. The absorbance at the excitation wavelength was about

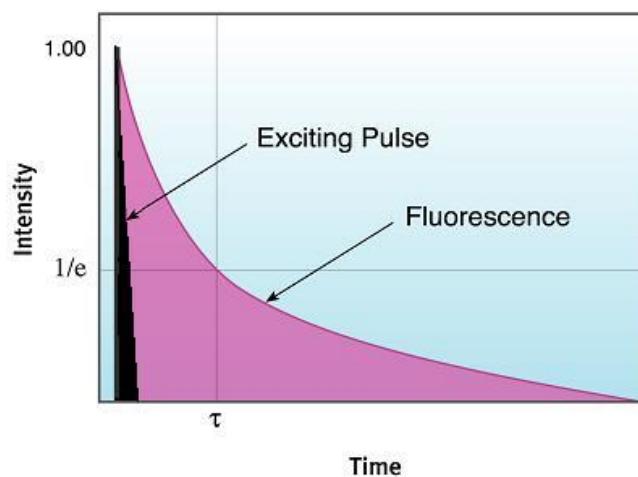


Figure 3. Example of an emission decay curve.

0.1. For most compounds studied here, 600 channels were used and 150 runs were signal averaged. The method used for recording fluorescent lifetimes was time-correlated, single photon counting (TCSPC).¹³ Here, results are presented as a graph of time (ns) against voltage (V). It is a highly sensitive method with good resolution. TCSPC determines the statistical distribution of the intensity decay by recording the arrival times of individual photons after the incident flash of light. A high-resolution PTI EasyLife set-up was used to collect data, pulsed laser diodes were used as excitation source with output at 310, 440, 505, 525 or 635 nm. The scattered laser light was measured using a solution of Ludox in distilled water to generate the instrument response (IRF).

Data analysis was carried out using Felix 32 software. In order to perform the analysis, the decay curve needs to be selected, the range of interest identified and highlighted. The method used was non-linear, least-squares iteration. This approach requires an initial estimate of the lifetime and the preferred method of analysis. A mono-exponential fit was usually the approach of choice, at least at the beginning of the analysis, unless there was a possibility of a second component. A range of time bases is needed and a small variation of count rates should be used to increase reliability of the output. Emission can be isolated from scattered laser light using optical filters in conjunction with a high-radiance monochromator. Wherever possible, different excitation wavelengths should be used. After analysis, it is necessary to judge the quality of the weighted residuals, the auto-correlation function and the deconvoluted decay. Data analysis was made at the instrument using software provided by the manufacturer. Protocols for assessing the quality of the fit were taken from the literature. (Figure 3), example of an emission decay curve.

7.5 Electrochemistry

Cyclic voltammetry (Figure 4) was carried out using dry solvents, usually anhydrous dichloromethane or acetonitrile; we thank Dr. Patrycja Stachelek for help with these measurements. The solvent was used to prepare a 0.1M electrolyte background solution. The background solution was purged with dried nitrogen in order to eliminate any dissolved oxygen, great care

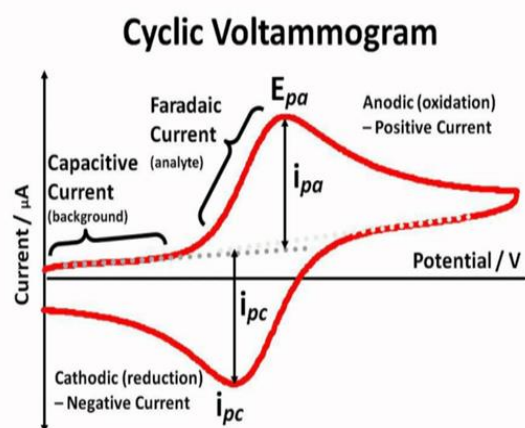


Figure 4. The cyclic voltammogram curve.

was taken to make sure the cell was kept dry and no water was present in the system before addition of the compound of interest at millimolar concentration. This was done by recording a background CV, once satisfied there is neither water nor oxygen present in the system the compound was added. Electrodes most often used were glassy carbon or platinum working electrodes and silver or platinum counter electrodes. The reference electrode was an Ag/Ag^+ electrode. The working and counter electrodes were polished using an alumina slurry before use. Ferrocene was used as an internal reference. The measurements were also done at a range of scan rates as this provides valuable information on the degree of reversibility of the oxidation/reduction reaction.¹⁴ The software used to record and extract information was Chi600.

7.6 Laser Flash Photolysis

Laser flash photolysis studies were made using an Applied Photophysics. LKS_70 spectrometer. The excitation was provided with a frequency-doubled Nd-YAG laser (FWHM= 5 ns) pumping an OPO to provide excitation at 440 nm for PXX in deoxygenated cyclohexane and for MBIC in deoxygenated 2-MTHF. The excitation wavelength was changed to 500 nm for Erythrosine. Typical pulse energies were in the region of 5 mJ and, at each wavelength, a minimum of five signals were averaged. The monitoring beam was provided by a pulsed xenon arc lamp. The signal was directed to a high-radiance monochromator and then to a fast response transient digitizer. A solution was prepared with an absorbance of about 0.3 at the excitation wavelength and bubbled for 15 minutes with purified N₂ prior to the experiment. Transient differential absorption spectra were compiled point-by-point.

7.7 Preparation of solid samples

Compressed disks were prepared by the grinding the appropriate weight of the compound with oven-dried KBr to obtain 1% w/w concentration. The powdered mixture was placed in the sample holder between the two metal dyes and compressed under mild vacuum. A special holder was constructed in the Machine Shop that allowed the translucent disks to be housed in each of the spectrophotometers. Blank disks, without the compound of interest, were used as control samples. In separate experiments, the water clear poly ester casting resin (Easy Composites Ltd.) was pretreated with the catalyst (i.e., methyl ethyl ketone peroxide) and poured carefully over a layer of crystals packed into a circular Teflon template. The liquid was set aside for 48h in the dark. After the setting solid, fresh cotton was used to polish the edges. The disk was inserted into a slot machined into the holder of the Teflon block that housed a silicon solar cell (Conrad 19-12-81, 0.5 V, 400 mA). A 250 W solar illuminator was used to illuminate the disk.

Single crystals of the compound (i.e., MBIC) (Figure 5) were mounted on a rod and put carefully inside the sample chamber of the instrument. Mixtures of MBIC and Rhodamine B were prepared in solution and set aside to crystallize slowly in the dark. To extract the Rhodamine B from the doped crystals, an aliquot of the MBIC was placed



Figure 5. Photograph of MBIC.

on a glass frit and then the cold water was used to wash the sample. The loading of the surface of quartz slides or dye adhered onto glass was measured in much the same manner.

Suspensions of latex beads packed with fluorescent compound were prepared as follows: The proper amount of the compound dissolved in acetone was subjected to a short burst in the ultrasonic bath and then filtered to give a stock solution. The amidine latex (4% W/V, 0.04 μm) (100 μl) was mixed with various amounts of the stock solution and diluted with glycerol before being put again in the ultrasonic bath. The fluorescence spectra were measured for the various mixtures, thereby allowing the relationship between fluorescence and concentration to be studied.

7.8 Light-initiated Polymerization

The solution of diphenyl iodonium chloride (DPI) (0.015 M) with methyl methacrylate (6.2 M) were prepared in methanol and deoxygenated with a dry N_2 stream. Then CXD (20 μM) was added to the solution under anaerobic conditions, and obtain the yellow colour with strong fluorescence with no effect on the viscosity, then after the illumination with UV light, the colouration was disappeared. The polymerization was followed through the checking on the viscosity of solution. The photo-polymerization of methyl methacrylate was done by methyl methacrylate dissolved in methanol (10ml) was put in the glass tube fitted with a subaseal stopper. The CXD (photo-initiator) (20 μM) was dissolved in a small amount of propylene carbonate and diphenyl iodonium chloride (0.015M) added and the solution was purged with dry N_2 for 20 min. Irradiation with white light from a 400W halogen lamp of the glass tube was continued for set time periods, IR radiation was removed through the filtration of the glass tube by a water bath. The course of polymerization was checked by the change in viscosity of the solution as the reaction proceeded. The dye (CXD) concentration was set at ca. 0.1 mg dissolved in CHCl_3 (10 ml), and the disc was put in the solution and left for 1 hour. The disc was cut from PMMA. The disc was removed and washed with acetone and CHCl_3 to remove any dye adhered to the surface and dried in air. The mixture of the dye (ca. 0.1 mg) and PMMA (ca. 100 mg) pellets in CHCl_3 was prepared and sonicated for 5 minutes. The solution was put onto clean glass slides and the solvent evaporated.

7.9 Photo-bleaching Studies

Broadband bleaching was performed by placing samples in front of a 400W HQI discharge lamp, filtered to remove IR radiation. Films and solutions were mounted in holders 50 cm from the lamp. To prevent polymer damage and to create a bleached area large enough to perform absorption measurements, a diffuser was placed 3.5 cm from the light source with the film a further 3 cm distant. Solutions were bleached and measured in stoppered 1 cm quartz cuvettes. The course of reaction was monitored by absorption spectroscopy. In separate studies, notably the work concerned with photo-bleaching of Phloxine B, Erythrosine and Riboflavin, an optical rail was built to facilitate monochromatic excitation of the dye. Here, a high-power LED was used as excitation source, together with a camera lens to focus

illumination onto the solution. A special stirrer motor was used to agitate the solution. The excitation beam was passed through the sample and detected continuously with a solar cell. The output signal was sent to a data logger and then to a PC for analysis. This latter set-up allows long illuminations to be followed without disturbing the sample. It also permits quantum yields and bleaching kinetics to be calculated. Solutions were routinely purged with air, oxygen or nitrogen as required.

7.10 Fluorescence Quantum Yield

Fluorescence quantum yield measurements were carried out with great care at room temperature. The samples were prepared as described above. In principle, the numbers of absorbed and emitted photons need to be measured in order to determine the emission quantum yield. Equation 7.2 is used to calculate quantum yield of fluorescence. Here, F_S is the area under the emission curve of the sample, whereas F_R is the area under the emission curve of the reference compound recorded over the same spectral range. The term A_R refers to the effective absorbance at the respective excitation wavelength for the reference compound (A_S is the corresponding value for the sample) and finally n_S and n_R are refractive index for the solvent used to dissolve the sample and for the reference respectively. Wherever possible, the same solvent was used for sample and reference. The spectral correction factor supplied with the instrument was used and all data manipulations were made after conversion from wavelength to wavenumber. As appropriate, reduced emission spectra were used.

$$\Phi = \frac{F_S \times (1 - \exp(-A_R \times \ln(10))) \times n_S^2}{F_R \times (1 - \exp(-A_S \times \ln(10))) \times n_R^2} \Phi_R \quad \text{Equation 7.2}$$

When measuring a fluorescence quantum yield great care needs to be taken as there are many possibilities for experimental error: These include inner filter, temperature, impurity effects amongst others. The use of a reference standard is a further source of error. There are very few reference compounds with a well-established fluorescence quantum yield that is free of potential problems. Often finding a reference with similar absorption transitions is a great challenge, however it is crucial for the measurement to be successful. Cresyl Violet is a good example of the sort of problems that might be encountered. This reference is useful for the red region but the reported quantum yield is sensitive to concentration and solvent, varying enormously over a modest range. We found quantum yields ranging from unity to less than 20% according to the experimental conditions.

Standard quartz cuvettes were used throughout, and the absorbance at the excitation wavelength was never higher than 0.1, this is crucial if one wants to avoid the inner filter effect. Often, Φ is dependent

on temperature, this is especially so for molecular-scale rotors. Therefore, all experiments are assumed to be carried out at 20°C unless stated otherwise. The rate of radiative decay is also dependent on solvent refractive index and therefore one will encounter studies on the effect of solvent on the rate of radiative decay (and by extension the fluorescence quantum yield). Experimentally, it is crucial to establish that the spectrophotometer is properly calibrated and we regularly employed a concentrated solution of Rhodamine 6G in ethanol to confirm the correction factor. In all cases, the absorbance at the excitation wavelength was checked before and after measuring the emission spectrum. This was done to confirm that the solution was stable and free from particulate material.

7.11 Jablonski Diagram

Much of the work described in this thesis relates to determining radiative and nonradiative decay routes for organic fluorophores. Such systems can be conveniently explained in terms of a Jablonski diagram¹⁵ (Figure 6). In fact, Jablonski diagrams have become popular in many areas of contemporary science as a simple way to express energy levels for electronically excited states and interconversion between these states. A conventional Jablonski diagram separates states according to their spin multiplicity. Internal conversion or intramolecular vibronic coupling allows interchange between states of the same multiplicity. Fluorescence is usually competitive only with internal conversion from the lowest-energy excited singlet state. Intersystem crossing, which is promoted by spin orbit coupling, allows states of different spin multiplicity to exchange. This route can be used to populate and deactivate excited-triplet states. Delayed fluorescence is favoured by reverse intersystem crossing from the triplet state to repopulate the lowest-energy excited-singlet state. We have made use of Jablonski diagrams throughout the thesis to provide a simple explanation of the photophysics of the molecule under study. It might be mentioned here that the conventional Jablonski diagram should be used in conjunction with potential energy surfaces. The latter contain important information about structural changes and state mixing that is not apparent from the Jablonski diagram.

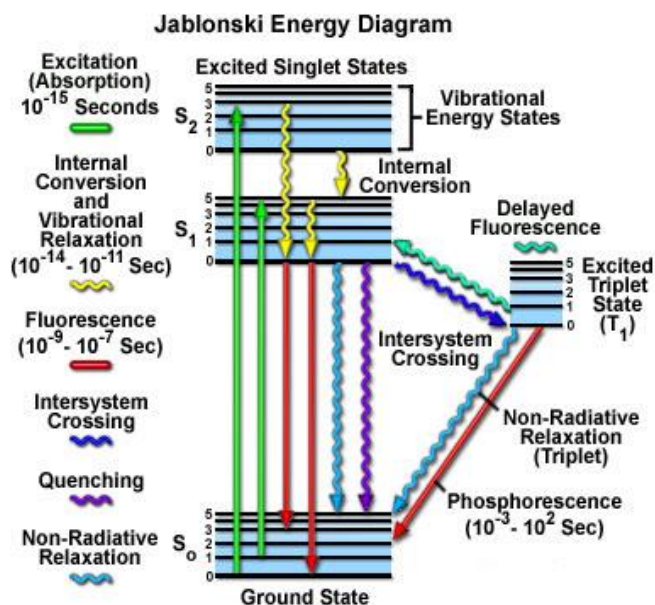


Figure 6. The Jablonski diagram.¹⁶

7.12 Radiative Rate Constant

The radiative rate constant^{17,18} describes the rate at which the excited state of the fluorophore relaxes by a process accompanied by photon emission. This is in competition with a non-radiative process that ultimately returns the molecule to the ground state. The radiative rate constant is determined experimentally from Equation 7.3.

$$k_{rad} = \frac{\phi}{\tau} \quad \text{Equation 7.3}$$

Here, ϕ is the experimentally determined quantum yield, τ is the corresponding excited-state lifetime (in seconds). This experimental estimate of the radiative rate constant can be compared to the theoretical value determined from the Strickler-Berg expression, Equation 7.4.¹⁹

$$k_{rad} = 2.88 \times 10^{-9} n^2 \langle \nu^{-3} \rangle_{av}^{-1} \frac{g_l}{g_u} \int \epsilon d \ln \tilde{\nu} \quad \text{Equation 7.4}$$

Here, n is the solvent refractive index, ν is the fluorescence maximum in cm^{-1} , $\int \epsilon d \ln \tilde{\nu}$ represents the area under the curve (only takes into consideration the lowest-energy transition), and finally $\frac{g_l}{g_u}$ refers to degeneracy of the respective upper and lower states. The Strickler-Berg expression is very useful, however it does have important limitations. Firstly, it needs to be taken into account that it works only for

compounds with a small Stokes' shift. A second important requirement is the mirror symmetry of lowest-energy transition in the absorption spectrum and the emission curve. It is also worth noting that it can only be applied safely when the quantum yield is relatively high, i.e. in excess of 10%. Nevertheless this is a very useful expression, it works very well with molecules that meet the conditions mentioned earlier but it is often applied to cases outside these limits. It might also be mentioned that some authors, notably Birks,²⁰ Knox²¹ and Phillips,²² have questioned the exact formation of the refractive index factor. Knox,²¹ in particular, has questioned the square dependence.

7.13 Non-radiative Decay

The Englman-Jortner energy gap law²³ has been proven to be largely appropriate to study non-radiative processes in a range of excited states. Equation 7.5 demonstrates that the rate constant for a radiationless transition decreases as the energy gap between two states increases.

$$k_{NR} = \frac{\sqrt{2\pi}}{\hbar} \times \frac{C^2}{\sqrt{k_B T h \omega}} \times \exp(-S) \times \exp\left(\frac{-\Upsilon \Delta E}{h \omega}\right) \quad \text{Equation 7.5}$$

Here, k_{NR} is the non-radiative rate constant, C is the electron-vibrational coupling matrix, ΔE is the energy gap between electronic levels, $h\omega$ is the vibrational mode, λ is the nuclear distortion, S is the Huang-Rhys factor Equation 7.6 and finally Υ is a coefficient that depends on the nature of the molecule under study Equation 7.7. It is normal practice to obtain a value for the non-radiative rate constant from the fluorescence quantum yield and excited-singlet state lifetime since it is difficult to monitor the radiationless rate constant directly. In many cases of interest, a new non-radiative channel is accessed at high temperature. As such, it is useful to measure the rate constant for non-radiative decay over a temperature range.

$$S = \lambda / h \omega \quad \text{Equation 7.6}$$

$$\Upsilon = \ln(|\Delta E| / S h \omega) - 1 \quad \text{Equation 7.7}$$

7.14 Vibrational Analysis

PeakFit software is used to deconstruct broad absorption and emission spectral traces into a series of components. We aimed to fit each spectrum into a minimum number of Gaussian-shaped bands. The software estimates the number of components needed, however the operator is able to adjust that estimate (add or remove components) in order to improve the fit and decides whether the estimates need to be of the same half-width. This is an important step as the spectral analysis needs to be scientifically plausible as well as being mathematically accurate. In order to perform PeakFit analysis, a spectral region of interest is selected (usually the lowest energy transition) and the spectra are converted from wavelength (nm) to wavenumber (cm^{-1}). While performing a spectral analysis using PeakFit it is also crucial to determine whether the baseline needs correcting for, if that is the case, the software offers a range of different baseline corrections. Figure 7 is an example of a PeakFit analysis, on the left hand side the experimentally obtained absorption is deconstructed into individual Gaussian bands, on the right hand side the parameters obtained from the spectral fitting are highlighted. Each Gaussian band corresponds to an individual transition, there are several crucial numerical data that can be obtained by carrying out PeakFit analysis like peak position (E_{00}), the full width at half maximum (FWHM), vibrational frequencies ($h\nu$) and peak intensity. This data can in turn be used to carry out more detailed spectral analysis. The reorganization energy is just one, Equation 7.8, example of an important parameter that is calculated using data obtained by spectral fitting.

$$\lambda = \frac{(\Delta\nu_{1/2})^2}{16\ln 2k_B T} \quad \text{Equation 7.8}$$

The success of the spectral fit is determined by evaluating the r^2 value and the standard error value. The r^2 value quantifies the goodness of fit, it's usually a fraction between 0 and 1. The higher the r^2 and lower the standard error the more successful the fit. These two values as well as 95% confidence error, standard deviation, t-values amongst others could be found and compared in the final output file produced by the software. Application of this fitting routine tends to work well when the analysis is of the same compound under different temperature or as a function of polarity of the solvent.

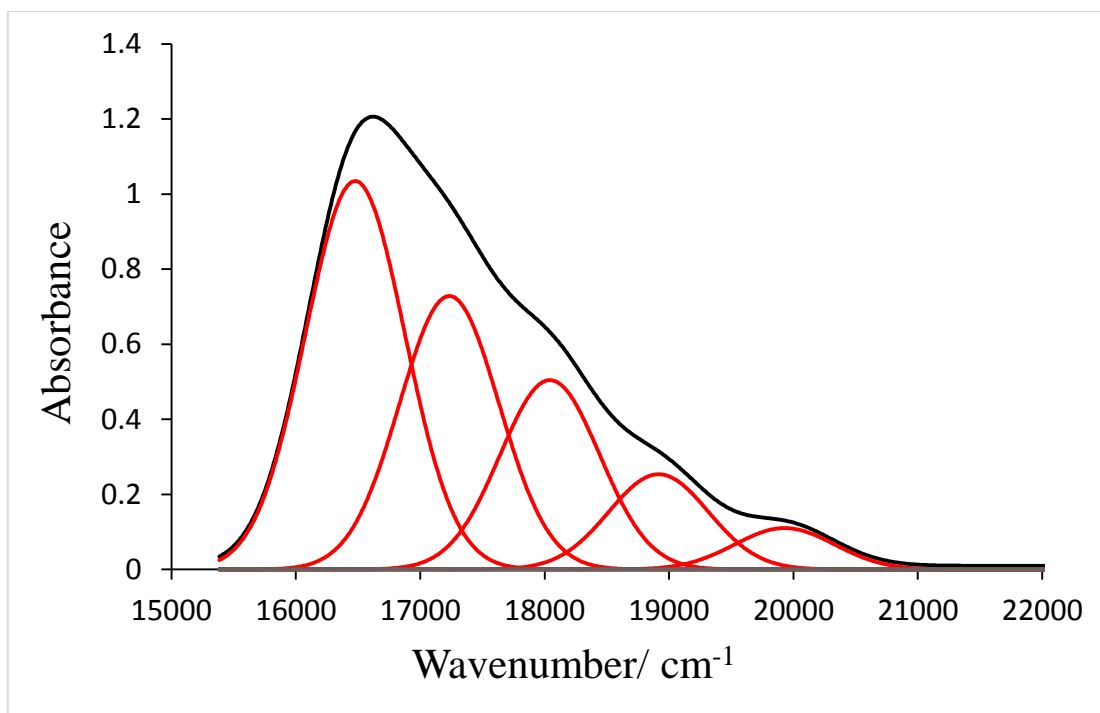


Figure 7. An example of a vibronic analysis, the black line is the original spectrum while the red lines are the individual Gaussian bands derived for CVP.

7.15 References

1. Abboud, J.-L. M.; Notario, R. *Pure Appl. Chem.* **1999**, 71, 645.
2. Harriman, A. *J. Chem. Soc., Faraday Trans. 2.* **1981**, 77, 1281.
3. Magde, D.; Brannon, J. H.; Cremers, T. L.; III, J. O. *J. Phys. Chem.* **1979**, 83, 696.
4. Isak, S. J.; Eyring, E. M. *J. Phys. Chem.* **1992**, 96, 1738.
5. Fischer, M.; Georges, J. *Chem. Phys. Lett.* **1996**, 260, 115.
6. Würth, C.; González, M. G.; Niessner, R.; Panne, U.; Haisch, C.; Genger, U. R. *Talanta.* **2012**, 90, 30.
7. Karstens, T.; Kobs, K. *J. Phys. Chem.* **1980**, 84, 1871.
8. Kubin, R. F.; Fletcher, A. N. *J. Lumin.* **1982**, 27, 455.
9. Fletcher, K. A.; Storey, I. A.; Hendricks, A. E.; Pandey, S.; Pandey, S. *Green Chem.* **2001**, 3, 210.
10. Jose, J.; Burgess, K. *J. Org. Chem.* **2006**, 71, 7835.
11. Beljonne, D.; Shuai, Z.; Pourtois, G.; Bredas, J. L. *J. Phys. Chem. A.* **2001**, 105, 3899.
12. Yang, W.; Zhao, J.; Sonn, C.; Escudero, D.; Karatay, A.; Yaglioglu, H. G.; Küçüköz, B.; Hayvali, M.; Li, C.; Jacquemin, D. *J. Phys. Chem. C.* **2016**, 120, 10162.
13. O'Connor, D. V.; Phillips, D. *Time-Correlated Single Photon Counting*; Academic Press Inc.: London, **1984**.
14. Bard, A. J.; Faulkner, L. R. *Electrochemical Methods: Fundamentals and Applications*; 2nd ed.; John Wiley & Sons, Inc.: New York, **2001**.
15. Jaffé, H. H.; Miller, A. L. *J. Chem. Educ.* **1966**, 43, 469.
16. <http://www.olympusmicro.com/primer/java/jablonski/jabintro/index.html>.
17. Werkhoven, C. J.; Deinum, T.; Langelaar, J.; Rettschnick, R.P.H.; Van Voorst, J. D. W. *Chem. Phys. Lett.* **1975**, 32, 328.
18. Tuszyński, J. A.; Dixon, J. M.; Engelborghs, Y. *Chem. Phys. Lett.* **2001**, 350, 509.
19. Strickler, S. J.; Berg, R. A. *J. Chem. Phys.* **1962**, 37, 814.
20. Birks, J. B.; Tripathi, G. N. R.; Lumb, M. D. *Chem. Phys.* **1978**, 33, 185.
21. Knox, R. S.; Amerongen, H. V. *J. Phys. Chem. B.* **2002**, 106, 5289.
22. Hirayama, S.; Phillips, D. J. *J. Photochem.* **1980**, 12, 139.
23. Englman, R.; Jortner, J. *Mol. Phys.* **1970**, 18, 145.

7.16 General conclusion and outlook

This thesis is based on the results of a series of investigations of the photophysical and photochemical properties of selected aromatic molecules. There is no deliberate relationship between the various compounds but a recurring theme running throughout the work has been the effect of local environment on the fluorescence yield and lifetime of the target compound. With 1H,3H-iso-chromeno[6,5,4-mna]xanthene-1,3-dione, we find that there is essentially no sensitivity towards solvent polarity and, to a large degree, this molecule behaves as a classical polycyclic aryl hydrocarbon. It is strongly fluorescent and relatively stable, even in the presence of active free radicals. Such fluorophores are attractive as luminescent labels and as photo-initiators for polymerisation. In principle, a series of derivatives could be made so as to modulate solubility or compatibility, leading to a wealth of new fluorescent compounds. Unlike many unsubstituted polycycles, the target compound does not self-associate or form excimers at reasonable concentration. A small change to the structure switches on intramolecular charge transfer. Thus, 4-N,N-dimethyl-1,8-naphthalic anhydride (MBIC) is a dipolar compound that crystallises readily. Individual molecules within the crystal lattice retain their own identity and do not interact with neighbours. Surprisingly, this leads to relatively strong fluorescence. Such photonic crystals could have interesting applications in the field of solar concentrators or solid-state emitters. We worked only with MBIC but it is easy to imagine that many related derivatives could be synthesized. Because the nature of the emission is associated with charge recombination it is likely that the HOMO-LUMO energy gap could be tuned by synthesis, thereby expanding the versatility of the compounds. It should be stressed that identifying fluorescent crystals, especially if a suitable range of emission wavelengths can be engineered, provides many new opportunities to design robust and photo-stable applications.

The O-doped polycyclic aromatic hydrocarbon PXX was introduced recently as a possible ingredient in molecular-based organic electronic devices. The molecule contains two oxygen atoms at key bridgehead positions and these heteroatoms cause minor structural perturbation. The resultant lack of planarity provides a source for dynamic fluctuation between what might be termed structural isomers. Although the geometry changes are small, the photophysical properties of PXX are dependent on temperature and on the viscosity of the surrounding medium. Such compounds compliment the well-known class of molecular rotors where largescale geometrical changes accompany excitation. Geometry fluctuations in PXX can be considered within the framework of Kramers' theory for weakly activated barrier crossing. It is remarkable that this theoretical model has stood the test of time and is still the most suitable tool for critical analysis of internal rotations in semi-rigid molecules. Structural perturbations are dampened in plastic films and in rigid optical glasses,

where PXX becomes strongly fluorescent. The polycyclic backbone is easily expanded and it is likely that these larger analogues will exhibit somewhat modified internal dynamics. We watch with interest to see if these O-doped polycycles offer advantages in molecular-scale electronics. If so, it will be worthwhile expanding our studies to include the larger derivatives.

As a variant on the above studies, we have examined the fluorescence properties of cresyl violet in solution. This compound is often used as a ratiometric standard for the red region but its photophysical properties are not well documented outside of simple alcohol solvents. We have seen a strong sensitivity towards the nature of the solvent. Dimerization of the perchlorate salt occurs in many solvents, including water. This, by itself, is not too surprising and has been reported for many other cationic dyes. However, in this case the dimer remains fluorescent. This is unusual. Our understanding of the effects of dimerization on the optical properties of cresyl violet is based on Kasha theory for excitonic splitting. The theory permits estimation of structural properties but we were not able to confirm these using NMR spectroscopy. The general conclusion is that cresyl violet makes a good fluorescence standard in methanol or ethanol but should not be used in other solvents.

In a final chapter, we study the photochemical bleaching of some typical food dyes. It is recognised that the detailed examination of the underlying mechanisms for photobleaching of organic compounds have been ignored for many decades. This is despite the numerous claims for applications of fluorescent compounds. The work reported here is part of a detailed study by the Molecular Photonics Laboratory to uncover the secrets of photofading of organic chromophores. This work should be of great interest to the photochemistry community but is slow and rather tedious. The triplet excited state plays an important role in photodegradation of Erythrosine, where singlet molecular oxygen initiates chemical breakdown. This might not be the case for other dyes, thereby opening interesting possibilities for comparison. It seems likely that more attention will be given to the use of “non-toxic” dyes because of the huge costs associated with getting approval from health authorities for new reagents. As such, our work on these food dyes might be seen as the starting point.